Investigation of Hypervelocity Impact Phenomena Using Real-Time Concurrent Diagnostics

Thesis by

Jonathan Michael Mihaly

In Partial Fulfillment of the Requirements

for the Degree of

Doctor of Philosophy

California Institute of Technology

Pasadena, California

2013

(Defended May 21, 2013)

For my family

Acknowledgements

I would like to thank my advisor Ares Rosakis for his guidance and support throughout my time at Caltech. Ares, you have given me the opportunity to pursue my interests in space exploration while somehow keeping me focused and directed towards the completion of my thesis. You have been an excellent mentor and role model. Your ability to lead and inspire, while maintaining a sharp technical prowess, is something I aspire to.

I would like also to acknowledge and thank the members of my thesis committee: Guruswami Ravichandran, Michael Ortiz, and Sergio Pellegrino. Thank you, Michael and Sergio, for taking the time to meet and provide me with invaluable insight and constructive feedback. Thank you, Ravi, for your advice and guidance over the past six years. In particular, thank you, Ravi, for encouraging me to pursue my goals while showing me to how to keep the big picture in mind.

Also, thank you to the remaining member of my candidacy committee, Professor Hiroo Kanamori. As an engineer, it has been a real pleasure to have the opportunity to interact with a pioneer in the field of geosciences. I feel very fortunate to have been a student at an institution where such collaboration is not only possible but encouraged.

I'd also like to thank Ares' administrative assistant, Donna Mojahedi, for her patience and support for the past 5 years. Despite Ares' dynamic and exhausting schedule, Donna somehow always found the time to submit my orders and arrange meetings with Ares.

My work has been supported by the Department of Energy National Nuclear Security Administration under Award Number DE-FC52-08NA28613. The PSAAP

program, under the direction of PI Professor Michael Ortiz, enabled the development of our SPHIR facility. Because of the PSAAP program, I was given the opportunity to operate and develop a world-class facility. Thank you Michael and the entire PSAAP community for your support. Also, a sincere thank you to Susan Powell for coordinating my PSAAP-related activities.

I think the best part of being a Caltech student is the exceptional quality of the people you interact with on a daily basis. During my time at Caltech, I have had the privilege and good fortune of working with Dr. Marc Adams from NASA JPL on a daily basis. I cannot adequately convey my gratitude for Marc and the time he has invested in my education. Having the chance to learn from Marc and being challenged to meet his high technical standard everyday has immeasurably enhanced my education at Caltech. The critical thinking and attention to detail that I have developed through working with Marc should prove invaluable throughout the course of my career.

I'm very grateful for having the chance to work with two incredible colleagues in Mike Mello and Jon Tandy. My best days in lab over the past 5 years were spent working with Mike or Jon.

An entire generation of GALCIT graduate students have been positively influenced by Mike Mello, and I am very fortunate to have been in the Rosakis group during Mike's time at Caltech. Mike frequently went above and beyond the call of duty in helping his fellow graduate students, often spending hours of his time to carefully and thoroughly explain complex optics concepts. My understanding of optics and opto-mechanics is in large part due to Mike's selfless commitment to teaching. Thank you, Mike, for your friendship and all of the time you spent working with me. I'll always fondly remember our long conversations about optics, the Red Sox, the Patriots, and NASA.

For a year, I had the privilege to work with Jon Tandy. The best experiments I conducted during my thesis work were completed with Dr. Tandy. Jon is a rare talent, who is both a pleasure to work with and extremely knowledgeable. Given what he accomplished in only 14 months at Caltech, I can only imagine what Jon will

do during his career in Academia. Thank you, Jon, for being an awesome colleague, friend, and labmate.

I'd also like to thank the other members of the Rosakis group who I had the opportunity to interact with: Vahe Gabuchian and Leslie Lamberson. Thank you, Vahe, for being an awesome officemate. Vahe, you are also responsible for two of my favorite memories during my time at Caltech: going to buy many video games after our qualifying exams finished and having a small speaking-role in the PhD Comics movie. Thanks for helping make my time as a graduate student interesting and fun. Also, thank you, Leslie, for all of your help showing me the ropes when I was starting in the SPHIR lab.

There are a number of other PSAAP collaborators who have helped me throughout my graduate career. I'd like to thank Bo Li, Professor Houman Owhadi, Tim Sullivan, Lenny Lucas, Professor Dale Pullin, and Professor Dan Meiron. I learned quite a bit from working with this multi-disciplinary group. Thank you Bo for all of our long, productive conversations about the physics and damage mechanisms we observe in our impacts.

Also thank you Dr. Andre Yavrouian, Jerami Mennella, and Tim O'Donnell at NASA JPL for helping me operate, maintain, and clean several components of the SPHIR facility. Special thanks to Phillip Ou for his diligence in hard work in cataloging the capture pack data. I would also like to thank and acknowledge my first year advisor Professor Beverley McKeon and Ae104 advisors Professor Joe Shepherd and Dr. Jay Polk.

I'd also like to thank Harsha Bhat and Professor Charles Sammis. Although much of the work on dynamic fracture I completed on the side with Harsha and Charlie was not included in my thesis, Harsha and Charlie were integral parts of my graduate education. I look very forward to our continued collaboration.

There were a number of other helping hands there to support my work in the lab. Thank you Petros Arakelian for all your help and hard work over the past five years: the facility would not work without you. The aero shop always treated me well and always found a way to get my parts completed on time. Thank you Joe Haggerty,

Brad St. John and Ali Kiani for the many parts in my experiment that you machined.

I would also like to thank the Keck Institute for Space Studies and, in particular, Michele Judd and Professor Tom Prince. My experience with the Keck Institute for Space Studies (KISS) developing the Caltech Space Challenge has been one of my most meaningful endeavors as a Caltech graduate student. Working with KISS on the Space Challenge has enhanced my education and supported my leadership development at Caltech in ways that classes and research cannot. This is a direct result of Tom's initiative to give students the opportunity to organize workshops. Thank you, Tom, for giving students like myself such an opportunity and for trusting us with considerable KISS resources.

My involvement with KISS continues to benefit me, months after the conclusion of the Space Challenge. The contacts that I have made because of KISS continue to provide me with unique opportunities and likely will have a significant effect on the trajectory of my career. My experience with KISS has been so beneficial, that I will likely not realize the full impact until I retire. This is in large part due to the dedication and personal investment in KISS students by Michele Judd and her staff. Nothing I write here can fully express my gratitude for Michele Judd. Thank you Michele for your continuing support and the many hours you have invested in me (and all of your KISS students). I consider myself extremely fortunate to have attended a graduate school with an Institute such as KISS so heavily committed to student development. I am forever grateful to Michele, Tom, and the entire Keck Institute for Space Studies.

My experience with the Space Challenge (and everything related thereafter) would not have been if it weren't for Prakhar Mehrotra. When Prakhar first asked me to help him write a KISS proposal for a small week-long mission design competition, I never would have imagined the ultimate scale and impact of the event. Prakhar is the type of student who enriches the graduate school experience for all of his peers. I am very grateful to have had the good fortune to work with a student like Prakhar. Thank you, Prakhar, for being an incredible friend and colleague. From the Venus Lander to the Space Challenge, I've truly enjoyed working with you. I sincerely hope

we have the opportunity to work together again in the future.

There were a number of other individuals who were critical in organizing the Caltech Space Challenge. Thank you Dr. Don Yeomans, Professor Paul Dimotakis, John Baker, Nathan Strange, Damon Landau, Lorraine Alexander, Nigel Angold, Aline Zimmer, Dimity Nelson, Paula Lonnergan, Sharon Bryant, and Julie Castillo-Rogez: your help and volunteered time has made a significant difference in the education of a large number of students around the world.

Throughout my education, I have been very fortunate to have a number of mentors. I'd like to thank my undergraduate research advisor, Professor Mark Glauser. Professor Glauser went out of his way to give me the opportunity to work in his lab the summer before my senior year. This experience likely contributed to my opportunity to attend Caltech and forever changed my life. I'd also like to thank Dr. Douglas O'Handley for his friendship and mentoring, since my time at the NASA Ames Academy in the summers of 2007 and 2008. Doug, you have helped shape the way I think about space policy and program management. I'd also like to thank Buzz Aldrin for taking me on as his intern. Dr. Aldrin, it has been an absolute privilege and honor to learn from and work with you. A sincere thank you to Michele Judd and Lou Friedman for recommending me to Dr. Aldrin for this once-in-a-lifetime opportunity.

Daily life at Caltech was made infinitely better by the amazing friends that I had the privilege of meeting along the way. Thank you to all my friends for being awesome. From daily lunches to softball to epic weekends at Big Bear, you really made my time at Caltech enjoyable. Thank you Nick Boechler, Mumu Xu, Ian Jacobi, Andy Richards, Christy Winiarz Schmidt, and all of my first-year classmates for helping me survive our one-year Masters program. And thank you Boechler for being a great friend and roommate. Also, thank you, Nick Parziale and Jason Rabinovitch, for taking on the second Caltech Space Challenge. You guys really did an incredible job, and because of your hard work, the Space Challenge continues on.

And last, but not least, I'd like to thank my family and amazing wife Shannon. Moving to California for graduate school has been difficult, but your support and

positive outlook has made it possible. Thank you Mom, Dad, and Sarah for your constant love and support. My father is the hardest working person I know, and the lessons he taught me of patience and hard work carried me through graduate school. Thank you Mom and Sarah for always being there. I'd also like to thank my wife's family for their love, support, and generous hospitality. I'm extremely fortunate to have such a caring, patient, and supportive family.

Shannon, you are the best thing that has ever happened to me. What can I say to thank the most important person in my life? You are the reason I am able to work hard towards our goals and you make every day better. Thank you for your unending love and steadfast support. Thank you for putting up with me while I was writing my thesis. Actually, I should really thank you for putting up with me for the past seven years. I would not be the person I am today without you. Now that this thesis is complete, I look forward to more adventures.

Abstract

Hypervelocity impact of meteoroids and orbital debris poses a serious and growing threat to spacecraft. To study hypervelocity impact phenomena, a comprehensive ensemble of real-time concurrently operated diagnostics has been developed and implemented in the Small Particle Hypervelocity Impact Range (SPHIR) facility. This suite of simultaneously operated instrumentation provides multiple complementary measurements that facilitate the characterization of many impact phenomena in a single experiment. The investigation of hypervelocity impact phenomena described in this work focuses on normal impacts of 1.8 mm nylon 6/6 cylinder projectiles and variable thickness aluminum targets. The SPHIR facility two-stage light-gas gun is capable of routinely launching 5.5 mg nylon impactors to speeds of 5 to 7 km/s. Refinement of legacy SPHIR operation procedures and the investigation of first-stage pressure have improved the velocity performance of the facility, resulting in an increase in average impact velocity of at least 0.57 km/s. Results for the perforation area indicate the considered range of target thicknesses represent multiple regimes describing the non-monotonic scaling of target perforation with decreasing target thickness. The laser side-lighting (LSL) system has been developed to provide ultra-high-speed shadowgraph images of the impact event. This novel optical technique is demonstrated to characterize the propagation velocity and two-dimensional optical density of impact-generated debris clouds. Additionally, a debris capture system is located behind the target during every experiment to provide complementary information regarding the trajectory distribution and penetration depth of individual debris particles. The utilization of a coherent, collimated illumination source in the LSL system facilitates the simultaneous measurement of impact phenomena with near-IR and UV-vis spec-

trograph systems. Comparison of LSL images to concurrent IR results indicates two distinctly different phenomena. A high-speed, pressure-dependent IR-emitting cloud is observed in experiments to expand at velocities much higher than the debris and ejecta phenomena observed using the LSL system. In double-plate target configurations, this phenomena is observed to interact with the rear-wall several µs before the subsequent arrival of the debris cloud. Additionally, dimensional analysis presented by Whitham for blast waves is shown to describe the pressure-dependent radial expansion of the observed IR-emitting phenomena. Although this work focuses on a single hypervelocity impact configuration, the diagnostic capabilities and techniques described can be used with a wide variety of impactors, materials, and geometries to investigate any number of engineering and scientific problems.

Contents

List of Figures

List of Tables

AGS	average grayscale
AR	accelerated reservoir
BLE	ballistic limit equation
CDF	cumulative distribution function
ISS	International Space Station
LSL	laser side-lighting system
MCP	micro-channel plate
MOD	meteoroids and orbital debris
OD	optical density
RMS	root mean square
RSS	root sum square
SPHIR	Small Particle Hypervelocity Impact

α	partitioned amount of kinetic energy used in blast wave
β	impactor yaw angle
Δp	change in pixel coordinate
Δt	instrument inter-frame time
ΔZ	change in measured debris cloud leading edge position
γ	ratio of specific heats
θ	impact obliquity angle
ρ	material density
σ_y	quasi-static yield strength
σ_Y	rate-dependent yield strength
A	perforation area
C	material heat capacity
c_0	material sound speed
c_p	longitudinal wave speed
c_s	shear wave speed
D	perforation diameter
d	impactor diameter
E	energy
h	target plate thickness
f	focal length
K	dimensionless constant from blast wave analysis
L	latent heat of fusion
l	impactor length
M	mv^n
m	impactor mass
N	stress dissipation exponent
n	velocity scaling exponent
P_{atm}	target chamber ambient atmospheric pressure
P	impact-induced shock pressure
R	radius of blast wave or IR-emitting cloud
R_{exp}	experimentally measured radius of IR-emitting cloud
R_{gas}	universal gas constant
R_w	radius of blast wave predicted by Whitham's dimensional analysis
S	pixel length scale
T	temperature
T_f	fraction of transmitted light intensity
t	effective instrument measurement time
t_{del}	programed instrument delay time
t_{exp}	programmed instrument exposure time
t_{trig}	delay between impact and trigger signal
u_s	shock speed
u_p	particle speed
v	impactor velocity, also v_{impact}
v_{deb}	debris cloud velocity, collinear with impact vector

Chapter 1

Introduction

1.1 Motivation

Hypervelocity impact of meteoroids and orbital debris (MOD) poses a serious and growing threat to spacecraft. Any spacecraft, particularly those intended for long duration spaceflight or entry, descent, and landing must be designed with the capability to withstand extended exposure to the MOD environment. The Columbia accident serves as a tragic reminder of catastrophic consequences [4] of significant impact damage. Furthermore, as international involvement in space expands, the severity of the orbital debris environment continues to grow at an increasing rate.

The risk of impact with space debris is not limited to spacecraft orbiting in Earth orbit. Meteoroids, or particles of debris originating from comets or asteroids, threaten inter-planetary spacecraft throughout their multi-year mission duration. For example, in October of 2014, Comet 2013 Al is likely to make a close approach of Mars. Current predictions estimate that the comet could come within $300,000$ km of Mars, which would expose the planet to the gaseous, dusty coma [48]. Consequently, comet dust particles traveling with relative speeds of 56 km/s or more could sandblast spacecraft in Martian orbit [9].

Hypervelocity impacts induce a complex dynamic material response, which includes numerous interacting phenomena such as mixed phase flow, fragmentation, spallation, melting, vaporization, and ionization. Due to such complexity, modeling success has been limited and remains inadequate. The current understanding of hy-

pervelocity impact damage is obtained largely through experimental evaluation [5] of MOD shielding systems. The empirical models used to describe this data are specific to the materials/component configurations used in the tests and the test conditions. Such models cannot be safely extrapolated to other materials or conditions. Furthermore, given the high operating cost of many impact facilities, the extensive shield testing required to adequately characterize the variability and uncertainty in shield performance can be prohibitively expensive. Often inadequate data exists to describe the stochastic damage mechanics that govern shield system performance. Therefore, the aerospace industry would greatly benefit from the development and implementation of concurrent real-time diagnostics to maximize experiment-output and advance the characterization of hypervelocity impact phenomena.

1.2 Significance and Objectives

The investigation of hypervelocity impact phenomena described in this work focuses on normal impacts of 1.8 mm Nylon 6/6 cylinder projectiles and variable thickness aluminum targets. The objectives of this work are threefold. The first objective has been the development of a hypervelocity impact facility with multiple concurrently operated diagnostics. This effort includes the development of a new optical technique to characterize debris cloud phenomena and its implementation in a comprehensive ensemble of *in situ* instruments. Such an approach is directed towards maximizing data output to provide the highest possible return on investment given the fixed cost of each impact experiment.

The second objective the application of the described diagnostics to characterize new impact phenomena and contribute to modern scaling laws used to describe hypervelocity impact damage. Currently, the vast majority of hypervelocity impact testing results and damage models are for spherical impactors. The effect of shape in impacts is not trivial, considering that for equivalent diameters, cylinders have 50% mass than cylinders and therefore carry 50% more momentum and translational kinetic energy. Furthermore, despite the stochastic nature of impact damage, such variability is not

accounted for in many of the models used to assess the risk posed to spacecraft by hypervelocity impact with space debris. Therefore, the use of cylindrical impactors and volume of repeated experiments in this work serves as an opportunity to address and contribute towards improvement of current methods for spacecraft protection.

The context of this work presents the third and final objective. The experimental work described within this thesis has been a part of a large program to support the development of predictive, numerical models for hypervelocity impact.

1.3 Definitions

1.3.1 Hypervelocity Impact

The conditions required for hypervelocity impact are not well defined. A large number of definitions have been proposed and implemented in the literature since the beginning of the space age. One common definition for hypervelocity is for impact speeds greater than the sound speed of the material target [72]. Another classification describes hypervelocity impact as the condition when shock effects are important. A popular description defines hypervelocity impact starting at impact speeds where the impactor and target materials are completely pulverized in the immediate region of impact by [67].

These definitions all refer to a state when the stresses involved in the impact are many times larger than the flow strength of the materials involved. In such a scenario, the material is assumed to have no shear strength and is mathematically described like a fluid. This is referred to as the hydrodynamic treatment [41], and the mechanics associated with this assumption are discussed in section 1.6.

Therefore, hypervelocity impact is most commonly defined as the condition when the hydrodynamic treatment is applicable. Accordingly, despite the variation in specific definitions, the current consensus is that the conditions for hypervelocity impact are material specific. Therefore, the hypervelocity regime can begin at impact speeds from 1.5 to 2.5 km/s for materials with low strength to density ratios, such as plastics

or some metals like lead or gold. For high materials with high strength-to-density ratios, such as hard ceramics and born metals, impacts speeds from 8 to 10 km/s are required for hypervelocity impact [67]. For aluminum, a widely agreed upon definition for hypervelocity impact is impact speeds of 5 km/s or above.

1.3.2 Target Perforation and the Ballistic Limit

A target plate is perforated if impact damage includes a through-hole allowing the transmission of light from one side of the plate to the other. Impact damage resulting in cratering, but no perforation, is referred to as partial penetration. Accordingly, perforation area is defined as the area projected by a collimated light source through the target and onto a plane parallel to the original target back-surface. Partial penetration is characterized as having zero perforated area.

The ballistic limit is defined as the transition condition separating target partial penetration and perforation. The parameter used in describing the ballistic limit is the variable considered when all other impact parameters are held constant. For example, the ballistic limit velocity is the minimum impact velocity where perforation is first observed given constant impact geometry and material properties. Similarly, the ballistic limit could be described as a critical thickness or projectile diameter.

The transition point from partial penetration to perforation is stochastic: variability in the response of a target for repeated impact conditions is observed. Therefore, in military ballistics the definition of a ballistic limit includes a statistical statement. For example, a typical ballistic limit would be described as the V_{50} speed: the impact speed at which 50% of the results (for constant target and impactor conditions) are failures [67]. However, in the context of spacecraft shielding ([5]) no formal definition is provided. Therefore, the ballistic limit in hypervelocity impact shield design is currently treated as a qualitative quantity referring to the minimum conditions observed to result in system perforation.

Within the impact shielding engineering community, the definition of ballistic limit to describe the onset of target perforation is not unique. The “failure” of a

system can be defined to correspond to anything from plate bulging, to detached spall, to perforation. Accordingly, the concept and definition of a ballistic limit can be extended to describe the occurrence of a given damage condition. However, in the context of the analysis presented herein, failure corresponds to perforation of a target plate. Therefore, the ballistic limit is henceforth used to describe the transition between partial penetration and perforation.

1.3.3 Impact Configuration, Obliquity, and Yaw Angle

The dimensions and geometry used in forthcoming discussion to describe impact conditions are defined herein. Consider a projectile with impact speed v_{impact} moving towards a target plate, as illustrated in Figure 1.1. The impact geometry shown, given the dimensions of the impactor and target, the impactor obliquity, and yaw angle is henceforth referred to as the impact configuration.

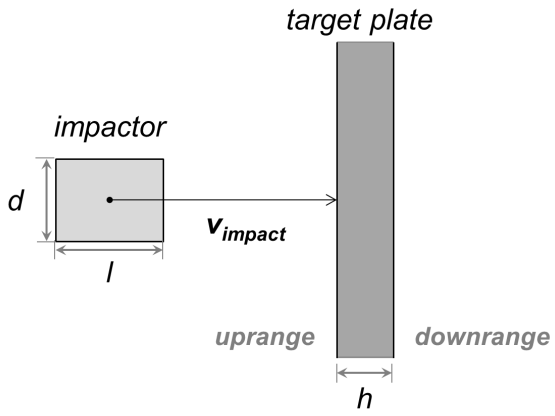

Figure 1.1: General dimensions in the considered impact configuration. An impactor of width d and length l travels at impact speed v_{impact} towards a target plate of thickness h.

The target plate is described by plate thickness h. Impactor length l also defines the direction of the impactor long axis. The cross-sectional area of the impactor along this axis is described by characteristic width d. Therefore, a cylindrical impactor is described with diameter d. An equiaxed projectile ($l/d = 1$) is often referred to as a "chunky" or "compact" impactor.

Figure 1.1 also depicts a common convention for direction in ballistics. Downrange corresponds to the direction of the impactor velocity vector. Uprange is the opposite of downrange. Accordingly, the uprange surface of the target is impacted during an experiment, as shown.

Impact obliquity angle is defined with respect to the target normal, as illustrated in Figure 1.2, such that $\theta = 0$ corresponds to alignment of the impactor velocity vector and target plate normal. A normal impact is defined as an impact with $\theta = 0$ impact obliquity. Note that this is the convention for θ used in the impact shielding community. However the planetary impact community defines impact obliquity as the complementary angle, such that 90^o corresponds to a normal impact.

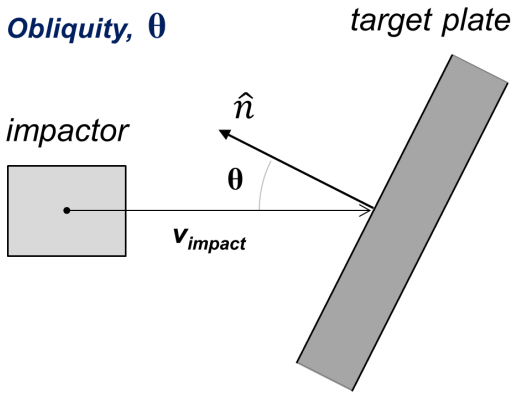

Figure 1.2: The definition of impact obliquity θ: the angle between the impactor velocity vector and target surface normal $\hat{n}$

.

Yaw angle β is defined as the angle between the impactor's long axis and the velocity vector. Impact yaw angle β_0 therefore describes the yaw angle at the time of first contact between impactor and target. An impact yaw angle of $\beta_0 = 0$ corresponds to alignment of the impactor velocity vector and long axis of the impactor. Impactor tumbling therefore results in variable yaw angle. The definition to yaw angle does not apply to spherical impactors. A graphical representation of yaw angle is provided in figure 1.3. Note that this definition for yaw angle is independent of the relative orientation of the plate surface normal. For a cylindrical or cubic impactor, $\beta_0 = \theta$ therefore corresponds to planar impact of the impactor with the target surface.

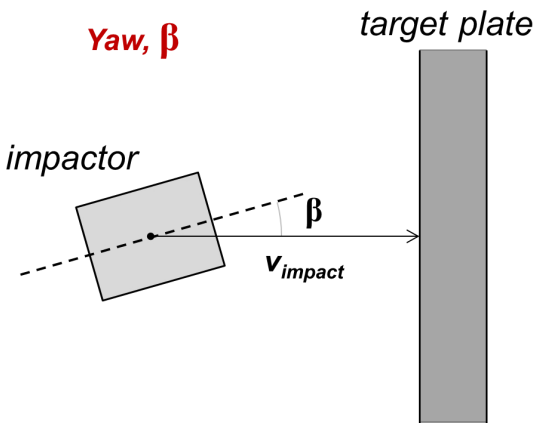

Figure 1.3: The definition of yaw angle β. Impact yaw angle β_0 corresponds to the angle between the long axis of the impactor and target surface normal $\hat{n}$ at the time of impact.

1.4 The Space Debris Environment

The space debris environment is composed of two populations of debris: orbital debris and meteoroids. Orbital debris includes nonfunctioning components or fragments of spacecraft orbiting the Earth. Meteoroids are naturally occurring particles that orbit around the sun [5]. A visualization of the space debris environment is presented in Figure 1.4, courtesy of the European Space Agency (ESA).

More specifically, orbital debris consists of metallic fragments, solid rocket motor exhaust, aluminum, paint, debris from explosive separation, and other spacecraft components. The largest orbital debris objects include upper-stages of rockets and defunct satellites. For debris risk assessment, the characteristic particle density for orbital debris is assumed to correspond to aluminum, 2.8 g/cm^3 [5]. The current model for orbital debris used to describe the size and speed distribution of particles is the Orbital Debris Engineering Model 2000 (ORDEM2000) [34].

In orbit at 400 km, the altitude of the International Space Station (ISS) orbit, the average speed is approximately 7.7 km/s. Because orbital debris particles populate a large number of orbits, the relative impact velocities range from 1 km/s to 15 km/s. The average orbital debris impact speed is estimated at approximately 9 km/s (at 400 km) [34]. Note that these impact speeds are independent of particle size.

Figure 1.4: Arts interpretation of the space debris environment in Earth orbit. Image courtesy of ESA.

Average impact speeds for meteoroids are typically higher than orbital debris, given that the Earth itself moves at about 30 km/s as it orbits the sun [72]. As described by the Meteoroid Engineering Model (MEM) [39], meteoroid impact speeds with spacecraft range from 2 to 72 km/s, with an average impact speed of approximately 19 km/s. The majority of meteoritic material encountered by spacecraft is believed to originate from comets. Accordingly the characteristic density of meteoroid particles is assumed by NASA [5] to range from 0.5 to 2.0 g/cm^3.

Note that the most-frequently encountered meteoroids are millimeter scale or below. Furthermore, the only way to protect a spacecraft from meter-scaled meteor is to avoid it entirely. Therefore, the impact shielding community often optimistically refers to meteoroids as "micrometeoroids." The term MMOD (micrometeoroids and

orbital debris) is often cited in the literature referring to the space debris environment described herein.

The distributions of space debris particle size are described as an area flux: the number of particles passing through a unit area over a prescribed amount of time. Given an orbit altitude and inclination, the described in the engineering models for space debris [34] and meteoroids [39] describe a flux of particles as a function of particle size. An example provided by the NASA handbook for MOD shielding [5] for the modeled flux of particles in the orbit of the ISS (400 km altitude, 51.6 degree inclination) is annotated and presented in Figure 1.5. The populations of both orbital debris and meteoroids for sizes up to approximately 1 mm are inferred from orbital impact mission data [22], [20], [34]. The population of particles with characteristic dimension above 5 mm is interpreted from radar. The intermediate range of particle size (between 1 mm and 5 mm) is interpolated from the measured length scales [58].

An important consideration in hypervelocity impact risk mitigation is the threat posed to spacecraft by the MOD debris environment is directional. The highest flux of particles and impact speeds are encountered on forward facing surfaces (faces oriented towards the spacecraft velocity vector). For example on the Long Duration Exposure Facility (LDEF) mission, on the forward facing surfaces there were 20 times more impact craters observed on the forward facing surfaces than those on the aft and 200 times more than observed on the Earth-facing (nadir) surfaces ([22]).

When in Earth orbit, the Earth provides a substantial amount of shielding from the natural meteoroid environment, which reduces the flux of meteoroids for all surfaces except space-facing (opposite nadir) surfaces [72]. Spacecraft operating in deep space are removed from the orbital debris environment, but the Earth no longer provides a directional-reduction in meteoroid flux.

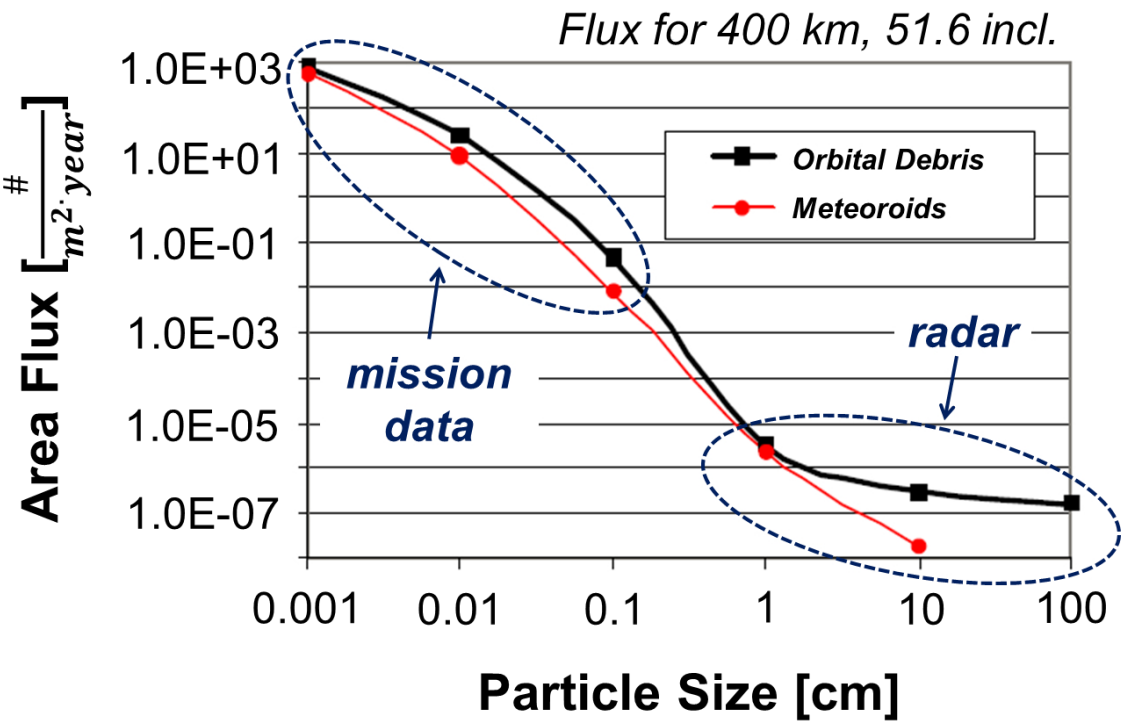

Figure 1.5: Flux of space debris particles vs. size for the orbit of the International Space Station (400 km altitude, 51.6 degrees inclination), as modeled by the Orbital Debris Engineering Model ORDEM2000 and Meteoroid Engineering Model (MEM). Annotations describe the populations of debris that are estimated using mission impact data and radar. The data describing flux is originally presented in the NASA Handbook for Designing MMOD Protection [5] on page 16.

1.5 Hypervelocity Impact Risk Mitigation

1.5.1 Impact Shielding Methods

To protect spacecraft from the dangers posed by hypervelocity impact the approach is two-fold. The risk is first mitigated through operational procedures to minimize the exposure of critical or vulnerable components to directions with high debris flux. A common technique is the orientation of the spacecraft such that mission-critical systems are shielded by lower-risk surfaces [5]. This strategy is therefore dependent upon the accuracy of the engineering models used to describe the orbital debris and meteoroid environment. Although this primary approach reduces the likelihood of

debris impact-induced system failure, hypervelocity impacts still occur. Therefore, the second component of hypervelocity impact protection is the use of specially engineered shielding systems.

The shielding systems used to protect spacecraft from hypervelocity impacts with space debris are multi-layer systems. The most common is a dual-plate system, often referred to as a "Whipple shield" or "bumper shield," which features a thin outer-layer plate separated by a stand-off distance in front of a rear-wall plate. For many spacecraft, the rear wall can serves as a pressure shell or system cover. An example of this shielding concept is provided in Figure 1.6 (a). This system uses the out-layer "bumper" as a sacrificial plate to break up an impactor. The resulting debris cloud consisting of multi-phase impactor and target material propagates at high-speeds towards the rear-wall plate. The stand-off distance between the bumper and rear-wall allow the debris cloud to volumetrically expand and distribute the impulse carried from the original impactor over a larger surface area on the rear-wall. Typical bumper stand-off distances can range from 5 to 30 cm [5]. The bumper shield concept can be used with a variety of materials, but typically both the bumper plate and rear-wall are aluminum. The use of this dual-plate system has been experimentally shown to provide mass-saving factors of 10 over the equivalent monolithic shield required to prevent rear-wall perforation [67]. Additionally, compared to a monolithic shield, a dual-plate system of equivalent mass provides a significant increase in the expected ballistic limit impactor diameter [5].

Compared to dual-plate systems, additional mass savings of 50% have been demonstrated experimentally using multi-layer systems consisting of 3 or 4 wall shields [5]. In addition to aluminum, Nextel ceramic fabric and Kevlar high-strength fabric are commonly used as layers of shielding material in such systems. A dual-plate aluminum shield with an intermediate blanket consisting of Nextel on-top of Kevlar, is typically referred to as a "stuffed" Whipple shield. A system implementing multiple bumper layers of Nextel in front of a rear-wall is known as the multi-shock shield. Both Kevlar and aluminum have been considered for use in the multi-shock shield. Examples of the stuffed bumper and multi-shock shield systems are provided in Fig-

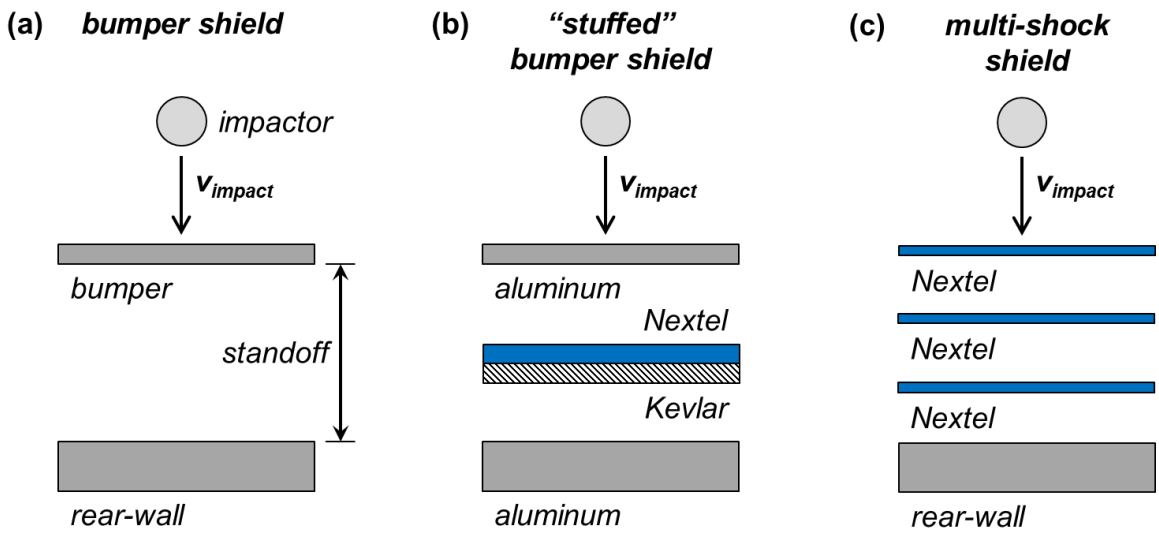

Figure 1.6: Three common types of hypervelocity impact shielding systems [5]. (a) The bumper shield, or Whipple shield. The bumper and rear-wall are typically aluminum, but a number of materials have been considered. (b) The "stuffed" bumper shield, consisting of aluminum bumper and rear-wall with an intermediate Nextel and Kevlar blanket layer. (c) The multi-shock shield is composed of multiple bumper layers, typically composed of Nextel. The rear-wall is commonly aluminum or Kevlar.

ure 1.6 (b) and (c) [5]. The three shielding system concepts presented in Figure 1.6 represent some of the most commonly implemented materials and designs. However, the variety of multi-layered systems considered, in terms of number of layers and materials used, is extensive.

The design of the described multi-layer system involves the selection of materials, plate thicknesses, and separation distances. Consequently, the multi-dimensional determination of the ballistic limit of these systems is complex. A description of the ballistic limit (failure criterion) is therefore required for each type of shielding system utilized.

Ballistic Limit Equations (BLE) used to design spacecraft shielding systems typically describe a critical impactor diameter corresponding to the onset of system failure. (Recall that system "failure" and the corresponding definition of ballistic limit are system specific.) The consideration a critical impactor diameter facilitates risk assessment and direct comparison with the size-flux distribution of particles in

the modeled debris environment [34], [39].

Such design equations are determined empirically based on a limited number of experiments for each shielding system configuration. The equations first consider the required bumper and rear-wall thickness required to prevent perforation of an impactor given impact speed, impactor material density, target material density and plate stand-off distance. Based on this empirically determined equation, the BLE is then presented as the critical impact diameter (above which a shield fails) as a function of impact speed, for a given bumper shield configuration (material and geometry).

1.5.2 Risk Assessment

Given the modeled flux of the debris environment [34],[39] the threat to an orbiting spacecraft (such as the ISS) is computed by NASA using a code known as Bumper [23]. Bumper estimates the number and size of impacts on a spacecraft, element by element, and evaluates the threat on the spacecraft given predictions of damage based on the ballistic limit equations and damage predictor equations. This approach there is used to determine the most vulnerable components of a spacecraft (the "risk drivers") [5].

Therefore, current methods for hypervelocity impact risk assessment are dependent on two classes of equations: the aforementioned ballistic limit equations and damage predictor equations. The damage predictor equations are empirically derived scaling laws, such as those by Cour-Palais [8] and Horz [20], to describe impact cratering and perforation.

1.6 Hypervelocity Impact Mechanics

1.6.1 The Hydrodynamic Assumption and Shock Waves

If the amplitude of stress waves is large, such that the hydrostatic component greatly exceeds (by several factors) the dynamic flow strength of the material, the corresponding shear stress can be neglected. The material can then be approximated as having

no shear strength and treated like a fluid [25, 41, 67]. This is known as the hydrodynamic treatment [41] and is the reason why numerical simulations of hypervelocity impact are often referred to as "hydrocode."

With the hydrodynamic assumption, the mathematical descriptions of shockwaves originally developed by Rankine and Hugoniot for fluids can be applied to the shock dynamics within a material [41]. Consider a one-dimensional, planar shock-front traveling with shock-speed u_s, as shown in Figure 1.7. Ahead of the shock front, assume the particles are stationary, $u_0 = 0$. At the shock front and behind it, the particles move with velocity u_p. Before passage of the shock front, the pressure is P_0, density is ρ_0 and energy is E_0. Behind the shock front, the pressure has increased to P, the density to ρ and energy to E. Considering a reference frame centered on the shock front, particles approach the shock front with velocity u_0 and recede behind the shock with velocity $u_p - u_0$. Accordingly, within this reference frame, the flow velocity is supersonic ahead of the shock and subsonic behind the front.

Using this shock-centered reference frame and applying the conservations of mass, momentum, and energy across the shock front, using the shock-centered reference frame results in the well-known Rankine-Hugoniot relations [25]: Eq. 1.1, Eq. 1.2, and Eq. 1.3.

$$\rho_0 u_s = \rho \left(u_s - u_p\right) \tag{1.1}$$

$$P - P_0 = \rho_0 u_s u_p \tag{1.2}$$

$$P u_p = \tfrac{1}{2}\rho_0 u_s u_p^2 + \rho_0 u_s \left(E - E_0\right) \tag{1.3}$$

In deriving the above relations, the following assumptions are made: the shock is a discontinuity with zero thickness, the shear modulus of the material is zero, body forces and heat conduction are negligible and there is no elasto-plastic material behavior [41]. A useful quantity to define is $\rho_0 u_s$, which is often referred to as the

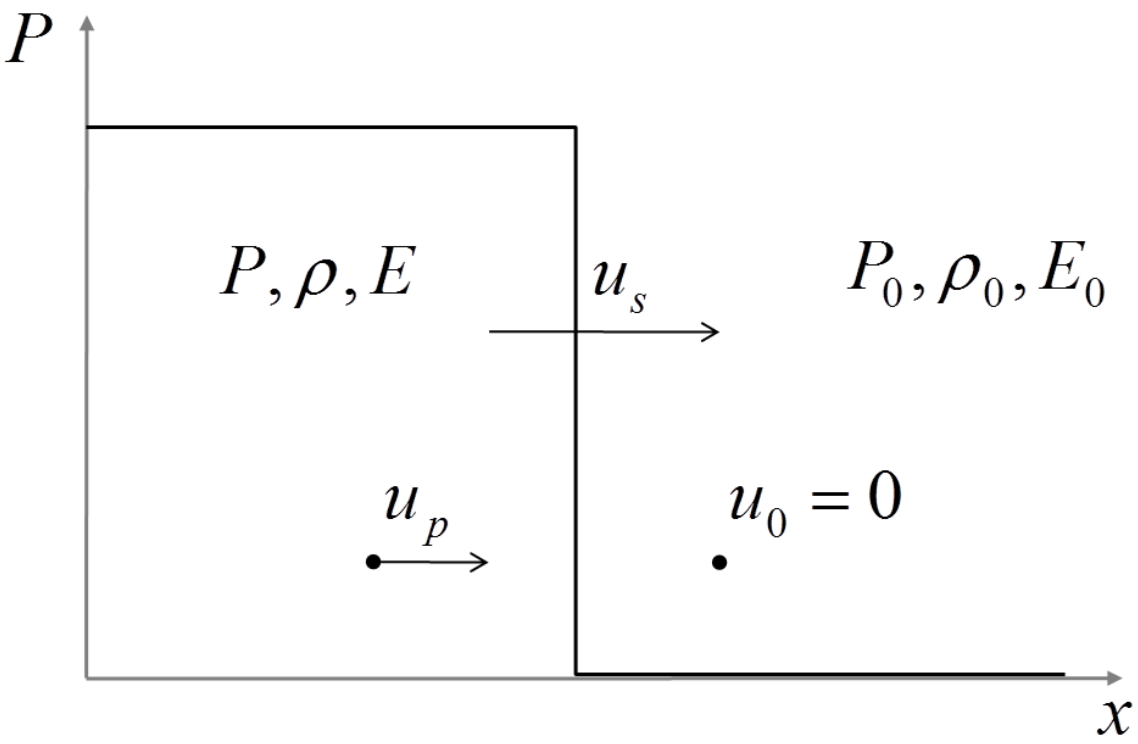

Figure 1.7: Shock front moving with velocity u_s and corresponding parameters considered in the conservation of mass, momentum, and energy [41].

shock impedance.

Substituting the conservation of mass (Eq. 1.1) into the conservation of momentum (Eq. 1.2) and considering the definition of specific volume ($V = 1/\rho$) results in Eq. 1.4.

$$\rho_0^2 u_s^2 = \frac{P - P_0}{V_0 - V} \tag{1.4}$$

Eq. 1.4 and the conservation of momentum can be substituted into the conservation of energy Eq. 1.3 to obtain Eq. 1.5 . This more common form of the conservation of energy is sometimes referred to as the Rankine-Hugoniot equation, but is most-commonly known as "the Hugoniot."

$$E - E_0 = \tfrac{1}{2}\left(P + P_0\right)\left(V_0 - V\right) \tag{1.5}$$

The Hugoniot defines the relationship between pressure and density and is de-

fined as the locus of shocked states in the material [41]. The Hugoniot, and corresponding pressure-density dependence, can be interpreted graphically as presented in Figure 1.8. The amplitude of the shock is described by what is referred to as the Rayleigh line: the straight line connecting the conditions (P_0, V_0) and (P_1, V_1) in Figure 1.8 (a). When the material is shocked, it changes discontinuously from the un-shocked (P_0, V_0) to the shocked (P_1, V_1) condition. Therefore, the intersection of the Hugoniot and Rayleigh lines defines the shock-state in the material.

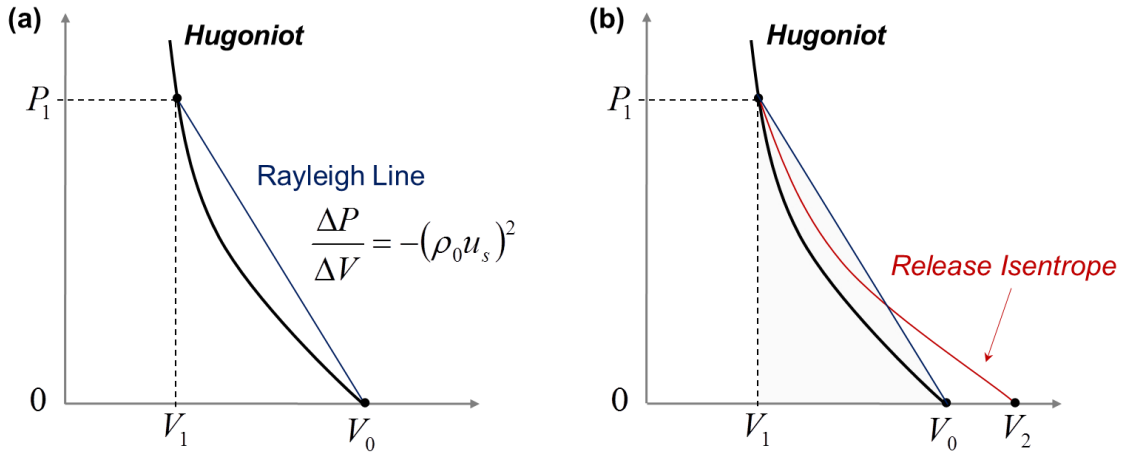

Figure 1.8: (a) The Hugoniot plotted in terms of pressure P vs. specific volume V (density) along with the Rayleigh line. [41] (b) The release isentrope plotted describing the isentropic release of the material from the shocked state. The lightly shaded region under the Rayleigh corresponds to the increase in specific internal energy across the shock.

The slope of the Rayleigh line describes the amplitude of the shock and is given by Eq. 1.6 (which is simply a variation of Eq. 1.4). Therefore, the amplitude of stress ($P - P_0$) in a shock is proportional to the square of the shock velocity. For an unloaded material at rest ($P_0 = 0$, $u_0 = 0$), the increase in specific internal energy across the shock is given by the area under the Rayleigh Line [25], as shown in Figure 1.8 (b). The change in pressure, density and temperature across the shock front is irreversible and differs from a reversible adiabatic change because of the increase in entropy. The

increase in entropy across the shock is of the third order in shock strength [25].

$$\frac{P - P_0}{V - V_0} = -\left(\rho_0^2 u_0^2\right) \tag{1.6}$$

The release of the material from the shocked state is isentropic. The material therefore returns to a lower stress state along a release isentrope as shown in Figure 1.8 (b). The entropy "trapped" in the material manifests itself as internal energy and increases the temperature of the material. This increase in temperature determines the phase of the material upon release from the shock state and for sufficiently large, it is possible for the material to melt or vaporize during unloading (or even loading) [25].

1.6.2 Shock Speed vs. Particle Speed

The relationship between the shock speed and particle speed can be empirically described using an n-th order polynomial (with parameters C_0, S_1, S_2, S_3, etc.), as shown in Eq. 1.7. The parameter C_0 corresponds to the speed of sound in the material at zero pressure whereas the remaining parameters S_n are determined experimentally.

$$u_s = C_0 + S_1 u_p + S_2 u_p^2 + ... \tag{1.7}$$

For most metals, the relationship between shock speed and particle speed is linear in the absence of phase transitions [41]. Therefore, for most metals, this relationship is typically reported in the form of Eq. 1.8, with values for parameters C0 and S1 often tabulated in the literature. With Eq. 1.8 and the previously described Rankine-Hugoniot relations (Eq. 1.1, 1.2, and 1.3), there are now 4 equations to describe 5 parameters: particle velocity, shock velocity, pressure, density and energy. Therefore, the measurement of one parameter can then be used to determine the remaining parameters.

$$u_s = C_0 + S_1 u_p \tag{1.8}$$

1.6.3 Planar Impact

First consider a one-dimensional, planar impact of two plates. A projectile plate (material 1) moving at speed v impacts a stationary target plate (material 2). Assume the plates impact each other normally, such that the flat, planar surfaces of the plates are parallel and the subsequent particle motion is perpendicular to this interface. As shown in Figure 1.9, shock waves form moving with speeds u_{s1} and u_{s2} and propagate into materials 1 and 2, respectively. The uncompressed region in the projectile continues to move with speed v while the uncompressed region in the target remains stationary.

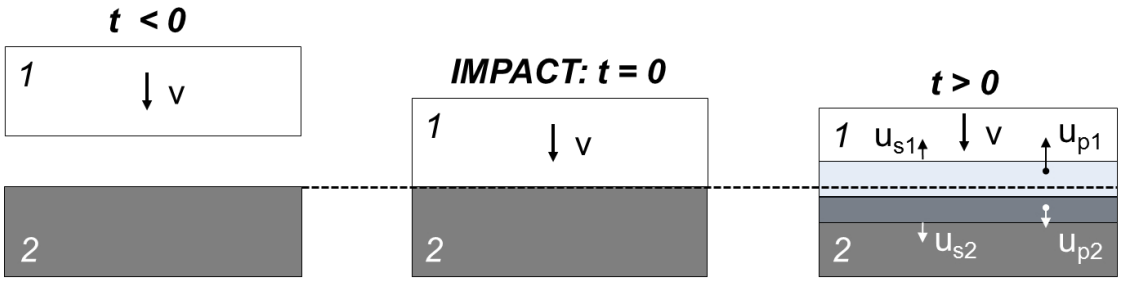

Figure 1.9: Example of a planar impact [41]. Before impact, material 1 is shown moving towards stationary plate 2 with speed v. Material 1 then impacts material 2. After impact, one-dimensional planar shock waves are formed in materials 1 and 2.

At the impact interface, the material is continuous: assume the contact between the two materials is constant and there no voids. In comparing the resulting material particle speeds, first consider a fixed reference frame with respect to the original material interface. After impact, the particle velocity in the compressed region of the projectile is the original impact speed reduced by the particle speed up1. Across the interface, the particle speed in the compressed region of the target is u_{p2}. Additionally, the pressure in the materials at the interface is equilibrated. Therefore, the boundary conditions at impact are given by Eq. 1.9 and Eq. 1.10.

$$v - u_{p1} = u_{p2} \tag{1.9}$$

$$P_1 = P_2 \tag{1.10}$$

Given these boundary conditions, the resulting compressive pressure and corresponding particle speeds can be determined. The pressure in each material can be determined as a function of particle speed by substituting Eq. 1.8 into Eq. 1.2. Because the material interface is continuous, the pressure in material 1 can be described using the particle velocity in the target material u_{p2} by utilizing Eq. 1.9. The pressures for each material can then be described as a function of target material particle speed, as shown in Eq. 1.11 and Eq. 1.12.

$$P_{1^*} = \rho_{01}\left(v - u_{p2}\right)\left[C_{0_1} + S_{1_1}\left(v - u_{p2}\right)\right] \tag{1.11}$$

$$P_2 = \rho_{02} u_{p2}\left(C_{0_2} + S_{1_2} u_{p2}\right) \tag{1.12}$$

Because the pressures are equal at the interface ($P_1 = P_2$), the target particle speed can be determined by equating Eq. 1.11 and Eq. 1.12. The solution is given by Meyers [41] as Eq. 1.13 and Eq. 1.14. With the particle speed of the target, the particle speed in the impactor is given by Eq. 1.9 and the pressure at the interface can be determined by conservation of momentum, Eq. 1.2.

$$u_{p2} = \frac{-\left(\rho_{02}C_{0_2} + \rho_{01}C_{0_1} + 2\rho_{01}S_{1_1}v\right) \pm \sqrt{\Delta}}{2\left(\rho_{02}S_{1_2} - \rho_{01}S_{1_1}\right)} \tag{1.13}$$

$$\Delta = \left(\rho_{02}C_{0_2} + \rho_{01}C_{0_1} + 2\rho_{01}S_{1_1}v\right)^2 + 4\rho_{01}\left(\rho_{02}S_{1_2} - \rho_{01}S_{1_1}\right)\left(C_{1_1}v - S_{1_1}v^2\right) \tag{1.14}$$

Note that when the projectile and target are of the same material, the resulting particle speed is equal to one half of the incident impact speed. In this case, the particles in the projectile transfer half of their momentum to the target.

When the projectile and target materials are not the same, the pressure and

particle speeds can also be determined graphically. Plotting equations Eq. 1.11 and Eq. 1.12 results into two pressure-velocity curves, as shown in Figure 1.10 for a Nylon 6/6 projectile impacting an aluminum 6061 target at 6 km/s. The intersection of the two curves (where the condition $P_1 = P_2$ is satisfied) provides the solution for pressure and particle speeds, as shown. For the example shown in Figure 1.10, given an impact speed of 6 km/s the pressure generated is 42 GPa and the corresponding particle speeds in the aluminum target and Nylon projectile are 2 and 4 km/s, respectively. Furthermore, note that the ratio of the particle velocities in the materials is given by the ratio of each material's shock impedances, as shown in Eq. 1.15

$$\frac{u_{p2}}{u_{p2}} = \frac{\rho_{01} u_{s1}}{\rho_{02} u_{s2}} \tag{1.15}$$

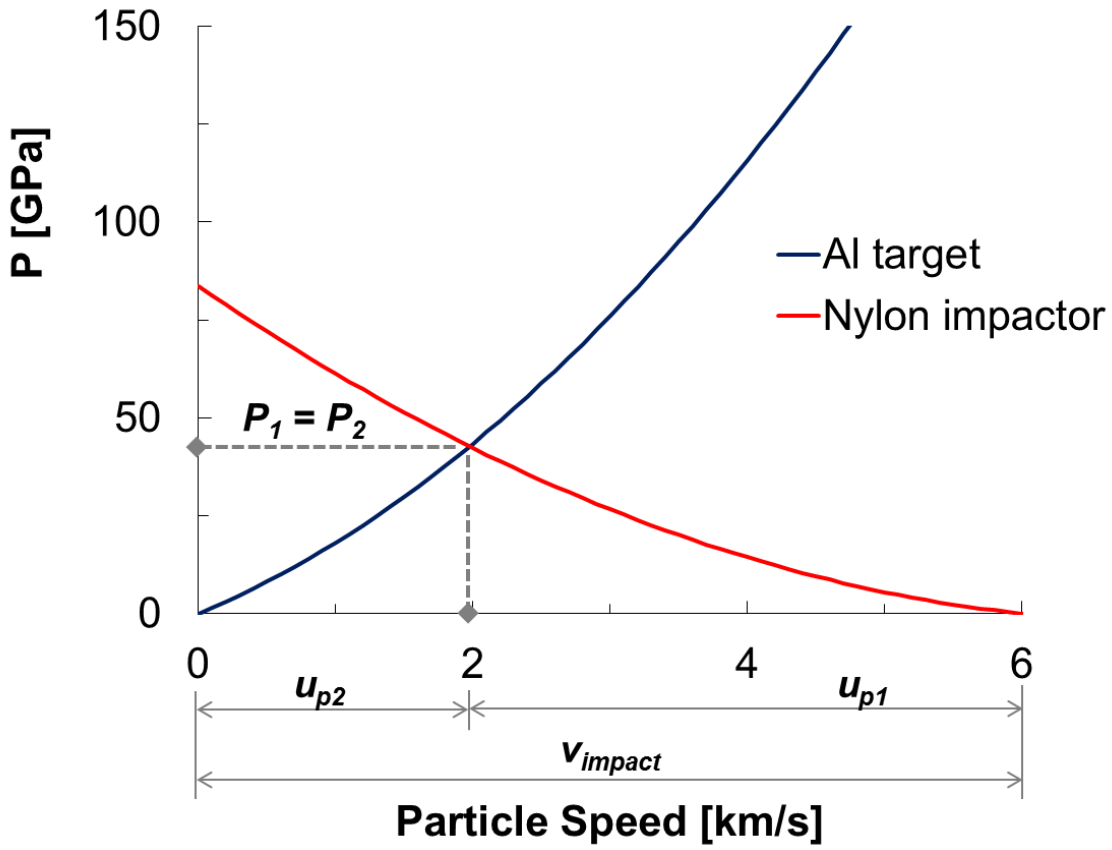

Figure 1.10: Graphical solution for the shock pressure and corresponding material particle speeds in a one-dimensional planar impact. Hugoniots shown for an aluminum 6061 target impacted by a Nylon 6/6 projectile at 6 km/s.

1.6.4 Projectile Impact

Consider a free-flying projectile of length l and width d moving with impact speed v_{impact} towards a target plate of thickness h, as illustrated in Figure 1.1. For now, assume a normal impact with a yaw angle of $\beta_0 = 0$: the impact vector, target plate surface normal, and impactor long-axis are all collinear.

Upon impact, in this configuration, the initial result is equivalent to the one-dimensional planar impact discussed in the previous section. A large pressure determined by the condition of equal pressure on the shock Hugoniots of each material is produced at the material interface. As a result, shock waves form and propagate into the impactor and target plate. This initial stage of impact is described graphically in Figure 1.11 for time t_1. After this moment, the wave mechanics depart from the previous one-dimensional assumption.

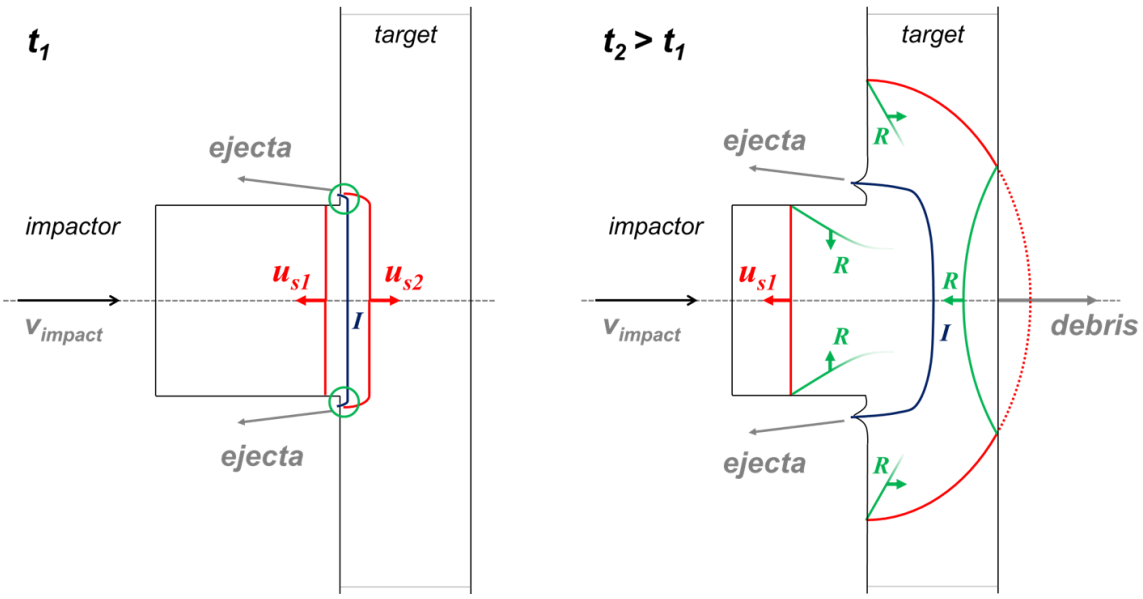

Figure 1.11: Illustration of the rudimentary wave mechanics. At time t_1, impact has occurred sending shockwaves moving at speeds u_{s1} and u_{s2} into the impactor and target material, respectively. Impactor and target material on the surface at the periphery of the interface I is released immediately after the formation and propagation of the compressive shock. Upon release, this material is ejected back uprange. At time t_2, release waves R have formed off of the free surfaces of the impactor and target plate. The release of the shock wave off of the back-surface can throw debris downrange behind the target.

In the impactor material, the shock wave propagates backward towards the rear-surface of the impactor with speed u_{s1}. As the shock wave is moving towards the rear surface, release waves (labeled as R in Figure 1.11 tor $t_2 > t_1$) form off of the radial free surfaces. These release waves move inward towards the centerline of the impactor. If the shock is sufficiently strong, upon release, the impactor material may undergo phase transition [25], [67]. Upon reaching the rear-free surface of the material, the incident compressive shock is reflected as a tensile release wave.

Upon formation and propagation of the compressive shockwave in the target, the target material on the surface immediately adjacent to the impactor-target interface (I) is released. This material, along with the impactor material circled at the periphery of the interface in Figure 1.11 for time t_1, is the first material thrown back uprange as ejecta. The release wave forming off the free uprange surface follows behind the initial shock pulse and moves in towards the center of the target.

In the target material, the initial shock wave propagates backward towards the target rear-surface with speed u_{s2}. This compressive shock pulse is reflected as a strong tensile release wave and sent back into the target. This process may result in spallation and or fragmentation of the target material and produces a cloud of debris thrown downrange behind the target (as indicated in Figure 1.11 for time t_2). Furthermore, this isentropic release from the shocked state determines the phase (and subsequent size [36]) of the material that is thrown downrange in such a debris cloud. A simplified model of this is described by Swift [67]. If the increase in internal energy exceeds the energy of fusion, the material returns from the shocked state as a liquid. Similarly, if the increase in internal energy is greater than the energy of sublimation, the material is vaporized. Although this interpretation does not incorporate all known mechanisms, it has been shown to predict the state of material in debris clouds [67].

If the target is thin compared to the impactor, it is possible for the release wave formed from reflection of the shock off the target back-surface to be transmitted into the impactor. Because release waves travel at the local material sound speed, which is a monotonically increasing function of pressure, it is possible for release waves transmitted back into the target to overtake and attenuate the incident shock in the

impactor [25]. The inverse is also possible if the impactor length is small with respect to the target thickness.

Furthermore, the initial (compressive) pressure that is formed at the interface of the impactor and target, as described in a planar impact, does not remain constant the as the shock pulse expands and moves through the target. The shock wave is volumetrically attenuated and dissipative mechanisms (such as the work of plastic flow and fracture) decrease the amplitude of the shock wave.

By definition, the material at the interface of the impactor and target experience pressures much larger than the respective flow strengths. However, given the dissipation of the initial shock, for sufficiently large targets and impactors, the amplitude of the stress pulse will eventually approach the flow strength of the materials for sufficiently large geometries. Therefore, for sufficiently large impactor s and or targets, the hydrodynamic assumption is not applicable throughout the damaged regions in each material. But, for sufficiently thin plates target plates (dh), the amplitude of the shock pulse remains large enough for the such that the hydrodynamic assumption remains valid in the effected target material [67].

1.7 Outline

The remainder of this work is organized as follows:

- Chapter 2 provides an overview of the Small Particle Hypervelocity Impact Range (SPHIR) facility at Caltech, the experimental setup of the research described herein, and the mass-velocity performance of the SPHIR facility two-stage light-gas gun.

- Chapter 3 describes results for the perforation areas produced by cylindrical impactors on target plates over a range of thicknesses. An overview of known scaling behavior is provided and the scaled results for perforation area are discussed and compared to previously developed models. Additionally, results are compared to the predictions by the OTM model.

- Chapter 4 describes a technique developed to observe hypervelocity impact and the subsequent formation of debris clouds. A novel optical technique to measure the two-dimensional optical density of the debris cloud is presented. Results describing the debris clouds formed from variable plate thickness and impact speed are discussed.

- Chapter 5 describes the concurrent real-time diagnostics implemented in the SPHIR facility to provide complementary measurements of impact phenomena. The UV-vis and IR spectrograph systems are described and characteristic results are presented. The debris capture system and analysis is also presented.

- Chapter 6 describes the dependence of the observed expansion of an IR-emitting "cloud" on the ambient atmospheric pressure in the target chamber. Dimensional analysis is used to describe the pressure-dependent expansion of the observed phenomenon.

Appendices A through C also provide further information on the following:

- Appendix A describes the experimental procedure for conducting an impact experiment in the SPHIR facility.

- Appendix B Reports the performance of the SPHIR facility for launching 22.7 mg steel spheres to impact speeds between 2 and 3 km/s. This appendix also provides the velocimetry techniques used when the impactor is not self-luminescent.

- Appendix C outlines the derivation by G. I. Taylor for constants required for dimensional analysis of a point-blast explosion.

Chapter 2

The SPHIR Facility

2.1 SPHIR Facility Overview

The Graduate Aeronautical Laboratories at the California Institute of Technology (GALCIT) has established the Small Particle Hypervelocity Impact Range (SPHIR), shown in Figure 2.1, an experimental facility designed to study MOD impacts [42], [44]. The 1.8 mm bore diameter two-stage light-gas gun utilized in this facility was designed, developed and fabricated by engineers at the Southwest Research Institute [12] and installed at Caltech in 2006.

The light-gas gun uses compressed hydrogen or helium gas to launch small particles with diameters of 1.8 mm, to velocities up to 10 km/s. The first-stage of the gun (see Figure 2.2) utilizes 0.9 g of smokeless black powder propellant to accelerate a 190 mg polyethylene piston into a 5.6 mm diameter barrel (pump-tube) containing the light-gas pressurized between 80 and 150 psi. The second stage consists of an accelerated reservoir (AR) section that focuses the pressure front into the opening of the launch-tube, bursting a 75 micron thick Mylar membrane and accelerating the launch package.

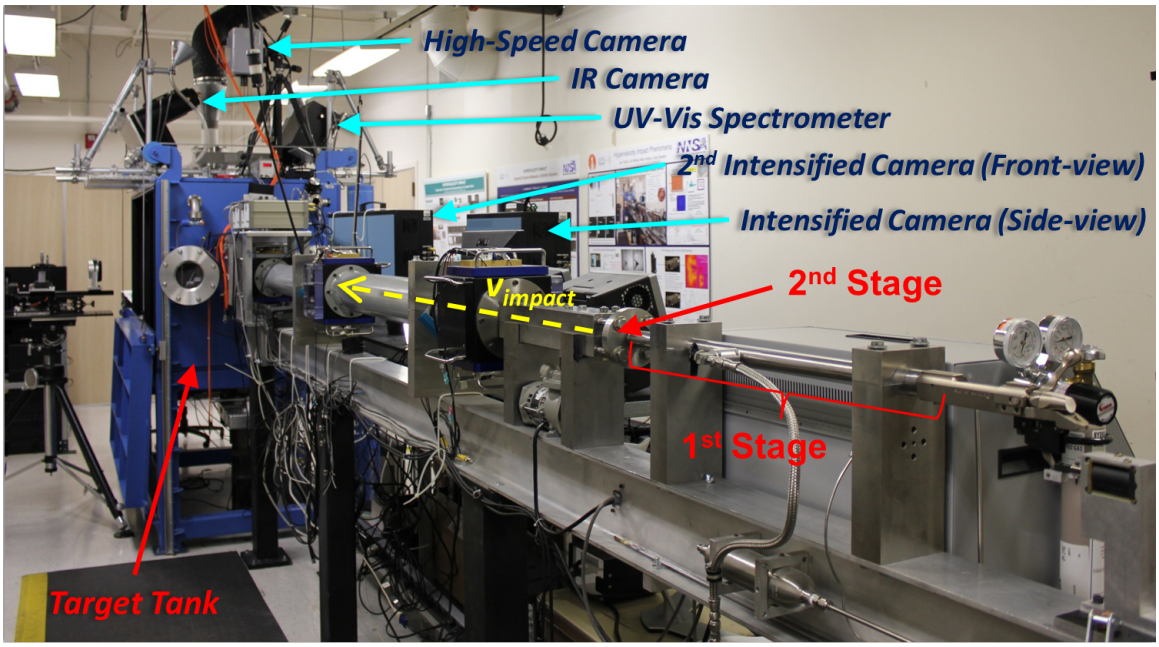

Figure 2.1: The Small Particle Hypervelocity Impact Range (SPHIR) Facility at Caltech. Diagnostics have been developed and implemented to complement this two-stage light-gas gun facility.

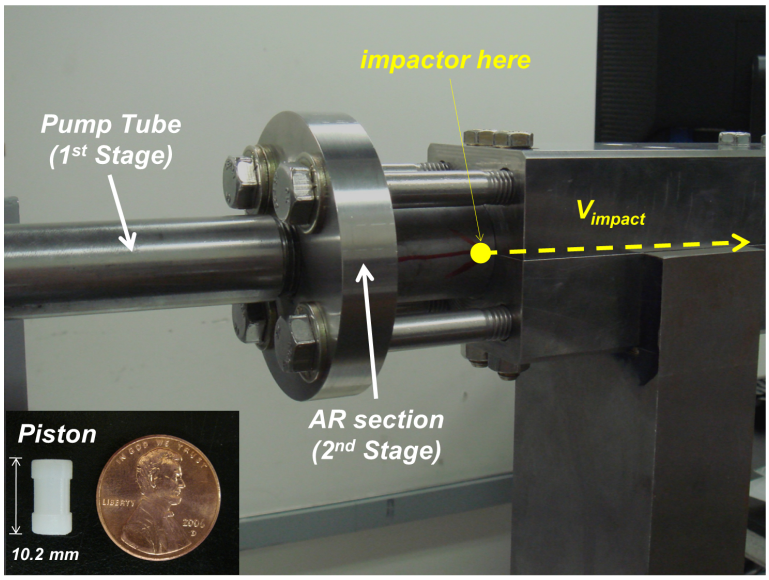

Figure 2.2: The connection between the pump-tube (first-stage) and acceleration reservoir (AR) section (second stage). Location of impactor (in launch-tube) illustrated. The piston used with in the first-stage is shown at bottom-left.

The 1.8 mm bore diameter of the launch-tube limits the size of the selected launch packages, which can have masses ranging from 1 to 30 mg. Figure 2.3 provides an example of several of the launch packages used in the facility. Each particular impactor has a range of expected impact speeds impactor velocities, as described along with average mass in Table 2.1. Note that in the work described herein, the nylon 6/6 cylinder is used as the primary hypervelocity impactor. The nylon sphere was not widely implemented given a high rate of failure (pre-mature fragmentation) of the impactor during experiments.

Figure 2.3: Three of the most commonly used impactors used in the SPHIR facility, each with a diameter of 1.8 mm.

label	Material	Geometry	Mass	Impact Speed
I.	440C Steel	1.8 mm diameter sphere	22.7 mg	2 to 3 km/s
II.	nylon 6/6	1.8 mm diameter, L/d=1 right-cylinder	5.6 mg	5 to 10 km/s
III.	*nylon 6/6*	1.8 *mm diameter sphere*	3.6 *mg*	5 *to* 6 *km/s*

Table 2.1: Impactors used in the SPHIR facility.

Launch packages are accelerated in a disposable, smooth bore (non-rifled) launch-tube, which is replaced after each experiment. The inexpensive, disposable launch-tube helps reduce the operational cost of the facility but makes the use of sabots more difficult: the small-scale and absence of sufficient centrifugal force precludes the

application of conventional sabot technology for the launching of impactors. Therefore, future expansion of the facility's mass-velocity performance envelope requires development of a small-scale sabot-separation system.

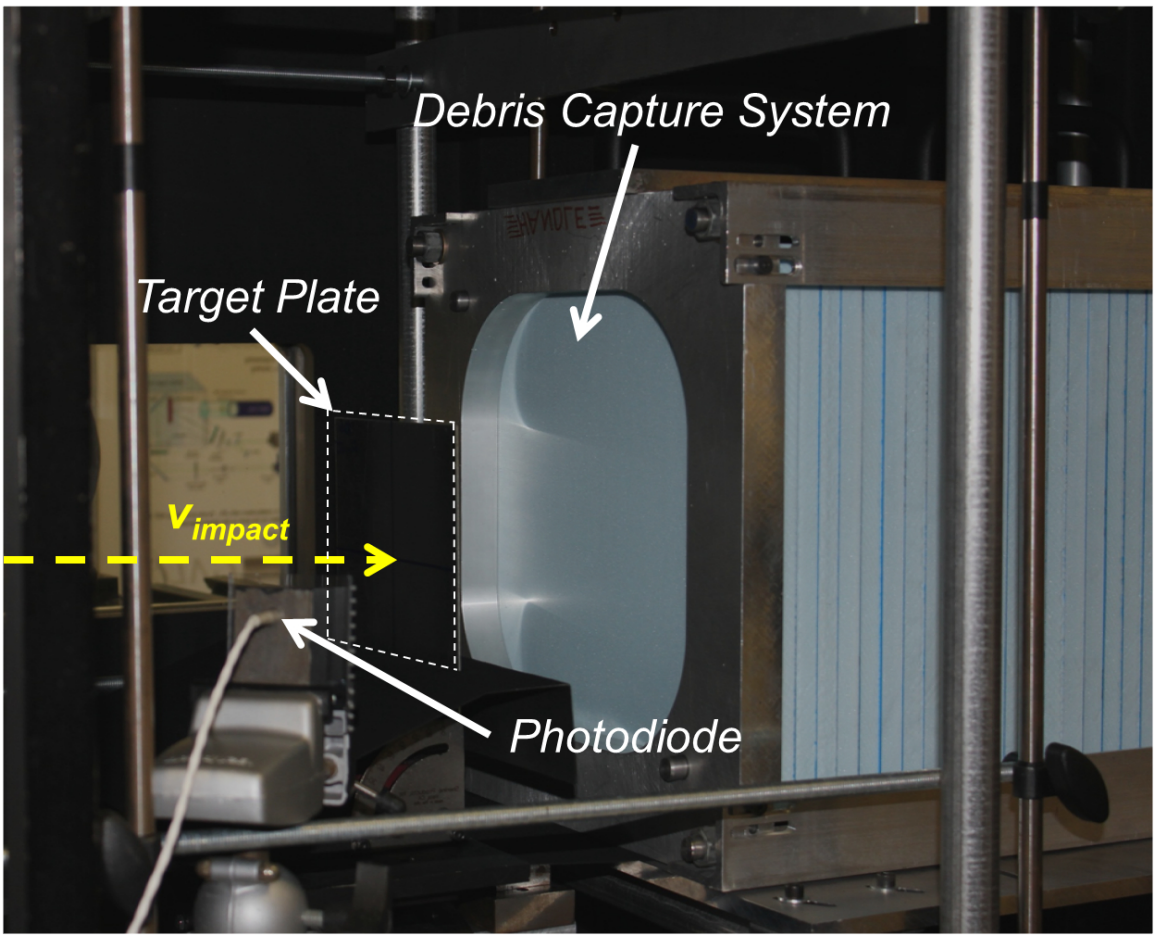

Figure 2.4: Target chamber of the SPHIR facility, with target plate and nominal impactor velocity vector identified. The photo diode used to trigger diagnostics and the debris capture system is also shown.

After exiting the launch-tube, the accelerated launch-package flies 3.6 m downrange into a 1 m x 1 m x 2 m target chamber with atmospheric levels maintained at pressures ranging between 0.13 to 6.67 kPa (1 and 50 mmHg). Target materials and systems are limited only to what can fit inside the large target chamber. The large target chamber features multiple view-ports enabling the simultaneous observation of the experiment with a suite of instrumentation described in the section to follow. Figure 2.4 presents an image of the target chamber interior.

All aspects of the light-gas gun operation can be performed by a single researcher and several experiments may be completed in single day. To ensure safe operation, impact experiments are always conducted with at least two individuals present. The full operations procedure is provided in Appendix A.

The masses launched and the velocities attained in this facility are a good analog for MOD studies, but are not particularly unique. However, the SPHIR facility is unique given its relatively low-cost and high output of data for each experiment. The diagnostics discussed in later sections are routinely employed in every experiment conducted at the SPHIR facility. This suite of instrumentation provides multiple complementary measurements that facilitate the characterization of multiple impact phenomena in a single experiment. As such, the extensive instrumentation of the facility maximizes the data output from each experiment and provides a high return on investment given the fixed costs of each shot. Because of this, experimental campaigns of several shots yield comprehensive data sets on a host of phenomena.

2.2 Facility Instrumentation

The SPHIR Facility is currently equipped with the following instrumentation:

1. Photron SA-1 Fastcam high-speed camera
2. Optimet MiniConoscan 3000 laser Conoscope
3. Cordin 214-8 Gated, Intensified Camera (x2)
4. UV Spectroscopy System
5. IR Spectroscopy System
6. Velocity Interferometer System for Any Reflector

A Photron SA-1 Fastcam high-speed camera is mounted on top of the target chamber looking down upon the flight tube entry. This non-intensified camera is

nominally operated at 150,000 fps with 192 x 112 pixel resolution. Slower framing rates with larger pixel resolution have also been utilized.

The Optimet MiniConoscan 3000 laser conoscope, not shown in Figure 2.1, is used to conduct post mortem target specimen surface profilometry. This instrument produces a three-dimensional (x,y,z) Cartesian coordinate map describing a surface of a target. The conoscope's laser probe is outfitted with a 75 mm focal length objective lens, which provides 18 mm working range (depth of field), 10 micron precision in the in-plane directions, and approximately 25 micron precision in the out-of-plane direction.

The Cordin 214-8 gated, intensified ultra-high-speed camera provides a series of up to 8 images with framing rates as high as 10^8 fps. The camera contains an array of 4 independent, intensified CCDs. Each of the 4 CCD provides 2 images with 1000 x 1000 pixel resolution. The second exposure of a given CCD must be taken no less than 3.7 µs after the first, limiting the maximum frame rate of 10^8 fps to 4 consecutive images. The SPHIR facility currently has two Cordin 214-8 cameras installed: the first is positioned to provide a side-profile perspective of the impact and the second observes the front of the target with an 11 degree offset from the impact velocity vector.

Princeton Instrument UV-vis and IR spectrograph systems are mounted above the target chamber and oriented to view the impact at an angle of approximately 27 degrees from vertical. The UV-vis system measures emission spectra in the wavelength range between 300 and 850 nm utilizing a high-speed PI-MAX 3 camera. The IR system, configured with a high-speed OMA V camera, captures a single full-field image of near-IR emission (0.9 µm to 1.7 µm) 320 x 256 pixel resolution. The field of view for each spectrograph system can be modified through the selection of lenses with focal lengths ranging from 8 mm to 90 mm.

A Velocity Interferometer System for Any Reflector (VISAR) system has also been installed for potential use in the SPHIR facility. This instrument measures the normal component of a surface velocity and is typically used to measure the back-surface of target plates in equation-of-state measurements in shock experiments. This

instrument is not utilized in the described work herein, but has been installed and calibrated in the SPHIR facility for use in potential future experiments.

2.3 Instrumentation Triggering System

An impact flash observing detector and trigger circuit, as previously shown in Figure 2.4, is used to provide the triggering signal for all of the simultaneously operated high-speed diagnostics utilized in the SPHIR facility. The triggering system was designed and installed in the SPHIR facility in 2007 by Tom Reynoso from NASA's Jet Propulsion Laboratory (JPL) [28]. The trigger system utilizes an LED photodiode positioned approximately 20 cm from the target to observe the impact flash produced during an experiment. With an angle of half-sensitivity of 20 degrees, the photodiode is able to detect an impact flash anywhere on the 15 cm x 15 cm target plate. The spectral bandwidth range of the photodiode is from 620 to 980 nm.

With a very low number of trigger failures (much less than 1% of all experiments), this triggering method has proven to be very robust. However, there is a finite delay between the actual impact and triggering of the instrumentation. This delay corresponds to the formation of the impact flash, detection of the flash's growing luminosity, and response time of the phototransistor. Analysis of the debris cloud and backward extrapolation of the debris front (described in section 4.5) can provide an estimate for the length of the triggering delay. Nominal trigger response (delay) times are on the order of 1 µs.

Upon flash detection, the trigger circuit outputs a 5V DC signal to a Berkley Nucleonics Corporation (BNC) Model 575 pulse generator. The four channel, BNC Model 575 pulse generator is capable of outputting four independent triggering signals with less than 200 ns delay [7]. The first BNC Model 575 is used to trigger a second BNC Model 575 pulse generator connected in sequence. The two pulse generators are programmed to output a 5V TTL (transistor-transistor logic) trigger signals to the active instruments and data acquisition systems. Figure 2.5 provides a schematic of the triggering system utilized for the high-speed diagnostics described herein.

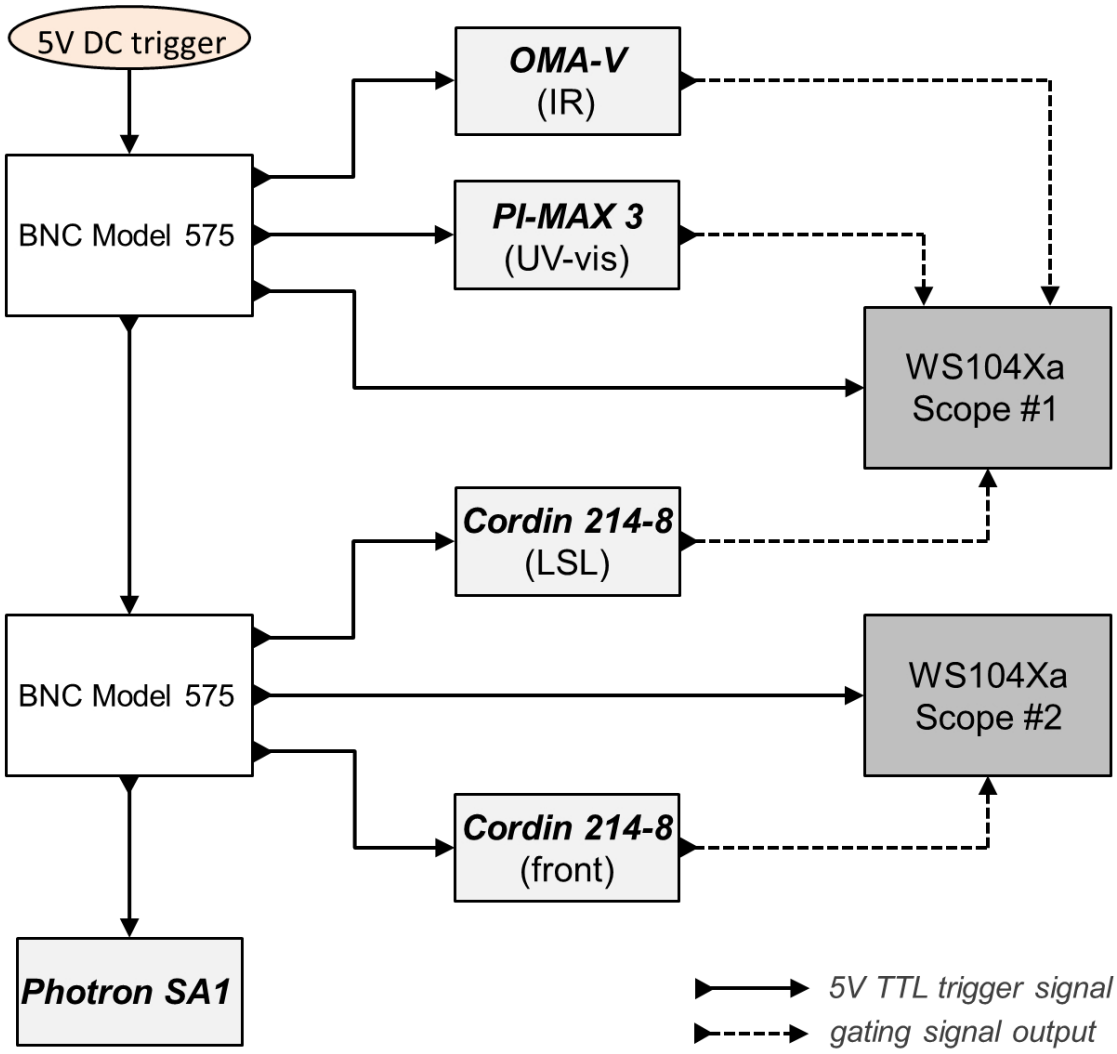

Figure 2.5: Triggering scheme used in the SPHIR facility to operate the described instrumentation and monitor time output

Gating signals output from the triggering instruments are monitored using two LeCroy WaveSurfer 104Xs-a oscilloscopes. These signals are generated by each instrument, with exception of the Photron SA1 camera, and describe the sequencing and exposure timing of each measurement. The oscilloscopes provide high-resolution monitoring of the instrument timing, with a 2.5 GSPS maximum sampling rate and 1 GHz bandwidth.

The first BNC Model 575 pulse generator is used to trigger the OMA V IR camera, the PI-MAX 3 UV-vis spectrograph, and WaveSurfer oscilloscope #1. The gating

signals produced by the OMA V and PI-MAX instruments are then recorded on oscilloscope #1. Triggering the oscilloscope with the pulse generator (as supposed to one of the instrument signals recorded) establishes t = 0 as the triggering time of the synchronized instruments.

The second pulse generator triggers both Cordin 214-8 cameras, the Photron SA-1 camera, and WaveSurfer oscilloscope #2. The gating signal produced by the Cordin camera used for the laser side-lighting (LSL) system — which is described in Chapter 4 — is recorded by the same oscilloscope monitoring the OMA V and PI-MAX instruments. This configuration enables synchronized monitoring of the LSL images, IR images, UV-vis spectra with the same reference time. Therefore, the exposure times of the LSL system are precisely measured with respect to both the simultaneous IR images and UV-vis spectra.

The gating signal produced by the front-viewing Cordin camera is output and monitored by oscilloscope #2. Lastly, the output of the Photron SA1 camera is connected only to its configured PC. During experiments, the camera is continuously recording and dumping memory until it receives the trigger signal. The Photron camera is programmed for center triggering: upon triggering, half of the available memory stored corresponds to observations made in time before the trigger was received. Therefore, the Photron camera is least-sensitive to a delay in the triggering signal and is thus triggered off of the second pulse generator.

2.4 Impact Configuration and Materials Selection

The investigation of hypervelocity impact phenomena described in this work focuses on normal impacts of 1.8 mm nylon 6/6 cylinder projectiles and variable thickness aluminum targets. Table 2.2 provides the definition of the considered standard impact configurations.

Impact Material	nylon 6/6
Impactor Geometry	1.8 mm diameter l/d=1 right-cylinder
Impact Speed	5 to 7 km/s
Target Material	aluminum 6061-T6
Target Thickness	0.5 mm, 1.5 mm, 3.0 mm
Impact Obliquity	0 degrees (normal impact)

Table 2.2: Definition of the standard impact configurations considered in this work.

2.4.1 The Impactor

Nylon 6/6 equiaxed right-cylinders ($l/d = 1$) with a 1.8 mm diameter are used as impactors. Given a material density of 1.2 g/cm^3, nylon 6/6 is one of the material analogs for meteoroids considered by NASA for use in validation testing for hypervelocity impact shields [3]. The material properties of nylon are presented in Table 2.3. Shock Hugoniot data is provided by Marsh [38]. The material properties for aluminum are those considered for use in the OTM numerical model (described in section 3.5).

Nylon 6/6		
ρ_p	1.22	g/cm^3
c_0	3.13	km/s
S_1	1.38	

Table 2.3: Material properties for nylon 6/6.

The nylon 6/6 spheres presented in section 2.1, were also considered for use in experimental campaigns. However, the nylon 6/6 spheres would often disintegrate upon acceleration. Therefore, given the lack of reliability, the nylon spheres were not utilized in the experiments described in later chapters.

Given the fixed launch-tube bore diameter, the SPHIR facility is limited to launching impactors with a 1.8 mm diameter. The use of smaller diameter impactors in the SPHIR facility requires the use of a sabot. A sabot is a launch vehicle used to accelerate the impactor, but not intended to hit the target. However, as described, the SPHIR facility's smoothbore launch-tube design delivers insufficient centrifugal forces on a launch package to employ conventional sabot technology. Furthermore, given the inherently small scale of the available impactors, use of conventional aerodynamic forces for sabot separation could result in unacceptable levels of target ablation. A

prototype sabot system has been developed for SPHIR to launch 0.9 mm diameter aluminum metallic projectiles to velocities of 4 to 7 km/s. Proof of concept has been demonstrated in achieving sabot separation and removal. However, the separation of the sabot has not been demonstrated to be consistent enough to warrant full-scale implementation in an experimental campaign. Accordingly, the improvement and implementation of a sabot system is reserved for future work in the SPHIR facility.

2.4.2 The Target

Aluminum 6061-T6 is considered as the primary target material. This material is a common material in aerospace structures and the predominant material in impact shielding systems on spacecraft [5]. Furthermore, aluminum 6061-T6 is inexpensive, readily available and the material properties are well-characterized. The material properties for aluminum are presented in Table 2.4. The material properties for aluminum are those considered for use in the OTM numerical model (described in section 3.5).

Aluminum 6061-T6		
ρ_t	2.7	g/cm^3
c_0	5.35	km/s
S_1	1.34	
c_p	6.4	km/s
c_s	3.15	km/s
σ_y	276	MPa
T_{melt}	833	K
C	0.9	J/gK
L	397	J/g

Table 2.4: Material properties for aluminum 6061-T6.

Targets plates were 150 mm x 150 mm and varied in thickness. Commercially available plate thicknesses of 0.5 mm, 1.5 mm, and 3.0 mm were selected to provide a full spectrum of target thickness to impactor diameter (h/d) ratios. Initial experiments for normal impacts of nylon cylinders into aluminum targets at approximately 5 km/s produced an estimated ballistic limit target plate thickness of at least 3.5 mm. Therefore, given the range of expected impact velocities, target plate thicknesses from

0.5 mm to 3.0 mm represent configurations above the ballistic limit. Therefore, such a selection facilitates the investigation of the perforation response and subsequent debris cloud phenomena with variable proximity to the ballistic limit. Normal impacts (impact obliquity $\theta = 0$) were primarily considered.

2.5 Impactor Velocimetry

Accurate, consistent, and reliable measurement of impact velocity is critical in the operation of any light-gas gun facility. A common method to measure the impactor speed in light-gas gun experiments is to use a series of laser barriers which are interrupted by the impactor during its flight to the target. However, several factors complicate the application of such a method in the SPHIR facility. First a luminous cloud of high temperature hydrogen gas precedes the exit of the impactor from the launch-tube and follows the impactor in its flight to the target. Additionally, the small bore (1.8 mm) of the SPHIR facility requires the use of impactors that are smaller than those utilized in many other light-gas gun facilities. As a consequence, the interruption of the detector signal produced by the passing of the small impactor at hyper-velocities is brief and often obscured by a low signal-to-noise ratio. These factors therefore would require the implementation of a specialized optical system [27] to utilize the laser barrier technique.

A simpler, less complex, solution is to use the Photron SA1 Fastcam to measure the impactor speed. When the impactor is traveling at greater than 4 km/s, the low-pressure atmosphere (0.13 to 6.67 kPa) in the evacuated target chamber is ionized directly in front of the impactor and forms a luminescent sheath surrounding and trailing the location of the impactor. This hot plasma sheath radiates sufficient light to enable high-speed imaging by self-illumination. When the impactor is accelerated to speeds less than 4 km/s, as is expected with heavier impactors like the 440C steel sphere, a different velocimetry technique (described in Appendix B) is implemented.

As shown in Figure 2.1, the Photron camera is mounted above the target chamber looking down upon the flight path of the impactor. The distance of camera to the

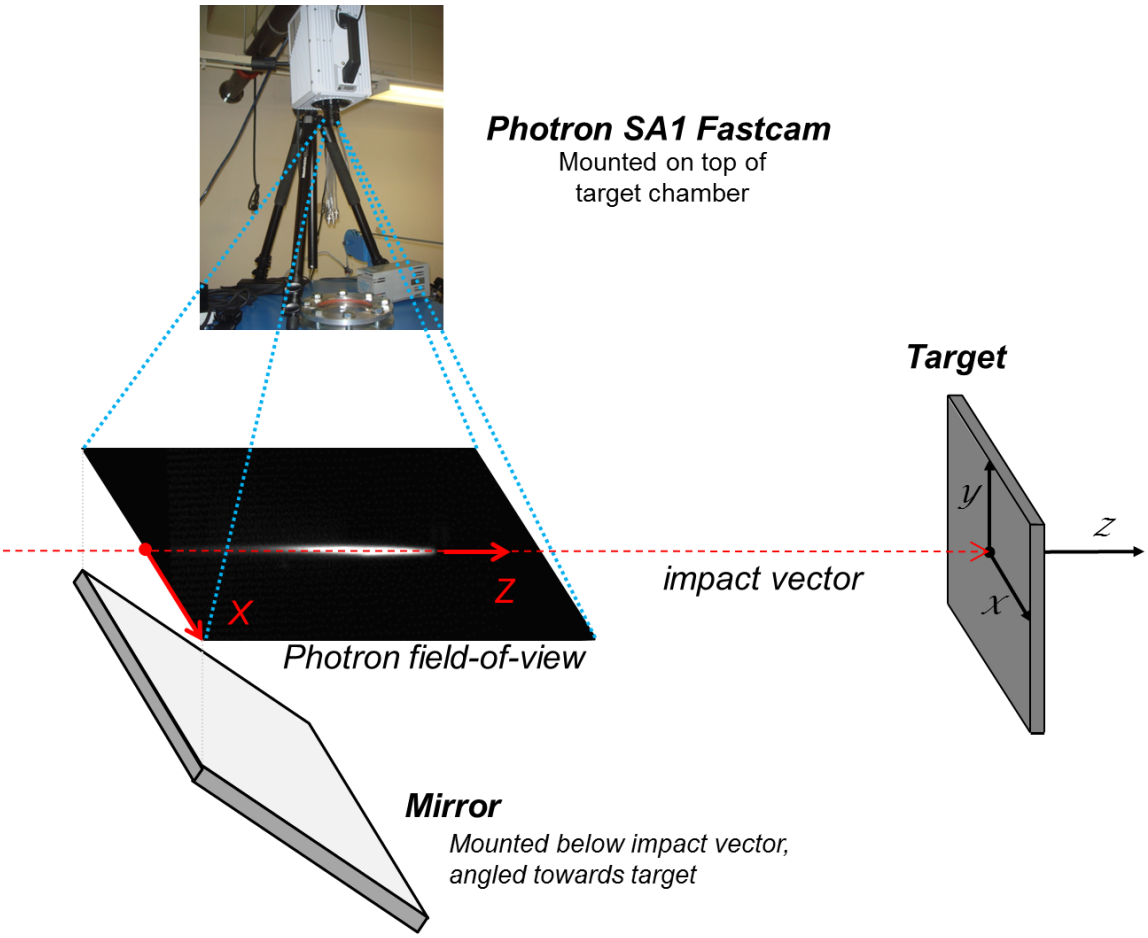

Figure 2.6: The configuration used with the Photron SA1 Fastcam to measure impactor velocity.

impactor velocity vector is approximately fixed at 1.2 m with respect to the camera. A 25 mm, $f/0.95$ lens is configured with the Photron camera and provides a field of view of approximately 160 mm x 94 mm. The lowest available relative aperture is used to collect the maximum amount of light radiated by the impactor. At the nominal operating framing rate of $150,000$ fps, this field of view is observed with 192 x 112 pixel resolution. A mirror, angled towards the target, is also located at the bottom of the target tank within the Photron camera's field of view. An illustration of this setup is provided by Figure 2.6. This configuration allows visualization of both the impactor in flight to the target and the subsequent target impact flash. An example of images taken by the Photron fast camera is provided in Figure 2.7 below.

The series of images presented depict the impactor visible as a "shooting star" passing below the camera before becoming visible again later as a reflection in a mirror when impact on the target occurs in frame n_0. With these images, the position of the impactor can be accurately determined at several positions at precise times.

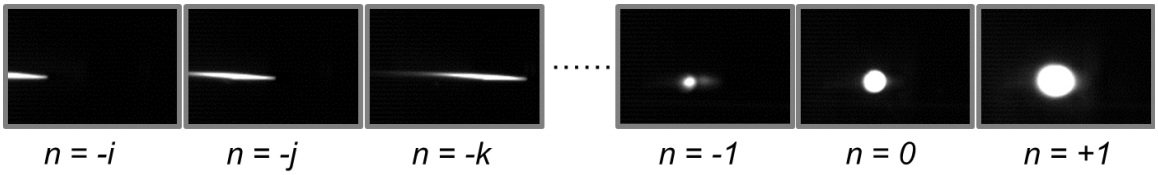

Figure 2.7: Sequence of images from the Photron fast camera used to measure the velocity of a 1.8 mm diameter nylon right-cylinder. The camera recorded this sequence at 150,000 fps. The three images on the left (frames -i, -j, -k) depict the self-illuminating impactor moving from left to right through the camera's field of view. The three images on the right visualize the target impact as a reflection in a mirror. Impact occurs in frame n = 0. The impactor is visible immediately before impacting the target in frame n = -1.

The impactor speed can then be computed from a single frame by considering the distance of the impactor from the target and the corresponding time of flight to the target. The field of view of the Photron camera is calibrated such that the distance to the target of each pixel is known. For example, considering Figure 2.7, the distance to the target is known from the shock-front observed in frame $n = -i$. The time of flight is then measured given the number of frames until the impact is observed in frame $n = 0$. With the distance traveled and time of flight known, the velocity of the impactor can then be estimated.

However, this method is limited by the uncertainty in the time of flight. At Photron framing rates of $150,000$ fps this corresponds to upwards of 6.67 µs, which can represent greater than 5% of the total time of flight. Including the uncertainty in measured distance to target, the corresponding uncertainty for this method would be $\pm 7\%$ or more for velocity measurements between 5 and 7 km/s.

A more accurate alternative is to measure the relative position of the impactor in sequential images taken with the Photron camera. The inter-frame timing of the Photron camera is very precise; therefore the accuracy of tracking the impactor is

dominated by the definition of the impactor position.

2.5.1 Determination of Impactor Position

This plasma sheath surrounding and trailing the impactor is visible in the Photron camera as a coma: an illuminated streak of excited gas particles. Assuming the plasma sheath surrounding the impactor is non-reactive, the shock-front is the brightest point in the plume [18]. Therefore, the position of the impactor, as measured through the camera, is related to the shock-front position of the tumbling impactor [18].

The observed position of the shock front is measured by considering the grayscale values recorded on the camera CCD by the observed coma. The coordinate system used in considering the CCD data is presented in Figure 2.6. The longitudinal Z-direction is defined as an axis collinear with the velocity vector of the impactor. Subsequently, the vertical axis in the Photron camera's image is parallel to the target in-plane x-direction. The origin used in the velocimetry analysis is the point on the left (uprange) edge of the CCD along the impactor velocity vector.

The grayscale of the coma is plotted in the longitudinal Z-direction (along the impactor velocity vector). Given the current default length-scale of the Photron field of view (0.83 mm/pixel), the entirety of the (original) impactor can be resolved with three pixels. Therefore, an analysis of the observed coma is performed by considering the grayscale profiles along three lines of constant X. The three X-coordinates are determined by first locating the X-coordinate with the highest cumulative grayscale and then identifying the two adjacent X-coordinates. The average of the grayscale of these three X-coordinates at each longitudinal (Z) position is computed to produce an average grayscale (AGS) curve for each of the images recorded in a sequence. The peak brightness of each observed coma is then quantified as the maximum of each AGS curve. An example of a sequence of AGS curves is presented in Figure 2.8.

To reduce errors associated with the determination of the coma's leading-edge and help define the uncertainty in the measurement, the leading-edge is defined using three methods. The first method is to locate the forward-most pixel with a grayscale

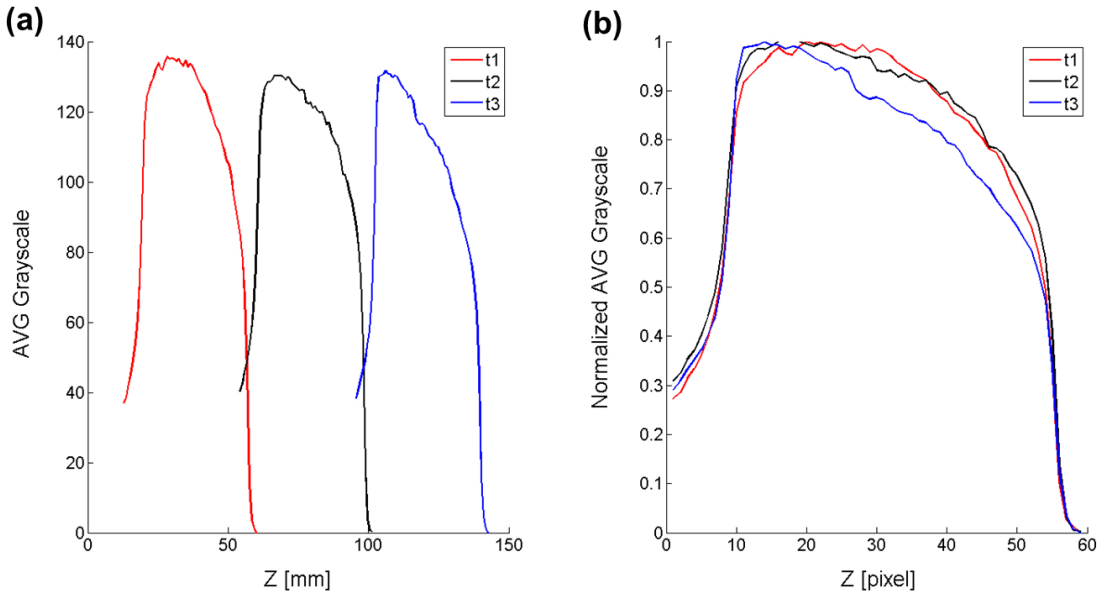

Figure 2.8: (a) Example of average grayscale (AGS) profile curves from subsequent images recorded by the Photron fast camera. Each AGS curve is obtained by averaging the three brightest grayscale profiles in the Z-direction. (b) Normalized AGS curves plotted together to illustrate structural similarity.

level higher than a defined threshold. This threshold is prescribed to distinguish the coma from the image's background grayscale (noise).

However, depending on the brightness of the shock-front and the sensitivity of the Photron CCD, the leading edge of the coma measured for each Photron image does not necessarily correspond to the physical location of the impactor's shock-front. This is a consequence of the impactor moving while the image is observed. The default exposure time used in the operation of the Photron camera is 6.67 µs, which corresponds to the nominal framing rate of 150, 000 fps. Therefore, at 6 km/s the impactor would traverse 40 mm across the camera's field of view. Consequently, the brightness (i.e., grayscale) measured on each individual pixel of the Photron CCD is the cumulative illumination recorded during this entire exposure time.

The stand-off distance of the shock-front with respect to the centroid of the impactor is approximately constant, independent of tumbling [18]. Therefore, when the amplitude of the observed coma brightness is similar, the relative physical position

of the impactor with respect to the observed coma remains constant. Accordingly, a comparison of sequential frames would provide an accurate measurement of the impactor speed, regardless of any uncertainty between the observed coma and relative physical impactor position. The peak brightness of the recorded comas has been observed to vary by small amounts between sequential frames. A cylinder with a non-zero angle of attack would lead to brighter self-illumination compared to a cylinder with zero degree angle of attack. Because the response of the CCD is approximately uniform with respect to a constant illumination source, the observable disparity in coma brightness is likely a consequence of impactor tumbling.

The two additional methods used to define the coma leading edge compensate for disparities in the observed coma brightness between frames by normalizing each AGS curve with respect to its peak brightness. Normalization is used to preserve the characteristic structure of each of the AGS curves. If the curves are characteristically the same shape, it is reasonable to conclude that the physical process creating the observed curves, and therefore defining the relative position of the impactor, is self-similar. Figure 2.8 provides an example of normalized curves plotted together for the purpose of demonstrating similarities in the structure of AGS curve during a sequence of high-speed images. The second method to determine the coma leading-edge defines the leading-edge as a constant value on the normalized AGS curve (typically between 0.2 and 0.4). The third and final technique considers the gradient of each normalized AGS curve and defines the leading edge as the steepest point on the (forward most) rising-edge common to each of the curves.

2.5.2 Impactor Velocity Measurement and Uncertainty

The location of the shock-front LE is defined, as described, using three different methods. For each LE definition, the impactor speed is then computed using Eq. 2.1. The positions of the LE in the first and last image of the sequence recorded by the Photron camera are considered to maximize the distance and time quantities and subsequently reduce measurement uncertainty. Results for impactor speeds using

each of the three LE definitions are similar, as presented in Figure 2.9 for a sample of experiments. The reported speed is then taken as the average of the speeds computed using the three LE definitions. Note that the scatter of the three velocities is within the reported uncertainty of the reported velocity measurement.

The uncertainty of the impactor speed measurement Eq. 2.2 is then quantified by considering the root-sum-square (RSS) of the independent error contributions from measurements of pixel distances (Δp), time (Δt), and pixel length-scale (S) used to compute the impactor speed.

$$v = \frac{S\Delta p}{\Delta t} \tag{2.1}$$

$$\epsilon_v = \sqrt{\left(\frac{\partial v}{\partial \Delta p}\epsilon_{\Delta p}\right)^2 + \left(\frac{\partial v}{\partial S}\epsilon_S\right)^2 + \left(\frac{\partial v}{\partial \Delta t}\epsilon_{\Delta t}\right)^2} \tag{2.2}$$

Comparison of the three LE definitions provides an estimate in the uncertainty in inter-frame pixel distance (ϵ_p): nominally only 1 pixel. The uncertainty of the timing of the Photron camera is less than 100 ns. Based on disparities in consecutive calibrations, the uncertainty of the Photron camera's field of view is estimated as 8.3×10^{-3} mm/pixel. Given the distance of the camera from the impactor velocity vector, a misalignment of the camera of 5 degrees with-respect-to vertical would correspond to an approximately 0.4% disparity in the observed field of view length. The corresponding effect on the camera pixel length-scale and uncertainty would therefore be minimal. With the described parameter uncertainties, a conservative estimate of the impact speed measurement uncertainty is nominally $\pm 1.5\%$. Therefore, for a measured impact speed of 6 km/s, the corresponding uncertainty is typically 0.09 km/s.

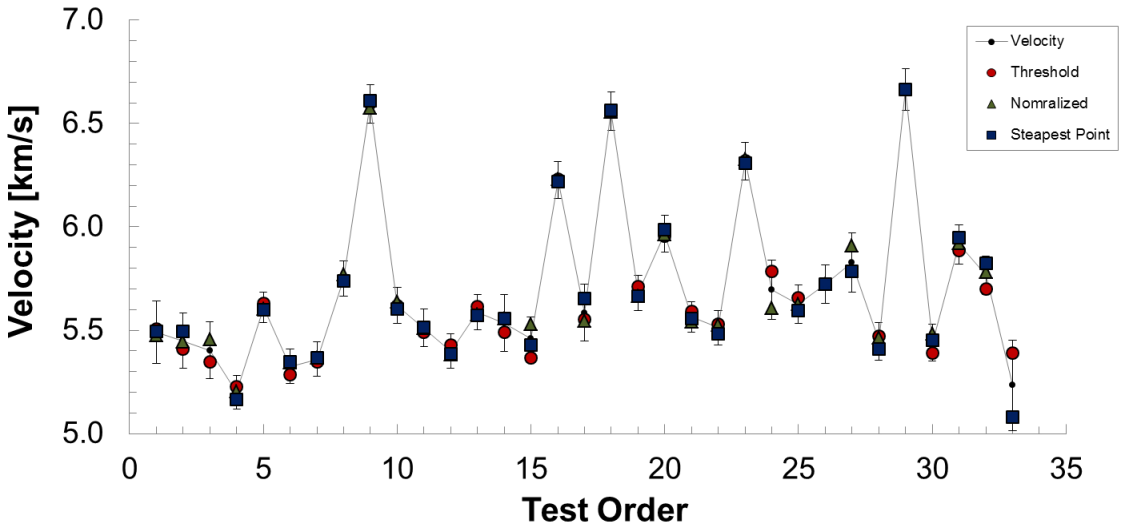

Figure 2.9: Comparison of the impactor velocities measured using each of the three leading edge definitions in addition to the reported impactor velocity and uncertainty

2.6 Facility Performance

2.6.1 The Effect of First-Stage Pressure on Impact Speed

The original standard operating pressure for the first-stage (pump-tube) during experiments was 150 psi. Using this pre-compression pressure for experiments with 5.6 mg nylon 6/6 right-cylinders ($l/d = 1$), the velocity results of 45 experiments are presented in Figure 2.10 as an empirical cumulative distribution function (CDF). The CDF was computed treating velocity as a random variable and making no assumptions regarding the underlying population distribution [35]. For the 45 velocity results observed for 150 psi pump-tube pre-compression, the target chamber pressure remained between 1 and 2 mmHg and all other launch parameters (such as piston mass or AR-section diameter) were within nominal ranges. The empirical CDF results for speeds produced from two additional, lower first-stage pressures are also presented in Figure 2.10.

For the velocity results presented for 150 psi, the 6 largest speeds appear to be considerably larger than the rest of the results. Furthermore, these outliers fall within the observed range of impact speeds produced using lower first-stage pressures. At the

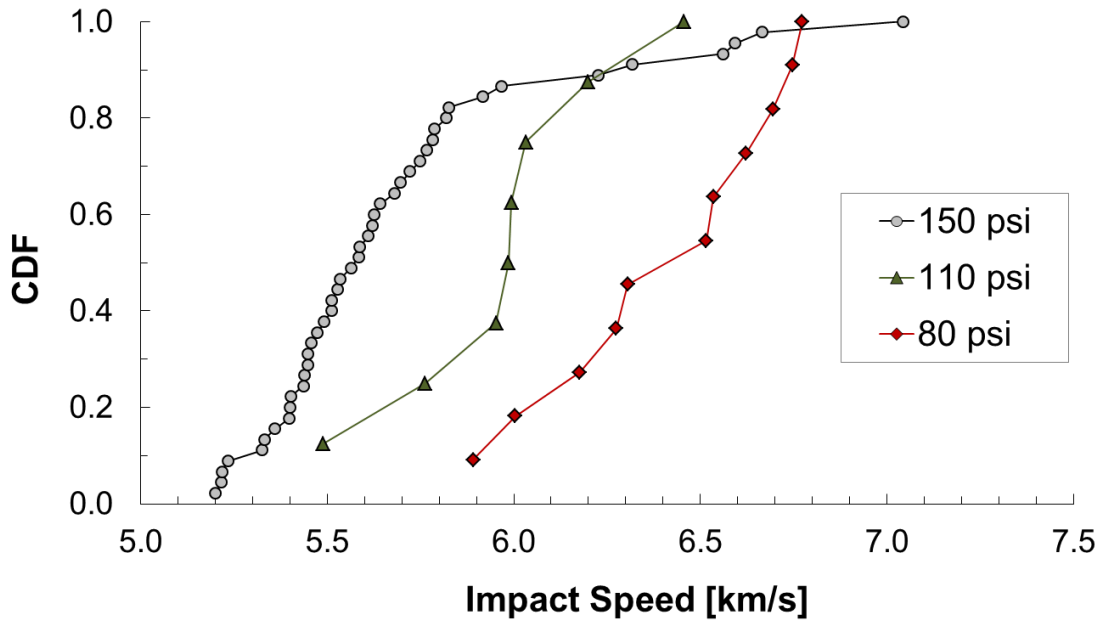

Figure 2.10: Empirical cumulative distribution functions for impact speeds produced using 150 psi, 110 psi, and 80 psi first-stage pressure

time of these experiments, the leak-rate of the piston and total time between pump-tube pressurization and trigger pull were not measured quantities. It is therefore possible that the results of the 6 outlier experiments for 150 psi are actually from a separate population produced by a lower first-stage pressure.

Therefore, the sample of velocities measured for 150 psi is considered without the 6 outlier points. Normal probability plots of the three samples are presented in Figure 2.11. The measured impact speed is dependent on a large number of independent, random variables, including (but not limited to) piston geometry, powder burn-rate, leak-rates, and AR-section geometry. Each of these parameters is governed by separate distributions. Therefore, given the Central Limit Theorem the resulting distribution of impact speeds produced should be normally distributed [45]. Inspection of the normal probability plots in Figure 2.11 indicate the results for speed are described by a normal distribution. Accordingly, this supports the removal of the outlier points for the 150 psi sample. The updated empirical CDF for 150 psi, the original results for 110 and 80 psi, and the corresponding normal distribution CDFs

for all three samples are presented in Figure 2.12. The observed sample means and standard deviations for 150 psi, 110 psi, and 80 psi are presented in Table 2.5.

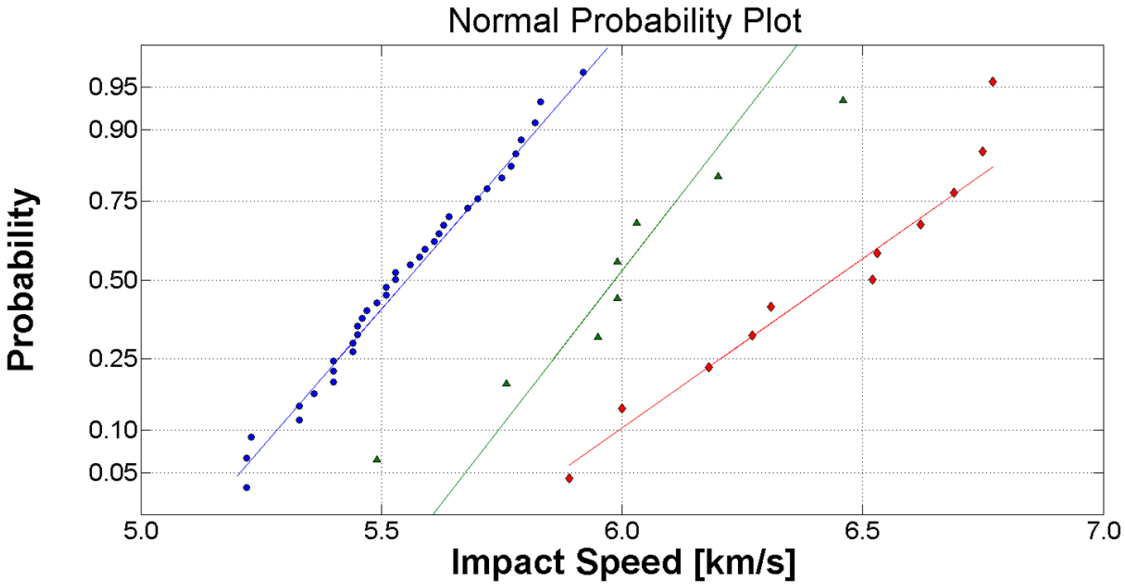

Figure 2.11: Normal probability plot for impact speeds produced using 150 psi (outliers removed), 110 psi, and 80 psi

	150 psi	**110 psi**	**80 psi**
sample mean, km/s	5.55	5.98	6.41
sample St. Dev., km/s	0.20	0.29	0.3
sample size	39	8	11

Table 2.5: Statistical parameters for the impact speed results for 150 psi, 110 psi, and 80 psi first-stage pre-compression pressure

The statistical significance in the observed difference can be determined using a two-sample t-test, given the observed normal distributions of the samples. Although, this method depends upon the assumption of normally distributed samples, moderate departures from normality do not adversely affect the technique [45]. The two-sample t-test evaluates the null hypothesis that the means of the populations of impact speeds produced by 150 psi and 80 psi are the same. Assuming the population variances are unknown and sample variances are unequal, the t-test results in a P-value of 8×10^{-7} indicating that the null hypothesis can be rejected. The P-value describes

the probability of obtaining the observed difference in sample means if the population means for 150 psi and 80 psi were the same. Therefore, it is extremely (better than 99%) probable that the reduction in first-stage pressure results in a higher impact speed. With 99% confidence, the population mean of impact speeds produced using 80 psi is between 1.16 km/s and 0.57 km/s larger than the population mean of impact speeds produced using 150 psi [45]. Overall, reducing the first-stage pressure from 150 psi to 80 psi is observed to increase the mean impact speed from produced by nearly 0.9 km/s. This corresponds to, on average, a 15% increase in impact speeds and 34% improvement in the kinetic energy delivered by the facility.

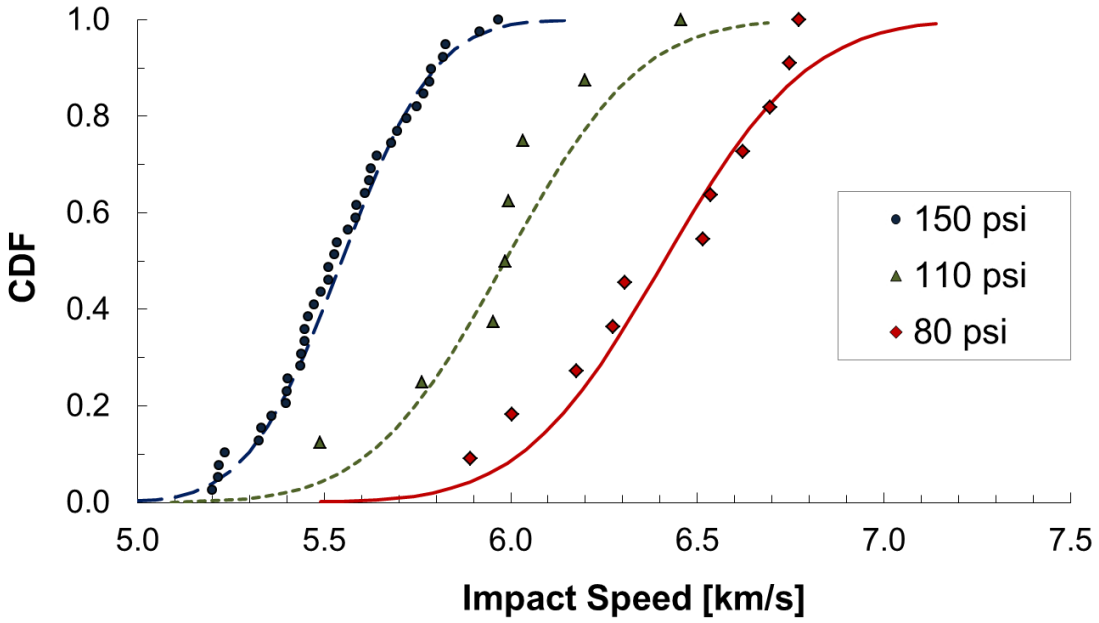

Figure 2.12: The cumulative distribution functions for impact speeds produced using 150 psi (outliers removed), 110 psi, and 80 psi. Both the empirical (points) and corresponding normal distribution (solid and dotted lines) CDFs are presented.

Additionally, after the experiments using 150 psi were conducted, the operating procedure for evacuating the atmosphere from the pump-tube was refined. As noted in Appendix A, the pumping-down of the first-stage is cycled to allow for a better seal of the piston. This cycling has been observed to considerably improve the seal of the piston in the first-stage and reduce the (positive and negative) leak-rate of

the pump-tube. The amount of atmosphere mixed with the light-gas and subsequent leak-rate of the compressed light-gas is therefore minimized. After this procedural change was made, the resulting impact speeds observed for 80 psi and 110 psi (as shown in Figure 2.10) did not exhibit any outliers as previously described.

As shown, there is still an inherent variability in the impact speeds generated by the SPHIR facility two-stage light-gas gun. However, the results presented herein have identified the first-stage pressure as a viable control to influence the impact speed produced. Results from a two-sample t-test indicate that reducing the first-stage pressure from 150 psi to 80 psi increases the average impact speed by at least 0.57 km/s, with 99% confidence. Such experimental controls are infrequently available in light-gas gun operation. Furthermore, the revision of experiment operating procedures has improved the consistency in the observed impact speed. These improvements have significantly improved the overall experimental capabilities of the SPHIR facility.

2.6.2 Mass-Velocity Performance Regime

The maximum impact speed achieved for the 5.6 mg nylon 6/6 cylinder, under ideal conditions (optimum alignment and zero component erosion) was 10 km/s. Using helium in the first-stage, impact speeds as low as 4 km/s have been observed for the 5.6 mg nylon cylinder. (However, a different method for velocimetry is required for speeds below 5 km/s, as the impactor is not self-illuminating.) Therefore, the extreme ranges of the for the SPHIR facility two-stage light-gas gun for launching 5.6 mg nylon 6/6 equiaxed right-cylinders is between 4 and 10 km/s. The SPHIR facility has also been used to launch 22.7 mg steel spheres and 3.6 mg nylon 6/6 spheres to impact speeds from 1.8 to 3.0 km/s and 5.0 to 6.0 km/s, respectively. (Appendix B described the SPHIR facility velocimetry and performance for launching the 22.7 mg steel spheres.) Therefore, the impactor kinetic energy produced by the SPHIR facility ranges from 35 J to 280 J.

The energy yield from the propellant burn is approximately $3,500$ J. Given the

reported range of impactor velocities, this represents a 1% to 9% range of conversion of propellant energy to kinetic energy of the impactor. The operating regime of the SPHIR facility describing the relationship between the impactor mass and speed is presented in Figure 2.13. Additionally, the cylinder impactors have been observed to tumble with high angular velocities estimated as at least 250,000 rpm. This corresponds to approximately 7 J of rotational kinetic energy and is not accounted for in the presented operating regime.

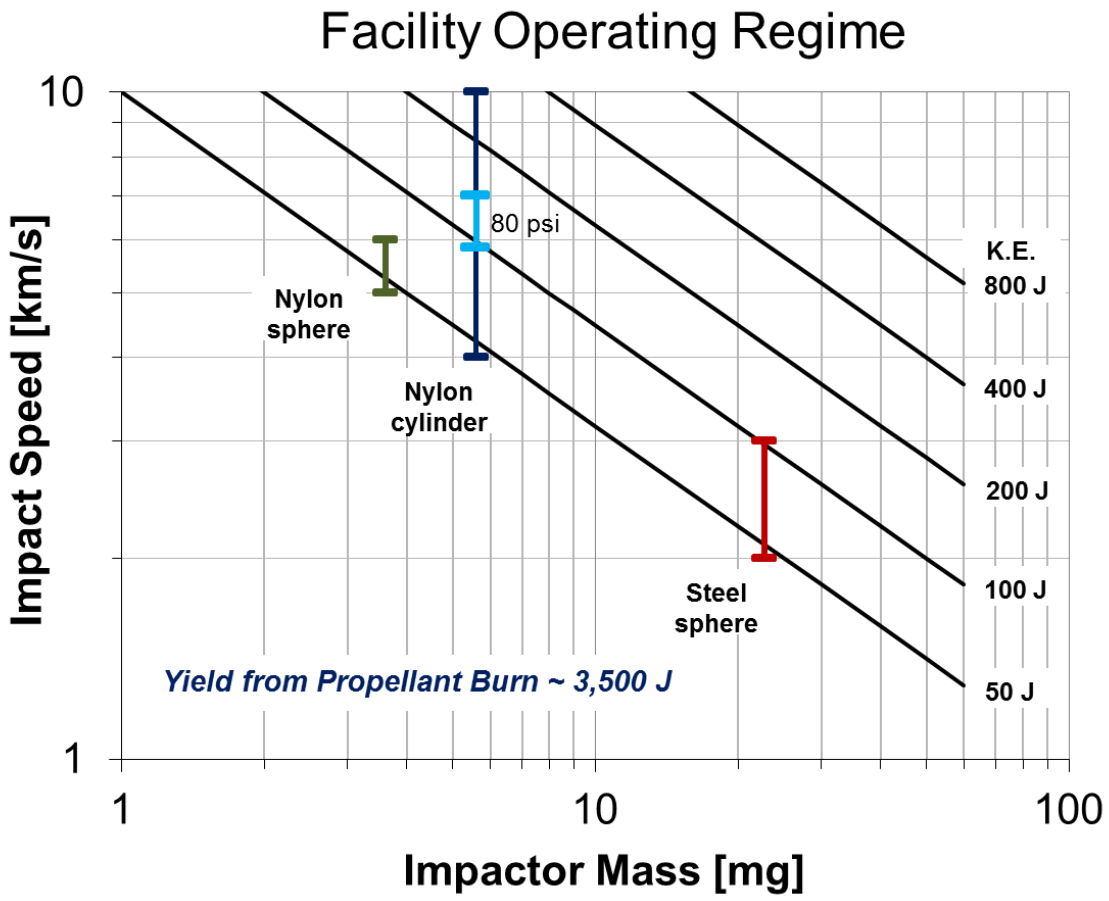

Figure 2.13: Mass-Velocity operating regime of the SPHIR facility two-stage light gas for three impactors: 22.7 mg steel spheres, 3.6 mg nylon spheres, and the 5.6 mg nylon equiaxed cylinder. For the primary impactor (5.6 mg nylon cylinder), the 2σ performance range for 80 psi first-stage pre-compression pressure is also given.

Chapter 3

Post Mortem Analysis of Target Perforation

3.1 Perforation Area as a Metric

The post mortem inspection of impacted surfaces has been used historically to evaluate numeric simulations and impact shielding systems. For target plates, the hole size (or perforation area) in particular has been commonly used as a performance metric. Perforation area is defined as the area projected through the target and onto a plane parallel to the original target back-surface by a collimated light source normal to the target.

The perforation diameter is defined as the characteristic diameter of the perforation area. Impact perforation geometry is typically not axisymmetric; however the measured perforation area is approximately circular. Therefore, the perforation diameter is determined by computing the diameter corresponding to a circle with an area equivalent to the perforation area.

For thicker targets, the diameter of the perforation hole can change through the thickness of a target. Therefore, it is important to specify the perforation diameter as the minimum observed hole diameter across the thickness of the target. This specification is consistent with the previously presented definition of perforation area in Chapter 1. The variation of a diameter through the thickness of a target is observed by Horz [20], whose work provides an example of the definition of perforation diameter

in Figure 3.1.

3.2 Scaling of Perforation Area

The majority of previous investigations on the perforation response of a target have focused on the scaling of ballistic limits. A historical overview of many of the empirically based ballistic limit equations is provided by Hayashida and Robinson [13]. However, previous work by Horz [20] and Cour-Palais [8] has been directed towards understanding the scaling of perforation diameter (and therefore area) in hypervelocity impacts.

Post mortem analysis of hypervelocity impact damage can be used to infer impact conditions, given an understanding of the scaling characteristics of such features. Current methods for perforation diameter scaling are used to infer the size distribution and population of space debris in Low Earth Orbit [19]. Measurements of impact crater and perforation diameters on space-exposed surfaces on missions such as the Long Duration Exposure Facility (LDEF) ([22]) are the basis for NASA's definition of the LEO orbital debris environment [34]. This approach is limited by the availability calibration data and adequacy derived of scaling relations.

Furthermore, the perforation diameter is related to volume and state of debris that is thrown downrange from a hypervelocity impact [67]. Debris clouds produced in hypervelocity impact have been shown to primarily consist of the material excavated by the projectile [50]. Accordingly, an understanding of the scaling relationship to describe perforation diameter help facilitate the engineering of hypervelocity impact shield systems. Therefore, a more complete understanding of the scaling of impact damage has implications on both the definition and mitigation of the threat of hypervelocity impact damage to spacecraft.

Furthermore, the majority of investigations considering the scaling of impact damage have spherical impactors. For equivalent diameters, cylinders have 50% mass than cylinders and therefore carry 50% more momentum and translational kinetic energy. Therefore, there exists less data to evaluate the effect of the shape of an equiaxed

($l/d = 1$) impactor on current scaling models.

The scaling behavior of perforation diameter D is considered by first normalizing the target damage respect to the projectile diameter d. The other pertinent length-scale is the target thickness h. The normalized target thickness h/d is the ratio of the target thickness to the projectile diameter. Accordingly, an semi-infinite target corresponds to $h/d \to \infty$ and as the target thickness goes to zero, $h/d > 0$.

The scaling of normalized perforation diameter (D/d) should be considered with regards to variation in three quantities: normalized target thickness h/d, impact speed v, and impact obliquity. It is important to consider that the scaling behavior of D/d is always with respect to the ballistic limit. The ballistic limit condition for velocity or plate thickness dictates the response of the target. Accordingly scaling relationships used to describe the response of the target have been shown to fail in proximity of the ballistic limit

Impact obliquity can play a dominant role in the ballistic limit and subsequent damage response of a target. However, the analysis and discussion of perforation area within this report is primarily on the scaling effects of variable impact speed and target thickness.

3.2.1 Scaling of Perforation Diameter: Variable Speed, Constant Target Thickness

The ballistic limit condition for a target configuration is heavily influenced by the impact speed of the projectile. The speed of the impactor dictates the stress and strain-rate as well as the subsequent deformation mechanisms (such as spallation, fragmentation, and phase change) in the target and projectile. Therefore, the damage response of a target and subsequent scaling behavior is heavily dependent upon the impact speed.

Previous work [20, 37, 72] has shown the scaling of perforation diameter with respect to impact speed to be dependent upon the normalized target thickness h/d. If the normalized target thickness is sufficiently small, the normalized perforation

diameter D/d has been shown to scale nearly linear with respect to impact speed [37].

A number of empirical models [16, 17, 72] present a large variety of scaling relations for D/d with respect to velocity, often in the form of an exponent. Other approaches for velocity scaling [20] utilize ballistic limit scaling arguments (such as [6]) to describe the evolution of D/d vs. h/d. Accordingly, the inclusion of impact mechanics to describe perforation diameter scaling with-respect-to impact speed could benefit future modeling and engineering efforts.

In bumper shield design, the scaling of shield failure (either rear-wall perforation or spallation) is described with respect to the fragmentation of the impactor. The extent of projectile fragmentation during impact determines the character of the debris cloud impacting the rear-wall. Therefore, the fragmentation of the impactor drives the damage response of the rear-wall [16] and is a primary factor in the scaling response of multi-wall shield failure. The scaling of impact penetration and perforation in bumper shied configurations is described with respect to the fragmentation of the impactor in three regimes: ballistic, fragmentation & partial melt, and melt & vaporization [5].

3.2.2 Scaling of Perforation Diameter: Constant Speed, Variable Target Thickness

For a constant speed, the normalized target perforation diameter (D/d) has been shown to scale with respect to normalized target thickness (h/d). Previous work by Horz [19, 20] has shown that this scaling relationship exists for absolute projectile and target dimensions ranging across several orders of magnitude.

At constant impact speed, a complex evolution of the perforation diameter is observed as h/d decreases from semi-infinite plates towards ultra-thin plates. The damage response of a target has been described by Horz [20] as a continuum ranging from partial penetration (cratering) to perforation, as shown in Figure 3.1.

Given an impact speed, when h/d is sufficiently large, the thickness of the target is effectively semi-infinite and the damage result on the target is determined by

cratering mechanics. Decreasing h/d results in a spall-plane approaching the bottom of the crater. As h/d approaches the ballistic limit, detached spall is possible without perforating the target. (Note that in shielding applications, this condition can sometimes be considered the failure point and thus defined as the ballistic limit).

As h/d decreases further, perforation is achieved at the ballistic limit and a measureable perforation diameter is produced. In the transition regime, the perforation diameter increases with decreasing h/d until a maximum is achieved. The h/d corresponding to this maximum in target perforation diameter is likely dependent upon the relative material shock speeds and is often approximated as $h/d = 1$ [20]. The perforation diameter then decreases monotonically as the perforation area approaches the area of the projectile. The regime characterized by the monotonic decrease in perforation size with target thickness corresponds to the "thin plate" assumption.

For increasingly thinner plates, the target perforation diameter approaches the projectile diameter. For "ultra-thin" plate ($h/d < 1/100$), it has been shown that $D/d = 1$ [72]. This complex behavior of target perforation, and corresponding variation in D/d is presented in Figure 3.2. Note that the normalized perforation size is not necessarily linear with normalized target thickness in the transition regime.

This perforation process described by Horz is an idealized description of the mechanics in hypervelocity impacts for some material configurations. The physical response of the target actually includes numerous additional material responses including rate and thermal effects. Furthermore, the introduction of other perforation mechanism (such as plugging and adiabatic shear, dynamic fracture, or dislocation motion) complicates the cratering and spallation process described by Horz in Figure 3.1. For example, stronger, rate-sensitive materials such as steel could exhibit adiabatic shearing, which would alter the spallation mechanics and subsequent D/d scaling described herein. However, this response and subsequent scaling of D/d described by Horz is observed experimentally in the SPHIR facility for the impact conditions and experiments described herein.

Therefore, as described in Figure 3.2 there is a transition from cratering mechanics to thin plate perforation mechanics. The scaling in this transition regime, and the

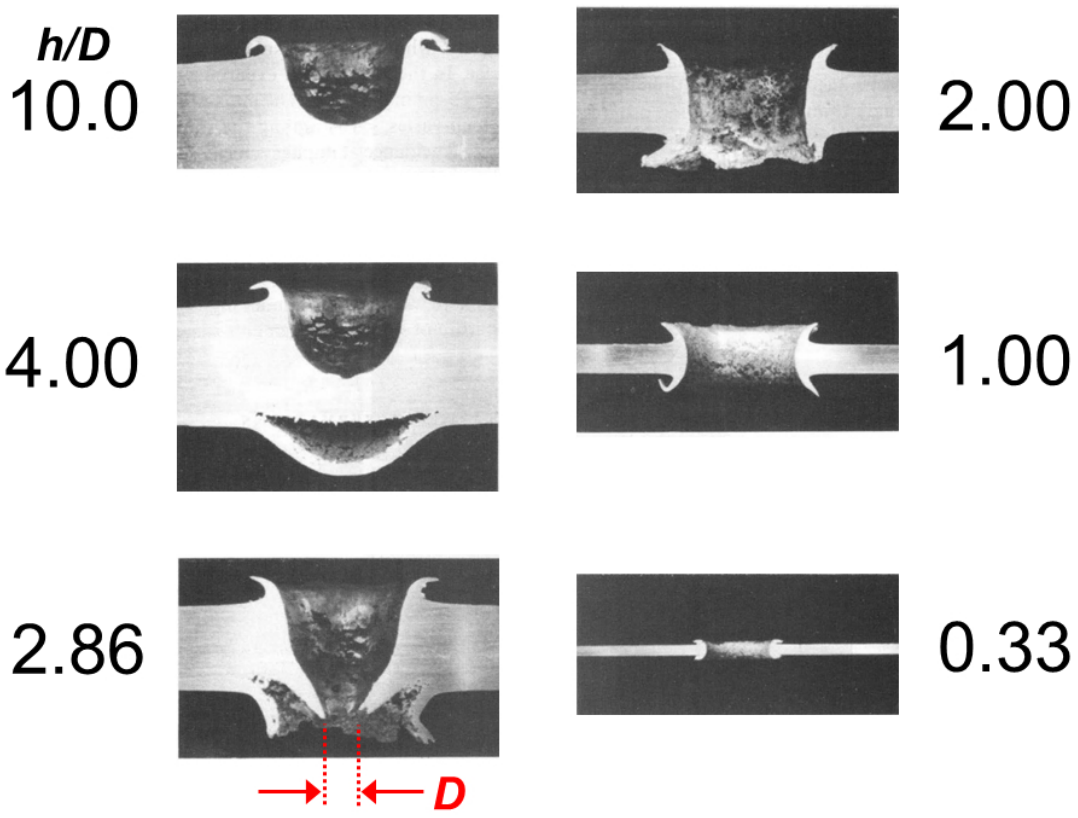

Figure 3.1: Annotation of a target images by Horz [20]: Cross-sectioned aluminum 1100 targets impacted by 3.2 mm soda-lime glass projectiles at 6 km/s by aluminum spheres. Variable d/h ratios are presented demonstrating the transition response from cratering to perforation. The definition of target perforation diameter is illustrated.

observed non-monotonic behavior D/d vs. h/d, has proven exceedingly difficult to describe. This transition regime was modeled by Horz using an 8th order polynomial of the common logarithm of $y = d/h$ and $x = D/h$, as shown in Eq. 3.1. (Note that in the work of Horz, the non-dimensional variable describing impact geometry is the normalized projectile diameter d/h.) Horz demonstrated that the form of this transition is consistent for two impact configurations with different material properties [20].

$$\log_{10} y = a_0 + a_1 (\log_{10} x) + a_2 (\log_{10} x)^2 + ... + a_n (\log_1 0x)^n \tag{3.1}$$

However, Horz (and most impact scaling laws) presents a scaling behavior derived from an empirically fit model. Consequently, application of the Horz scaling relation to a different material configuration requires specific empirically determined parameters or a large range of scaled results.

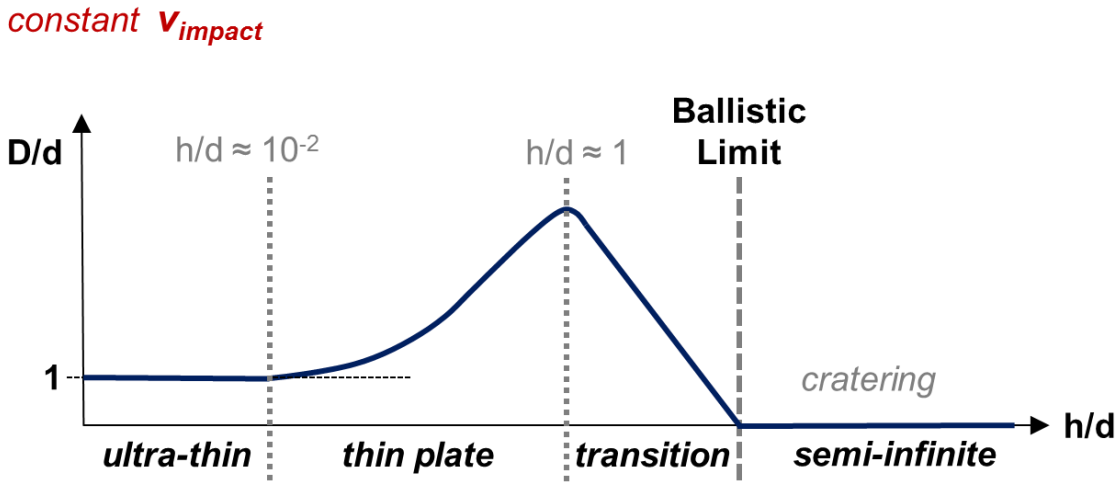

Figure 3.2: The (qualitative) variation in normalized target perforation diameter D/d as a function of normalized target thickness h/d for constant impact speed.

3.2.3 Models for the Scaling of Perforation Diameter

There have been a number of empirically determined scaling models to describe the perforation size, given an impact speed, geometry, and material properties. An overview of many of the empirical models used to describe hole size is provided by Hill [17]. In this work, Hill develops a multivariable empirical model built upon a power series of non-dimensional parameters describing impact speed, material sound speed, material density, and impact geometry. The coefficients for each non-dimensional parameter are then determined empirically from results for a large range of materials and geometries. Empirical models for both spherical and cylindrical impactors are presented by Hill, and provided in Eq. 3.2 and 3.3, respectively. The corresponding coefficients are presented in Table 3.1. Overall, the model was shown to describe the scaled perforation size over a large range of normalized target thicknesses at least

as well and often better than previous models. An important feature of the model described by Hill is a lack of material specific empirical parameters: the coefficients described can be applied to materials with a variety of densities and sound speeds.

$$\left(\frac{D}{d}\right) = c_0 \left(\frac{v}{c_p}\right)^{c_1} \left(\frac{v}{c_t}\right)^{c_2} \left(\frac{\rho_p}{\rho_t}\right)^{c_3} \left(\frac{h}{d}\right)^{c_4} \tag{3.2}$$

$$\left(\frac{D}{d}\right) = c_0 \left(\frac{v}{c_p}\right)^{c_1} \left(\frac{v}{c_t}\right)^{c_2} \left(\frac{\rho_p}{\rho_t}\right)^{c_3} \left(\frac{l}{h}\right)^{c_4} \left(\frac{h}{d}\right)^{c_5} \tag{3.3}$$

	c0	**c1**	**c2**	**c3**	**c4**	**c5**
Sphere	3.309	0.033	0.298	0.022	0.359	0
Cylinder	2.627	-0.016	0.213	0.147	0.145	0.285

Table 3.1: Parameter exponent values for the Hill model, Eq. 3.2 and 3.3 to describe perforation diameter [17].

Watts et al. [72] conducted a dimensional analysis to describe the scaling of crater diameters for thin plate ($h/d < 1/100$) impacts. The approach extends a mechanical approximation used to describe the radial expansion of craters to thin plates: radial expansion of a crater stops when the local hoop stress drops to below the target (quasi-static) yield stress. This criterion used by Watts is presented in Eq. 3.4, where σ_Y is the yield stress, σ_r is the local hoop stress at radius r from the impact, dt is the wave transit time, c_t the target material sound speed. The wave transit time, given by Eq. 3.5, is used to describe the time required for the impact-induced stress wave to transit the thickness of the material and return, assuming constant wave speed.

In thin plates, the radial propagation of stress is limited by the release waves reflected off the back and front surfaces. The rapid return of release waves therefore limits the effective shock pulse duration and causes stress to decrease rapidly with radial distance. The analysis of Watts therefore includes a factor, N, to describe the decay of stress from the impact position (Eq. 3.6). In thick targets, conservation of momentum implies $N = 2$ in the absence of dispersive mechanisms (such as plasticity), as observed in Eq. 3.7. A unique feature of Watts' analysis is the use of Bernoulli stress, given by Eq. 3.8 to describe the source stress at the interface of the projectile

and target. By setting the local hoop stress to yield stress and accounting for the shock pulse duration, the perforation diameter scaling relation is presented by Watts et al. [72] as Eq. 3.9.

$$\sigma_y = \sigma_r \Delta t \frac{2c_t}{D_c} \tag{3.4}$$

$$\Delta t = 2h/c_t \tag{3.5}$$

$$\sigma_r = \sigma_0 \left(\frac{r_p}{r}\right)^N \tag{3.6}$$

$$\sigma_r r^2 = \sigma_0 r_p^2 \tag{3.7}$$

$$\sigma_0 = \frac{\frac{1}{2}\rho_p u_0^2}{\left(1+\sqrt{\rho_p/\rho_t}\right)^2} \tag{3.8}$$

$$\left(\frac{D_c}{d}\right) = \left(\frac{\rho_p}{\rho_t}\right)^{\frac{1}{N+1}} \left(\frac{\rho_t}{\sigma_y}\right)^{\frac{1}{N+1}} v^{\frac{1}{N+1}} \left(\frac{2h}{d}\right)^{\frac{1}{N+1}} / \left(1+\sqrt{\rho_p/\rho_t}\right)^{\frac{2}{N+1}} \tag{3.9}$$

Given the form of Eq. 3.9, for $N >> 2$, D_c/d goes to 1. This feature in Watts' analysis is consistent with experimental for thin plates. To include the dependence of h/d on this monotonic decrease to 1, Watts proposes the form of exponent N described in Eq. 3.10 where $m = 1/6$. The definition of N is derived from an imposed requirement to have the thin-plate scaling equation (Eq. 3.9) equal the Watts' cratering diameter equation for larger h/d. As observed in Eq. 3.9, the dimensional scaling analysis by Watts [72] based upon impact geometry includes a description of the scaling of D_c/d with velocity.

$$N = 2\left(1 + m\frac{d}{h}\right) \tag{3.10}$$

However, an important distinction of Watts' analysis is the consideration of the

crater diameter and not the target perforation area diameter (as defined herein). The crater diameter is only equal to the perforation diameter well above the ballistic limit as the perforation diameter begins to approach the projectile diameter. By construction, the dimensional analysis of Watts is thus incapable of describing the non-monotonic scaling of D/d in the transition regime after the ballistic limit and before the thin plate regime (as illustrated in Figure 3.2). Therefore, the scaling approach of Watts is applicable, at best, until the maximum in D/d is achieved for increasing h/d. Accordingly, the formulation of N by Watts (Eq. 3.10) may be inadequate to describe perforation diameter with variable h/d: such discussion will be presented in section 3.6.4.

3.3 Measurement of Perforation Area

A plate is perforated if impact damage includes a hole or crater that would allow the transmission of light from one side of the plate to the other. Accordingly, perforation area is defined as the area projected by a collimated light source through the target and onto a plane parallel to the original target back-surface. Partial penetration is characterized as having zero perforated area.

An Optimet MiniConoscan 3000 laser conoscope system is used to measure the post mortem geometry of the impacted target plate. This instrument produces a three-dimensional (x, y, z) Cartesian coordinate map of a surface. The conscope's optics are mounted and fixed over a motorized stage consisting of a base on a two-track mechanism. Each track uses a stepper-motor to translate the target plate in the two in-plane directions (x and y) beneath the stationary laser emitting probe. The probe is configured with a 75 mm focal length objective lens, which provides an 18 mm working range (depth of field), 10 micron precision in the in-plane directions, and approximately 25 micron precision in the out-of-plane (z) direction. The target plate is translated in the x and y-directions under the stationary laser emitting probe, which measures the subsequent z-coordinate. The data from the Conoscope for the target back surfaces is visualized using TrueMap V.5.6.2 software.

The Conoscope is used to measure the perforation area of each impacted target plate, as in previous work [2]. The target is held in-place on the conoscope's stepper-motor-driven base using a custom-built three-point support fixture. This system is illustrated in Figure 3.3. The fixture bolts into the conoscope's motorized base and three $\frac{1}{4}$-inch steel ball bearings then sit in three conical indentations. The target plate, with three conically indented caps (adhered to the uprange target surface), then rests on top of the ball bearings. Conical indentations and ball-bearings were used as the mounting mechanism for the plates given their ease of manufacture, inherent stability, and ability to compensate for slightly non-planar target plate surfaces.

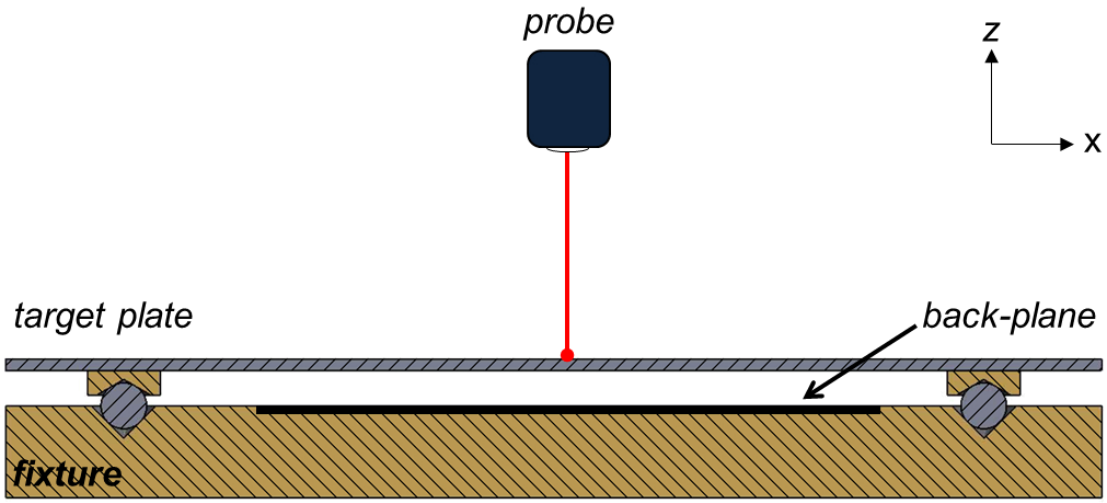

Figure 3.3: Crosshatch view of the system used to measure the target plate post mortem geometry and perforation area with the Optimet MiniConoscan 3000 laser conoscope. The target plate is supported by a fixture. This fixture translates in the x- and y-directions under the stationary laser emitting probe, which measures the z-coordinate. The back-plane, a plane parallel to the measured surface, is beneath the target. Any points measured on the back-plane correspond to perforation area.

The three contact-points supporting the target plate define a stable plane for the system to elevate the plate several millimeters above a flat reference-plane. This reference plane, referred to as the back-plane (observed in Figure 3.3, is at least 8 mm below the target plate and well within the working range of the conoscope's optics. Coordinates measured on the back-plane correspond to perforation area and are easily

differentiable from coordinates measured on the target surface. For a target that is not perforated (i.e., partially penetrated), this back-plane would not be observable by the laser probe (as is the case in Figure 3.3, which is consistent with the definition of partial penetration as having zero perforated area.

Accordingly, the perforation area measurement is conducted by first scanning the target plate with the described system then using a MATLAB script to count the number of coordinates measured on the back-plane, underneath the target plate. The uncertainty of the measurement is estimated by adding and subtracting one pixel from the boundary of the perforation area. To do so, the perforation area is first idealized as a circular area and corresponding area radius is determined. The area is then computed for radii that are one pixel longer and one pixel shorter. These new areas provide the upper and low bound estimates for the perforation area measurement. Estimate for perforation area measurement uncertainty are then taken as the differences of these areas with the measured area. For the perforation areas considered herein, this corresponds to an average uncertainty of 2.4%.

3.4 Experimental Results for Perforation Area

Perforation area results for 65 experiments, for normal impacts on plate thicknesses of $h = 0.5$ mm, 1.5 mm, and 3.0 mm are presented for analysis. (Recall the selection of the plate thicknesses was described in Chapter 2). Figure 3.4 presents the results for perforation area for the three target plate thicknesses considered. As presented, the results for perforation area exhibit a highly variable, complex response with respect to target thickness and impact speed. The intermediate plate thickness ($h = 1.5$ mm) demonstrates the largest areas and increases at a greater rate with velocity when compared to the thinnest ($h = 0.5$ mm plate). The thickest plate ($h = 3.0$ mm) produces a highly variable response, as the ballistic limit appears to be just below the considered velocity range.

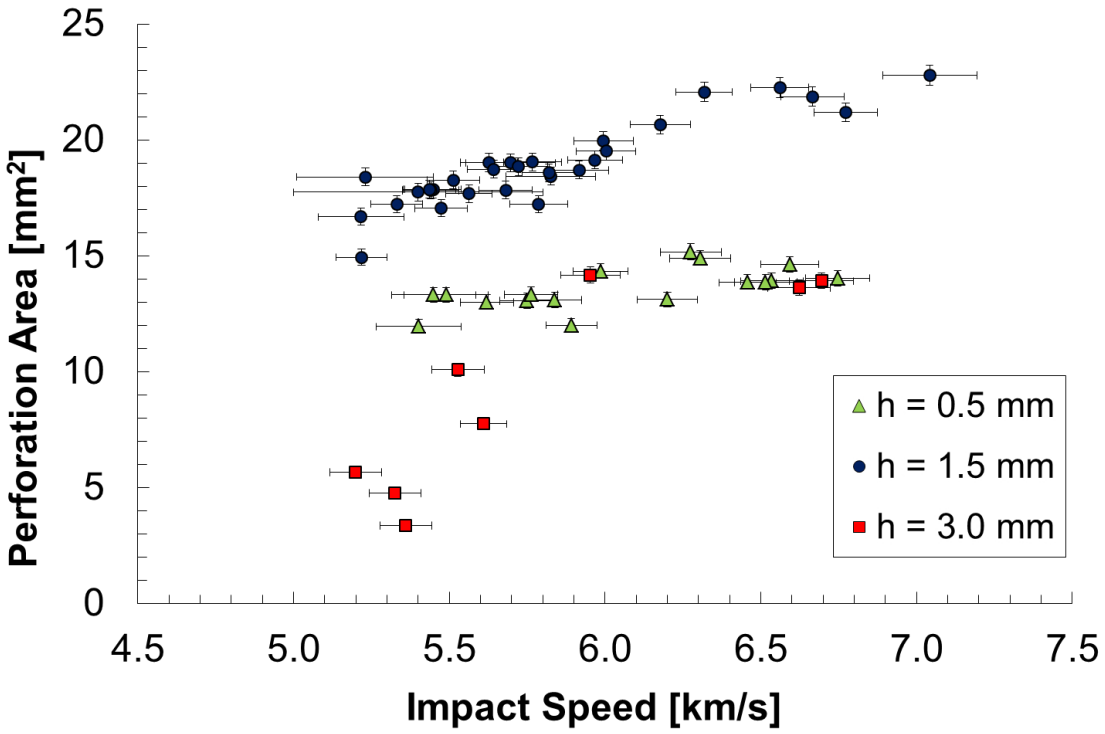

Figure 3.4: Perforation area results as a function of impact speed given for three target thicknesses: $h = 0.5$ mm, $h = 1.5$ mm, and $h = 3.0$ mm

3.5 Comparison with OTM Model Prediction

The experimental results for perforation area described herein have been used in a campaign to extend the capabilities of the OTM (optimum transportation meshfree) model developed by Li et al. [32] to numerically simulate hypervelocity impact.

The results for perforation area produced by the OTM model [1] for the three considered thicknesses at zero degrees impact obliquity are shown in Figure 3.5. As shown, the model results are discretized for every 0.1 km/s. In the OTM model, the yaw angle was a variable ranging between 0 and 45 degrees with a uniform probability distribution. For each velocity condition, simulations were run separately using at least three random yaw angles and the average resulting perforation area was reported.

A normalized comparison of the model is presented in Figure 3.6, where the model values are normalized by the corresponding experimental result. Accordingly, normal-

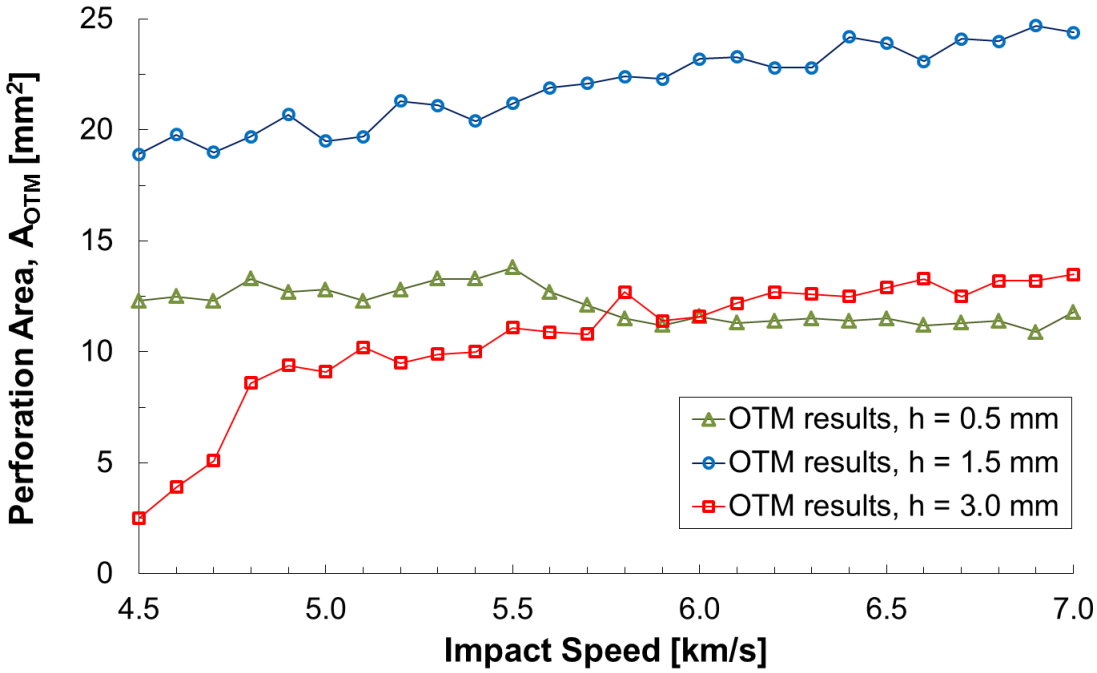

Figure 3.5: OTM model results for perforation area for the three aluminum target plate thicknesses considered impacted normally between 4.5 and 7.0 km/s [1]

ized values greater than 1 correspond to an over-prediction of perforation area of the model. Similarly, normalized values less than 1 correspond to an under-prediction of perforation area. Linear interpolation was used to determine the specific model value at the discrete velocity measured for each experiment. A comprehensive quantification in the uncertainty in OTM model's result with respect to the experimental results is presented in [1].

Overall, the OTM model is shown to provide good agreement with the experimental values, nominally within 20%. Such results are encouraging, given the large range of normalized target thicknesses considered. Between 5 and 6 km/s for the $h = 1.5$ mm plate, the disparity between the model and experimental results are approximately constant. A similar observation is made for the thinnest $h = 0.5$ mm plate between 6 and 7 km/s. Therefore, at times, the net effect of the damage mechanisms in the model is scaling with velocity at the nominally the same rate as what is observed experimentally.

For the thinnest plate ($h = 0.5$ mm, $h/d = 0.3$) between 6 and 7 km/s impact

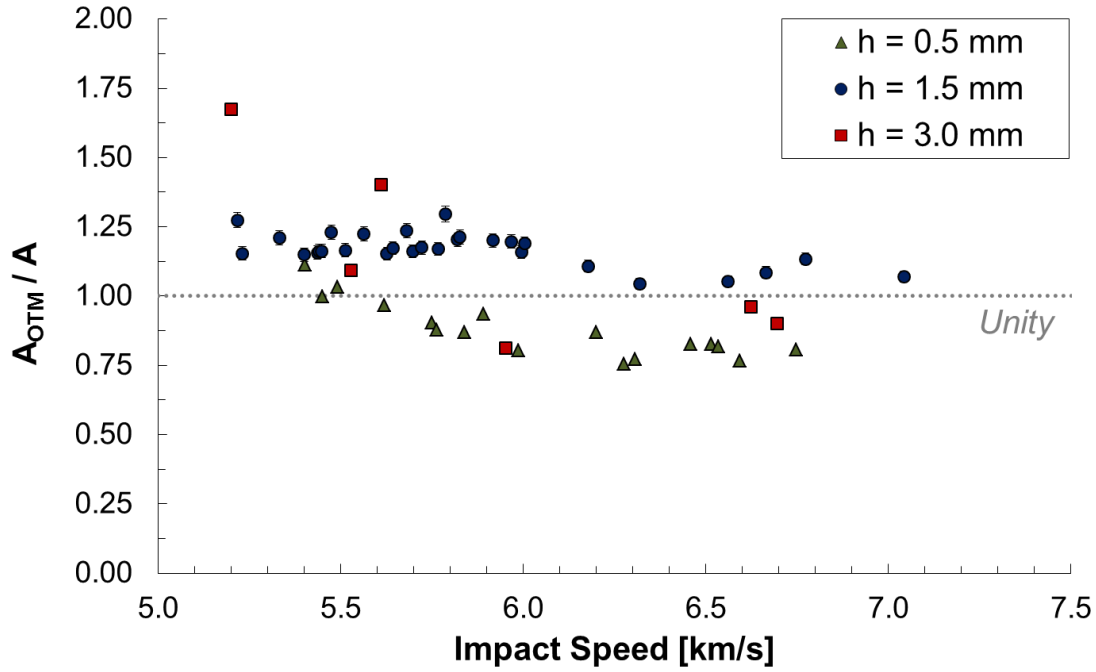

Figure 3.6: OTM model perforation area results normalized by the corresponding experimental results. Normalized values greater than 1 correspond to an over-prediction by the model. Normalized values less than 1 correspond to an under-prediction of perforation area by the model.

speed, the model predicts a result observed by many for thin-plate mechanics [20] where the perforation area result is near-constant with respect to velocity. Over the majority of the velocities presented in Figure 3.6, the numerical results for the $h = 0.5$ mm plate under-predict what is observed in the experiment. This response is likely a consequence of the material model used for the nylon 6/6 impactor [1] and subsequent short pulse duration following impact. Though the cohesive energy density of the nylon 6/6 impactor is modeled as a function of temperature, the material elements in the model use a modified polytropic equation of state [31] and therefore do not correctly describe the thermal response of the nylon impactor. As a result, given the short pulse duration, the modeled nylon impactor does not completely break apart or vaporize and ionize. Experimental results for the $h = 0.5$ mm plates from the UV-vis and IR spectrograph systems suggest a significant amount of nylon vaporization and ionization does occur [44].

Overall, the under-prediction of perforation area by the model is attributed to the partial impactor fragmentation and lack of expansion of the vaporized nylon impactor. Therefore, an improved material model for nylon 6/6 to better predict the shocked response of the cylindrical impactor and subsequent fragmentation/vaporization would likely improve the agreement with the experimental results.

For the medium thickness plate ($h = 1.5$ mm, $h/d = 0.8$), the inverse is observed: the model over-predicts the perforation areas measured in the experiment. As described, an isentropic model is used for the material elements of the impactor and therefore could not correctly simulate the process of fragmentation, vaporization and ionization of nylon 6/6. Consequently the contact time is over predicted and more kinetic energy of the impactor is deposit into the target. In addition, a variational thermo-mechanical coupling model is used for the material elements of the target, which monotonically increases the temperature. As a result, the strength of the target elements surrounding the penetrating impactor is greatly reduced due to the lack of a radiation model, facilitating an increased radial displacement of target material [31].

The largest disparities in the OTM model results with the experiments are for the perforation areas for the thickest $h = 3.0$ mm target plate. As shown in figure 3.5, the model predicts the ballistic limit for the $h = 3.0$ mm plate impacted at zero degrees is less than 4.5 km/s. Experiments suggest the ballistic limit in this configuration is between 4.5 and 5.0 km/s. Therefore, when the perforation area observed in experiments is in the nascent stage of formation just after the ballistic limit, a more fully expanded area is predicted in the model. This under-prediction of the ballistic limit by the OTM model results therefore results in the large model-experiment disparities for $h = 3.0$ mm observed in Figure 3.6 for impact speeds below 6 km/s.

An engineering model for aluminum 6061 is used to describe the target material and does account for strain hardening, rate sensitivity, and thermal softening [2]. The material fracture criterion is based on a critical energy release rate. However, this criterion is not dependent on temperature and strain rate and therefore does not capture the thermal softening and rate effects on the material fracture [31]. For

the thickest plate, ductile fracture of the target material is observed in both the model and experiment, therefore the lack of thermal effects on the material fracture response is another limitation and source of model-experiment disparity. Because thickest target plate represents the largest contact time between the impactor and target, the disparities in the physical and modeled damage response of the system are most observable.

3.6 Scaling Results of Perforation Area

3.6.1 Scaling of Perforation Area Results

To compare the perforation area results obtained in this work, to previous empirical and numerical results, the perforation area A is converted to perforation diameter D and normalized by the impactor diameter d. In doing so, the perforation area is assumed circular ($A = A_c$). The perforation area diameter D is then computed using Eq. 3.11: the diameter corresponding to a circular area equivalent to the perforation area is computed. The target thickness h is also normalized with respect to impactor diameter d. The full, scaled results for perforation area are presented in later in section 3.7.2.

$$D = \sqrt{A_c/\pi} \tag{3.11}$$

3.6.2 Uncertainty in the Normalization of Perforation Area and Target Thickness

The uncertainty in scaling results for perforation area is taken by considering both the uncertainty in the measured perforation area and the impactor geometry. The uncertainty in the impactor geometry is by estimated by considering measurement error in the length of the impactor, variability in the length of impactors used, and the potential for impactor erosion from acceleration in the launch tube and ablation from the approach to target. It has been estimated that the impactor, during acceleration

down the launch tube (before free flight) may undergo a few thousandths of an inch erosion [3]. The greater error may be in the measurement of impactor length, which varies by 2 to 4 thousandths of an inch. Therefore, the uncertainty in the length of the impactor is prescribed as 0.1 mm. The process for determining the uncertainty in the measured perforation area is described previously in section 3.3, with typical area measurements of 2.4%. The subsequent uncertainty $\epsilon_{D/d}$ in the scaled perforation size (D/d) is described the RSS uncertainty, described by Eq. 3.12, as a function of uncertainties in perforation diameter $\epsilon_{D/d}$ and projectile diameter ϵ_d.

$$\epsilon_{D/d} = \sqrt{\left(\frac{\epsilon_D}{d}\right)^2 + \left(\frac{-D\epsilon_d}{d^2}\right)^2} \tag{3.12}$$

The uncertainty in normalization of target thickness to impactor diameter is also computed using the RSS uncertainty method and an analogous equation to Eq. 3.12. The uncertainty in the target plate thickness is taken as the maximum observed disparity in plate thicknesses between batches: 0.088 mm.

3.6.3 Energy and Momentum Scaling of Perforation Area

For hypervelocity impact cratering into a semi-infinite target, the volume has been shown by many to scale linearly with impact kinetic energy [67]. This relationship between crater volume V_c and projectile kinetic energy E_p is given in Eq. 3.13, where K is an empirically determined value for the considered impactor and target material combination. Therefore, assuming the crater is hemispherical, the diameter D_c of the crater can be shown to scale to the 2/3 power of impact velocity, as shown in Eq. 3.14.

$$V_c = KE_p \tag{3.13}$$

$$\frac{D_c}{d} = \left(\frac{\rho_p K}{4}\right)^{1/3} v^{2/3} \tag{3.14}$$

The scaling of crater diameter with impactor energy therefore inherently includes the contribution of mass. The scaling relations previously presented in include a char-

acteristic impactor length scale and material density, however, do not consider the impactor volume. Therefore the impactor shape and subsequent mass is not considered. The contribution of shape in scaling laws is potentially significant considering that an equiaxed right-cylinder carries 50% more volume than a sphere with equivalent diameter. Therefore, a right-cylindrical impactor has at least 50% more momentum and energy. Similarly, a cube of characteristic length d carries 91% more mass, momentum, and energy than a sphere of equivalent diameter d. Accordingly, this represents a significant increase in the amount of momentum and energy conserved in an impact.

Therefore, the question arises whether the characteristic diameter of the perforation area scales with energy. More specifically, the role of mass in the scaling of the perforation diameter has long been considered in ballistics [3]. Some current approaches for damage prediction, such as that proposed by Williamsen et al. [75], utilize a momentum scaling factor to account for the effect of mass and velocity. Energy-scaling factors have also been widely used [16]. In conventional military velocity ranges (typically up to 2 km/s), an power of 1.6 has been used on velocity has been observed to characterize the mass-velocity scaling of the perforation area diameters [3]. Given the range of treatments for the mass-velocity scaling of perforation diameter, the application of kinetic energy or momentum for use in scaling approaches remains ambiguous.

The scaling of the presented perforation area with respect to mass and velocity is therefore investigated. The combined effect of mass and velocity is considered through variable M (Eq. 3.15) as the product of mass with velocity raised to the power n. Therefore, $n = 1$ corresponds to impactor momentum and $n = 2$ corresponds to impactor kinetic energy.

The scaling of area with respect to mv^n is then evaluated using linear regression of perforation area vs. M for values of exponent n ranging between 1 and 2. The linear regression coefficient of determination (R^2) [45] is then used as a metric to evaluate the quality of the scaling relationship between A and mv^n. Accordingly, the scaling of area with M is based upon the quality of predicting perforation area

using equation Eq. 3.16, where k and c are the linear slope and intercept coefficients determined through linear regression.

$$M = mv^n \tag{3.15}$$

$$A = kM + c \tag{3.16}$$

The results for linear regression coefficient of determination as a function of velocity exponent n are presented in Figure 3.7, for the $h = 0.5$ and $h = 1.5$ mm plate thicknesses. The corresponding linear regressions for $n = 1$ (momentum scaling) and $n = 2$ (energy scaling) are presented in Figure 3.8.

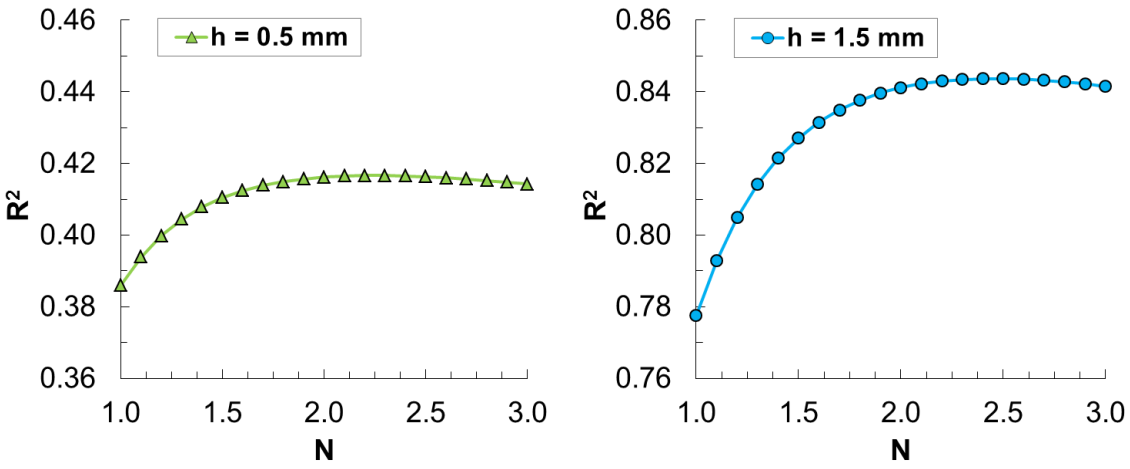

Figure 3.7: Coefficient of determination R^2 as a function of velocity exponent n, for the linear regression of mv^n vs. normalized perforation diameter D/d.

Overall, the scaling results for both target thicknesses produce a similar response, with maximum R^2 coefficients obtained for n parameters just greater than 2. Therefore, the results for target thicknesses, as presented in figure 3.7, suggest the perforation area, in this velocity regime, scales slightly better with kinetic energy than momentum. However, the improvement in the linear scaling with kinetic energy over momentum is small and therefore not significant given the uncertainties in the results for perforation area. Therefore, the current results demonstrate the current ambiguity

in the effect of mass on the scaling of perforation area with velocity. Consequently, the results suggest the scaling of perforation area requires multi-variable consideration beyond just mass and velocity, supporting the approaches of many previous models[8, 17, 72].

One possible reason for ambiguity in mv^n scaling results is that only the linear, translation impact velocity of the impactor is considered. As previously described, given the moment intertia of a tumbling cylinder, rotational energies of at least 5% of the impactor translational kinetic energy have been observed in the SPHIR facility [44]. Therefore, the addition of large (10% or more) amounts of rotational energy in the considered mv^n scaling could potentially provide insight to the effect of mass on the velocity scaling of perforation area.

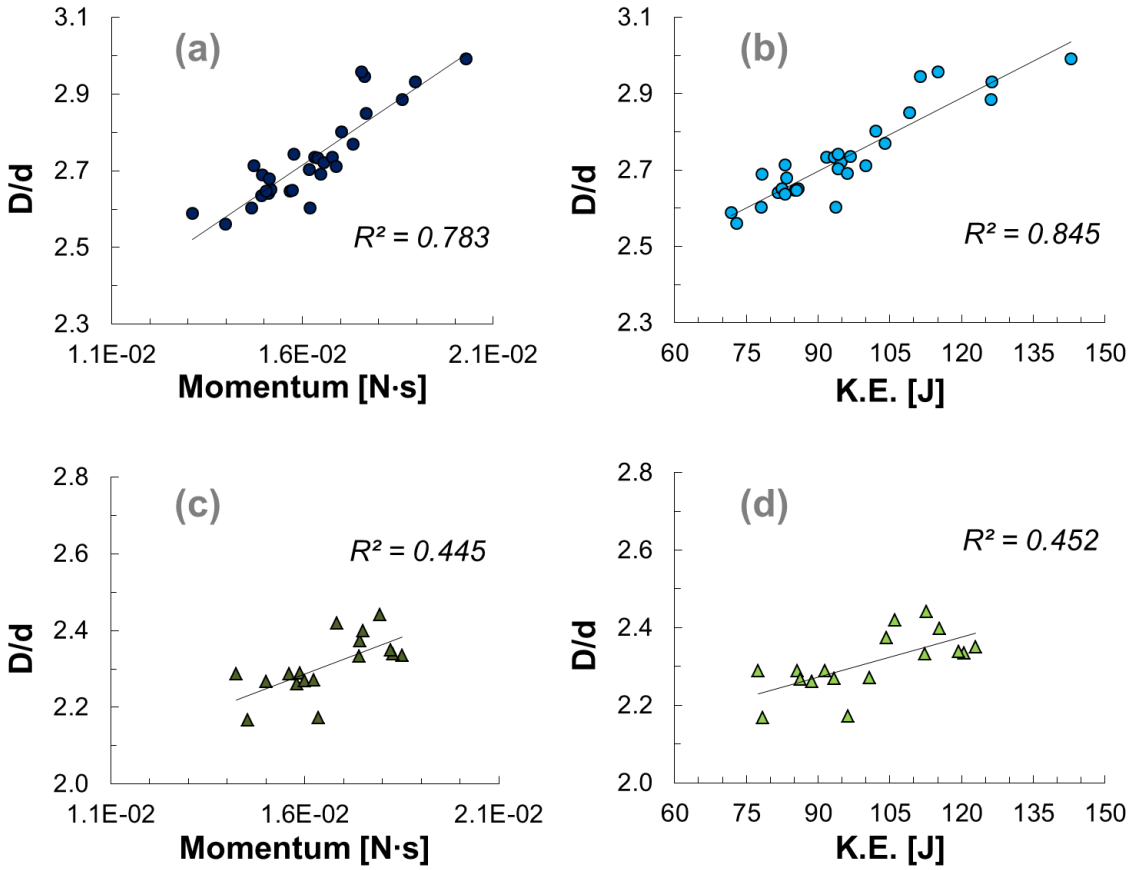

Figure 3.8: Scaling results for normalized perforation diameter D/d with linear regression and coefficient of determination (a) D/d vs. impactor momentum for $h = 1.5$ mm (b) D/d vs. impactor kinetic energy for $h = 1.5$ mm (c) D/d vs. impactor momentum for $h = 0.5$ mm (d) D/d vs. impactor kinetic energy for $h = 0.5$ mm

3.6.4 Comparison of Scaled Results for Perforation Area with Previous Work

To facilitate comparison with previous work [19, 20, 72] the scaled perforation area is plotted with respect to normalized target plate thickness on curves corresponding to constant velocity. Figure 3.9 presents the scaling results for three impact velocities: 5.65 km/s, 5.95 km/s, and 6.65 km/s. The presented scaled perforation results for each impact speed were determined by averaging the experimental results for a given thickness within 50 m/s of the reported speed. The uncertainty of the normalized perforation diameter is reported as described in section 3.6.2.

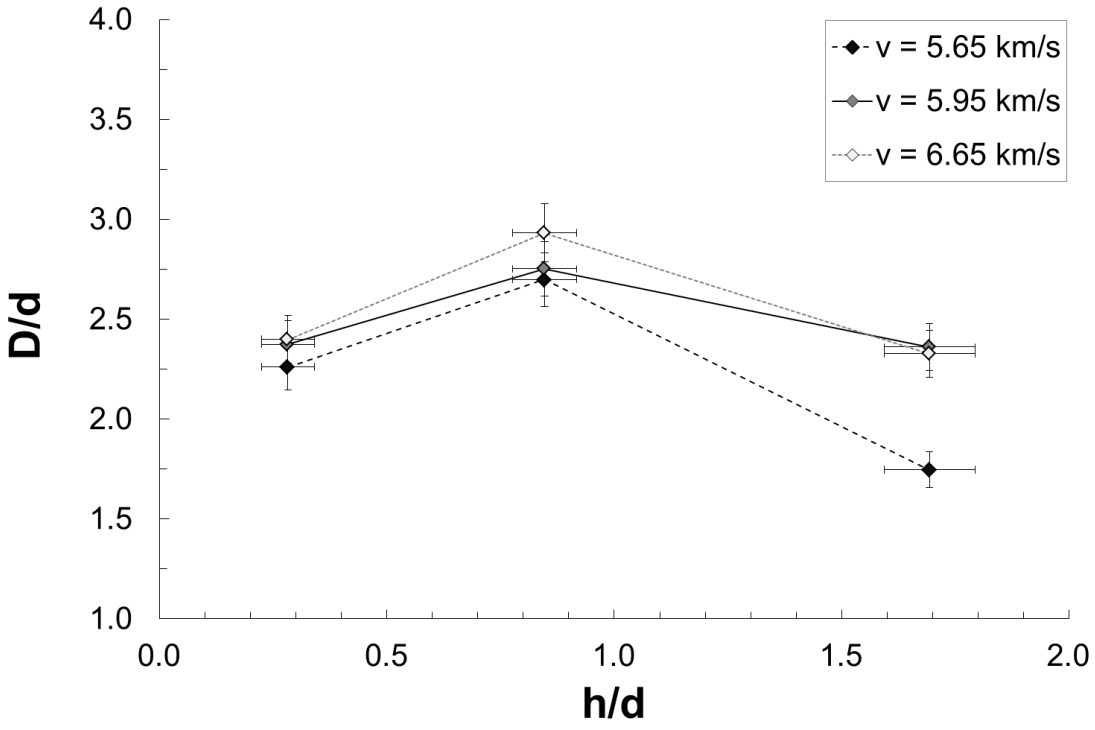

Figure 3.9: Normalized Perforation diameter vs. normalized target thickness for three impact velocities.

As observed in Figure 3.9, the perforation diameter at constant impact velocity demonstrates a non-monotonic behavior with the local maxima observed at the h/d ratio closest to one. Such behavior is consistent with the scaling results described

by Horz [20]. A disparate change in normalized perforation diameter with velocity is also observed for the three thicknesses considered. For the thickest target plate, $h/d = 1.7$, a considerable drop-off is observed as the velocity decreases. Such a decrease in perforation size is unsurprising as the velocity is decreased towards the plate ballistic limit velocity. For the remaining plate thicknesses, the intermediate plate thicknesses ($h/d = 0.8$) demonstrated a greater increase in D/d with respect to impact speed. This result is consistent with the observations made by Maiden for thin plates [37].

The results for perforation size can be compared to the previously discussed models by Watts [72] and Hill [17]. Figure 3.10 provides such a comparison with the experimentally obtained results for nylon cylinders impacting aluminum 6061-T6 plates at an impact speed of 5.95 km/s. The figure also includes the normalized results for the OTM model presented in section 3.5. As presented in Figure 3.10, the mechanics-

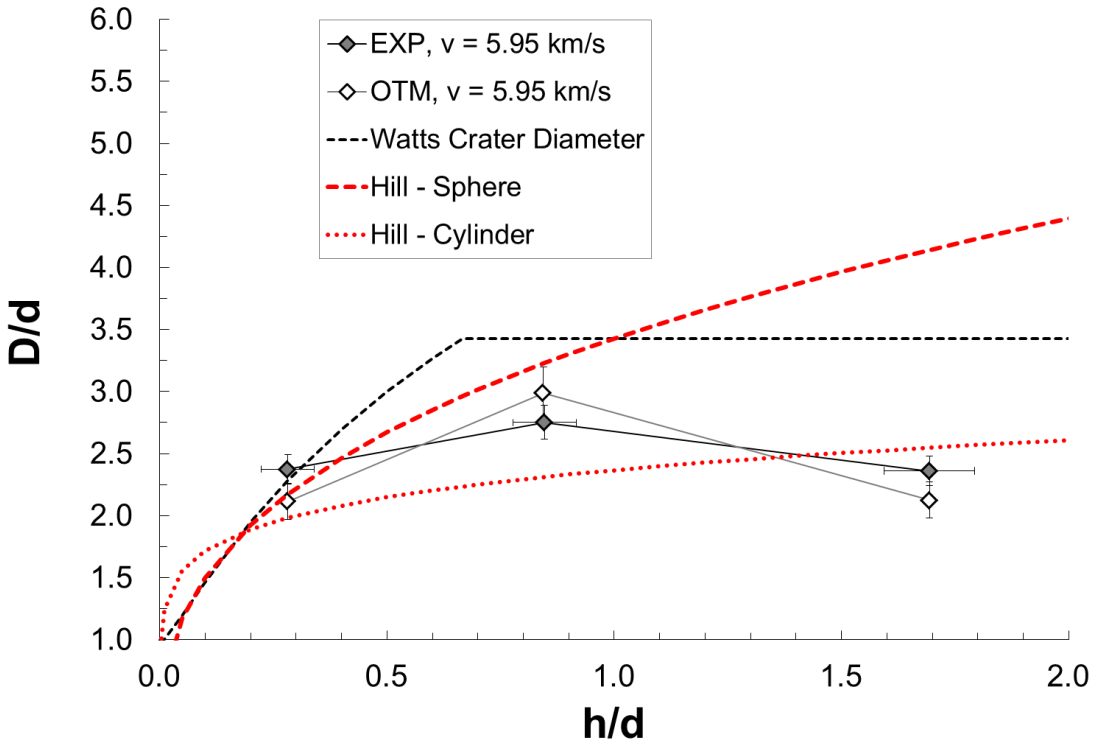

Figure 3.10: Comparison of normalized perforation diameter results for 5.95 km/s to the OTM model and scaling models presented by Watts [72] and Hill [17].

motivated model by Watts (Eq. 3.9) to describe crater diameter shows exceptional agreement with the thinnest target plate. However, as the normalized target thickness increases, the Watts model over-predicts the perforation diameter. Such a departure is expected considering that as h/d increases, the crater diameter is no longer equal to the perforation diameter, making the Watts model inapplicable.

The empirically based model by Hill for spherical impactors (Eq. 3.2) is also observed to provide a good representation of the observed perforation for the thinnest plate, but over-predicts the intermediate thickness. The Hill model for spherical impactors does a remarkable job in predicting the results produced by the OTM model.

The complementary model by Hill obtained for cylindrical impactors (Eq. 3.3) was determined empirically considering a wide-range of impactor aspect ratios. The impact mechanics of for a low or high aspect ratio impactor varies greatly from that of the equiaxed cylinder considered herein. Therefore, it is not surprising that the experimental data is best described by the Hill model for spherical impactors.

3.7 Modified Watts Model for Perforation Diameter

A modification of the Watts model, previously presented in section 3.2.3 is presented herein to describe the considered perforation diameters produced from hypervelocity impact of nylon cylinders on aluminum target plates. As described, the Watts model describes the formation of perforation diameter as being limited by the return of release waves off of the target (downrange) free surface. Accordingly, the radial expansion of the perforation is assumed to cease when the local hoop stress falls below a critical value of stress. This criterion to describe the extent of the perforation diameter is given by Eq. 3.17.

$$\sigma_Y = \sigma_r \Delta t \frac{2c_t}{D} \tag{3.17}$$

The first modification to the Watts model is the use of a rate-dependent yield stress σ_Y accounting for work hardening of the target material. For the aluminum 6061-T6 target, the critical stress for plastic yielding is given by Eq. 3.18, where σ_y is the quasi-static yield strength, is the ϵ^P Mises effective plastic strain, and $\dot{\epsilon}^P$ is the plastic strain rate [2]. This material model is implemented in the OTM model for the aluminum target material [1, 2], which is experimentally validated by Yadav et al [77]. The rate-sensitive strength model considered herein, for simplicity, does not consider the thermal effects. Accordingly the model parameters considered are: $n = 13.5$, $m = 11.5$, reference plastic strain $\epsilon_0^P = 10^{-3}$, and reference plastic strain rate $\dot{\epsilon_0}^P = 10^3$. Accordingly, the yield strength considered for use in the modified Watts model is 702 MPa, corresponding to the reference plastic strain with effective strain rate of 10^5. In the target plate the effect strain-rate varies with time and space and thus could be described as a range of values. As such, the effective strain rate prescribed is an approximation based upon numerical simulations [31].

$$\sigma_Y = \sigma_y \left(1 + \frac{\epsilon^P}{\epsilon_0^P}\right)^{1/n} + \sigma_y \left(\frac{\dot{\epsilon^P}}{\dot{\epsilon_0^P}}\right)^{1/m} \tag{3.18}$$

The second modification is the use of the one-dimensional planar impact pressure, described in chapter 1 as the impact-induced stress σ_0. The use of the shock pressure, P, accounts for the Hugoniots and equations of state for both the impactor and target. Accordingly, the impact-induced shock pressure is determined by first computing the target material particle speed u_p, as given by Eq. 1.13. With the target material and particle speed, the impact-induced pressure induced in the target and corresponding shock speed can be determined by Eq. 1.2 and 1.8.

Considering the shock speed in the target material u_s, the third modification is made to the Watts model. The wave transit time Δt is described to account for the initial transit of the shock wave and return of the attenuation wave moving at the material sound speed. Therefore, Δt is approximated using Eq. 3.19. The material sound speed is a function of pressure, however for simplicity it is assumed constant here as c_t. The speed of radial expansion of the stress state is assumed to remain at

the material sound speed, given the release waves moving off the target free surface adjacent to the impact position.

$$\Delta t = h/u_s + h/c_t \tag{3.19}$$

Lastly, the incident impact-induced stress is assumed to exponentially decay radially from the impact interface, as described by Watts with Eq. 3.6, where for a non-dispersive system $N = 2$ [72]. Given this relation and the use of the planar shock-induced pressure P, the stress at the radial limit of the perforation diameter ($r = D/2$) is then described by Eq. 3.20.

$$\sigma_r = P\left(\frac{d}{D}\right)^N \tag{3.20}$$

Watts proposes a form for N dependent on h/d such that the resulting scaling relation describes the crater diameter in a semi-infinite target. Physically, exponent N describes the radial decay of the impact-induced stress. In a plate, volumetric attenuation of the shock wave suggests $N \approx 3$. The inclusion of dissipative mechanics such as plastic flow, fracture, and void nucleation suggests that $N > 3$. Substitution of Eq. 3.18 - 3.20 into Eq. 3.17 provides the modified model for the scaling of perforation diameter: Eq. 3.21.

$$\left(\frac{D}{d}\right) = \left[\left(\frac{P}{\sigma_Y}\right)\left(\frac{c_t + u_s}{u_s}\right)\left(\frac{h}{d}\right)\right]^{\frac{1}{N+1}} \tag{3.21}$$

As such, the scaling of the perforation diameter is described by a single physically-meaningful parameter corresponding to the dissipation of the impact-induced stress wave. Using this model, with the described material properties for aluminum 6061-T6 and nylon 6/6, a dissipation exponent of $N = 4$ provides excellent agreement with the scaled results for perforation area. The modified Watts model is presented in Figure 3.11 along with the previously presented models.

Furthermore, as h/d decreases towards the ultra-thin plate regime, the modified Watts model does not asymptotically approach 1, and therefore is greater than

the other models presented in Figure 3.11 herein. Therefore, it is expected that as $h/d \rightarrow 0$, the modified model will produce less accurate estimations of perforation diameter. Furthermore, by construction, the modified Watts model (and the majority of models) cannot describe the non-monotonic behavior of D/d as h/d approaches the ballistic limit condition. Therefore, thicker plates ($h/d > 1$) require a separate scaling consideration.

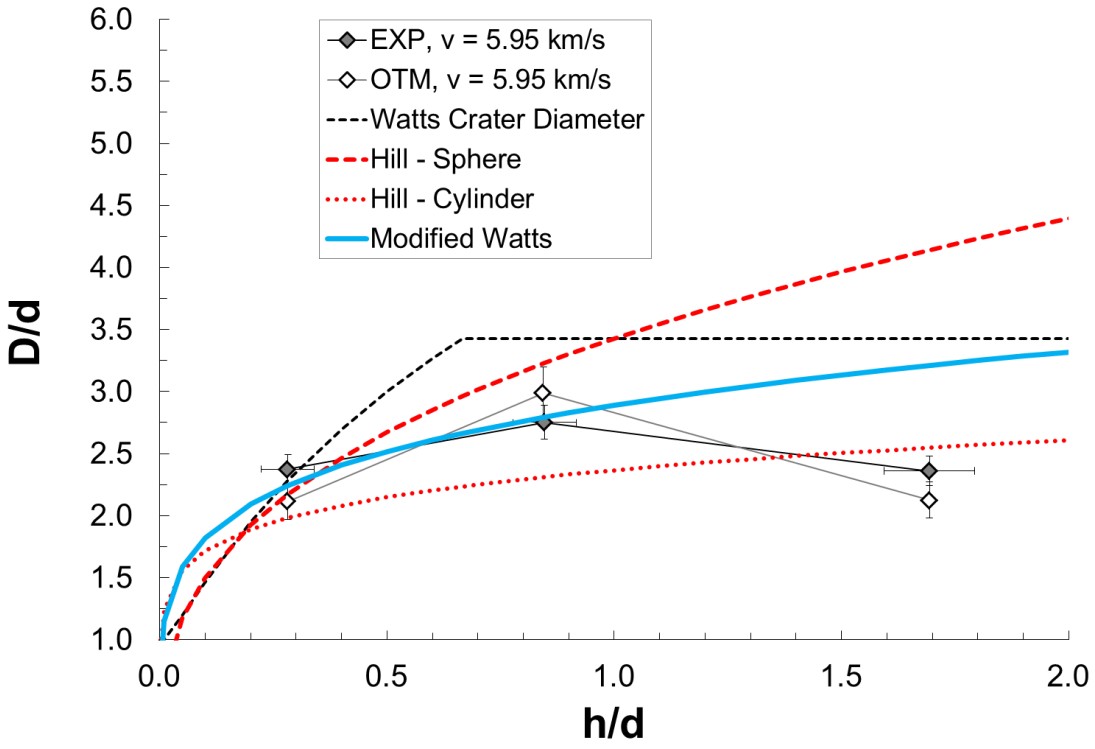

Figure 3.11: Comparison of normalized perforation diameter results for 5.95 km/s to the modified Watts model, OTM model, and previously presented scaling models.

3.7.1 Melt Approximation for Perforation Diameter in Thick Targets

For the thickest plate, we can estimate the perforation diameter by computing the volume of aluminum plate that could be melted using the all of the incident kinetic energy from the impactor. The kinetic energy available from the impactor, accounting

for only the translational energy, is given by equation (Eq. 3.22), where m is the mass of the impactor and v is the impact speed. The mass of the impactor can be written in terms of the impactor density and cylindrical geometry given Eq. 3.23.

The energy required to melt a volume of mass m_V of the aluminum material is computed using Eq. 3.24, which accounts for the energy required to raise the material to the melting point and the latent heat of fusion. In Eq. 3.24, α is the heat capacity, ΔT is the change in temperature, and L is the latent heat of fusion of the aluminum target. The change is temperature is assumed to go from room temperature to the melting temperature of aluminum. The heat capacity of aluminum is assumed constant.

The perforation diameter is then estimated assuming the incident impactor kinetic energy is used to melt a cylindrical volume uniformly through the plate thickness. Given a target thickness h, this volume is defined by an area and therefore diameter, which then corresponds to perforation diameter D. Accordingly, substituting equation Eq. 3.25 into Eq. 3.24 describes the size of the melted cylinder given an available energy. Setting this energy equal to the impactor kinetic energy for a $l = d$ impactor (Eq. 3.22 and 3.23) then provides an estimate for the normalized perforation diameter, as given by Eq. 3.26.

$$E = \tfrac{1}{2} m v^2 \tag{3.22}$$

$$m = \tfrac{1}{4} \pi \rho_p l d^2 \tag{3.23}$$

$$E = m_V (\alpha \Delta T + L) \tag{3.24}$$

$$m_V = \rho V = \rho h \pi D^2 / 4 \tag{3.25}$$

$$\left(\frac{D}{d}\right) = \left[\left(\frac{\rho_p}{\rho_t}\right)\left(\frac{h}{d}\right)\left(\frac{v^2}{2\left(\alpha \Delta T + L\right)}\right)\right]^{1/2} \tag{3.26}$$

This model neglects penetration mechanics and the known thickness variation in hole geometry for thicker plates [20]. However, for thicker plates — targets that absorb higher fractions of the incident impactor kinetic energy — this model serves as a first-order energy argument to predict the size of a perforation. For thinner target plates, an increasing amount of the incident impactor kinetic energy is carried through the target and partitioned into the debris cloud. Therefore, this model greatly over-predicts the perforation size for thinner plates. Accordingly, given the underlying assumptions used to predict the perforation area, this model is only suitable as an approximation for thick target plates.

3.7.2 Comparison of New Models to Experimental Results

The combination of the modified Watts model (for thin plates) and the melt approximation (for thick plates) provides a description of the reported non-monotonic behavior in normalized perforation diameter. Figure 3.12 presents the experimental results for D/d for a single impact speed (5.95 km/s) and the OTM model results in comparison to the modified Watts and melt approximation models. Overall, the two models together describe the increase and decrease in normalized perforation diameter. The prediction of the maximum diameter and corresponding normalized plate thickness from the two models is likely inaccurate, given the melt approximation over-predicts perforation size as target thickness decreases. However, the consideration of both models together demonstrates reasonable agreement with the experimental results and provides a physically-motivated approach to describing the scaling of perforation diameter from the ballistic limit to the ultra-thin plate regime.

For a range of impact speeds, the modified Watts model can be used to predict the experimental results for $h = 0.5$ mm and $h = 1.5$ mm. Figure 3.13 provides a comparison of the normalized perforation diameter results for $h = 1.5$ mm and $h = 0.5$mm with the predicted values from the modified Watts model as a function of impact speed. As presented, for a stress dissipation exponent of $N = 4$, the modified Watts model provides good agreement with the experimental results for a nylon 6/6

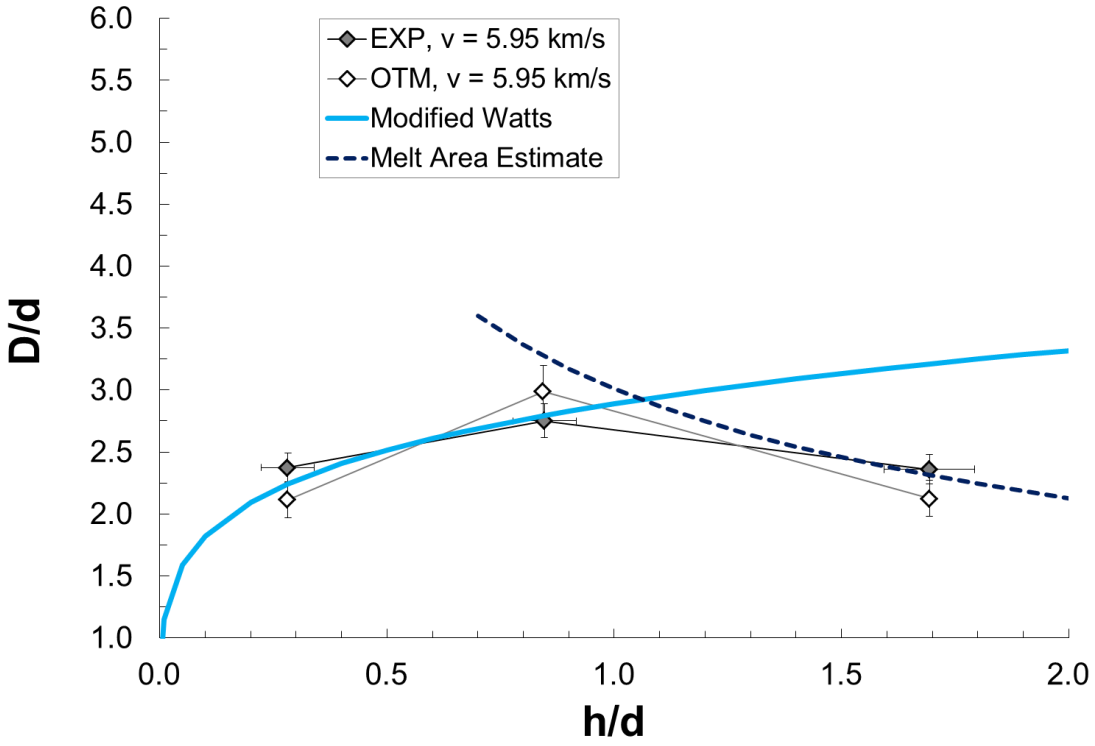

Figure 3.12: The modified Watts model and the melt area estimate compared to the experimental results for normalized perforation diameter results for 5.95 km/s.

projectile impacting an aluminum 6061-T6 target between 5 and 7 km/s. Similarly, the melt approximation can be used to estimate the perforation diameter results for the $h = 3.0$ mm experiments as a function of impact speed (Figure 3.14).

Overall, the melt approximation is observed to provide an over-estimate of the perforation size and is less accurate as velocity decreases towards the ballistic limit. As previously described, the melt approximation also over-predicts hole size for thinner plates, given that more incident kinetic energy is carried through the target (and dissipated in debris a cloud). Accordingly, the melt approximation serves as a first-order energy argument to provide a conservative approximation of the perforation diameter for a thick plate above the ballistic limit. As presented, the modified Watts model describes the perforation diameter within the measurement uncertainty of the data over a span of nearly 2 km/s. This mechanics-based model includes the rate-dependent strength, wave speeds, and shock Hugoniot of the material. With these

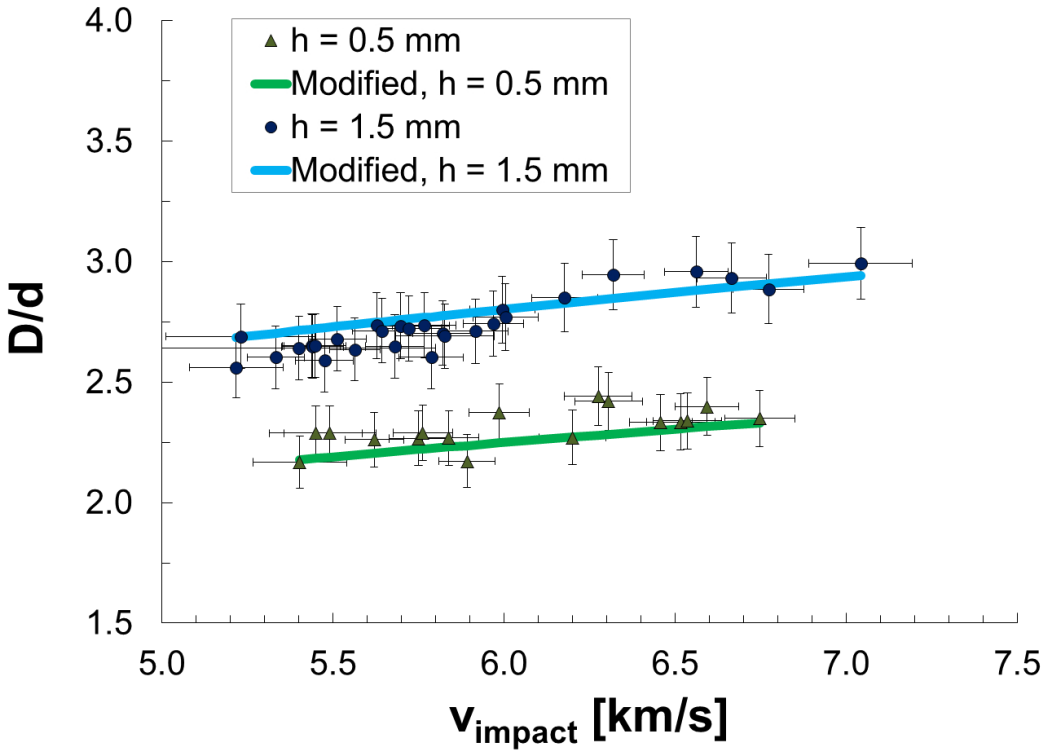

Figure 3.13: Normalized perforation diameter results for $h = 1.5$ mm and $h = 0.5$mm with the predicted values from the modified Watts model as a function of impact speed.

material considerations, the model is demonstrated to describe the data with the selection of a single, physically meaningful parameter to describe the dispersion of impact-induced stress. Such a model provides a considerable advantage over many of the current scaling models, which often require several empirically determined parameters and consider only quasi-static material properties.

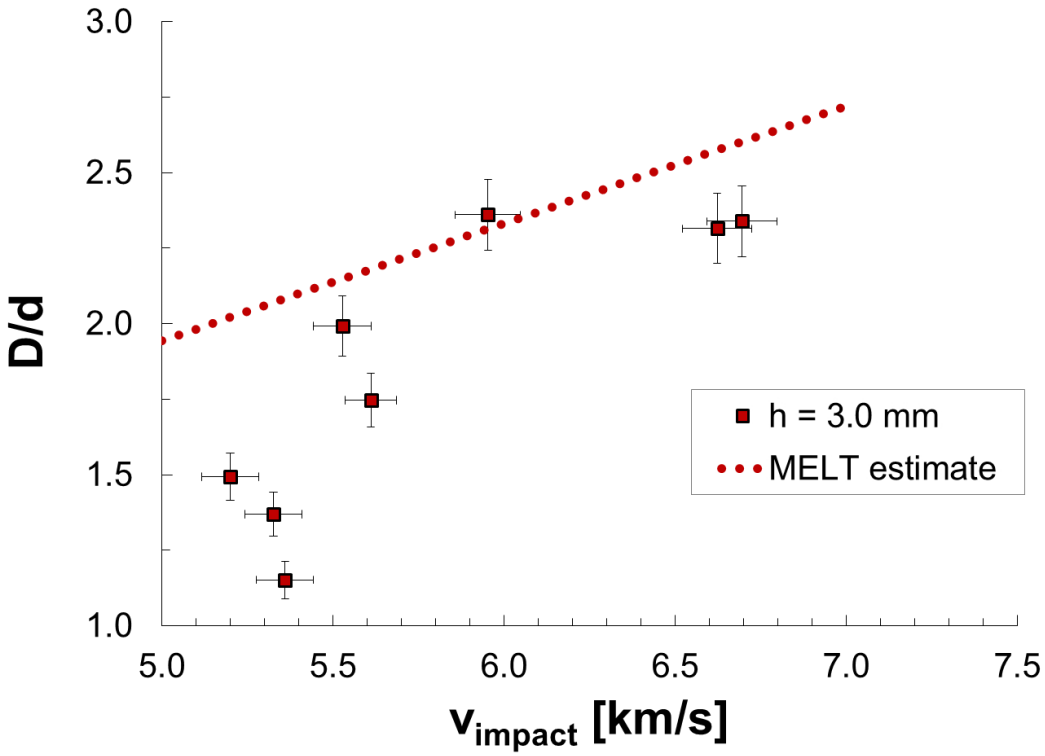

Figure 3.14: Normalized perforation diameter results for $h = 3.0$ mm with the estimated values from the melt approximation model as a function of impact speed.

Chapter 4

In Situ Measurements of Debris Clouds Produced in Hypervelocity Impacts

4.1 Debris Clouds in Hypervelocity Impacts

Debris clouds formed in hypervelocity impact drive the design of impact shielding systems. Therefore, debris cloud dynamics and composition have been studied since the 1960's. Many have studied hypervelocity impact debris clouds, although the most-widely cited work in debris cloud shape and dynamics is by Piekutowski [49, 51, 53]. Historically, flash radiography ("flash x-ray") systems have been used to observe and analyze the evolution of debris clouds [11, 49]. Figure 4.1 provides an example of a sequence of super-imposed flash x-ray images taken by Piekutowski of a debris cloud produced by a spherical impactor on a 1.5 mm thick target at 6.46 km/s.

High-speed photography has also provided an alternative to the imaging of hypervelocity impact debris formation [26]. Advances in modern digital photography have improved both the quality and utility of high-speed photography as a method to study debris phenomena in hypervelocity impact experiments [10], [74]. Many digital photography systems [56] commonly utilize flash lamps to provide diffuse white light as an illumination source. Coherent laser light has also been recently implemented as the basis for diagnostics used in the study of ejecta [15] and debris [78] phenomena.

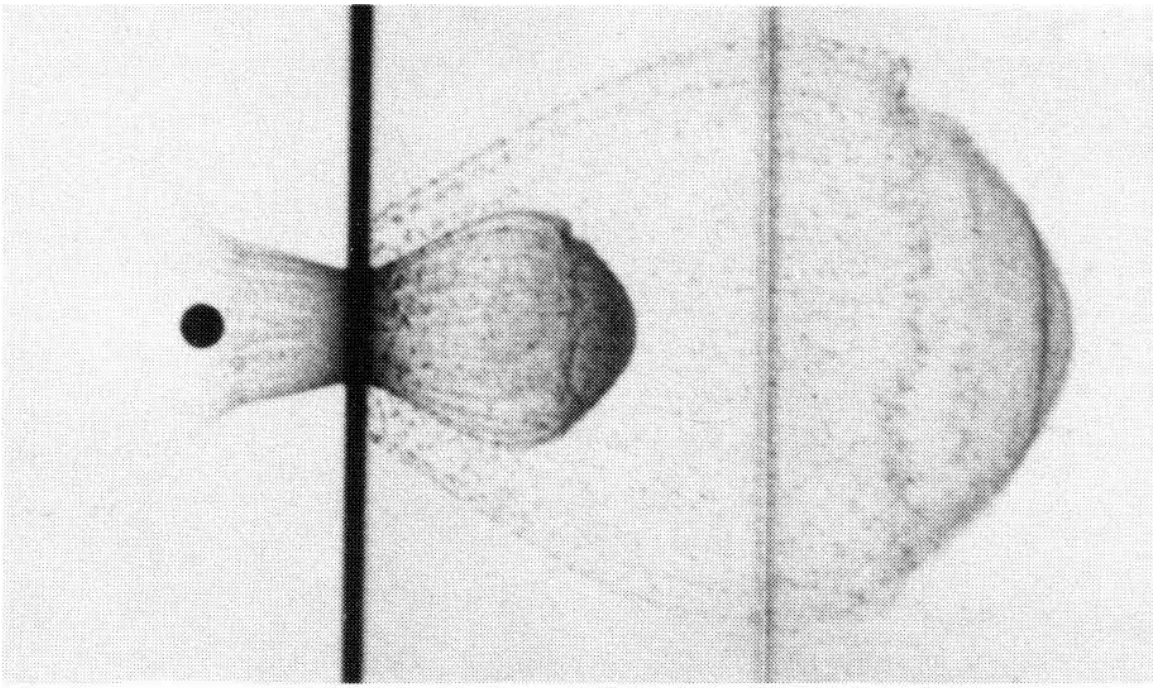

Figure 4.1: Flash radiography images by Piekutowski [50] for a 1 g copper ball impacting a 1.52 mm thick copper bumper at 6.46 km/s.

4.2 Laser Side-Lighting (LSL) Ultra-High-Speed Photography

An optical technique has been developed to create shadowgraph images of hypervelocity impact events with very short exposure times ($\leq$ 25 ns) and short inter-frame times (less than 1 µs). This short exposure time enables sharp visualization of impact features with very little motion blur at the test speeds of 5 to 7 km/s. This technique uses illumination orthogonal to the projectile flight direction to provide a shadowgraph image of the impact on the target with a perspective similar to those produced by Piekutowski [49]. The distinguishing feature of this optical imaging system is the use of a collimated, constant wave, and coherent light source.

The LSL system offers several operational advantages over the conventionally used high-speed imaging techniques. Flash x-rays require extensive safety measures (given the aggressive radiation hazard) and therefore can be expensive to acquire large data

sets. The LSL system currently uses 600 mW (or less) laser illumination and therefore represents less of a safety hazard. Once installed, the LSL system is very inexpensive for continued operation.

Additionally, unlike many other techniques, the LSL system enables continuous high-intensity illumination of the target. The laser can be turned and left on for the duration of the experiment, enabling a simpler system triggering setup. This system is therefore advantageous for facilities without a reliable method to pre-trigger the illumination source. The constant illumination of the target also reduces operational complexity of the imaging system compared to pulsed laser photography systems [24].

Furthermore, the use of a coherent light source enables the measurement of additional phenomena, such as rarified atmosphere shock waves, which are immeasurable with other techniques. The use of coherent light allows the LSL system, with small modification, to be used for several interferometry techniques such as Schlieren imaging [60] and Coherent Gradient Sensing [57] to measure the impact phenomena. Collimated, coherent light has also been used in the SPHIR facility [29] to observed and characterize dynamic crack growth induced by hypervelocity impact in transparent materials. Lastly, the use of directed (collimated), monochromatic light does not interfere with any simultaneous spectroscopic measurements of the impact event during experiments.

4.2.1 System Hardware

The laser side-lighting (LSL) system produces side-profile shadowgraphs using the Cordin 214-8 gated, intensified CCD camera. The Cordin camera contains 4 double-exposed CCD sensors to provide 8 images with 1000 x 1000 pixel resolution. The camera is capable of providing exposure and inter-frame times as low as 10 ns. The second exposure recorded on a given CCD must be delayed by at least 3.7 µs from the first exposure to allow the corresponding micro-channel plate (MCP) intensifier to reset. However, four consecutive images may be obtained by using each of the four CCDs once with a maximum framing rate of 50×10^6 fps.

A Coherent Verdi V6 diode-pumped solid-state laser is used to provide 532 nm (continuous wave) light as the illumination source. The laser beam is expanded to a 100 mm diameter collimated beam using two Keplerian beam expanders and then directed into the target tank. A large mirror is used to steer the laser illumination towards an imaging solution consisting of a Keplerian beam reducer, a focusing lens, and the Cordin camera's field lenses. The Verdi V6 laser is capable of producing 6 Watts of illumination intensity. The cross section spatial intensity profile of the laser beam is approximately Gaussian. A more uniform intensity can be delivered to the ultra-high-speed camera through isolation of the laser beam's center and removal of the less-bright perimeter of the beam. Given that a small fraction (approximately 10%) of the available laser power is required to provide sufficient illumination intensity, the most-radial portions of the incident laser beam can be discarded. Therefore, a more uniform illumination source is achieved through over-expansion of the beam before re-collimation in the second Keplerian beam expander.

4.2.2 System Specifications

The laser illumination provided by the Verdi V6 laser is delivered into the target tank orthogonal to the impactor velocity vector. Figure 4.2 provides a conceptual illustration of the LSL system setup. The primary distinction of this method from flash x-ray is that the shadowgraphs generated by this method are produced by the absorption and diffraction of laser illumination by debris particles and subsequent interference of the coherent light. Constructive interference of the collimated laser source is created by gradients in the index of refraction corresponding to gradients in density, pressure, and temperature of the atmosphere surrounding the debris.

The required laser intensity is dictated by the illumination and MCP intensifier gain settings required to observe the hypervelocity impact event with an exposure time approaching ns (the limit of the Cordin camera). Such an exposure time is required to reduce motion blur of the observed phenomena and prevent pixel saturation of the impact flash. A laser power of 600 mW is capable of delivering exposure times between

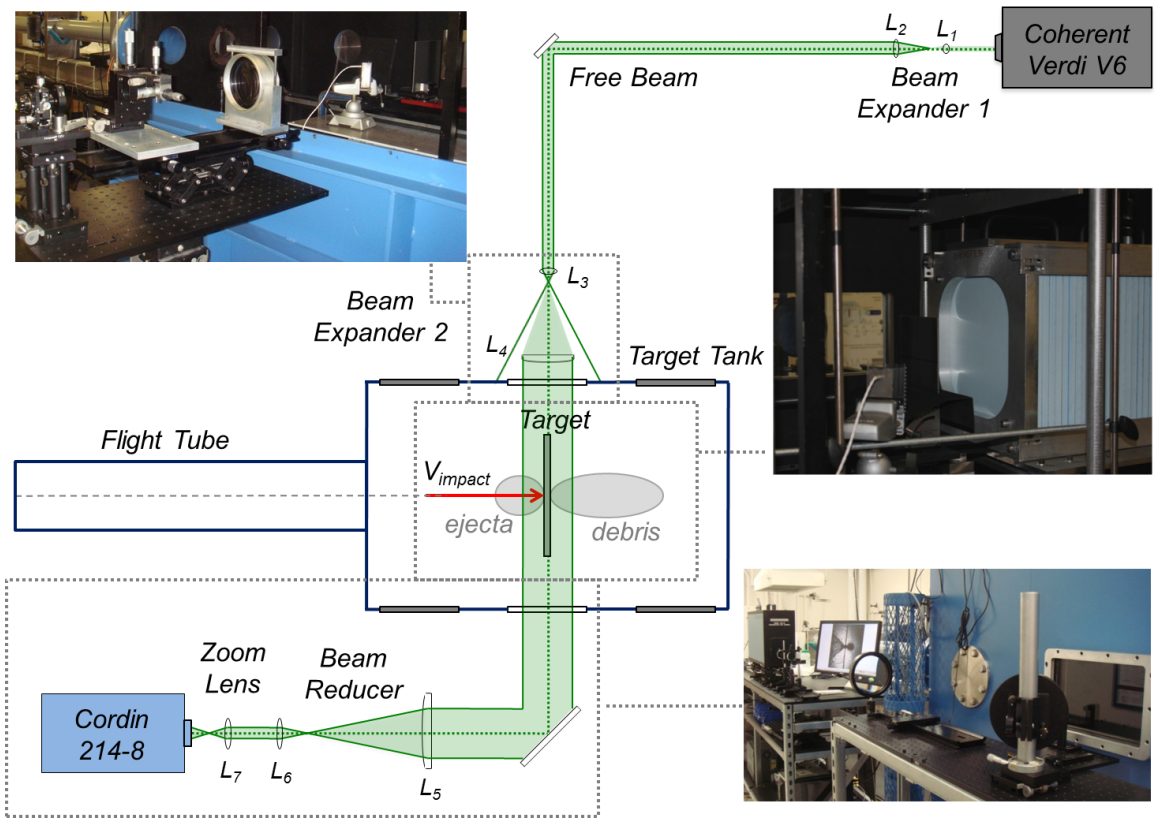

Figure 4.2: Illustration of the laser side-lighting system and various views (illustration not to scale).

10 and 20 ns with the Cordin recommended MCP intensifier settings. Increasing the MCP intensifiers to their maximum settings, a laser power of 60 mW may also be used.

The current maximum field of view with this system is defined by the diameter of the expanded laser beam: 100 mm. Given that the illuminated field of view is circular, two options are considered to utilize the 1000 x 1000 pixel square CCD. The primary imaging solution utilized inscribes the circular illuminated field of view within the square CCD. This image solution represents the highest possible pixel resolution (0.1 mm/pixel) for the largest field of view. However, with this configuration, the corners of the square CCDs are not illuminated, and therefore unused. An imaging solution can be defined to utilize all 1000 x 1000 pixels of the CCD by inscribing the square CDD within the circular illumination field. Such an imaging solution provides

a pixel resolution of approximately 0.07 mm/pixel. Figure 4.3 provides a graphical representation of these two imaging geometries.

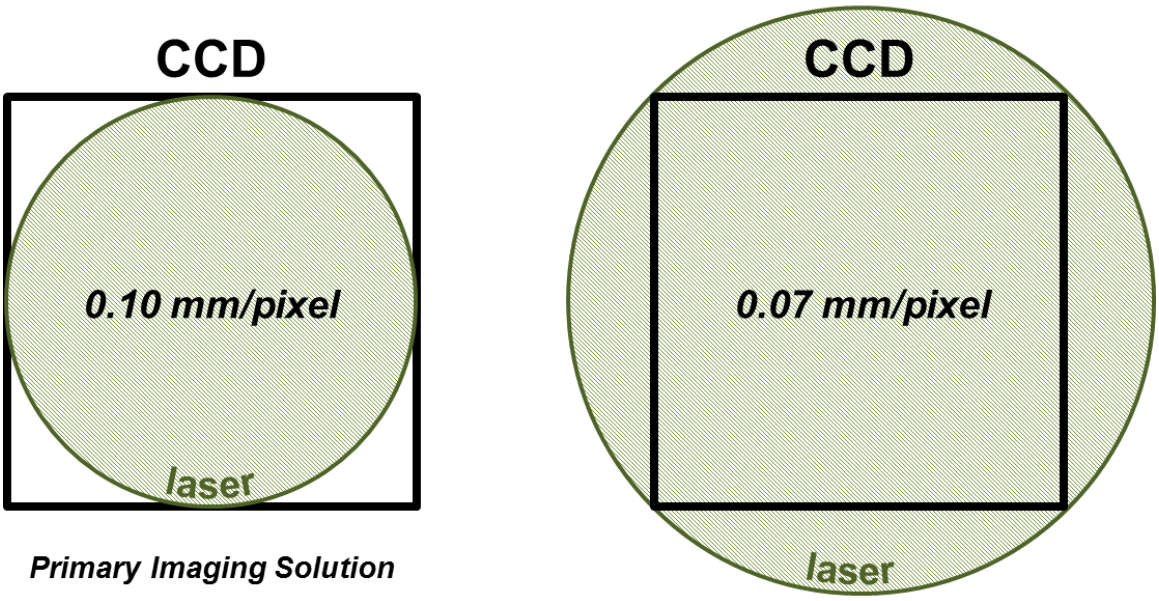

Figure 4.3: The two imaging options considered. The primary imaging solution (left) provides a 0.1 mm/pixel resolution by inscribing the laser illumination within the square Cordin CCD. The second option inscribes the CCD within the illuminated field providing 0.07 mm/pixel resolution.

4.2.3 Opto-Mechanical Design

The opto-mechanical design of the LSL system can be described as three primary components: the initial beam expander, the primary Keplerian beam expander, and the imaging solution.

The initial beam expander is used to diametrically expand the beam output by the Coherent Verdi V6 laser. This Keplerian beam expander is composed of two achromatic lenses (L_1 and L_2) separated by the sum of their focal lengths ($f_1 + f_2$). Table 4.1 provides a summary of the lens components used in the opto-mechanical setup of the LSL system.

The primary Keplerian beam expander is composed of an infinity-corrected objective lens and a 100 mm clear aperture (clr aptr), 250 mm focal length (f) achromat

Component	type	f [mm]	clr aptr [mm]
L1	Thorlabs AC254-040	40	25
L2	Thorlabs AC254-080	80	25
L3	Leica 440 Objective	4.6	8
L4	X-ZAR #31	250	100
L5	Melles Griot	1000	145
L6	Thorlabs AC508-150	150	50
L7	Thorlabs AC254-060	60	25
L5*	Melles Griot	1000	145
L6*	Thorlabs AC508-150	150	50
L7*	Thorlabs AC254-040	40	25

Table 4.1: Optical components of the laser side-lighting (LSL) System: lens type, focal length (f) and clear aperture (clr aptr). *Lenses used for the 0.07 mm/pixel illuminated field of view.

lens. The clear aperture of the collimating lens is the limiting factor in defining the illuminated field of view. In order to obtain a larger field of view, a collimating lens with a larger clear aperture would be required. The initial expansion of the laser beam floods the first lens in the primary Keplerian beam expander. As a result, the beam is over-expanded going into the collimating lens, resulting in isolation of the (more-uniform) central portion of the beam's Gaussian profile.

The imaging solution is composed of three lenses. First-order paraxial beam theory [14, 40] was used to design the approximate imaging solution. After setup in the SPHIR facility, the precise positioning of each lenses was then adjusted to optimize image focus. The positions of the lenses used in the LSL system for the two imaging solutions considered herein are presented in Table 4.2. Figure 4.4 presents the definitions of the reported dimensions graphically.

config.	X_a	X_b	X_c	X_d
0.1 mm/pixel	1391	1257	248	137
0.07 mm/pixel	1588	1118	208	121

Table 4.2: Positioning of the lenses (in mm) used in the opto-mechanical set-up for the two field of view (fov) configurations used in laser side-lighting (LSL) System.

Both imaging solutions utilize a 150 mm focal length plano-convex lens to reduce the 100 mm diameter beam, after passing through the target chamber, followed by

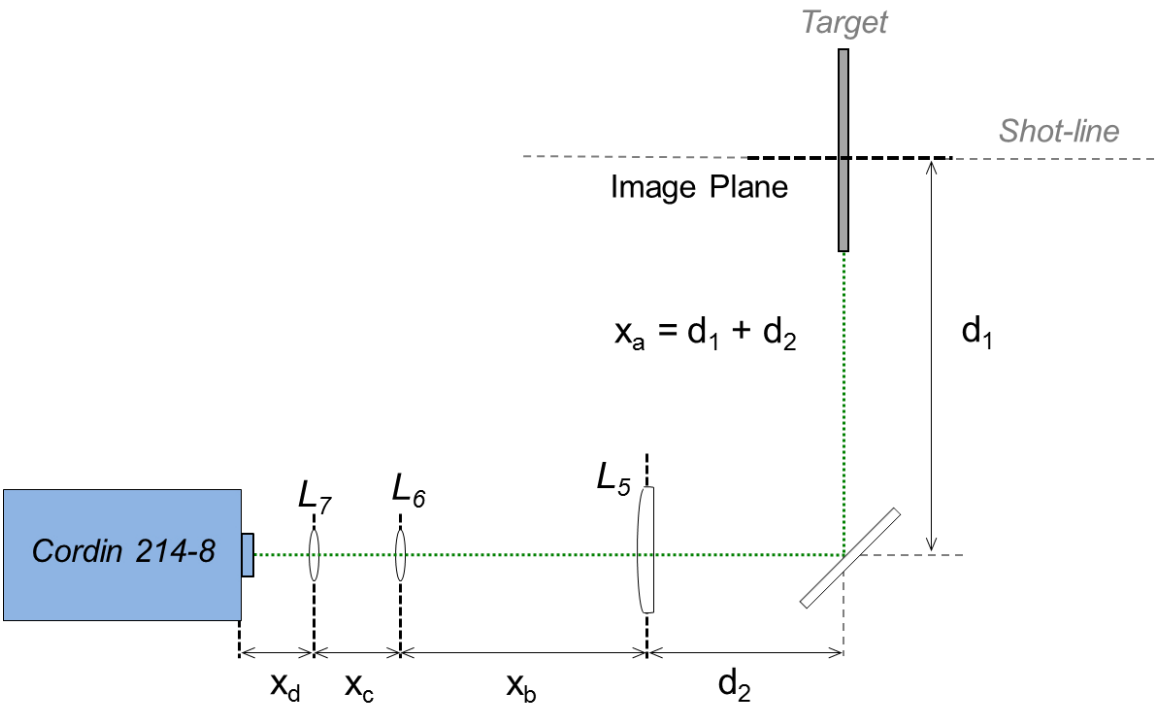

Figure 4.4: Definitions of the lens positions used in the imaging solutions reported herein.

a 150 mm focal length lens. The differences between the two imaging solutions are the final imaging lens used before the Cordin camera and the spacing of all the described lenses. Additionally, for optimal focus using the 0.07 mm/pixel configuration, the beam is large enough going into the final 25 mm clear aperture lens to cause a pincushion distortion along the periphery of the illuminated field of view. The effect on analysis is minimal, given that the largest distortions are not projected onto the Cordin CCD.

Note that a band-pass filter, centered on 532 nm, can be deployed between the final lens and the Cordin camera. This would isolate only illumination of the Verdi laser and prevent pixel saturation from impact flash phenomena. However, the exposure time of the Cordin camera is often sufficient to prevent impact flash-induced pixel saturation. For comparison to the concurrent diagnostics utilized in the SPHIR facility, the detection of intense visual range flash emission was desired. Furthermore, the band pass filter would require increases laser illumination intensity.

The Cordin camera is configured with two fixed, internal field lenses. The first lens is an Edmund optics $f = 100$ mm plano-convex lens (32-897). The second lends is a Melles Griot $f = 300$ mm meniscus lens (01LPMP027). The separation distance between these two lenses (x_f), within the body of the Cordin camera, is approximately 12 mm. The effective focal length of the combination of Cordin field lenses can be computed using Eq. 4.1 [61]. This approximation assumes the effective lens is positioned midway between the field lenses and can be used in the first-order paraxial beam theory design of the imaging solution. For the focal lengths and lens separation distance described, the field lens combination in the Cordin camera has an effective focal length of 77 mm. The set distance between the second Cordin field lens and the photo-cathode array is approximately 330 mm.

$$f_{ab} = \frac{f_a f_b}{(f_a + f_b - x_f)} \tag{4.1}$$

4.3 Cordin Camera Calibration

4.3.1 Temporal Drift of Cordin Grayscale Intensity

The use of the Cordin camera to observe debris cloud phenomena requires an understanding of the background illumination intensity and how it changes with time. The identification of a debris front and the determination of the lower bound of measurable changes in optical density is dependent upon the stability and dynamic range of the background illumination intensity. Therefore, the limiting factor in the LSL technique (and other optical techniques utilizing intensified cameras) is the performance of the Cordin camera's four MCP intensifiers.

The background illumination intensity, i.e., pixel grayscale values, has been observed to change with time. This drift in ambient pixel values has been observed to in two forms: temporal drift and power-cycle drift. As described, the background illumination grayscale values change with time for each pixel. The grayscale of each pixel was also found to change when the camera power was cycled on and off. Upon

rebooting the Cordin camera, for identical settings, the measured ambient grayscale values were not always within the previously monitored temporal drift. Furthermore, the observed amplitude of grayscale oscillation with time has been observed to be dependent upon both the considered CCD and intensity of the incident laser illumination.

Therefore, given the temporal drift of the Cordin camera, images taken before and during experiments cannot be directly compared. Such a comparison to describe observed debris cloud behavior would require a comprehensive, time-intensive calibration procedure to characterize ambient grayscale levels at the time of an experiment.

Accordingly, the measurement of a debris front and farthest expanded (least dense) debris material, given a dynamic ambient background grayscale level, requires a new technique to differentiate debris from background. The edge-finding technique developed to do so is described in section 4.4.2.

4.3.2 Cordin Camera Optical Density Calibration

The response of ambient illumination grayscale level to variation in optical density of the optical path length was determined using a Thorlabs NDL-25S-4 optical density step filter. The step filter provided optical densities (OD) of 0.1 to 4.0. Optical density is defined [71] using Eq. 4.2, where T_f is the fraction of transmitted light intensity. For example, $OD = 2$ corresponds to 1% transmission.

$$OD = \log_{10}\left(\frac{1}{T_f}\right) \tag{4.2}$$

To calibrate the grayscale response to changes in optical density, while accounting for the temporal drift of the Cordin, a series of 12 images were taken with and without the filter. The images were obtained using 1 minute intervals and with the filter added or removed after every sixth image series taken. For each pixel on both exposures (A and B) from each CCD, the average grayscale value was determined for both the filtered and non-filtered sets. Then, for each pixel, the average filtered grayscale was normalized by the average unfiltered grayscale. Lastly, the calibration curve

was constructed by considering the average and standard deviation of the normalized average pixel grayscale within each optical density region on the step filter.

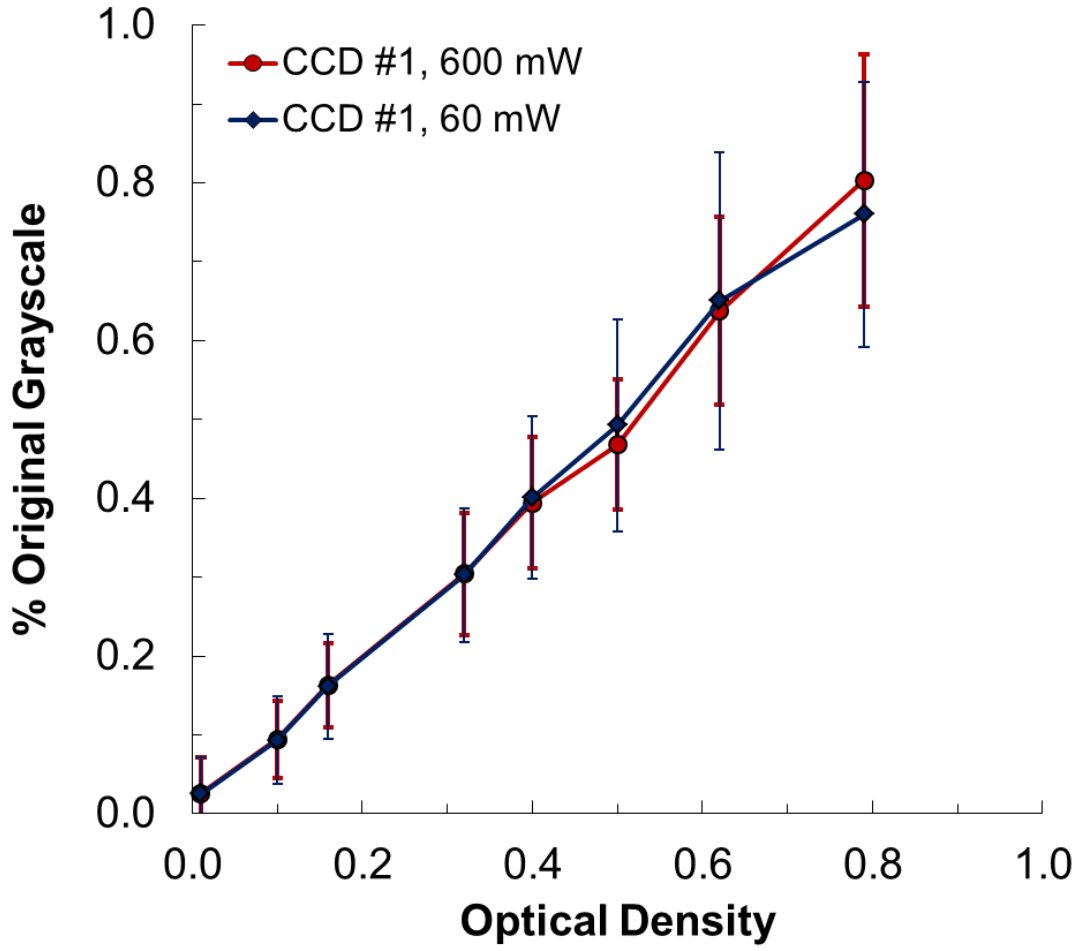

Figure 4.5: Characteristic grayscale response curve for variable optical density for the Cordin 214-8 camera used in the LSL system. The average grayscale is normalized by the average original (unfiltered) grayscale and plotted with respect to optical density.

The optical density response was considered at the two laser illumination levels considered herein: 600 mW and 60 mW. Grayscale response curves for variable optical density were also obtained at locations to rule-out spatial dependence on the observed calibration. A characteristic result for the resulting response curve of each Cordin camera CCD to variable optical density is provided in Figure 4.5. In the presented calibration curve, the average filtered grayscale normalized by the average unfiltered

grayscale is plotted with respect to T_f (% transmission). As shown for CCD #1, at both 600 mW and 60 mW, the optical density response curve is approximately linear. For example, an optical density corresponding to 60% transmission produces, on average, a grayscale intensity of 60% the original unfiltered grayscale. The error bars correspond to plus and minus two standard deviations of the response of all of the pixels in a given filter region. The variability of grayscale response at higher levels of transmission is expected, given that the background illumination is itself noisy.

The calibration curve has implications for the determination of the debris front, as the grayscale response to optical density defines the lower bound for measurable changes in optical density. Furthermore, the characterization of a normal, predictable response of pixel grayscale that is independent of CCD or laser illumination intensity enables the determination of debris cloud optical density contours. This technique and results for debris cloud optical density are presented and discussed in section 4.4.4.

4.4 Image Analysis

4.4.1 Image Processing

The pixel length-scale for each image is determined through the pre-experiment imaging of a Cartesian grid. An example calibration grid image with 10 mm grid spacing is provided in Figure 4.6. During the instrument triggering tests before each experiment, a 3.75" long 4-20 screw is placed within the field of view. The screw remains next to the target during the pre-experiment set-up to ensure the LSL system remains in focus during preparation. The screw later serves as a convenient fiducial marker and auxiliary source for pixel length-scale measurement, given the precise mechanical tolerances on the positions of the screw threads.

During image analysis, a median filter is used on the entire image to reduce random or "salt-and-pepper" noise. The median filter is applied, as supposed to a low-pass filter, because it is able to preserve the edges of features [33], thus minimizing the effect on the phenomena to be measured. When applying the median filter, an N

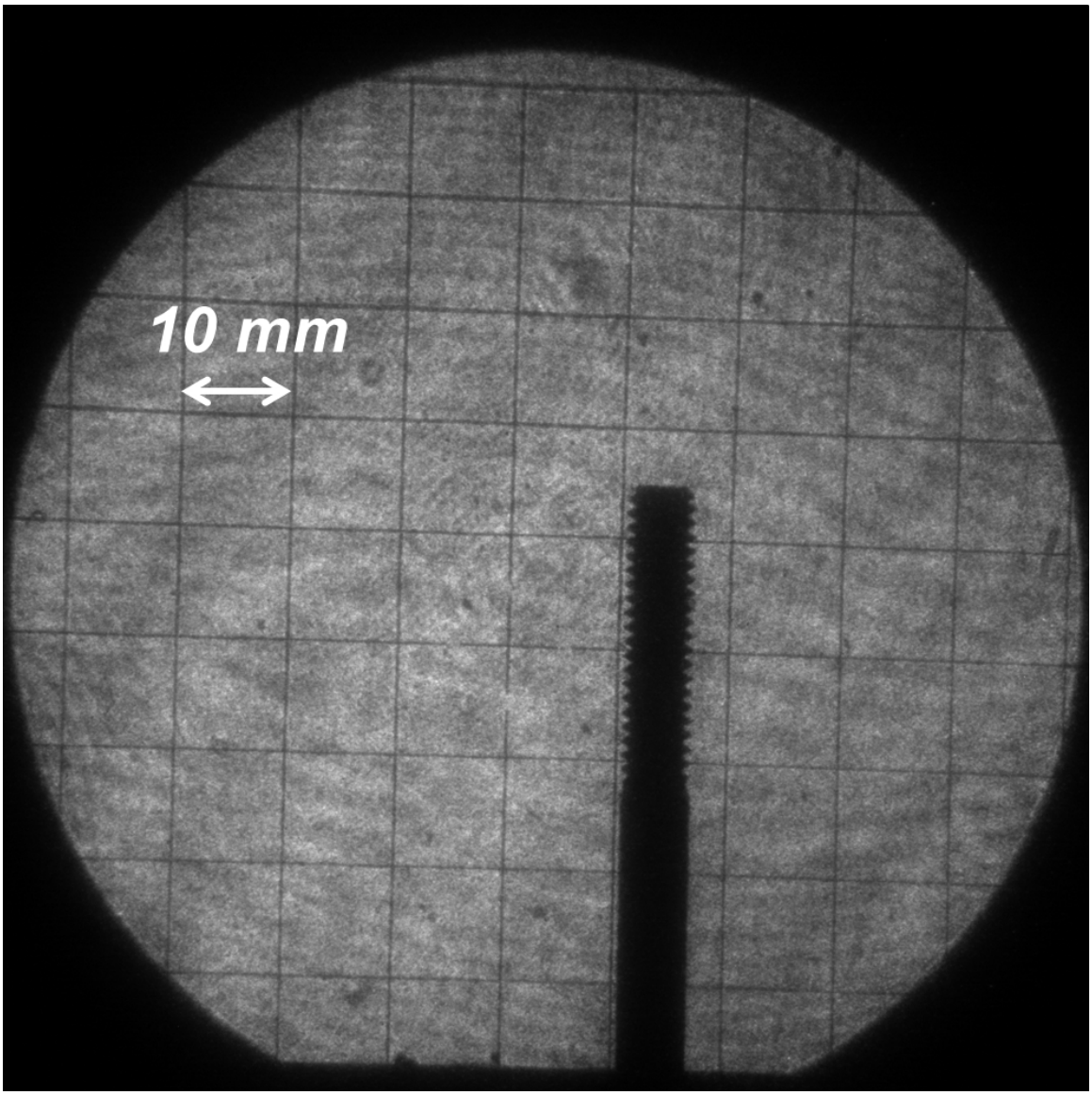

Figure 4.6: Example Cordin camera field of view calibration image featuring both the 10 mm Cartesian grid. The image also includes the 4-20 screw included in pre-experiment practice trigger images used for clarity confirmation and fiducial marking.

x N matrix is considered centered on each pixel. The pixel value is then replaced by the median grayscale value within that window. The size of the median filter matrix ("window") was minimized to 3 x 3. This window size eliminates salt and pepper noise while avoiding edge smoothing and preserving the internal structure of the debris cloud.

The Cordin camera, containing four individually programmable CCDs, features

internal beam-splitting optics to deliver the incident beam to each of the CCDs. Consequently, there are small disparities between observed physical features and the corresponding CCD pixel coordinate. It is important to note that in the image analysis described in this Chapter, the position of debris fronts are all measured relative to plate surfaces. Therefore, changes in debris cloud position are determined with respect to the change in the relative position of debris with respect to the plate in each image. As such, uncertainty in physical location of each pixel on differing CCDs does not contribute to the analysis. Furthermore, analysis is conducted on each image without any translation, rotation, or spatial manipulation of pixels.

4.4.2 Edge-Finding Analysis

The stability of the MCP intensifiers in the Cordin camera and resulting fluctuation in background grayscale levels precludes the use of background comparison with the pre-test images to determine the position of measurable debris. Therefore, an edge-finding algorithm is required to determine the position of the debris in each analyzed LSL image. The edge-finding algorithms analyzes pixel grayscale profiles in the longitudinal z-direction along lines of constant y. Two edge-finding algorithms developed for the analysis of LSL images are described herein.

The first edge-finding algorithm utilizes a moving average. Along each (horizontal) line of pixels, each pixel grayscale is considered as the average grayscale of the 5 adjacent pixels in each direction. The corresponding span of 11 pixels total corresponds to a physical length of between 0.8 and 1.1 mm (depending on the selected LSL field of view). Using this approach, the moving standard deviation is also computed for each pixel. Lastly, the gradient of the moving grayscale average is considered. The starting point for this analysis is manual selection of the approximate debris front location. The edge-finding algorithms are applied to a horizontal (z-direction) range of at least 100 pixels downrange (7 to 10 mm) from this starting point,. Note that in the convention used here, a white pixel has a grayscale of 255.

The debris boundary (i.e., "edge") is then limited to points where the gradient

is large (within 25% of the maximum) and positive (corresponding to a transition from dark to bright). Within this subset of pixel coordinates, the debris boundary is identified at the pixel corresponding to the maximum in the standard deviation. The use of the moving average and standard deviation removes local maxima that may skew the result. Figure 4.7 provides an example of this algorithm and edge-finding result with an illustration of the defined boundary and corresponding grayscale analysis.

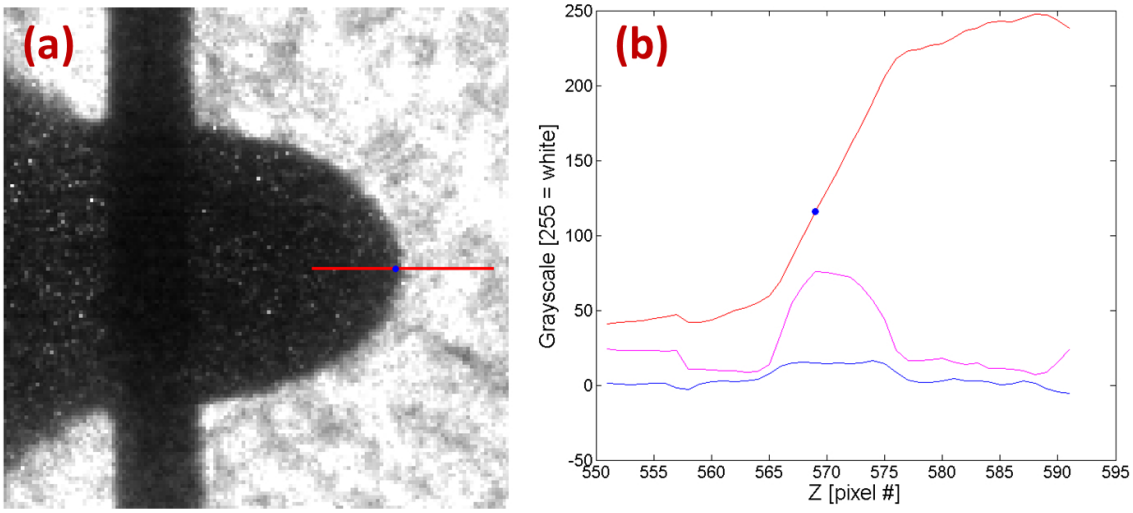

Figure 4.7: (a) Enlarged LSL image of debris cloud formation. The boundary identified by the maximum standard deviation edge-finder is identified by the blue dot. (b) The moving average of the grayscale (red), moving standard deviation (magenta) and gradient (blue) plotted for the pixel profile corresponding to the red line in the adjacent LSL image. The boundary defined by the maximum st. dev. edge-finding criterion is marked by the blue dot.

The uncertainty of the debris front position can then be quantified based on the length of the transition region of grayscale and standard deviation. In the example shown in Figure 4.7, this would correspond to an error of approximately 5 pixels or less resulting in an accuracy of ± 0.3 mm. This methodology provides a consistent way to define debris front position in a single image. However, a Lagrangian approach to debris tracking, where a specific particle is observed in consecutive images, is not possible with this technique. Although a consistent definition is used to define

the boundary, the identified coordinate in consecutive images does not necessarily correspond to the same physical material. Consequently, for debris front measurements, this edge-finding approach is limited to when the transition from dark to bright grayscale is similar. As the debris cloud propagates away from the target, the material spreads, resulting in a more gradually broadening transition of grayscale.

Therefore, for the analysis of a moving debris cloud, an edge-finding method is required to determine the farthest debris measurable by the LSL system. To account for unknown ambient background grayscale level, a criterion to locally distinguish measurable changes in optical density from spatial background variation is required. These requirements motivate the use of a second, improved edge-finding algorithm which is the primary technique used to measure debris front propagation.

The primary debris front-fronting technique uses linear regression to model the ambient background grayscale level and subsequent spatial variation. Considering pixel grayscales moving in the uprange direction, the farthest debris measureable from the target plate is identified as the first deviation of grayscale outside of a 99% confidence interval on the linear regression of the downrange grayscale.

Such a method is therefore dependent upon the identification of downrange pixels to conduct linear regression and establish an ambient background behavior. The downrange end point is considered at least 100 pixels (7 mm to 10 mm) from the initial manually selected starting point. This wide range of pixels mitigates error introduced by the initial manual selection of a starting point. The selection of an uprange bound to define the domain for background pixel linear regression is has three steps. First, the moving standard deviation is computed at each pixel, using the previously described approach. The maximum of standard deviation corresponding to the largest transition in grayscale from dark to bright — a first estimate of the boundary — is used as a first bound. From the set of pixels downrange from this point, the second step is the determination of the global minimum of the local minima. This minimum value (which is not necessarily the minimum grayscale) is used as a threshold value. Lastly, the pixels considered for linear regression are all of the pixels located downrange of the maximum moving standard deviation with grayscale values

larger than the global minimum of local minima.

With the downrange pixels selected, linear regression is used to estimate the ambient grayscale level and spatial variation. Using the MATLAB polyconf function, a 99% (minimum) confidence interval is generated. This confidence interval is then used to define the ambient background level as a function of spatial coordinate z. Accordingly, pixels observed with grayscales below the confidence interval are likely a change in the optical density in the target chamber corresponding to debris. Therefore, considering pixel grayscales in the z-direction moving uprange, the first pixel observed with a grayscale below the confidence interval of the background linear regression is identified as the farthest measurable position of debris from the target plate.

Figure 4.8 provides two example of this algorithm, where the blue trace represents the (median filtered) image pixel grayscale values as a function of z. The red pixels correspond to those used for linear regression to define the ambient background grayscale (in magenta). The dashed magenta lines depict the confidence interval of the linear regression which defines the threshold for distinguishing ambient background. Lastly, the leading edge of debris identified by the algorithm is marked with the black point.

As presented in Figure 4.8, the background grayscale in front of the observable phenomena oscillate at times by as much as ± 25 grayscale units. Furthermore, the background grayscale varies spatially: Figure 4.8 (a) depicts a case where the background grayscale increases leading up to the debris front and Figure 4.8 (b) depicts the ambient background decreasing leading up to the debris front. This spatial variation has been observed to be a consequence of the stability of the Cordin MCP intensifiers, which dominates any disparity in the incident illumination source and can change with time. Through the use of a regression confidence interval, the technique provides a statistical method to account for this spatial variation. Accordingly, this method has two primary advantages to other potential methods. First, this technique provides a local criterion implemented row by row on the CCD to identify a departure from ambient background grayscale. Second, this method requires no knowledge a

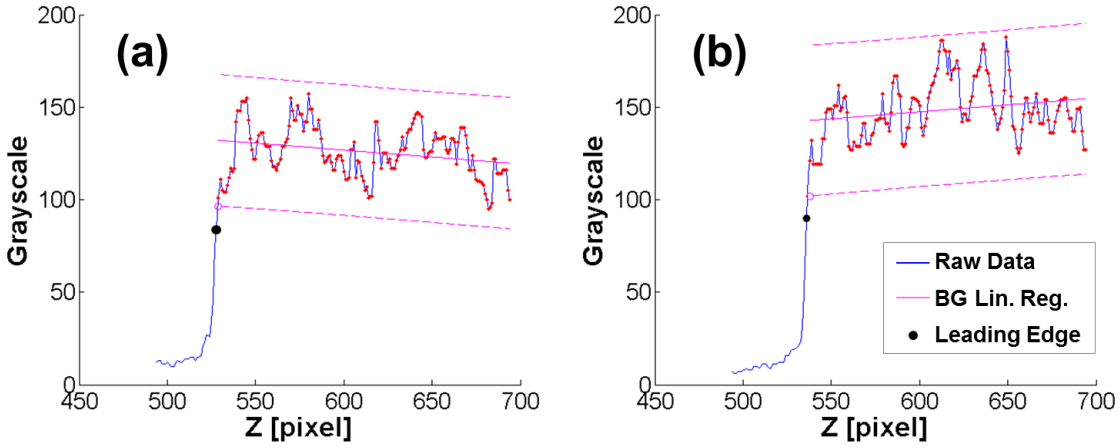

Figure 4.8: Two examples of the debris front-finding algorithm to measure the most downrange position of debris. The blue trace is the image pixel grayscale, red pixels were used for linear regression to establish the ambient grayscale background (magenta). Dashed magenta lines are the 99% confidence interval of the background linear regression. The algorithm identified leading edge marked in black. (a) Case where the ambient background increases leading up to debris front (b) Case where the ambient background decreases leading up to debris front.

priori of the expected background grayscale levels.

4.4.3 Debris Front Measurement and Uncertainty

The edge finding analysis presented in section 4.4.2 is used to measure the position of the debris front produced in an impact experiment. Tracking of the position of this front in subsequent images is then used to determine the speed of the debris cloud propagating along the incident impact velocity vector. Note that the position of the debris cloud is measured with respect to the back-surface of the target plate. Therefore the measurement of debris cloud speed is computed as the change in relative position with respect to the downrange surface of the target plate. The origin considered in the analysis presented in this work is the position on the back-surface of the target plate along the axis of the impact vector.

Figure 4.9 (a) provides an example of the edge-finding analysis for a $h = 0.5$ mm aluminum target plate, impacted at 5.84 km/s by a 5.48 mg nylon 6/6 cylinder in 1.3 mmHg target chamber atmosphere. As presented, the identified debris cloud

front is highlighted (in red) on the initial LSL sequence image. The debris front position, as measured in the subsequent images, is superimposed on this initial image. The corresponding physical coordinates of these debris front positions is presented in Figure 4.9 (b). For this example, the debris cloud is observed to propagate downrange at 4.91 km/s.

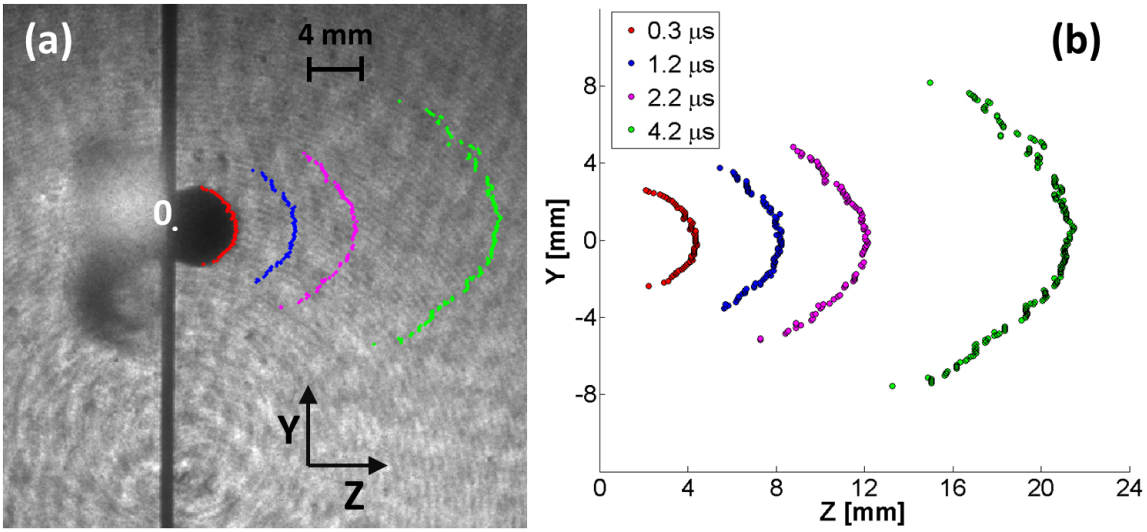

Figure 4.9: An example of the edge-finding analysis for a $h = 0.5$ mm aluminum target plate, impacted at 5.84 km/s by a 5.48 mg nylon 6/6 cylinder in 1.3 mmHg target chamber atmosphere. (a) The identified debris front in the initial image (red) superimposed with the debris front positions measured in subsequent images. (b) The physical coordinates of the highlighted debris positions in the adjacent image, relative to the marked origin.

This debris tracking technique is implemented when the debris front is best defined, for the first 5 to 8 µs after impact. As the debris front moves downrange it volumetrically expands, decreasing the optical density of the cloud. Consequently, the clarity of the "leading edge" of the debris cloud decreases, making font-finding with the described algorithm less accurate.

The uncertainty in the measurement of debris cloud position relative to the target downrange surface is estimated as 5 pixels. Therefore, the uncertainty in the inter-frame change in position with respect to the rear surface plate, given as the RSS of the uncertainty from two images, is approximately 7.1 pixels. Optical distortion by

the Cordin camera, measured in the calibration grid image for each CCD, is observed to be small (1 to 3 pixels) compared to the described uncertainty contribution from the determination of the debris position. Accordingly, the inter-frame uncertainty in measurement in change of debris position is estimated as 9 pixels.

The uncertainty in the measurement of debris cloud speed is a function of the uncertainties in measurements for change in debris position ΔZ, Cordin pixel length scale S, and Cordin image inter-frame time Δt. Therefore, given Eq. 4.3 to compute debris cloud speed v_{deb}, the uncertainty in the measurement is computed as the RSS of the uncertainty contributions, as described by Eq. 4.4. Given the excellent temporal resolution and precision of the monitoring of the Cordin image gating signal, the uncertainty in the inter-frame time is approximated as 10 ns, corresponding to the rise time of the gating signal. The uncertainty in the length scale of the LSL images is estimated as 1×10^{-3} mm/pixel, based upon the disparity in measured resolutions in consecutive attempts. The resulting uncertainty in the measured debris cloud speed ranges from 70 m/s to 200 m/s, ranging from 5% to 8% of the measured speed.

$$v_{deb} = \frac{\Delta Z S}{\Delta t} \tag{4.3}$$

$$\epsilon_{v_{deb}} = \sqrt{\left(\frac{\partial v_{deb}}{\partial \Delta Z}\epsilon_{\Delta Z}\right)^2 + \left(\frac{\partial v_{deb}}{\partial S}\epsilon_S\right)^2 + \left(\frac{\partial v_{deb}}{\partial \Delta t}\epsilon_{\Delta t}\right)^2} \tag{4.4}$$

4.4.4 Technique to Measure Two-Dimensional Optical Density of Debris Cloud

During an experiment, when the debris cloud has expanded such that the measurement of the leading edge is difficult with the presented methods, the LSL system can be used to measure the two-dimensional optical density of the cloud. The technique utilizes the optical density calibration curve presented in section 4.3.2. As presented, the relation between the optical density (% transmission) and observed amplitude of original pixel intensity is approximately linear. Furthermore, the variance of this

relationship is shown to increase with decreasing optical density.

The two-dimensional technique computes the effective optical density of each pixel in a debris cloud image by comparison to a pre-experiment level. The pixel is then assigned an optical density based on the percent change in grayscale intensity. Given the observed temporal drift of the pixel grayscale, 5 discrete optical density levels are prescribed. These 5 discrete optical density levels are based on the standard deviation on the calibration curve: the center of each optical density level is two standard deviations from the start of the next level. Accordingly, a camera system with less intensifier-induced grayscale drift would therefore be capable of resolving a large number of optical density levels. In producing the optical density contour map, the assigned optical density levels represent the minimum optical density of a region. For example, the $OD = 0.2$ (60% transmission) regions represent all pixels with grayscale values between 41% and 60% of the pre-experiment value.

Figure 4.10 provides an example of the measurement of debris cloud optical density, where the image to the left is the original (median filtered image) and the image to the right is the corresponding optical density contour map. Consideration of the two-dimensional image pixel-by-pixel measures the total integrated optical density across the optical path length through the debris cloud for each spatial coordinate (y,z).

The results of optical density maps presented in this image are produced with highly characterized grayscale background drift at the time of the experiment. During this experiment, for each exposure of each CCD, a series of 5 images (taken one image/minute) are taken before and after the experiment. These images are then averaged to describe the average ambient illumination grayscale of each CCD during the time of the experiment. This grayscale calibration then provides the reference for comparison with pixels from a debris cloud image to produce the presented optical density images. Therefore, the optical density images presented in this section represent the highest accuracy possible given the current specifications of the ultra-high-speed camera used in the LSL system. However, the conservative assignment optical density levels for image analysis accommodates the temporal pixel grayscale

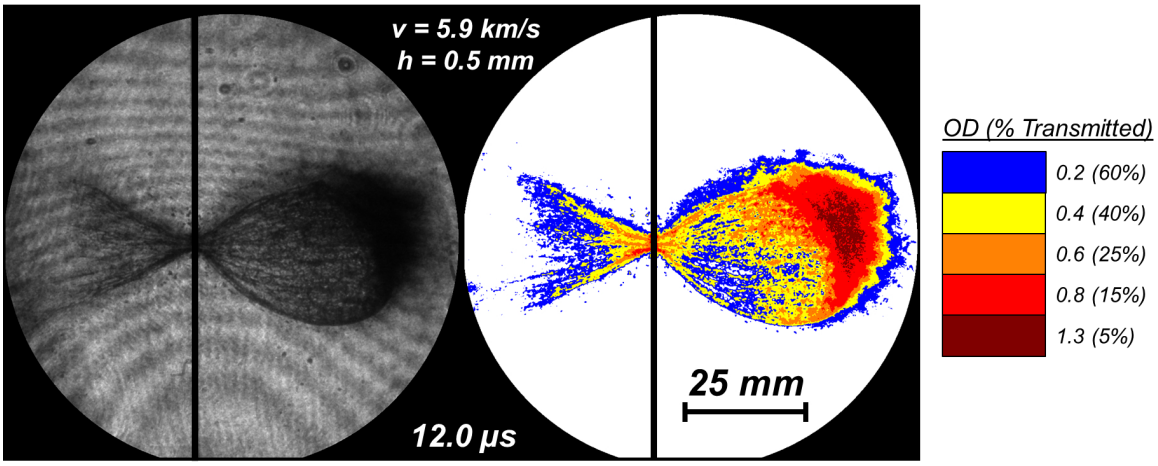

Figure 4.10: Example of the measurement of two-dimensional debris cloud optical density. The image on the left is the original (median filtered image) compared to the corresponding optical density on the right. The color-map for optical density represents the minimum optical density of each region. Example provided for a $h = 0.5$ mm target, 12 µs after trigger, impacted normally at 5.9 km/s.

drift and enables extension of this technique to results with less rigorously calibrated ambient grayscale values.

This technique, in addition to being limited by the temporal drift of grayscales caused by the Cordin MCP intensifier, is also limited by the dynamic range of the CCDs. The resolution of debris cloud internal structure is dependent upon a large grayscale dynamic range. CCDs #1 and #3 are limited by a small grayscale dynamic range and therefore produce images without adequate contrast within the debris cloud. Consequently, optical density measurement with the current LSL system presented herein are limited to CCDs #2 and #4 (both A and B exposures).

4.5 Trigger Delay Measurement with LSL

All diagnostics are triggered using a photodiode positioned to observe the impact flash. Although this triggering method has demonstrated robust reliability (0 failures in over 200 experiments), the time for formation of the impact flash introduces a small delay between the impact of the projectile and triggering of the instrumenta-

tion. Therefore, the physical time t of an instrument's measurement is given by in Eq. 4.5, where t_{trig} is the finite delay between impact and subsequent generation of the triggering signal. The instrument delay time t_{del} and frame exposure (shutter) time t_{exp} are programmed for each instrument and monitored with high precision.

$$t = t_{trig} + t_{del} + t_{exp} \tag{4.5}$$

Analysis of the ejecta and debris propagation using the LSL system can provide an estimate of the delay between the impact and the instrumentation trigger signal. The one-dimensional velocity in the z-direction of the front-ejecta (debris ejected uprange, opposite of the impact vector) is measured and then used to estimate the time of impact. To do so, the z-position of the most uprange front-ejecta is first determined with respect to the impacted surface. Figure 4.11 provides an example of the measurement of the forward-most front-ejecta position in LSL images for an $h = 1.5$ mm thick 6061-T6 aluminum target plate impacted by a $d = 1.8$ mm nylon 6/6 ($l/d = 1$) right cylinder at 6.32 km/s.

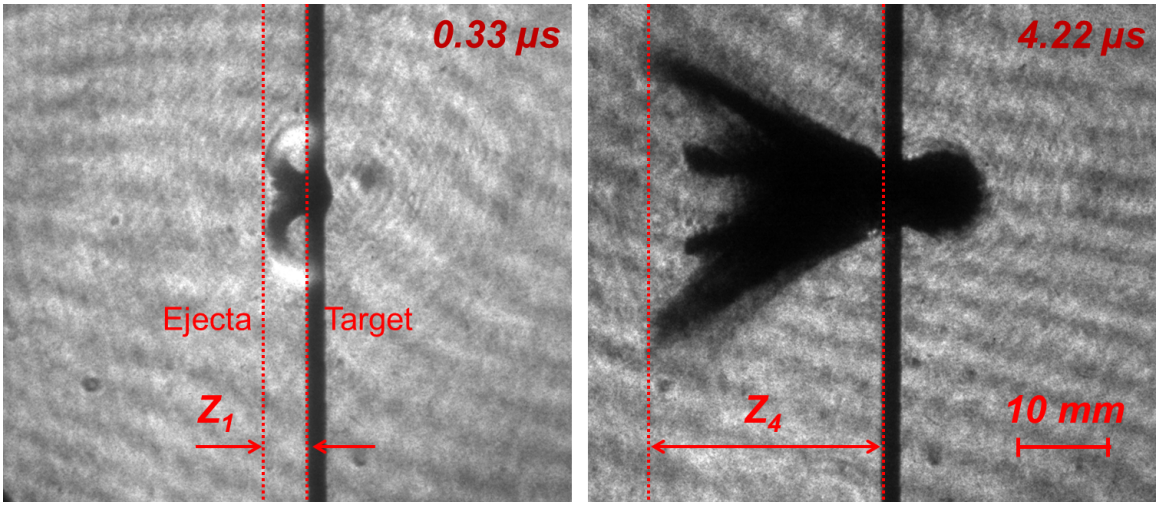

Figure 4.11: Example measurements of the position of debris ejecta uprange following an impact. Such measurements are used to compute the z-component of the impact's front-ejecta velocity, which is then used to accurately measure t_{trig}. Ejecta images shown for an $h = 1.5$ mm thick 6061-T6 aluminum target plate impacted by a $d = 1.8$ mm nylon 6/6 ($l/d = 1$) right cylinder at 6.32 km/s.

The one-dimensional front-ejecta velocity (v_{ejecta}) in the z-direction is then estimated using least-squares linear regression analysis of the measured sequential front-ejecta positions. Figure 4.12(a) provides an example of the z-position vs. image timing for the previously presented example (Figure 4.11). The time required for the ejecta to propagate from the impacted target surface to the observed position can then be estimated for the first LSL image. Subtracting the effective time t_1 of the LSL image ($t_{image} = t_{del} + t_{exp}$) then provides the trigger delay time t_{trig}, assuming a constant front-ejecta speed and immediate ejecta of particles at impact. This approximation is described by Eq. 4.6 and graphically illustrated in Figure 4.12 (b).

$$t_{trig} = \frac{z_1}{v_e ject a} - t_1 \tag{4.6}$$

$$\epsilon_{t_{trig}} = \sqrt{\left(\frac{\partial t_{trig}}{\partial z_1}\epsilon_{z_1}\right)^2 + \left(\frac{\partial t_{trig}}{\partial v_{ejecta}}\epsilon_{v_{ejecta}}\right)^2 + \left(\frac{\partial t_{trig}}{\partial t_1}\epsilon_{t_1}\right)^2} \tag{4.7}$$

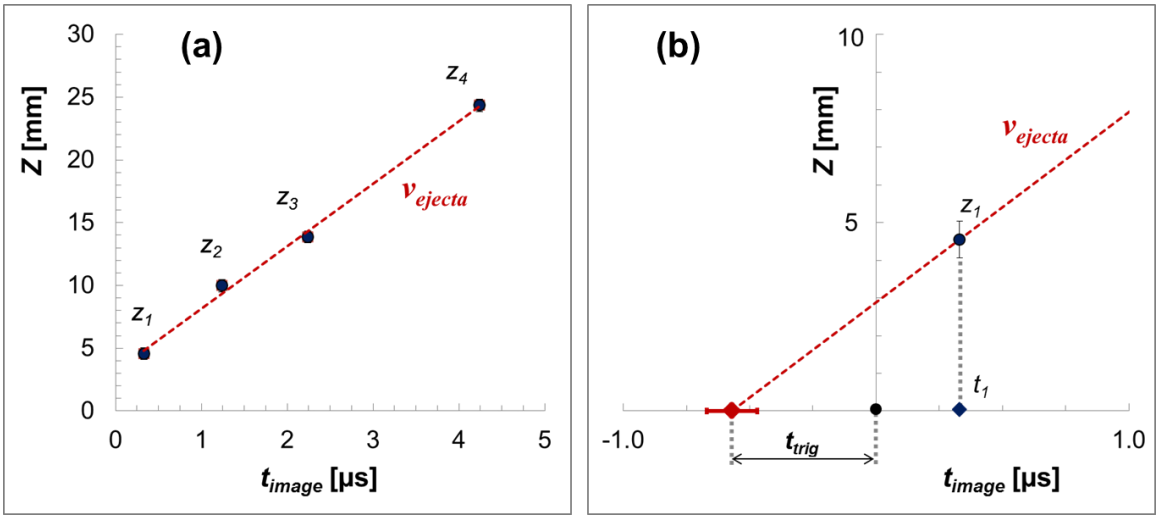

Figure 4.12: (a) Z-position vs. image time measured for the front-ejecta presented in Figure 4.11. Least-squares linear regression is then used to estimate the one-dimensional front-ejecta velocity, v_{ejecta}. (b) Geometrical representation of the use of v_{ejecta} to determine the trigger delay time t_{trig}, given the front-ejecta position measured in the first image.

The measurement of individual debris particles or identifiable ejecta cloud features

in consecutive frames is not feasible with the current LSL system. However, the measurement of the forward-most aggregate position of (many) ejecta particles to compute a one-dimensional velocity component mitigates this limitation. Such a measurement in one-direction also reduces the dimensionality of the uncertainty in the definition of the debris position: errors in the identification of the position of ejecta are accounted for in only one-direction. The relative positions of the forward-most front-ejecta with respect to the target plate are measured with uncertainties of 8 pixels. Gating signals from each instrument are precisely monitored allowing t_{del} and t_{exp} to be measured with an uncertainty of only 10 ns. For typical ejecta velocities observed, these uncertainties produce a RMS uncertainty of the ejecta speed of approximately 5%. The estimate of the trigger time t_{trig} uncertainty is then computed given Eq. 4.7, with typical values ranging between 100 and 200 ns. Furthermore, strong linear regression correlation coefficients (typically 0.98 or above) between the measured z-positions and image times supports the accuracy of this method.

4.6 Measurement of Debris Cloud Phenomena

Implementation of the laser side-lighting (LSL) system and the analysis techniques described in section 4.4 facilitate the investigation of the debris clouds produced in hypervelocity impacts of nylon equiaxed cylinders and aluminum target plates. The majority of previous investigations of debris cloud phenomenology featuring modern imaging capabilities have involved aluminum or metallic impactors on aluminum targets. The work considered herein provides insight into the debris clouds formed by a lower shock impedance impactor (nylon) on an aluminum target. For the range of target plates considered, the effects of normalized target thickness and velocity on debris clouds are discussed. Similarly, the operational effects of laser illumination intensity and target chamber pressure are also presented herein.

4.6.1 Selection of Debris Cloud Image Timing

Given the finite number of images produced by the Cordin camera, the selection of image exposure times must be considered. Accordingly, the ultra-high-speed camera is programmed to facilitate observation of both the early formation of the debris cloud and the expansion of the debris cloud following plate separation.

The observation of debris formation at early time after impact ($t < 5$ µs after trigger) enables the measurement of debris cloud shot-line speed using the described edge-finding analysis. At later times, when the debris cloud has expanded, the structure of the debris cloud may be investigated via the optical density measurement technique. Observation of the expansion of the debris cloud requires an approximation a priori of the debris cloud speed in order to visualize the expanded debris cloud before it exits the limited field of view of the LSL system.

Furthermore, when considering the effect of target thickness and impact velocity, a comparison of debris cloud propagations at similar times and for equivalent spatial expansion is desirable. Results for initial impact experiments were used to select LSL image exposure times for such a comparison. For example, at 80 psi pump-tube pressure, the average impact velocity is approximately 6.25 km/s. Given debris cloud shot-line velocity results for each target thickness (presented in the next section), debris cloud expansion of approximately 30 mm is anticipated at 5.75 µs and 12 µs for the $h = 0.5$ mm and $h = 1.5$ mm target plates, respectively. Therefore, the LSL system was programmed to observe the debris event at these times using the best performing CCD channels on the Cordin camera (#2 and #4).

4.6.2 The Effect of Target Thickness and Impact Velocity

Over the range of velocities produced by the SPHIR light gas gun for nylon impactors (5 to 7 km/s), the three target thickness considered each produce debris cloud of varying speed, composition, and shape. The results presented in this section are characteristic of a large number of debris cloud observations obtained using the LSL system.

Figure 4.13 provides an example sequence of images taken with the LSL system for a $h = 0.5$ mm thick 6061-T6 aluminum target plate impacted by a 5.5 mg nylon 6/6 cylinder at 5.84 km/s. As presented, the equiaxed nylon cylinder produces a debris cloud characteristically similar in shape to debris clouds produced by aluminum and copper spherical impactors in Figure 4.1 [52]. For this example, the debris cloud is measured to propagate downrange with a shot-line velocity of $v_{debris} = 4.9$ km/s. Although the impact flash is observed in the earlier images, the short exposure time (15 ns) coupled with the collimated illumination source prevents the observed impact phenomena from being entirely masked by camera pixel saturation from the impact flash.

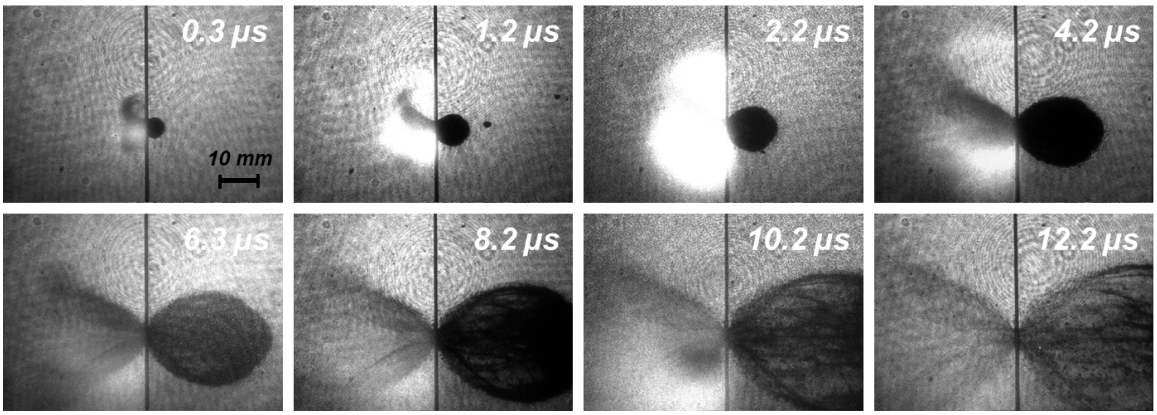

Figure 4.13: A sequence of laser side lighting images with the ultra-high-speed camera taken for a $h = 0.5$ mm thick 6061-T6 aluminum target plate impacted by a 5.5 mg nylon 6/6 cylinder at 5.84 km/s. Timestamps displayed are the effective time of the image after triggering.

When the cloud has expanded, optical density measurements can be made to evaluate structure of the debris cloud. Figure 4.14 provides an example of two debris produced at different impact speeds for the thinnest plate ($h = 0.5$) mm observed 12 µs after trigger. For the two impact velocities presented, differing by nearly 1 km/s, the overall nature of the debris cloud is not different. While the difference in the impact yaw angle in each experiment is unknown, for both results presented, the densest component of the debris cloud is observed to be approximately hemispherical. This behavior is consistent is consistent with observations by Piekutowski [52] and

Williamsen [74] of debris clouds produced by metallic impactors for similar normalized target thickness ratios. The internal structure and shape of debris clouds produced by cylindrical impactors was demonstrated by Piekutowski to be determined by the impact yaw angle [49, 50]. Therefore the azimuthal asymmetry in the distribution of optically dense debris material in Figure 4.14 is likely the effect of the variable impactor yaw due to tumbling. In general, the structure and composition of the debris clouds produced in impacts with the thinnest plates remain similar with increasing impact speed, although slight elongation of the debris cloud has been observed in experiments with higher impact speeds (greater than 6.2 km/s).

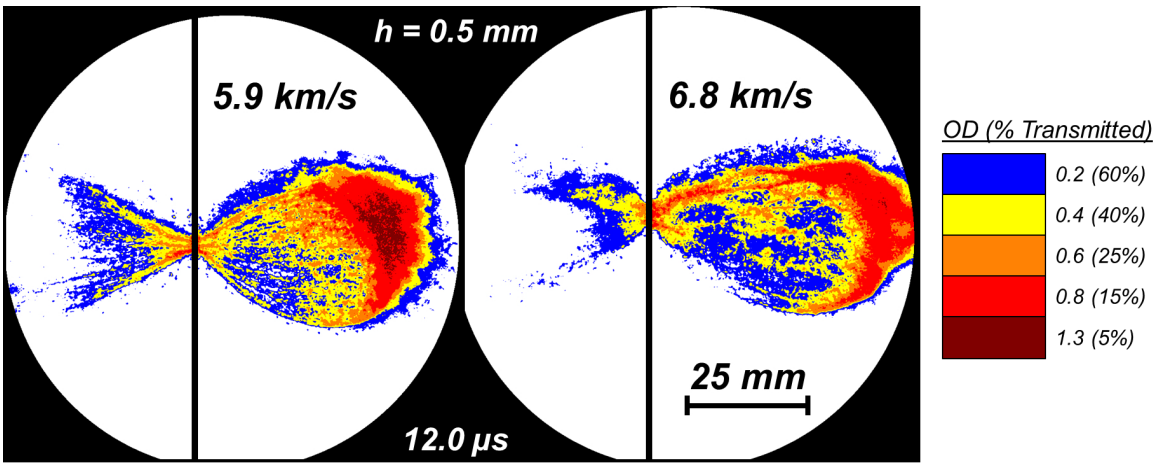

Figure 4.14: Optical density measurements for debris clouds produced by $h = 0.5$ mm plates impacted at 5.9 km/s and 6.8 km/s, observed 12 µs after trigger.

The debris clouds produced in impact experiments for the intermediate thickness plate ($h = 1.5$ mm) represent a departure from the debris phenomena observed for the thinnest plate. Figure 4.15 provides an example sequence of images taken with the LSL system for a $h = 1.5$ mm thick 6061-T6 aluminum target plate impacted by a 5.4 mg nylon 6/6 cylinder at 5.56 km/s. The increase in target thickness is observed to decrease the radial (orthogonal to shot-line) expansion of the produced debris cloud, resulting in an elliptical shape. Such phenomena has been observed by Piekutowski [52] and Morrison [46], amongst others [76]. Additionally, for the impact speed of 5.56 km/s presented in Figure 4.15, relatively large (mm-scale) solid fragments are

observed, particularly in the periphery of the debris cloud.

Results for the intermediate thickness indicate that an increase in impact speed is accompanied by an increase in the amount of vapor, or diffuse debris material, observed in the debris cloud. Figure 4.16 presents a characteristic result for the $h = 1.5$ mm target plate impacted at a higher speed (above 6 km/s). In comparing the LSL results for impact speeds of 5.56 and 6.32 in Figures 4.15 and 4.15, respectively, the increased volume of diffuse debris material obscures the internal structure of debris that is observable at similar times for the lower speed result.

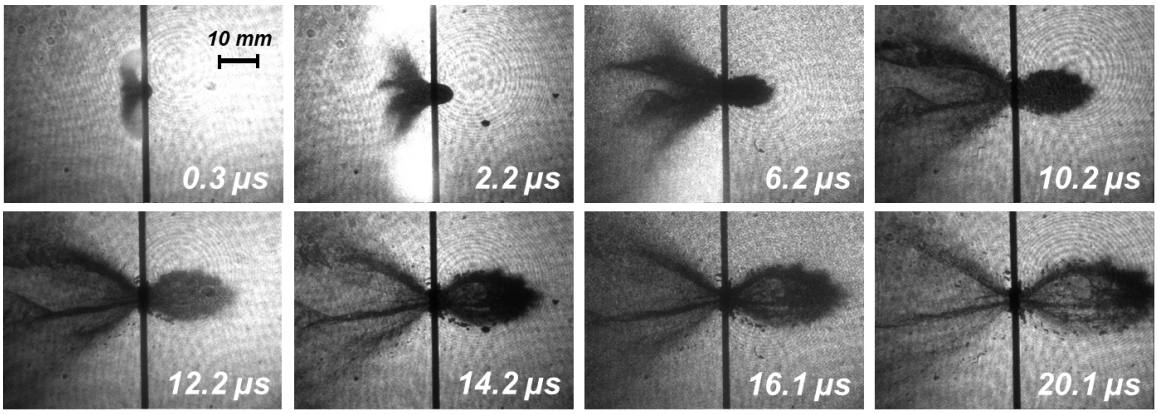

Figure 4.15: A sequence of laser side-lighting images with the ultra-high-speed camera taken for a $h = 1.5$ mm thick 6061-T6 aluminum target plate impacted by a 5.4 mg nylon 6/6 cylinder at 5.56 km/s. Timestamps displayed are the effective time of the image after triggering.

The shock pressure produced at the interface of the projectile increases with impact velocity squared [41]. A stronger shock state produced in a hypervelocity impact results in a higher increase in entropy of the target material. Because the subsequent release from the shock state is isentropic, a larger amount of energy is trapped with the target material. This trapped residual energy increases the debris material temperature and has been shown to correlate with the fragmentation and vaporization of debris [36]. Therefore, the diffuse debris typically observed for the $h = 1.5$ mm thickness target at higher impacts speeds is likely pulverized material from the aluminum target.

Additionally, this diffuse material observed for the intermediate target thickness

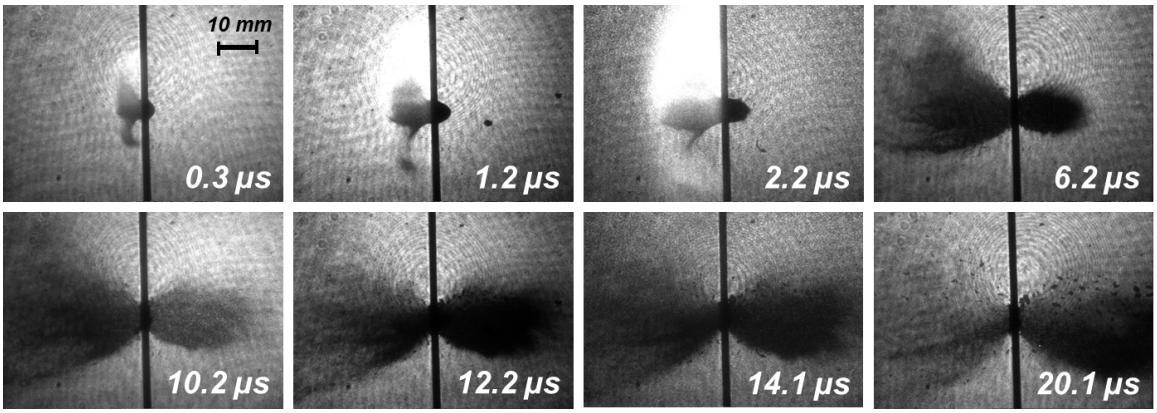

Figure 4.16: A sequence of laser side lighting images with the ultra-high-speed camera taken for a $h = 1.5$ mm thick 6061-T6 aluminum target plate impacted by a 5.6 mg nylon 6/6 cylinder at 6.32 km/s. Timestamps displayed are the effective time of the image after triggering.

typically demonstrates a more gradual gradient in the measured pixel grayscale values at later times. This suggests a distribution in the debris particle velocities. Work by Piekutowski [51, 52] to describe the structure of debris clouds and corresponding material origin has indicated a distribution in debris particle velocities. Furthermore, a change in physical state of debris cloud material has been observed to effect the shape evolution of a debris cloud [50]. This "debris spreading" phenomena make the definition of a "debris front" difficult, if not impractical, at times not long after impact ($t > 4$ µs) for the $h = 1.5$ mm plate.

The evolution of the debris clouds formed by the $h = 0.5$ mm and $h = 1.5$ mm target plates can be compared using the two-dimensional optical density measurement technique for the LSL system. Figure 4.17 provides a comparison of optical density measurements at 5.7 µs and 12.0 µs after trigger. In this comparison, the disparity in the both the shot-line and radial expansion of the debris clouds are immediately apparent. The debris generated from the impact with the intermediate target thickness propagates downrange at approximately half the speed of the debris produced by the thinnest plate. Furthermore, at approximately the same spatial expansion ($t = 12.0$ µs for $h = 1.5$ mm and $t = 5.7$ µs for $h = 0.5$ mm) the intermediate thickness target is observed with significantly less radial expansion and a more gradual transition in

the optical density of the forward moving debris.

Previous work on the effect of impactor shape, pioneered by Morrison et al. [46], has indicated that cylindrical projectiles impacting a target with a non-zero yaw angle produce more damage to rear walls than equal mass spheres or normal impacting cylinders. This result is likely the consequence of resulting shock impulse, producing a reduced level of impactor and projectile fragmentation. Therefore, the yaw angle of the nylon cylindrical impactor and subsequent shock pulse on the target plate may affect the degree of vaporization and diffuse debris observed by the LSL system.

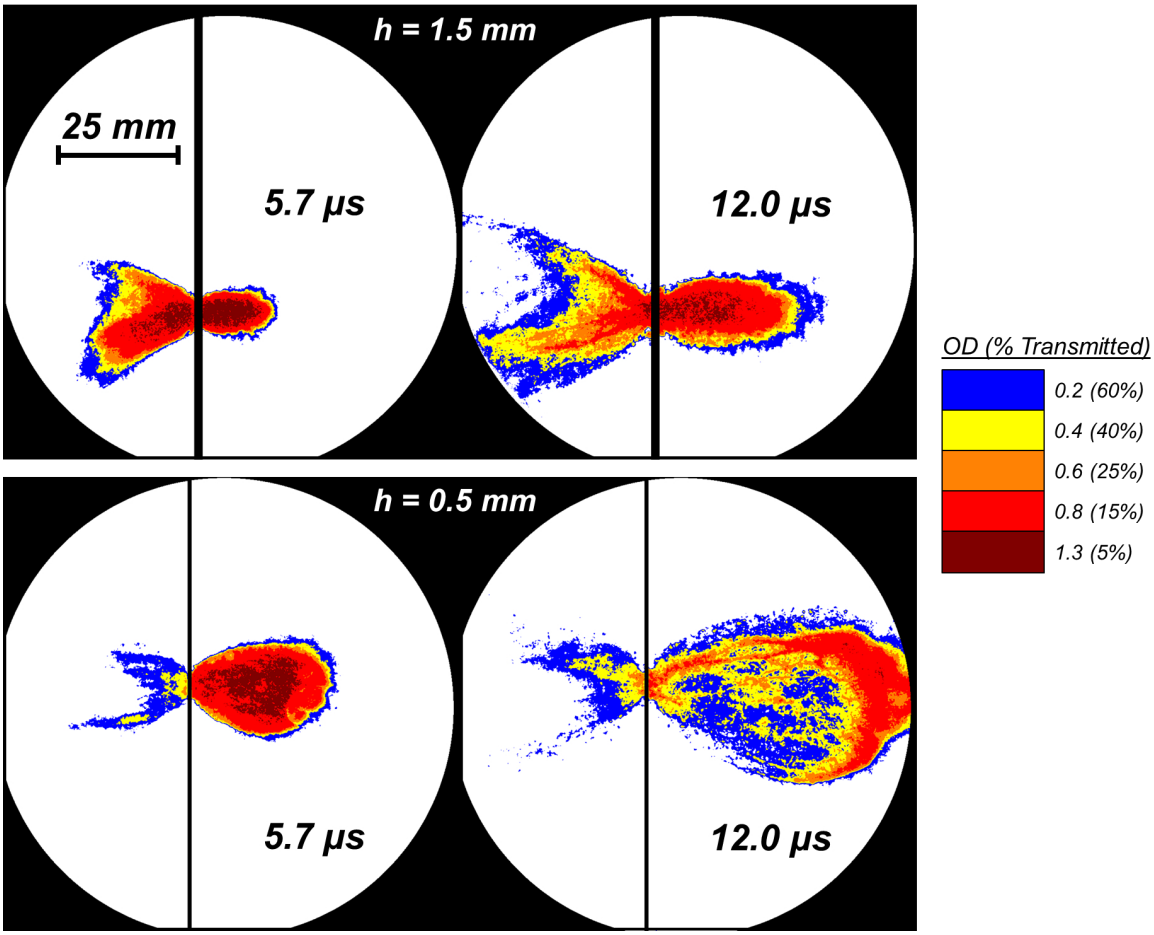

Figure 4.17: Two-dimensional optical density measurements of the evolution of debris clouds produced by $h = 1.5$ mm (top row) and $h = 0.5$ mm (bottom row) for impact speeds of 6.77 and 6.75, respectively.

The debris observed from impacts on the thickest target plate ($h = 3.0$ mm) is fundamentally different than the debris clouds observed for the thinner plates. Fig-

ure 4.18 provides a side-by-side comparison of the three considered target thicknesses impacted at impact speeds between 6.0 and 6.3 km/s. Overall, the volume of material that is ejected uprange (opposite impact) is observed to increase with increased target thickness. Furthermore, the formation of a bulge and subsequent separation of debris fragments occurs subsequently later for the thickest plate. At $t = 10.3$ µs after trigger, debris appears to just be separating from the thickest plate while debris clouds for the thinner targets have already formed. At $t = 30.3$ µs, the debris cloud produced for the thinnest plate has completely separated while fragments from the thickest plate are still are forming. Considering the extent of target material fragmentation at later times after impact and in the periphery of the debris cloud for the intermediate thickness, it is apparent that the hydrodynamic assumption becomes invalid for the two thicker targets. Furthermore, these observations suggest that multiple wave reflections in the two thicker targets play a role in the late-stage formation of debris.

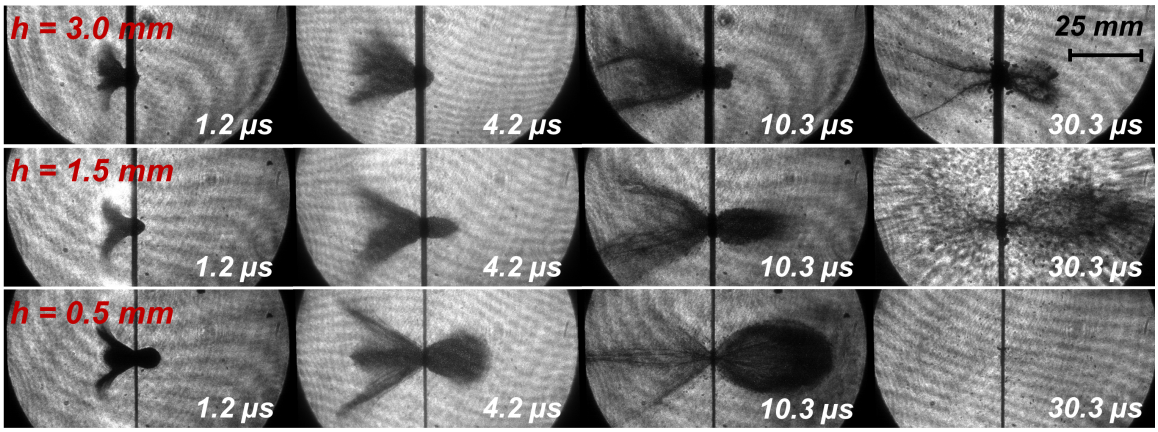

Figure 4.18: Comparison of debris clouds produced by $h = 3.0$ mm (top-row), $h = 1.5$ mm (middle-row), and $h = 0.5$ mm (bottom-row) target plates impacted at impact speeds of 6.0, 6.0, and 6.3 km/s, respectively.

Using the previously presented edge-finding technique, results for the debris shot-line velocity v_{debris} for the three considered thicknesses are presented in Figure 4.19. Results presented are normalized by the impact speed and the p-wave speed of the aluminum target material is also shown as a reference. These debris shot-line velocities

were measured for images observed less than 5 µs after trigger and later ($t < 10$ µs) for the thickest target. The thinnest plate produced debris clouds closest to the impact speed, with shot-line velocities ranging from 4.6 to 5.1 km/s. For the intermediate thickness plate, the debris cloud is observed to propagate downrange along the impactor shot-line at between 1.7 km/s and 2.3 km/s. Lastly, the speed of the late-time debris thrown from the thickest plate has shot-line velocities 0.6 km/s and 0.9 km/s.

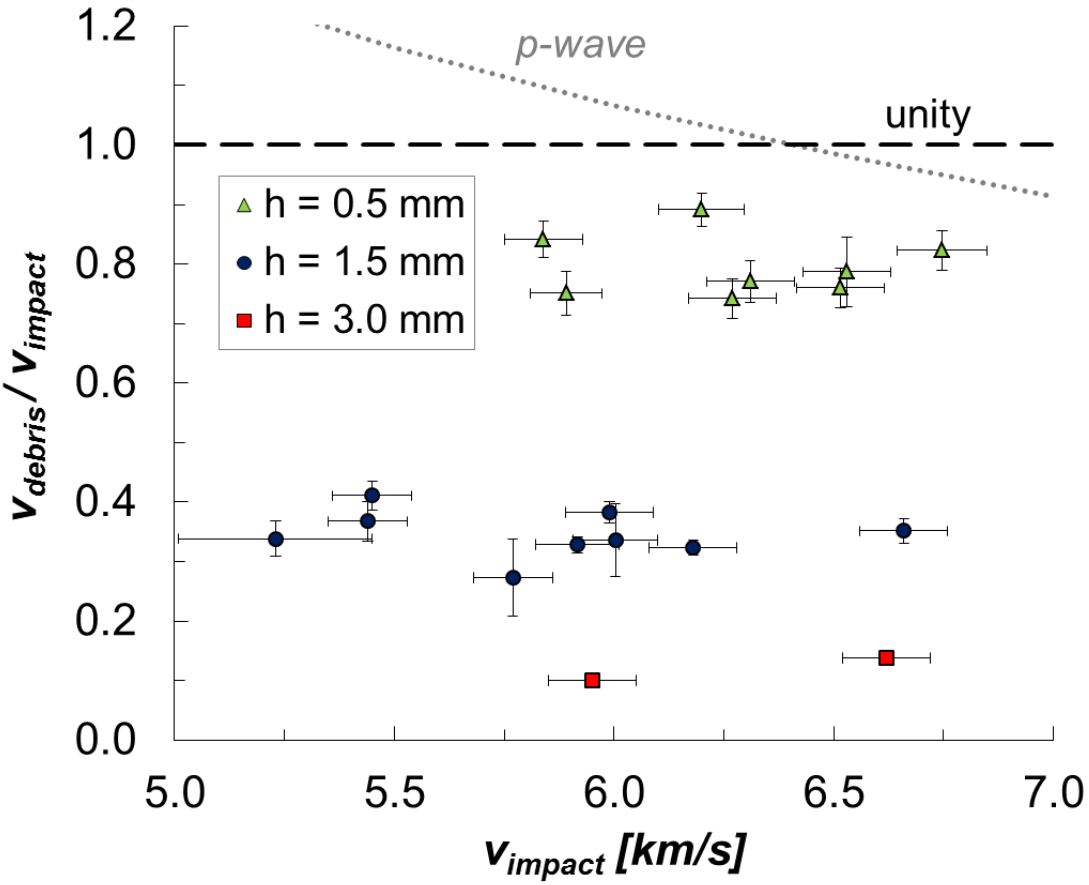

Figure 4.19: Results for shot-line debris velocity v_{debris} normalized by the impact speed for the three target thicknesses considered. The dilatational (p-wave) speed of the aluminum 6061-T6 target is also plotted for reference.

As presented in Figure 4.19, the intermediate thickness exhibits variability in the debris speed outside of the computed measurement uncertainty. Previous work [50] has demonstrated that the relative velocity of different components of the debris cloud

is dependent upon the impact yaw angle. For example, a non-zero yaw angle has been observed to decrease the speed of forward components of debris clouds for impacts of similar normalized target thickness. Therefore, yaw angle of the impactor (which is unmeasured in current SPHIR experiments) may play a role in the observed variation in debris speeds for the intermediate thickness.

4.6.3 The Effect of Laser Illumination Intensity

The laser intensity used in providing the illumination for the LSL system affects the measured phenomena in a given experiment. Figure 4.20 provides an example of experimental results for a $h = 0.5$ mm target observed with 600 mW (76 W/m^2) and 60 mW (7.6 W/m^2) laser intensity for impact speeds of 6.31 and 6.27 km/s, respectively. As presented, the impact flash is more visible at earlier times using the lower illumination intensity. Additionally, the lower illumination intensity series of reveals additional phenomena emanating from the uprange face of the target. This material appears be ejected from the impact site soon after impact. Such phenomena appear only for results obtained using the lower (7.6 W/m^2) illumination intensity.

The effect of laser illumination intensity may also be investigated by comparing the two-dimensional optical density measurements from each experiment. Figure 4.21 provides the optical density maps for the considered example at 3.2 µs and 10.2 µs after trigger. Overall, the structure of the observed debris clouds is qualitatively the same. However, the lower laser intensity results exhibits an increase in measurement noise, particularly for the least dense ($OD = 0.2$) region. The selection of laser illumination intensity therefore is demonstrated to have an affect the measurement of impact phenomena. A lower illumination intensity requires less of a perturbation by phenomena to affect a pixel on the CCD. Thus, in the absence of a narrow band-pass filter, the lower illumination intensity configuration requires less visible emission from impact phenomena (such as the impact flash) to be visible and register on a pixel. Furthermore, operation at the lower illumination intensity requires an increase in the gain setting of the Cordin MCP intensifier. Consequently, the resulting images

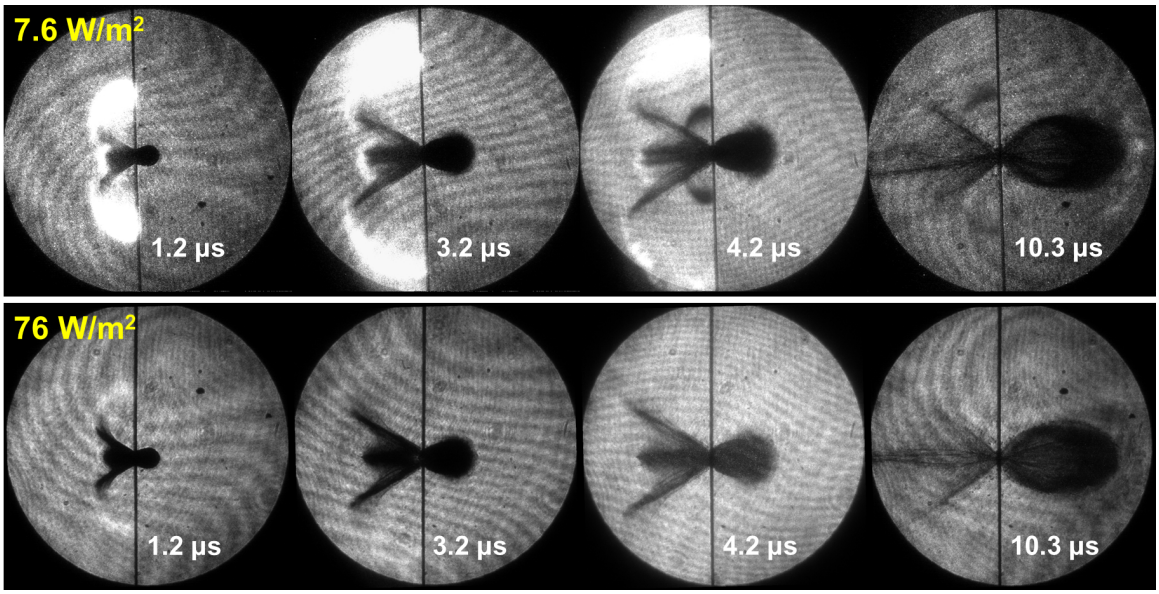

Figure 4.20: A series of LSL images for a $h = 0.5$ mm target observed with 600 mW (76 W/m^2) and 60 mW (7.6 W/m^2) laser intensity for impact speeds of 6.31 and 6.27 km/s, respectively.

have increased amplitude of pixel grayscale noise relative to the background ambient level. This principle is observed in the optical density calibration curves for the Cordin camera as higher standard deviations are measured for the lower illumination intensity. Additionally, the lower laser intensity has a lower number of grayscale units per absolute change illumination intensity. This increased sensitivity enables the observation of phenomena with smaller changes in optical density.

Although the measurement of phenomena is affected given the selection of laser intensities, the overall measured result of an experiment remains the same (for the range of laser intensities considered). In the example shown in Figure 4.20 the shot-line debris cloud velocities were measured as 4.87 km/s and 4.66 km/s. Given the measurement uncertainties of approximately 0.2 km/s for debris speed and 0.1 for impact speed, this difference is not significant. Furthermore, as described in Figure 4.21, the internal structures of the debris clouds inferred from the two-dimensional optical density are not substantially different beyond what may be attributed to differences in impact conditions. Therefore, given the analysis presented in this work for the

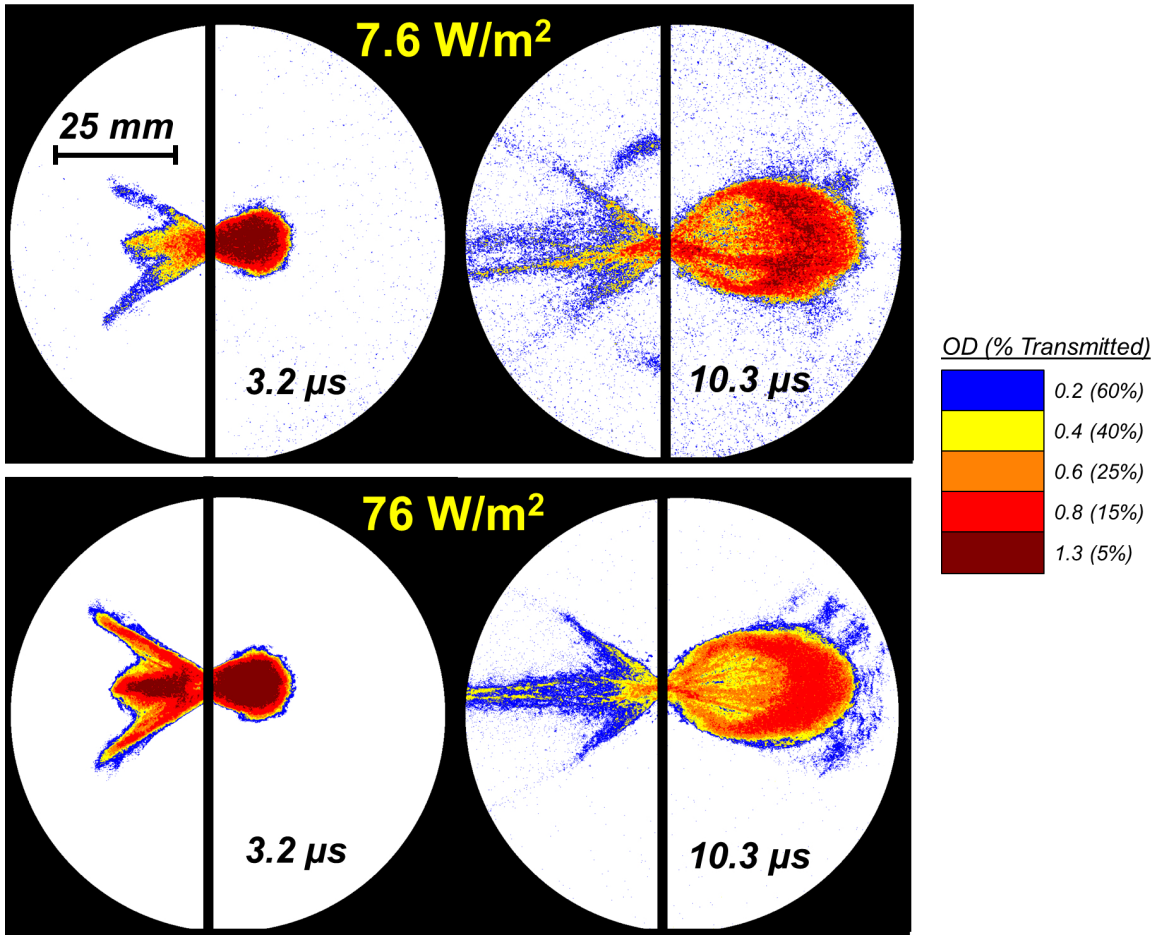

Figure 4.21: Optical density measurements for a $h = 0.5$ mm target plate observed with 600 mW (76 W/m^2) and 60 mW (7.6 W/m^2) laser intensity for impact speeds of 6.31 and 6.27 km/s, respectively.

range of laser illumination intensities considered, the selection of laser level intensity does not change the overall conclusion of the measured results.

4.6.4 The Effect of Target Chamber Atmospheric Pressure

The use of collimated, coherent light in the LSL system enables the observation of additional impact features in experiments where the atmospheric pressure in the target chamber is increased above the nominal 1 mmHg. At higher pressures, waves emanating from the impact site are visible much like those observed in Schlieren shadowgraphs. The observation of these phenomena is enabled by strong gradients

in the index of refraction of the rarefied atmosphere constructively interfering with the coherent light source. An example of this observation is provided in Figure 4.22 for a $h = 0.5$ mm plate impacted at 4.7 km/s in 52.0 mmHg atmospheric pressure. A slight defocussing of the LSL system greatly increases the contrast in the observed shock waves. Measurement of these waves can enhance understanding of the temporal sequence of the impact phenomena and provides a further basis for comparison with other metrics discussed herein.

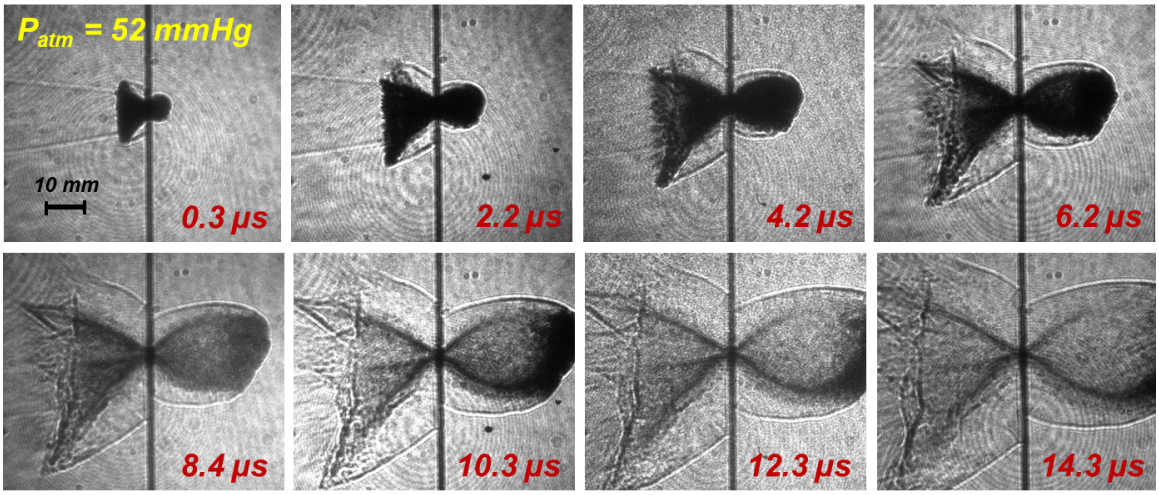

Figure 4.22: A sequence of laser side-lighting images taken with the ultra-high-speed camera for a $h = 0.5$ mm aluminum target plate impacted at 4.87 km/s with 52.0 mmHg target chamber pressure. Times displayed are the image after triggering.

4.6.5 Comparison of Debris Cloud Measurements to Numerical Models

The results for debris cloud speed and two-dimensional optical density provide potential metrics for comparison with numerical models. Figure 4.23 provides a comparison between LSL results for a $h = 1.5$ mm target plate impacted at $v = 5.84$ km/s and a OTM simulation [32]. The OTM model is shown to produce qualitatively similar results for the debris clouds produced in hypervelocity impacts of nylon cylinders with aluminum targets. Efforts to quantitatively compare the debris cloud speeds pre-

dicted by the OTM model, independent of numerical resolution, to those measured experimentally are on-going [31].

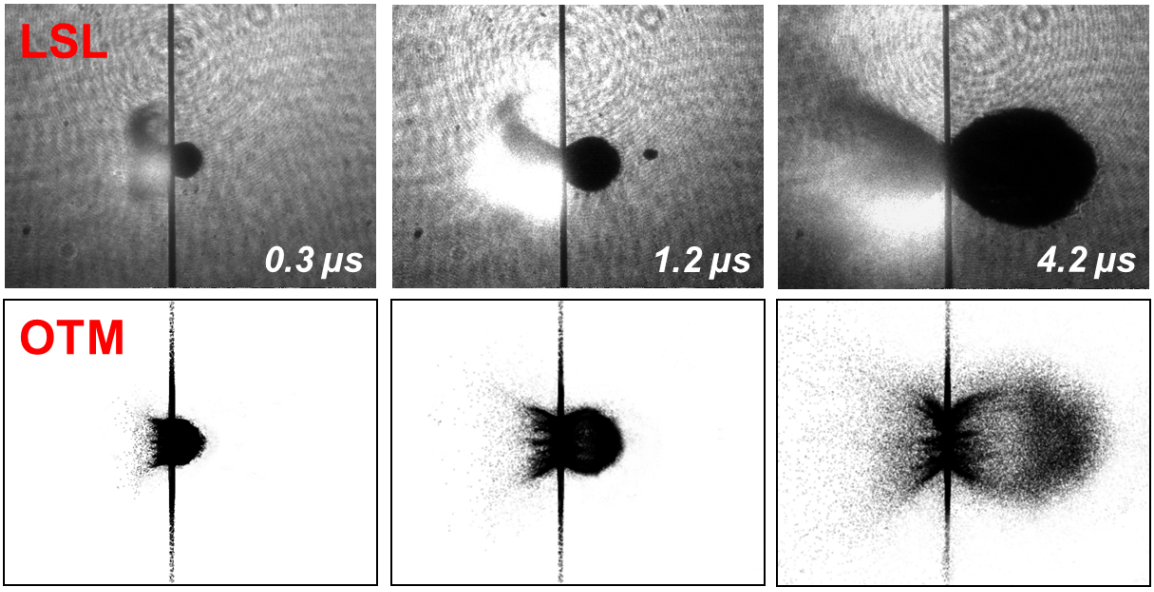

Figure 4.23: Comparison between laser side-lighting (LSL) results for a $h = 1.5$ mm target plate impacted at $v = 5.84$ km/s and a OTM simulation [32].

The debris cloud optical density technique may also serve as a basis for comparison to describe the distribution of debris materials. Such a technique would be particularly useful in evaluating a model prediction of debris in a with non-zero yaw angle. Because the two-dimensional optical density measurement is made pixel-by-pixel, the technique measures the total integrated optical density across the optical path length through the debris cloud. A method would therefore be required to compare the debris particle density produced numerically and the corresponding empirically measured optical density for each spatial coordinate (y,z) in a debris cloud.

If the scale of debris produced in an impact is significantly smaller than the pixel-scale in the image (nominally 0.1 mm for the presented LSL results), than Monte-Carlo simulations can be used to describe the effective coordinate optical density as a function of the areal density of debris particles [3]. This approach also requires an assumption regarding the optical density of a discrete particle and negligible light diffraction. However, given a large range of observed debris particle sizes, many of

which are larger than a single pixel, such a method is inadequate for the currently described LSL system. Therefore, a quantitative comparison of numerically predicted debris distribution and empirically measured optical density would require the development of a ray tracing algorithm. Such an algorithm would be used on numerical results to evaluate the number of particles along the optical path of a debris cloud coordinate (y,z) and determine the corresponding obscuration of those particles.

Chapter 5

Concurrent Diagnostics for the Observation of Hypervelocity Impact Phenomena

5.1 Concurrent Observation of Impact Phenomena

A comprehensive ensemble of in situ diagnostics has been implemented in the SPHIR Facility, available for simultaneous implementation in every impact experiment. The utilization of a coherent, collimated illumination source for imaging of debris cloud with the laser side-lighting system enables the use of simultaneous measurements of phenomena with near-IR and UV-vis spectrograph systems. This suite of concurrently operated instrumentation provides multiple complementary measurements that facilitate the characterization of multiple impact phenomena in a single experiment.

Accordingly, the investigation of hypervelocity impact phenomena presented in previous chapters is complemented by real-time spectrographic measurements. A passive debris collection system, henceforth referred to as the capture pack, is also included in each experiment. This chapter describes the capabilities and analysis of this ensemble of complementary diagnostics. Characteristic results for each system are also presented and the observation of newly observed phenomenon in hypervelocity impact testing is introduced.

The extensive diagnostic capabilities and techniques described can be used with

a wide variety of impactors, target materials and target configurations to address a wide variety of engineering and scientific problems. However, the observation of phenomena in this chapter is focused on the primary impact configuration considered herein: aluminum 6061-T6 targets impacted by nylon 6/6 cylinders.

5.1.1 IR and UV-vis Spectrograph Systems

In order to more closely examine the hypervelocity impact emission, the SPHIR facility utilizes two Princeton Instruments spectrograph systems. Both the UV-vis and IR spectrographic systems, operated by collaborator Jon Tandy, utilize an Acton SP2560 spectrograph. The systems are mounted above the SPHIR target chamber, as previously shown in Figure 2.1, oriented at an angle of approximately 27 degrees from vertical.

The IR system is coupled with a high-speed OMA-V camera (minimum exposure time 1 µs), with a 320 x 256 pixel liquid nitrogen cooled InGaAs detector array, to measure the near-IR emission in the range from 0.9 µm to 1.7 µm during each impact event. The OMA camera is operated by the WinSpec32 software provided by Princeton Instruments. The field of view for the near-IR camera may also be altered by utilizing lenses with focal lengths ranging from 8 mm to 90 mm, yielding fields of view between 60.0 cm x 48.5 cm and 5.3 cm x 4.3 cm respectively. This camera nominally utilizes a 25 mm lens giving a field of view of 25.1 cm x 20.0 cm [44]. Before each experiment, a pre-image is taken to characterize the background grayscale values corresponding to no impact-induced IR emission. The background image is subtracted from the subsequent IR image taken during the experiment to isolate the emission-induced change in pixel grayscale. This process increases the sensitivity of emission measurement by increasing the effective range of the grayscale corresponding to IR emission and removes the effect of inconsistencies in the different pixel responses. [69].

The UV-vis spectrograph system utilizes a high-speed PI-MAX 3 camera (minimum exposure time 28 ns) with an intensified 1024 x 256 pixel CCD detector to

observe impact-gengerated emission from approximately 275 nm to 825 nm. The field of view of the UV-vis camera is determined both by the camera lens and the spectrograph slit width (variable) and height (fixed). In general, a 20 mm focal length lens is used with a slit width of 100 µm, yielding a field of view of approximately 1.3 cm (width) x 12.7 cm (height) [44]. The PI-MAX 3 camera is operated by LightField software, also provided by Princeton Instruments.

Both spectrograph systems are able to record either a single image or spectrum of the emission by utilizing an internal directing mirror or a 150 g/mm, 600 g/mm or 1200 g/mm grating, enabling observation of broad spectra or individual spectral bands. Currently, the OMA-V camera is primarily employed for imaging, while the PI-MAX 3 system is used to obtain emission spectra [44, 69].

5.1.2 Debris Capture System

A capture pack system, as seen in previously in Figure 2.4, was designed and constructed to measure some of the important characteristics of the debris cloud thrown behind the target. The pack consists of alternating, 12 mm thick plates of low density (0.027 g/cm^3) polystyrene foam and 0.2 mm thick sheets of colored cellulose acetate plastic. The areal density of each foam plate is 0.035 g/cm^2 and the areal density of each plastic sheet is 0.016 g/cm^2. The stack of plates and sheets is aligned by precision ground rods that pass through two diagonal corners of the stack and is slightly compressed by four threaded rods that pass between the front and back aluminum plates. The front (uprange) face of the capture pack is located 127 mm behind the back (down range) surface of the target. The precision of alignment of this fixture is sufficient to ensure that positions on the plates and sheets can be determined to within 1 mm of the hit position on the target. A schematic of the coordinate system describing the target plate and capture pack system placed behind the target is presented in Figure 5.1.

After the target is impacted, the pack is removed from the target chamber and disassembled. Most debris material is contained within the foam plates but often

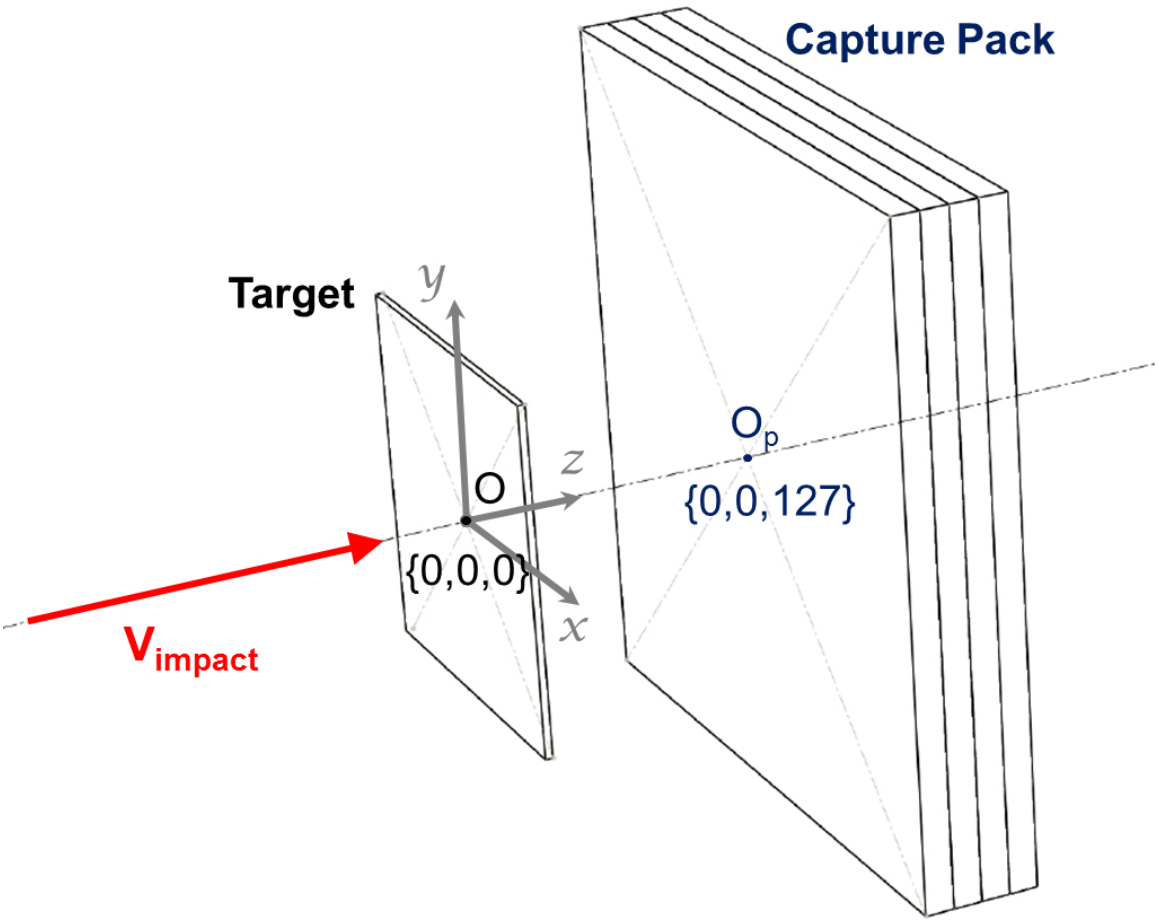

Figure 5.1: Schematic of the coordinate system describing the target plate and capture pack system placed behind the target.

particles will be trapped at the interface between a foam and plastic layer. Recovery of the debris particles is simple but time consuming.

Measurement of the debris patterns are accomplished using a light table, transparent alignment plate and digital camera. Each plastic sheet is placed on the alignment plate resting on the light table and a coordinate system is established using fiducial markings, which correspond to the ground alignment rods of the test fixture. A photograph is taken of the entire sheet and an image analysis program (Image J) is used to characterize various properties of the perforation pattern in each sheet, e.g., number of perforations, location of each perforation, perforation area, etc. These measurements are easily made by inverting and thresholding the digital image such

that the perforation holes are black (grayscale = 0) on a white (grayscale = 255) background. Digital photographs of the target facing surface of the first foam plate are also taken using angled illumination. Often these can be analyzed in the same fashion describe above for the plastic sheets.

5.2 Real-Time, Concurrent Spectrographic Measurement Results

The near-IR and UV-vis spectrograph and camera provides complementary measurements to the results obtained using the LSL by providing full-field IR-emission images and spectra of the diffuse vapor/plasma cloud that accompanies the observed ejecta and debris.

Figure 5.2 provides an example of a UV-vis spectrograph measurement with the corresponding IR image. Results presented in this figure correspond to the experiment presented in Figure 4.16 for a $h = 1.5$ mm thick 6061-T6 aluminum target plate impacted by a 5.6 mg nylon 6/6 cylinder at 6.32 km/s. In Figure 5.2 the approximate field of view of the UV-vis spectrograph slit (100 m) is overlaid on the cropped near-IR image. In this experiment the slit was positioned approximately 2.5 cm in front of the target to measure the uprange vapor/plasma cloud emission. The PI-MAX 3 camera captures all UV-vis emission that passes through the field of view of the spectrograph slit during the 2 s exposure of the camera. The resulting UV-vis recorded using the described spectrograph slit, over the same time exposure as the presented IR image, is also presented. The spectrum exhibits strong emission from several atomic and molecular species originating from both the target (aluminum) and projectile (nylon 6/6) materials.

The IR image presented in Figure 5.2 describing the expansion of an IR-emitting vapor cloud can also be compared to the corresponding images observed using the LSL system. Figure 5.3 presents the IR image with the two LSL images corresponding to the approximate start time (a) and end times (b) of the 2 µs IR camera exposure.

The field of view of the LSL system is also overlaid on the IR image. The simultaneously observed IR and LSL images illustrate distinctly different phenomena. These differences and subsequent implications are discussed in section 5.2.2.

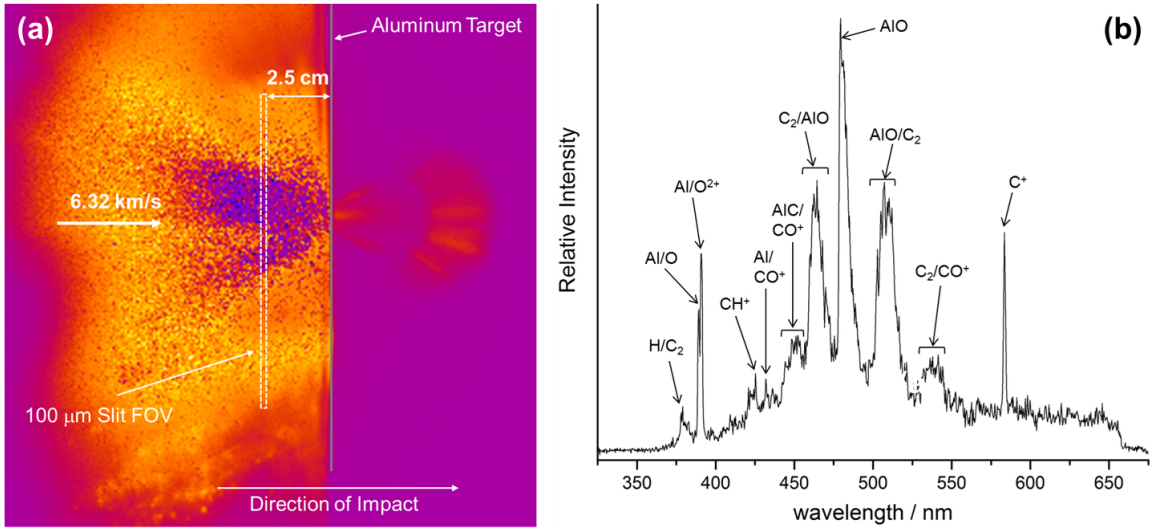

Figure 5.2: (a) The approximate field of view of the UV-vis spectrograph slit (100 µm) is indicated on the cropped near-IR image. The slit was positioned approximately 2.5 cm in front of the target. The target position and direction of impact are indicated and artificial color is added to improve clarity. [44] (b) The corresponding UV-vis spectrum of a 1.8 mm nylon 6/6 projectile impacting a 1.5 mm thick aluminum target at an angle of 0 degrees from vertical. The impact velocity was 6.32 km/s and the chamber pressure was 1.2 mmHg. The spectrum was taken from 12.3 µs after trigger and with an exposure time of 2 µs. The wavelength range was from 324.86 nm to 674.92 nm with an instrument defined spectral resolution of 1.3 nm. Preliminary assignments for each observed spectral band are indicated [21, 47]. Figure courtesy of Jon Tandy [44].

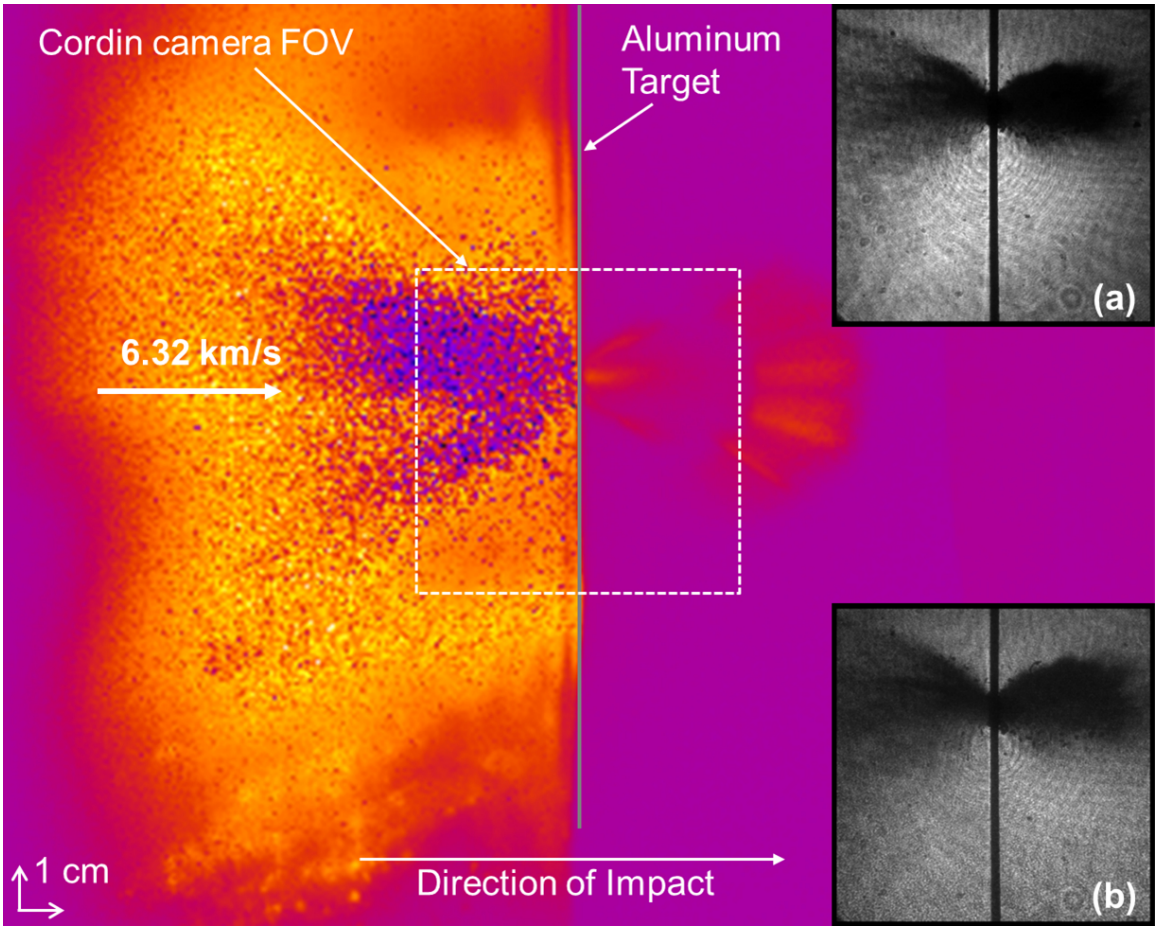

Figure 5.3: Near-IR image of a nylon 6/6 projectile impacting a $h = 1.5$ mm thick aluminum target at an angle of 0 degrees from vertical. The impact velocity was 6.32 km/s and the chamber pressure was 1.2 mmHg. The image was captured from 12.3 µs after trigger with an exposure time of 2 µs. The field of view of the image is 25.1 cm x 20.0 cm (W x H). Two LSL images corresponding to the approximate start time (a) and end time (b) of the 2 µs IR camera exposure are overlaid with the field of view of the Cordin camera also shown. The target position and direction of impact are indicated and artificial color is added to improve clarity. [44].

5.2.1 Phenomena Observed in a Bumper-Shield Target Configuration

Consider the example of concurrent measurement of impact phenomena on a double-plate system. Two $h = 0.5$ mm plates are mounted in the SPHIR target chamber with 50 mm of separation. The spacing and thicknesses of the target configuration are characteristic of those use in spacecraft shielding systems [5]. The target configuration is then impacted by a 5.59 mg nylon 6/6 equiaxed cylinder at 6.53 km/s. Figure 5.4 provides the sequence of shadowgraph images produced by the LSL system. Analysis of the formation of uprange ejecta provides an estimate for trigger delay time of 2.9 µs. (Therefore, the images presented in Figure 5.5 are labeled with respect to the time after impact.)

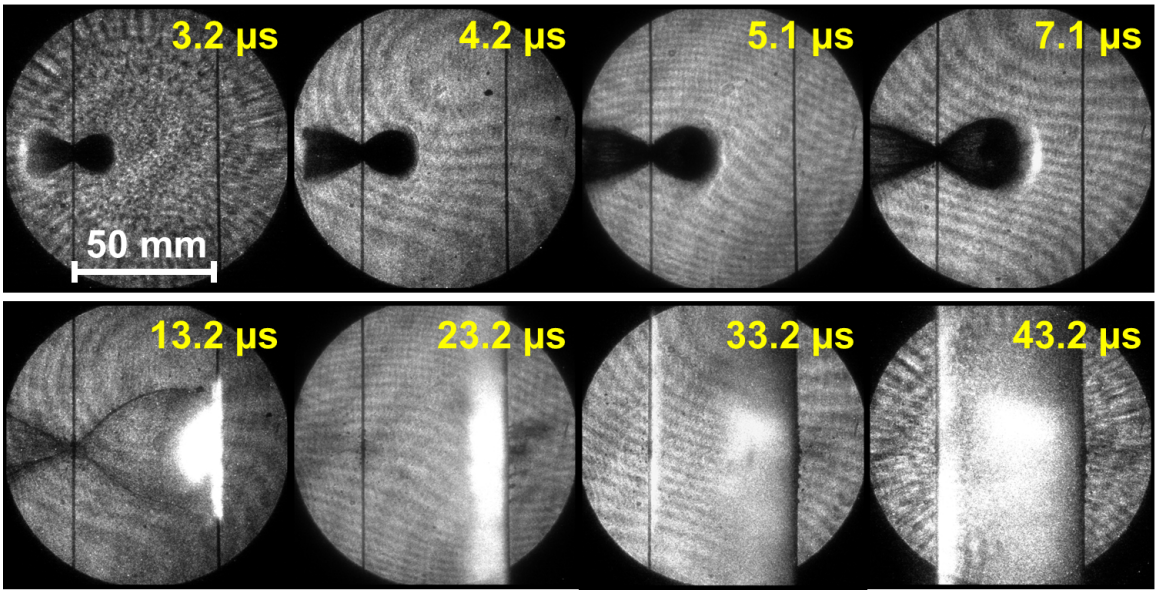

Figure 5.4: Laser side-lighting system results for a double-plate target configuration. Two $h = 0.5$ mm target plates, with 50 mm separation, are impacted by a 5.59 g nylon cylinder at 6.53 km/s. Timestamps shown indicate image time after impact.

As presented in Figure 5.4, the debris cloud is observed to travel downrange with a shot-line velocity of 5.1 km/s. By the fifth frame at 13.2 µs after impact, the debris cloud has impacted the second plate and by 23.2 µs, the rear-wall plate has been perforated. A visible emitting phenomenon is then observed to travel back uprange

and interact with the downrange face of the first target.

The complementary measurement of IR emission for this experiment, at 4.2 µs after impact, is presented in Figure 5.5. The figure presents the IR image and the corresponding LSL image taken at the same time. The field of view of the LSL system is depicted on the IR image. At 4.2 µs after impact, the IR-emitting cloud is observed to be interacting with the second plate 50 mm downrange, while the observable debris in the LSL image has only propagated 12.8 mm downrange.

Given the LSL results and measured debris cloud speed, backwards extrapolation from the observed debris cloud position estimates that the IR image corresponds to 3.4 µs after the debris was thrown from the back-surface of the target plate. Given this time and a 50 mm separation distance between the two-plates, the minimum speed of the IR-emitting cloud observed downrange striking the rear-wall plate is approximately 14.5 km/s.

In the LSL image shown in Figure 5.5, there is no observable aberration in grayscale beyond the observed debris cloud. The LSL image was taken at the lowest possible illumination source intensity, 60 mW. Given the 100 mm diameter illuminated field of view, the background illumination density in the LSL image presented in Figure 5.5 is 7.64 W/m^2. With this configuration, the system is most sensitive to variations in optical density of the fluid medium surrounding the target. Therefore, given this evidence, it is likely the source of IR emission interacting with the downrange second target plate is of negligible mass. Furthermore, given the observable spectrum of the Cordin camera from 400 nm to 900 nm, there is no complementary emission in the visible range with greater than 7.64 W/m^2 intensity.

5.2.2 Discussion of IR Results

The images presented in Figures 5.3 and 5.5 demonstrate the different phenomena observed using the IR and LSL imaging systems. Primarily, the scale of the uprange IR-emitting cloud is significantly larger than the ejecta material concurrently observed in the LSL system [44]. However, the shape of the phenomena observed in the LSL

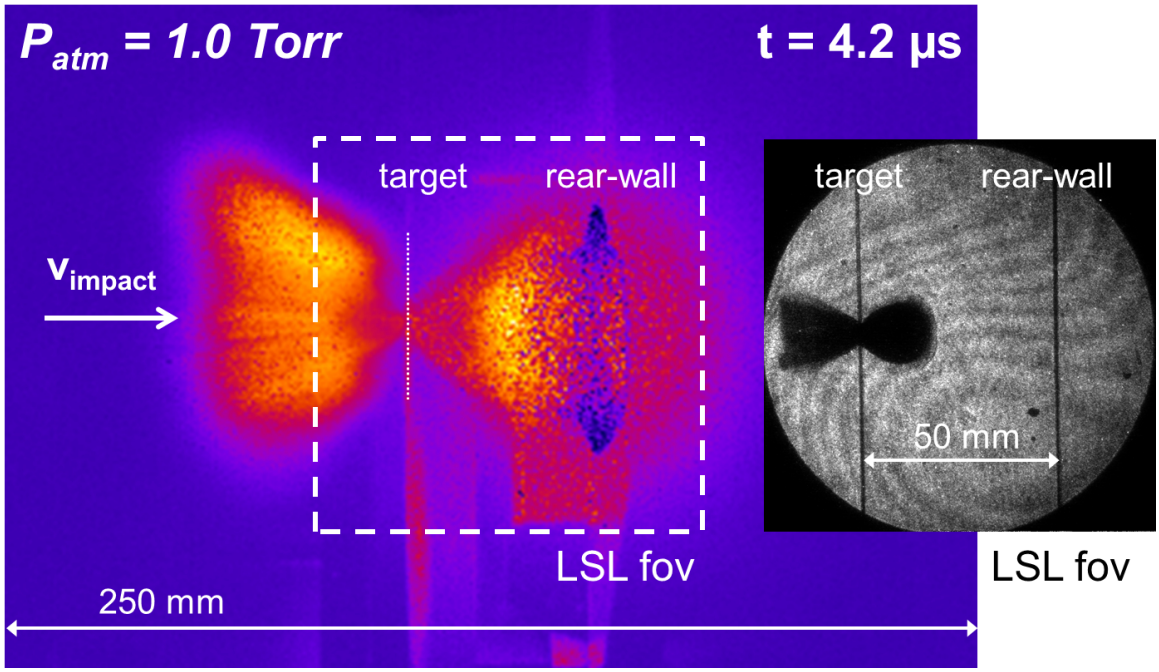

Figure 5.5: Concurrent IR and LSL image results for a 6.53 km/s impact on a double-plate target configuration consisting of two 0.5 mm aluminum plates separated with a 50 mm stand-off distance.

and IR images are strikingly similar. In particular, direct comparison of the IR and LSL images presented in Figure 5.5 indicate that the darker region in the uprange and downrange IR-emitting cloud are of the same shape and scale as the debris material observed in the LSL image. This suggests the formation of the IR-emitting cloud is related to the debris observed with the LSL system.

Therefore, one possibility is that the IR-emitting phenomenon is a relatively diffuse vapor/plasma cloud [44], similar to that observed by Sugita and Schultz [64], [62], [63]. They describe an impact-induced vapor cloud as chemically and thermally heterogeneous entity with components each having different mass, momentum, and energy [62]. Thermal modeling of the impact-induced vapor cloud by Sugita suggests that high-temperature radiation observed in hypervelocity impact experiments is attributed to ablation vapor from the surface of extremely small, high-speed fragments entrained in the vapor cloud [63]. Another potential hypothesis is that the IR-emitting phenomenon is caused by charged particles ejected at high speeds from

the impact.

The damage induced by vapor clouds to impact shielding rear-walls is well-documented [5]. Rear-walls of bumper shields must be made massive enough to prevent spallation and buckling in response to the blast wave loading of the vapor clouds. However, for the observed IR-emitting phenomenon interacting with the rear-wall in Figure 5.5, simultaneous results from the LSL system indicate no measurable mechanical response or deformation on the rear-wall. Results from similar experiments configured with thinner rear-walls of films and foils also indicate no measurable mechanical response of the rear-wall in conjunction with the arrival of the observed IR-emitting phenomenon with the rear-wall.

Previous and ongoing research investigating plasmas produced during hypervelocity impact suggest the generation of electrical effects are capable of damaging spacecraft systems [30]. Analysis of the UV-vis spectra indicate strong emission in the regions of observed debris from species originating from the nylon impactor [44]. Such results may provide insight into the origin and composition of the observed IR-emitting phenomena. However the characterization of the IR-emitting materials on the leading edges of the observed IR-emitting clouds would be challenging, given the high-speed of the observed front [68].

Therefore, the implications of the observed IR-emitting phenomenon on hypervelocity impact shield design and spacecraft protection are currently unknown. Similarly, it is also currently unknown if the IR-emitting phenomenon observed to interact with the rear-wall carries a charge. However, the repeatable occurrence of a pressure-dependent IR-emitting phenomenon interacting with a rear-wall, independent of the subsequent debris cloud, has been characterized for the first time.

5.3 Analysis of the Debris Capture System

Analysis of the capture pack provides considerable information about the nature of the debris cloud produced by perforation of the target. An example of the such analysis is provided in this section. Since positions on each sheet/plate are referenced

to the hit position on the target, the angular distribution of the individual debris particles can be determined. The penetration path length of a given particle through the pack is a measure of the total areal density of material required to bring the debris particle to rest, which is a measure of its penetration capability (lethality) and related to the particle's mass, speed and penetrating cross section. The maximum depth of debris particle penetration into the pack is a measure of the lethality of the debris cloud produced by that target and impact condition [44].

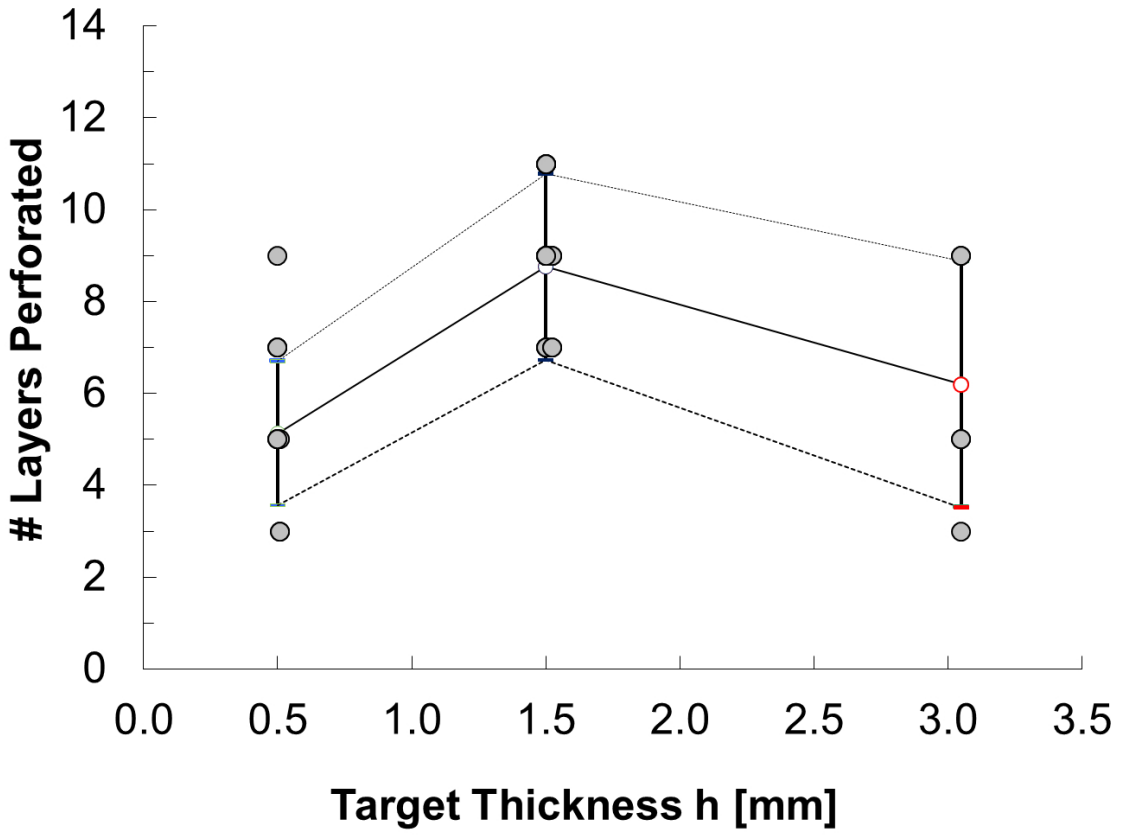

Figure 5.6: Number of capture pack layers perforated by debris produced in impact experiments for the three considered target plate thicknesses: $h = 0.5$ mm, $h = 1.5$ mm, and $h = 3.0$ mm. Results correspond to impact speeds between 4.7 and 6.5 km/s

Figure 5.6 presents the number of capture pack layers perforated by debris produced in experiments for the three target plate thicknesses with impact speeds be-

tween 4.7 and 6.5 km/s. The data presented plots the mean number of perforated layers (over the range of impact speed) with plus and minus one standard deviation. In Figure 5.6, the presented results indicate that the debris produced in impacts with the intermediate plate thickness ($h = 1.5$ mm) is the most penetrating. Note that the observed number of perforated layers presented in Figure 5.6 is relatively insensitive to the impact speed, as shown in Figure 5.7. Therefore, compared to the $h = 1.5$ mm target plate, the thinnest target plate ($h = 0.5$ mm) is more effective (and mass efficient) for shielding against the 1.8 mm diameter nylon 6/6 projectile for impact speeds between 4.7 and 6.5 km/s.

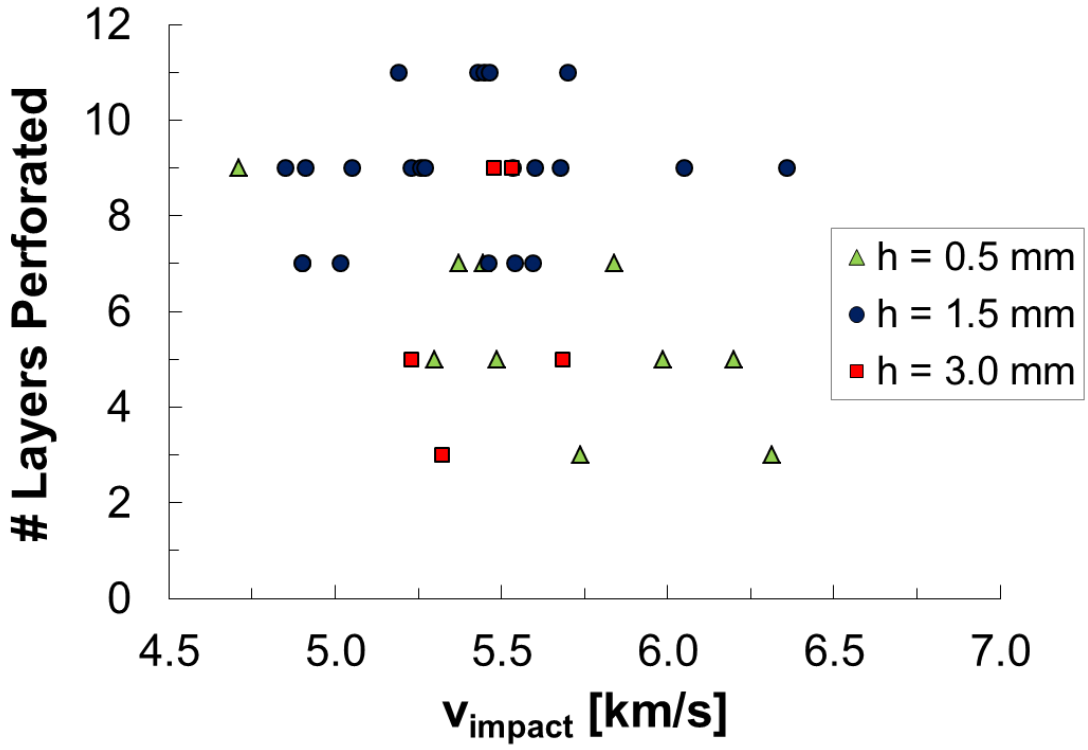

Figure 5.7: Number of capture pack layers perforated by debris as a function of impact speed for the three considered target plate thicknesses: $h = 0.5$ mm, $h = 1.5$ mm, and $h = 3.0$ mm.

For an example of the detailed analysis possible from a single experiment, consider the capture pack data produced for the same experiment described in the previous section (originally presented in Figure 4.16). Figure 5.8 provides an example of the

(x,y) hit position of individual debris particles in the layered medium of the capture pack. As observed, the most aggressive (largest and fastest) debris particles are asymmetrically distributed. The deepest penetrating particles are spread near horizontally and biased below the horizontal plane of impact. This data provides a metric for comparison to simulations by providing information regarding the number and distribution of large debris particles. Furthermore, the three-dimensional information regarding the trajectory of the debris particles can be compared to the two-dimensional debris cloud image produced with the LSL system.

Using the (x,y) hit position data, the angular and radial distributions of the debris cloud can be computed for each layer of the acetate film in the capture pack. Figure 5.9 provides an example of such analysis for the first layer ($P1$) in the considered experiment. The angular distribution is computed by binning the number of perforations contained in 5 degree sectors surrounding the impact position. The radial distribution is computed by considering the number of perforations in annular areas centered about the impact position. For any experiment, changes in the angular distribution in subsequent layers can be used to evaluate whether the trajectory of the debris particles remains straight while decelerating through the capture pack. Additionally, for multiple experiments, the effect of impactor tumbling can be quantified through analysis of the radial and angular distributions of debris particles.

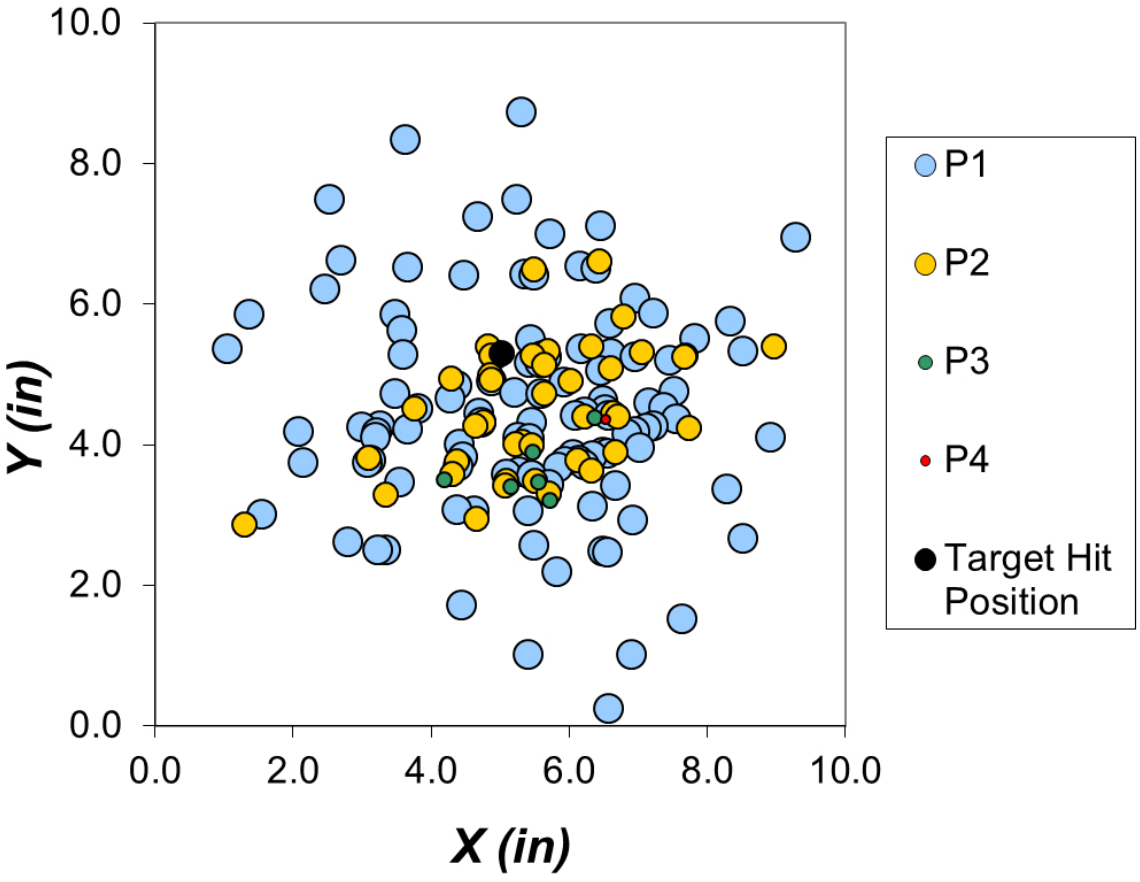

Figure 5.8: Spatial distribution of perforations in the capture pack system for layers $P1$ through $P4$ generated by the debris produced in the experiment presented in Figure 4.16: a $h = 1.5$ mm thick 6061-T6 aluminum target plate impacted by a 5.6 mg nylon 6/6 cylinder at 6.32 km/s.

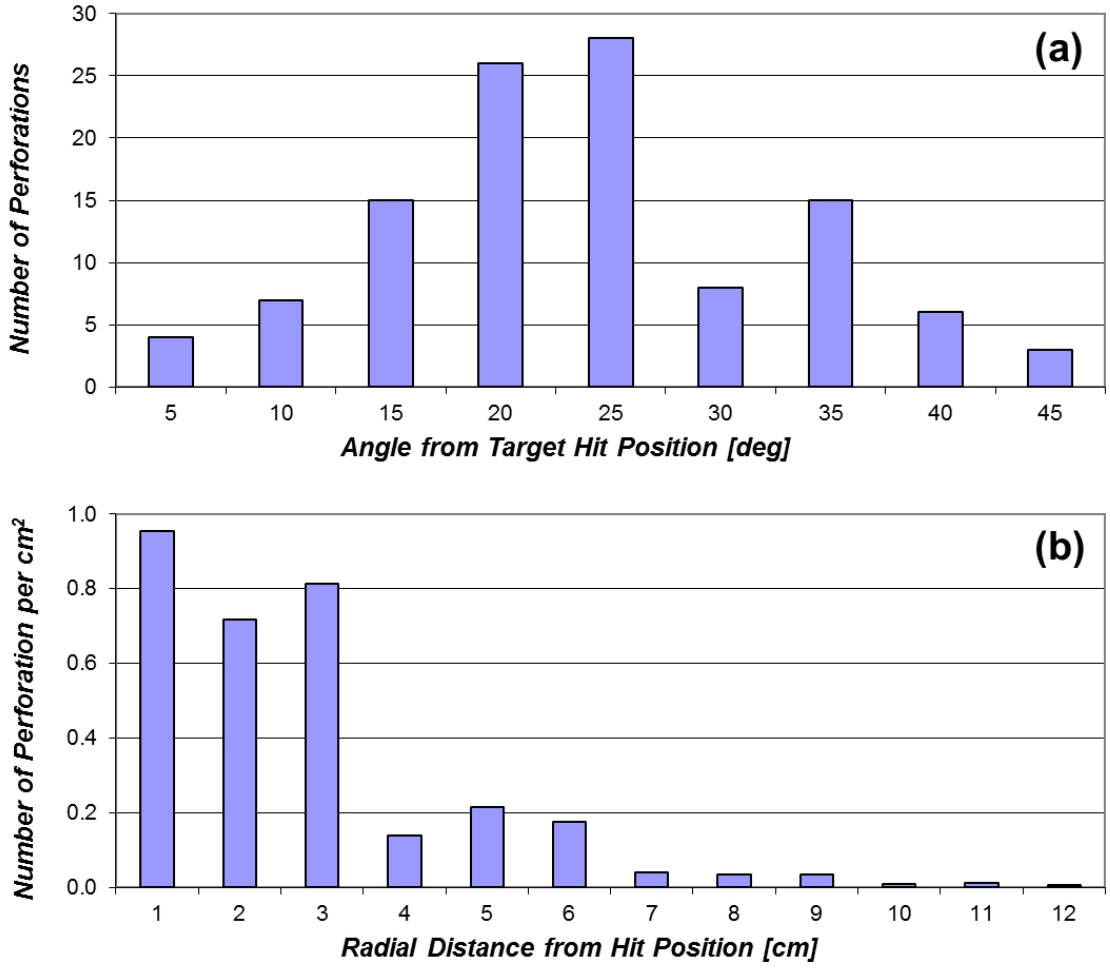

Figure 5.9: Angular (a) and radial (b) distributions of perforations in the capture pack system for layer the first later ($P1$) generated by the debris produced in the experiment presented in Figure 4.16: a $h = 1.5$ mm thick 6061-T6 aluminum target plate impacted by a 5.6 mg nylon 6/6 cylinder at 6.32 km/s.

Chapter 6

The Effect of Target Chamber Pressure on Observed IR-Emitting Phenomena

6.1 Target Chamber Atmospheric Pressure and IR Emission

The ambient atmospheric pressure P_{atm} in the target chamber at the time of the experiment has been shown to affect the observed impact phenomena. For example, at higher chamber pressures, shock waves are observed to form and propagate with the debris cloud and ejecta, as shown in section 4.6 [43]. Experiments conducted with variable ambient pressures also demonstrate a strong correlation between the scale of measured IR emission and the ambient pressure. A series of four IR images observed during impact experiments with ambient pressures ranging from 1.1 mmHg to 21.5 mmHg are presented in Figure 6.1. The IR images display the total integrated emission seen by the detector over the length of the programmed exposure time (1 µs). The position of the target, the direction of the incident impact vector, and artificial coloring has been added to the images presented in Figure 6.1 to improve clarity.

A series of impact experiments were conducted with variable atmospheric target chamber pressures ranging from 0.9 to 21.5 mmHg. The expansion of an IR-emitting cloud was observed using the IR imaging system installed in the SPHIR facility [44]. Dimensional analysis, originally presented by Whitham to describe the expansion of

a blast wave [73], is applied to attempt to describe the observed pressure-dependence of the IR cloud expansion.

The range of atmospheric pressure conditions considered are similar to those considered in previous work by Shultz and Sugita on impact-induced emission [59, 62, 64–66]. Furthermore, the considered atmospheric pressures are similar to those in light-gas gun experiments to enable drag-induced separation of sabots from impactors [54]. Therefore, observations of phenomena presented herein may have broad implications on hypervelocity impact testing.

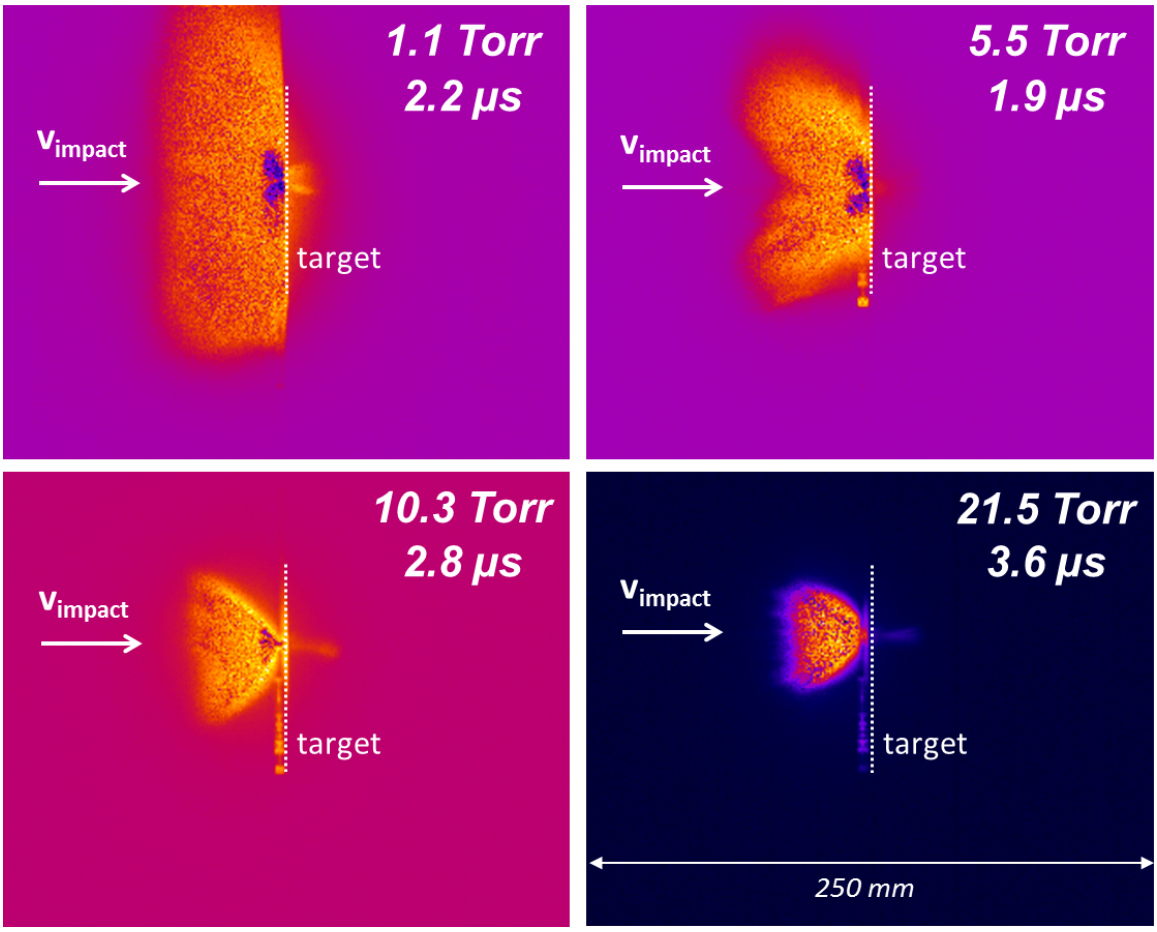

Figure 6.1: IR images for four experiments with a range of atmospheric chamber pressures. Images shown with false color to add contrast.

6.2 Experiment Configuration

The primary series of five experiments considered herein use $h = 1.5$ mm thick aluminum 6061-T6 target plates with dimensions 150 mm x 150 mm. Nylon 6/6 right cylinders ($d = 1.8$ mm, $l/d = 1$) were accelerated to impact speeds ranging from 6.0 to 6.6 km/s. Impact obliquity was held constant at 0 degrees (normal impact). Ambient atmosphere pressures in the target chamber were varied from 0.9 to 21.5 mmHg. Table 6.1 provides a summary of the experimental parameters of the five primary experiments considered. Only experimental results with IR images produced using an exposure time of 1 µsec are considered. The effective time of each image (presented in Table 6.1 as t_{IR}) is the sum of the exposure time and delay time (after impact) of each image.

ID	P_{atm} **[mmHg]**	v **[km/s]**	m **[mg]**	t_{IR} **[µs]**	h **[mm]**
A1	0.9	6.00	5.77	2.3	1.5
A2	1.1	6.18	5.72	2.2	1.5
A3	5.5	6.32	5.63	1.9	1.5
A4	10.3	6.25	5.73	2.8	1.5
A5	21.5	6.05	5.67	3.6	1.5

Table 6.1: Parameters of the 5 experiments corresponding to the primary series of IR image results discussed herein.

6.3 Dimensional Analysis of a Point-Blast Explosion

Dimensional analysis described by Whitham [73] can be used to describe the pressure-dependent expansion of a blast wave produced in an explosion. The explosion is idealized as a sudden, symmetrical release of energy E concentrated at a point. It is also assumed that energy is the only dimensional parameter introduced by the explosion. Lastly, the disturbance is assumed sufficiently strong such that the initial pressure and sound speed of the ambient air are negligible compared to the pressures and velocities in disturbed flow. In this case, the strong shock relations apply. With

these assumptions, the only dimensional parameter relating to the ambient gas is density ρ [73].

The only parameter involving length and time is given by Eq. 6.1, with dimensions L^5/T^2. Therefore the dimensional analysis solution to describe the radius of the blast-wave as a function of time is given by Eq. 6.2, where K is a dimensionless number. The kinetic energy E of the impactor is described by Eq. 6.3, where m is the mass of the impactor, v is the impact speed, and α is the partition of the impactor incident kinetic energy going into the blast wave. At the lowest chamber pressure considered (0.9 mmHg), the particle mean free path is approximately 50 µm [55] and, therefore, continuum theory is applicable. Assuming the fluid in the target chamber is an ideal gas, the density of the ambient air can be computed given the target chamber's atmospheric pressure (in mmHg) as described in Eq. 6.4.

$$\frac{E}{\rho} \tag{6.1}$$

$$R\left(t\right) = K\left(\frac{E}{\rho_0}\right)^{1/5} t^{2/5} \tag{6.2}$$

$$E = \tfrac{1}{2}\alpha m v^2 \tag{6.3}$$

$$\rho_0 = \frac{P_{atm}}{R_{gas}T} \tag{6.4}$$

Along with the definition of available energy (Eq. 6.3), the idea gas equation can then be substituted into the dimensional analysis solution for blast wave radius (Eq. 6.2). The predicted radius (Eq. 6.5) can then be determined as a function of the experimental parameters and a dimensionless constant C (Eq. 6.6), which includes the dimensionless parameters K and α.

$$R\left(t\right) = C\left(\frac{m v_{impact}}{P_{atm}}\right)^{1/5} t^{2/5} \tag{6.5}$$

$$C = 3.16K\alpha^{1/5} \tag{6.6}$$

6.4 Analysis

The analysis presented herein investigates whether the observed pressure dependence of the IR-emitting region can be described by the dimensional analysis for blast waves by Whitham. This requires a comparison of the experimentally measured radii of the IR-emitting region (R_{exp}) with the radii predicted by the Whitham blast wave theory R_w. Such a comparison requires the measurement of the empirically observed radii and the determination of parameters K and α from Eq. 6.2 and 6.3.

6.4.1 Definition of IR-Emitting Cloud Radius

Measurement of the experimentally observed IR-emitting cloud radius R is challenging, as they are often highly asymmetric. Such asymmetry is not surprising, considering that the mass of ejecta following the impact is not symmetric, as observed in the LSL results. Furthermore, as a consequence of the relatively slow exposure time (1 µs) with respect to the blast wave speed, the boundary of the observable IR-emitting areas is a gradual transition in grayscale. Therefore, analysis of the presented IR images requires a consistent method to define the radius of the IR-emitting cloud. To define a threshold value to differentiate between the IR-emitting cloud and the background, the empirical CDF (cumulative distribution function) of the grayscales of the image pixels (uprange from the target) is considered by ranking pixel grayscales. The threshold levels for each image are then defined as the grayscales corresponding to cumulative probabilities of $p = 95\%$ on the cumulative distribution function. An example CDF, describing the IR image taken with $P_{atm} = 5.5$ MmHg, is provided in Figure 6.2.

To isolate the IR-emitting region, image thresholding is performed on each IR image using the $p = 95\%$ threshold grayscale definition. The spatial coordinates remaining pixels in the resulting image are transformed into a radial-coordinate system

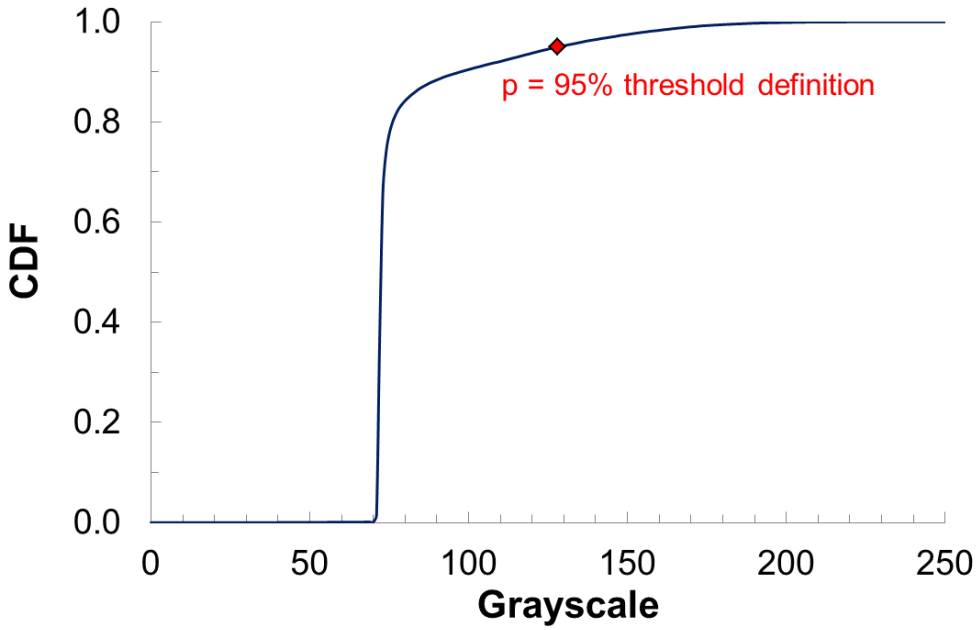

Figure 6.2: Cumulative distribution function (CDF) of an IR image pixel grayscale distribution and the $p = 95\%$ grayscale used to define the image threshold value.

with respect to the impact position as an origin, where $\theta = 0$ corresponds to upward direction along the vertical axis in the IR image. The boundary of the IR-emitting region is then defined for each integer value of theta by taking the average of the three largest corresponding radial coordinates. The observed radius of the IR-emitting region (R_{exp}) for each IR image is then defined as the maximum observed boundary radius. This definition therefore facilitates the theoretical prediction of the farthest expansion of IR-emitting cloud. An example of this process for the $p = 5.5$ MmHg experiment is provided in Figure 6.3.

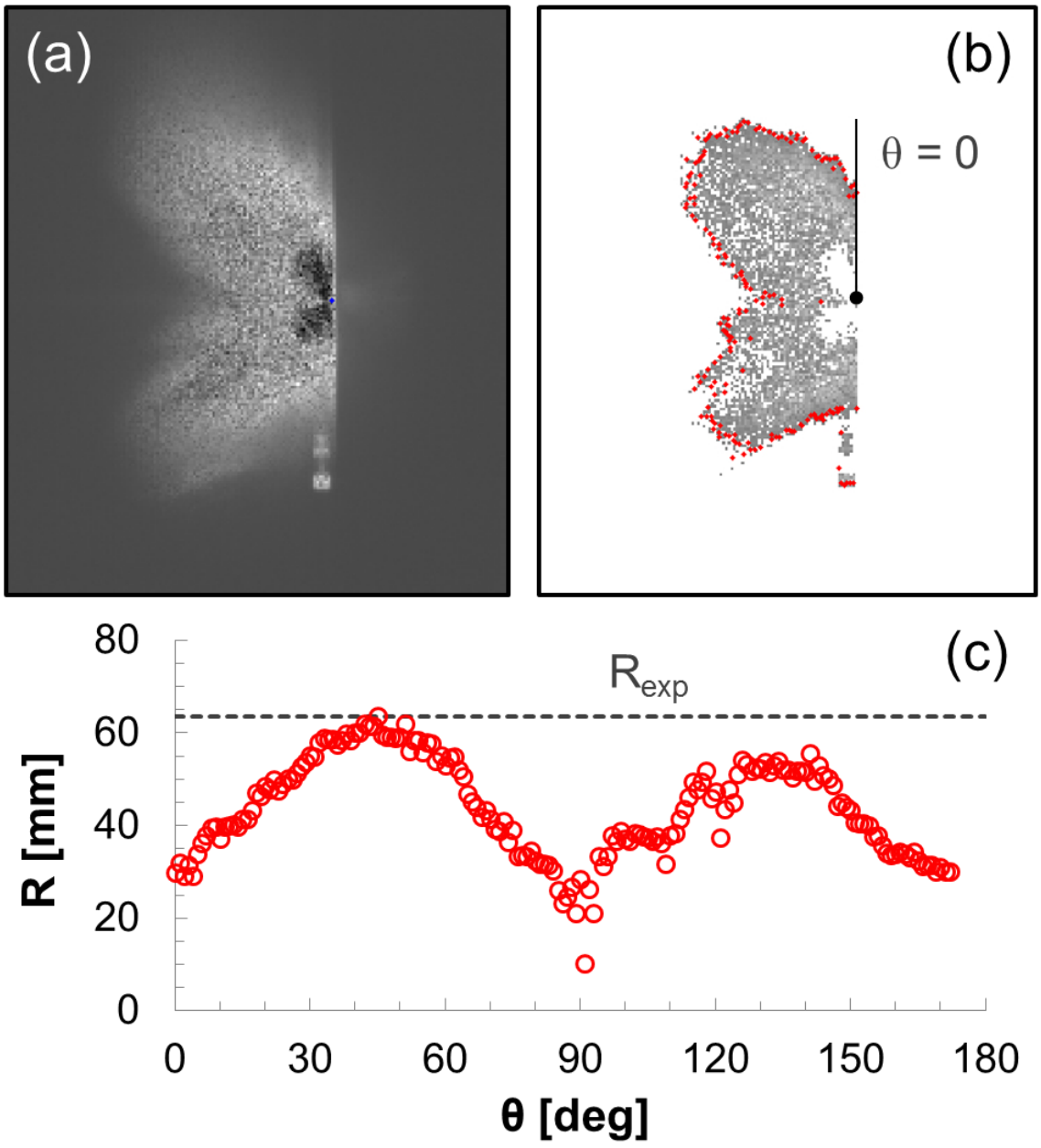

Figure 6.3: (a) Cropped IR image before grayscale level thresholding. (b) IR image after grayscale thresholding based on the $p = 95\%$ grayscale level. (c.) R-theta plot of the boundary pixels in the IR image and definition of the experimentally observed radius, R_{exp}.

The results for implementing this radius-defining process on each of the five primary experiments considered are presented in Figure 6.4. As shown, the $p = 95\%$ threshold level definition and subsequent process produces observed radii that adequately describe the farthest propagation of the IR-emitting cloud. The consideration of other threshold definitions, such as $p = 90\%$ and $p = 99\%$, facilitates the estimation of the uncertainty in the experimentally observed IR cloud radii.

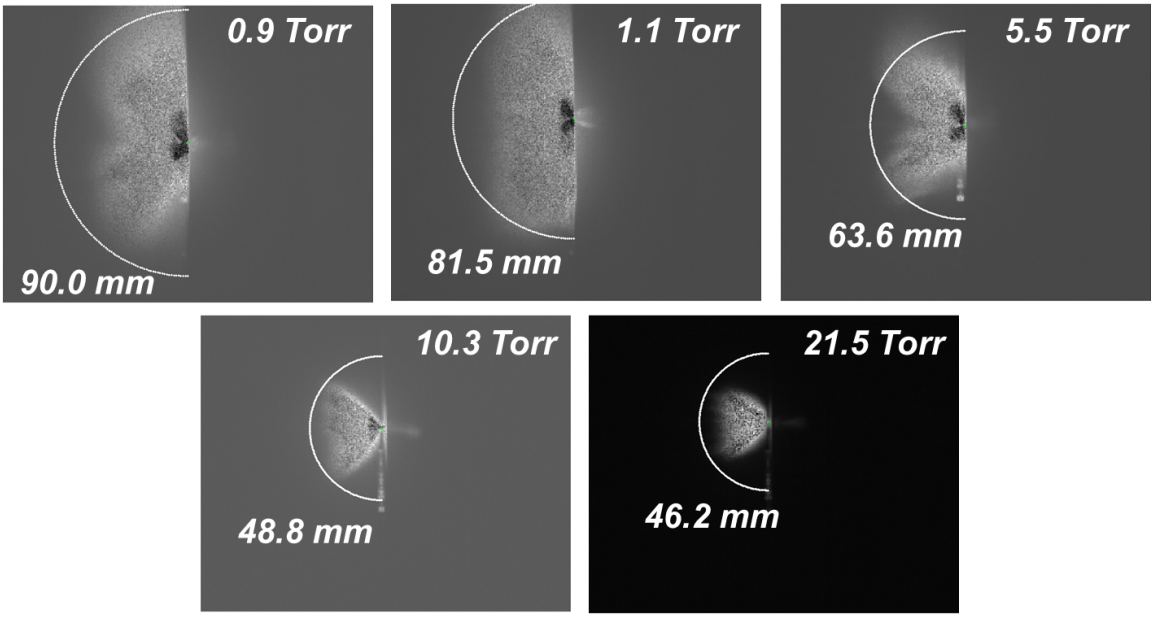

Figure 6.4: Radii of IR cloud expansion measured for each IR image considered.

6.4.2 Determination of Blast-Wave Dimensional Analysis Constants

The parameters K and α are first considered as empirically fit parameters. Given that α is defined as the percent of impactor's incident kinetic energy used in forming the blast wave, α must be less than 1. The optimum K and α are then determined by minimizing the root-mean-square (RMS) error between R_{exp} and R_w using a least-squared minimization routine. Considered values for α ranged from 0 to 1 with increments of 0.01. Preliminary correlation analysis indicated that values for $K < 4$ would best describe the data. Considered values for K were then considered from 0

to 4 with increments of 0.01.

Whitham describes constant K in Eq. 6.2 as a dimensionless number that is fixed from the definition of E as the total energy in the flow [73]. Reference is made by Whitham to work by G. I. Taylor [70], who provides an analytical solution for constant K. Taylor describes K as a function of only the ratio of specific heats γ. This is an idealized assumption for a spherical blast wave. The radius of the blast wave, R, is thus described by Taylor by Eq. C.1.

$$R = K(\gamma)\left(\frac{E}{\rho_0}\right)^{1/5} t^{2/5} \tag{6.7}$$

As described by Whitham, K is fixed from the definition of the total energy in the flow. Taylor defines the energy in the flow using contributions from both kinetic energy and heat energy. Using similarity assumptions and dimensional analysis, Taylor provides an approach to numerically determine the effective K for a given value of γ. The derivation and numerical integration conducted to compute K following Taylor's approach is provided in Appendix C. For $\gamma = 1.4$, corresponding to air, K is approximated as 1.03. For $\gamma = 5/3$, the value of K is found to be 1.13.

6.4.3 Uncertainty in Experimental and Theoretical Results

A full comparison of results requires consideration of the uncertainty in both the empirically measured cloud radii and theoretically predicted blast wave radii. The uncertainty of the experimental results is characterized by the range of maximum cloud radii measured by varying the threshold definition on each image's grayscale CDF (described in section 6.4.1) from 90% to 99%.

The uncertainty in the predicted blast wave radius from the Whitham theory is characterized accounting for experimental uncertainties in the measurement of impactor mass, velocity, chamber pressure, and image time. The root-sum-square (RSS) error of the product of the partial derivatives of Eq. 6.5 and corresponding parameter uncertainties is used to estimate the uncertainty in the dimensional analysis predicted radius (Eq. 6.8). The uncertainties for the effective time for each image is described

in Table 6.2. The uncertainty in the measurement of impactor velocities [44] for each experiment was 0.1 km/s. Chamber pressure and impactor mass have uncertainties of 0.2 mmHg and 0.1 mg, respectively.

$$\epsilon_R = \sqrt{\left(\frac{\partial R}{\partial m}\epsilon_m\right)^2 + \left(\frac{\partial R}{\partial v}\epsilon_v\right)^2 + \left(\frac{\partial R}{\partial P_{atm}}\epsilon_{P_{atm}}\right)^2 + \left(\frac{\partial R}{\partial t}\epsilon_t\right)^2} \tag{6.8}$$

ID	t_{IR} **[µs]**	ϵ_t **[µs]**
A1	2.3	0.14
A2	2.2	0.14
A3	1.9	0.10
A4	2.8	0.16
A5	3.6	0.19

Table 6.2: Uncertainties in the effective time of the IR images.

6.5 Predicting IR-Emitting Cloud Radii Using Dimensional Analysis

Using the experimentally measured radii presented in Figure 6.4, the optimum dimensionless parameters K and α were determined using the previously described least-squares RMS error routine. This routine is applied to empirically determine K and α by first considering all of the experiments. Because the Whitham blast wave analysis was derived considering ambient levels of atmospheric pressure, the optimum values for K and α were also determined for the two experiments with the highest atmospheric pressures (10.3 mmHg and 21.5 mmHg). Figure 6.5 plots K corresponding to the lowest RMS error as a function of α, for results fitting all five primary experiments and also fitting just the two highest pressure experiments. As shown in Figure 6.6, the corresponding minimum RMS error as a function of α is approximately constant (to within $3 \times 10^{-}3$). Results shown in Figure 6.6 correspond to the case considering all experiments, but this result has been observed for all parameter-fitting results for K and α.

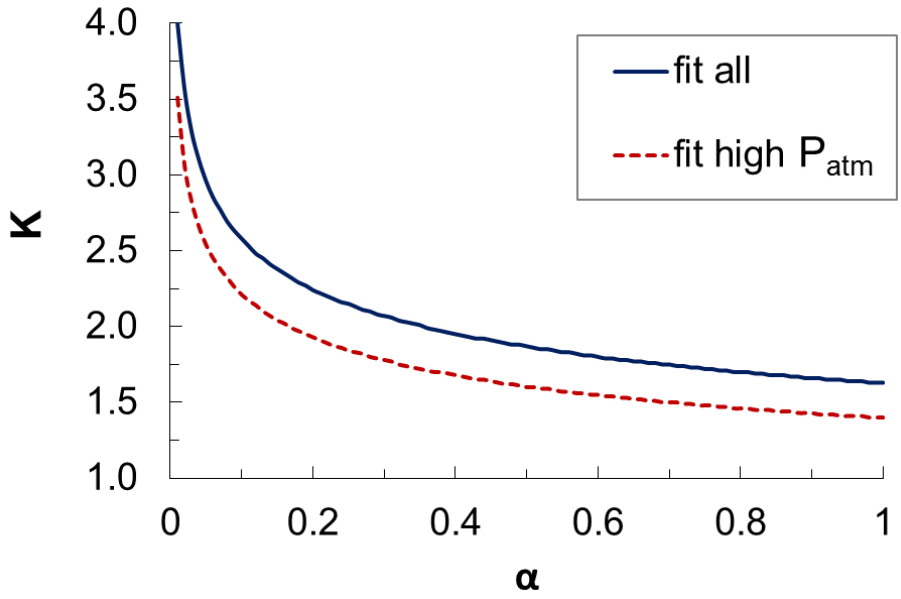

Figure 6.5: Optimum value of K (lowest RMS error) vs. α determined empirically by considering all five experiments for $h = 1.5$ mm target plates. The results for K vs. α determined using only the two higher atmospheric pressure experiments are also presented.

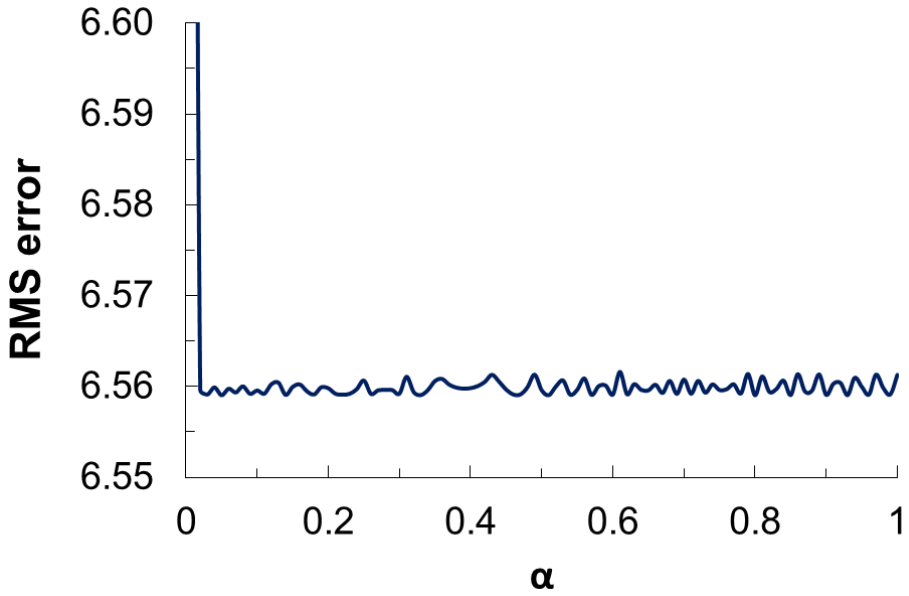

Figure 6.6: Minimum RMS error as a function of α.

Using the solution family for K and α considering all five primary experiments, the resulting predicted blast wave radii are plotted with the corresponding experiments in Figure 6.7. Graphically, the predicted blast waves provide an estimation of the expansion of the observed IR-emitting phenomena.

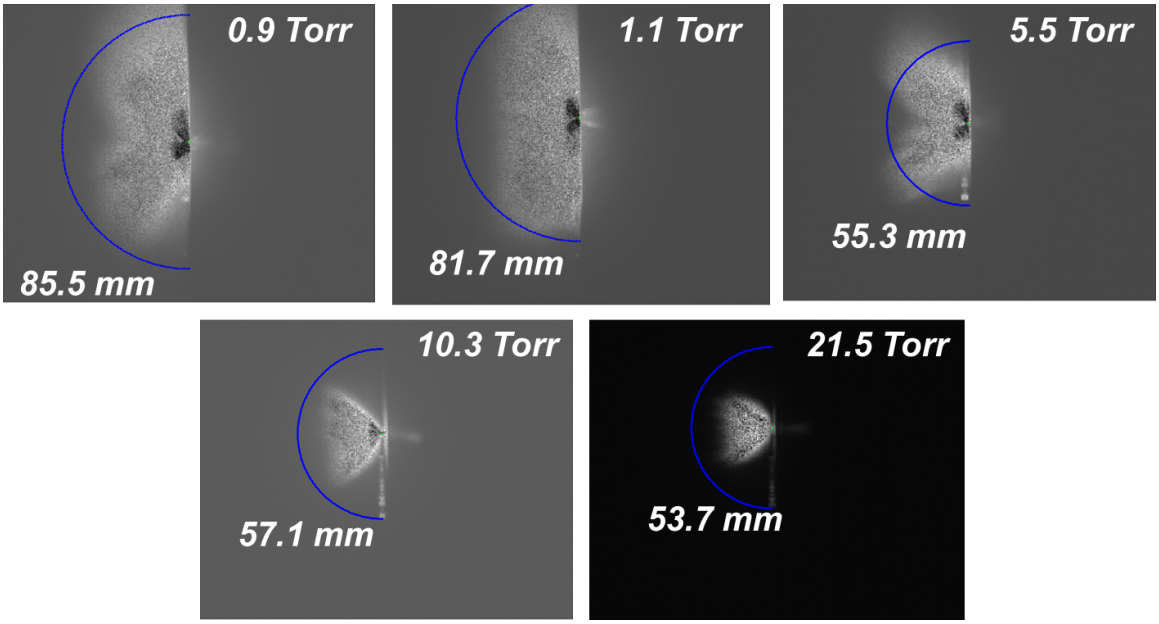

Figure 6.7: Predicted radii of the IR cloud expansion for each IR image using the Whitham blast wave dimensional analysis and empirically determined values for K and α.

Figure 6.8 provides a graphical comparison of the observed radii with the theoretically predicted results (for empirically determined K and α). In this figure, the experimental results are plotted against the dimensional analysis predicted radii as a function of target chamber pressure. Each experiment produces a different Radius-curve as a function of chamber pressure, given small differences in the parameters presented in Table 6.1. The uncertainty in each curve, described by Eq. 6.8, is included and incorporates the contribution of the experimental uncertainty in chamber pressure. The uncertainty of the experimentally measured radii, determined as described in section 6.4.1, is also included. Plotted in terms of chamber pressure, the experimentally observed radii conform to the characteristic non-linear decay as a function of pressure. Overall, the dimensional analysis solutions for the blast-wave

radii describes the observed radii largely within the described uncertainties. A direct comparison of the experimental and theoretical results are presented in Figure 6.9 and Table 6.3.

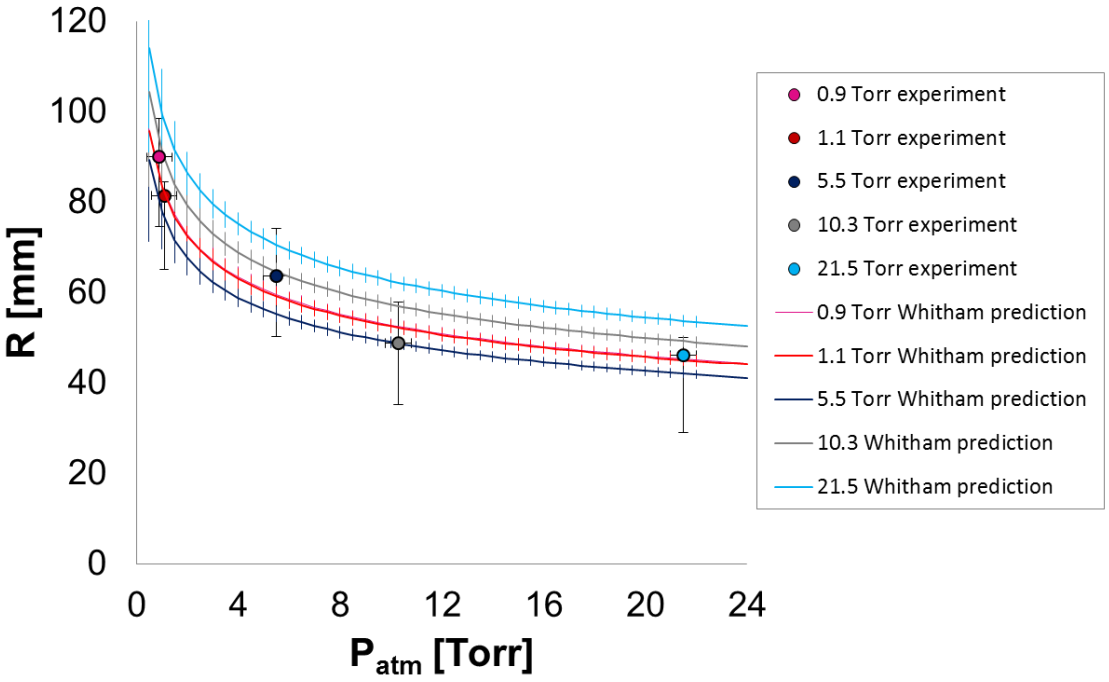

Figure 6.8: Measured expansion radii vs. the corresponding predicted radius as a function of pressure for each impact experiment.

ID	R_{exp} **[mm]**	ϵ_{R+} **[mm]**	ϵ_{R-} **[mm]**	R_W **[mm]**	ϵ_{R_W} **[mm]**
A1	90	9	15	83	9
A2	81	3	16	80	7
A3	64	11	13	56	1
A4	49	9	14	53	1
A5	46	4	17	48	1

Table 6.3: Summary of results for experimentally measured IR expansion radii R_{exp} and predicted Whitham blast wave radii R_W, along with corresponding values of uncertainty

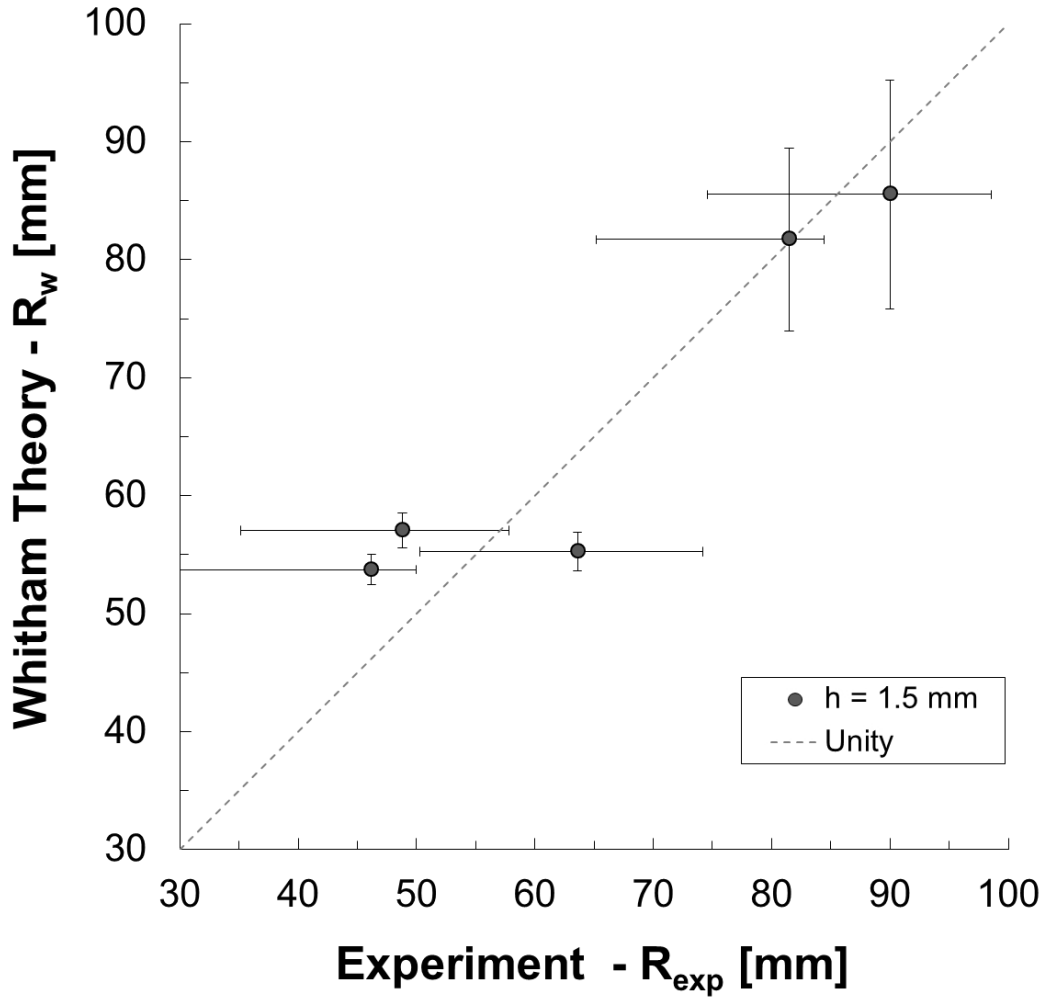

Figure 6.9: Measured expansion radii vs. the predicted radii using the Whitham dimensional analysis and empirically determined values for K and α.

As presented, the dimensional analysis solution presented by Whitham [73] for the radial position of a blast wave describes the observed pressure-dependent expansion of an IR-emitting cloud following impact. The optimum value for the dimensionless parameter K is observed to be $K > 1.4$. However, as described by Taylor [70], the expected value for K in air ($\gamma = 1.4$) is $K = 1.03$. For $\gamma = 5/3$, $K = 1.13$. Therefore, the ideal theoretical values for K significantly under-predict the empirically observed IR-emitting cloud radii. The maximum predicted radii (corresponding to $\alpha = 1$) for the idealized values of K (for $\gamma = 1.4$ and $\gamma = 5/3$) are presented in Table 6.4 along with the empirically observed and predicted values for the fitted value of K.

ID	R_{exp} **[mm]**	$R(K = 1.03)$ **[mm]**	$R(K = 1.13)$ **[mm]**	$R(K = 1.4)$ **[mm]**
A1	90	54	59	83
A2	81	52	57	80
A3	64	35	38	56
A4	49	36	40	53
A5	46	34	37	48

Table 6.4: Comparison of the experimentally observed expansion radii, the theoretically predicted radii for the idealized values of K, and the lowest empirically determined value for K.

It is unlikely that this disparity is the result of a systematic error in the determination of the effective time-after-impact, t_{IR}, of each image. Such a delay would correspond to the inertial delay between initial target-impactor contact and ejecta thrown uprange [44]. To account for the discrepancy described in Table 6.4, an additional time-delay between 2 and 4 µs would have to be added to each IR image's effective time. This time would correspond to at least 5 transits of the shock wave within the target plate and therefore is highly improbable given observed results from the laser side-lighting system describing debris and ejecta [44].

The dimensional analysis described by Whitham and corresponding analysis by Taylor assumes idealized conditions for a spherical blast-wave is considered. The impact experiments feature tumbling cylinders and asymmetric impact conditions, as observed in the LSL system. Therefore, the discrepancy between ideal theoretical and empirically optimum K values could be a consequence of non-simplified impact

conditions.

Additionally, what is not accounted for in the consideration of the incident impactor energy is the kinetic energy associated with the tumbling of the impactor. Cylinder impactors have been observed to tumble, at times, with angular velocities of at least $250,000$ rpm. At 6.2 km/s, this corresponds to rotational energy that is approximately 7% of the incident impactor kinetic energy. Such an increase in available kinetic energy is capable of changing the predicted radii by a few mm and improving the agreement between experimentally measured and predicted radii.

Furthermore, given the measured radius of expansion at the time of each image, the defined fronts of the IR-emitting clouds have observed velocities ranging from 12.9 km/s (for the 21.5 mmHg, 1.5 mm plate) to 38.5 km/s (for the 0.9 mmHg, 1.5 mm plate experiment). The blast wave velocities described by the Whitham dimensional analysis ranges from 7 km/s (for 21 mmHg at 3.5 µs) to 14 km/s (for 0.9 mmHg at 2.3 µs after impact). In comparison, the ejecta and debris phenomena observed with the LSL system produce substantially slower velocities ranging between 0.6 and 5.1 km/s. Such a disparity suggests that the IR-emitting cloud is a distinctly different phenomenon to both the uprange ejecta and downrange debris observed using the LSL technique.

6.6 Variable plate Thickness Experiments

Additional experimental results for IR images with 1 µs exposure times were obtained for impact configurations with thicker and thinner plates. Table 6.5 provides a summary of the parameters for the additional experiments considered with $h = 0.5$ mm and $h = 3.0$ mm target plates.

Using the previously reported procedures to define the boundaries of the IR-emitting regions and characterize uncertainties, the results for effective image time and observed radii are reported in Table 6.6. The corresponding IR-emitting region radii are presented graphically with each IR image in Figure 6.10.

Using the dimensional analysis values K and α determined empirically for the

$h = 1.5$ mm target plate results, the blast wave radii can be predicted for the results obtained for thicker and thinner plates. The predicted radii for the $h = 3.0$ mm and 0.5 mm plates are plotted with respect to the observed radii in Figure 6.11, along with the previously reported data from the $h = 1.5$ mm experiments.

ID	P_{atm} **[mmHg]**	v **[km/s]**	m **[mg]**	t_{IR} **[s]**	h **[mm]**
B1	1.1	6.0	5.7	2.4	3.0
B2	1.1	6.6	5.5	2.0	3.0
C1	1.1	6.3	5.3	2.4	0.5
C2	1.0	6.3	5.7	2.4	0.5

Table 6.5: Parameters of additional impact experiments considered for plate thicknesses of $h = 3.0$ mm and $h = 0.5$ mm

As observed, the measured radii produced in experiments impacting $h = 3.0$ mm and $h = 0.5$ mm are decidedly less than the predicted radii. Note that the predicted radii were based on results for K and α that were empirically determined using results obtained for $h = 1.5$ mm experiments. These results suggest that, if K was consistent in all experiments presented (based on atmospheric conditions), the energy used to generate the blast wave is different for impacts on different plate thicknesses.

Overall, the partitioning of the incident impactor kinetic energy in each experiment is expected to vary for different plate thicknesses. For example, the perforation areas and debris cloud velocities have been shown to be dependent upon the thickness of the target. The over-prediction for the 0.5 mm and 3.0 mm plate thicknesses presented in Figure 6.11, could be accounted for by using a smaller value of α. Therefore, the results suggest that, if K is constant, a smaller amount of kinetic energy is used in the generation of blast waves in impacts on the $h = 0.5$ mm and 3.0 mm plates. An interesting observation is that the relative sizes of the perforation area presented in chapter 3 therefore correlates with the relative values of α.

Shot ID	t_{IR} **[µs]**	$epsilon_t$ **[µs]**	R_{exp} **[mm]**	ϵ_{R+} **[mm]**	ϵ_{R-} **[mm]**
B1	2.40	0.15	63.7	13	16
B2	2.00	0.10	65.3	11	12
C1	2.42	0.11	60.8	7	15
C2	2.41	0.20	63.3	7	12

Table 6.6: Summary of the measured IR cloud expansion radii with corresponding image time and uncertainties.

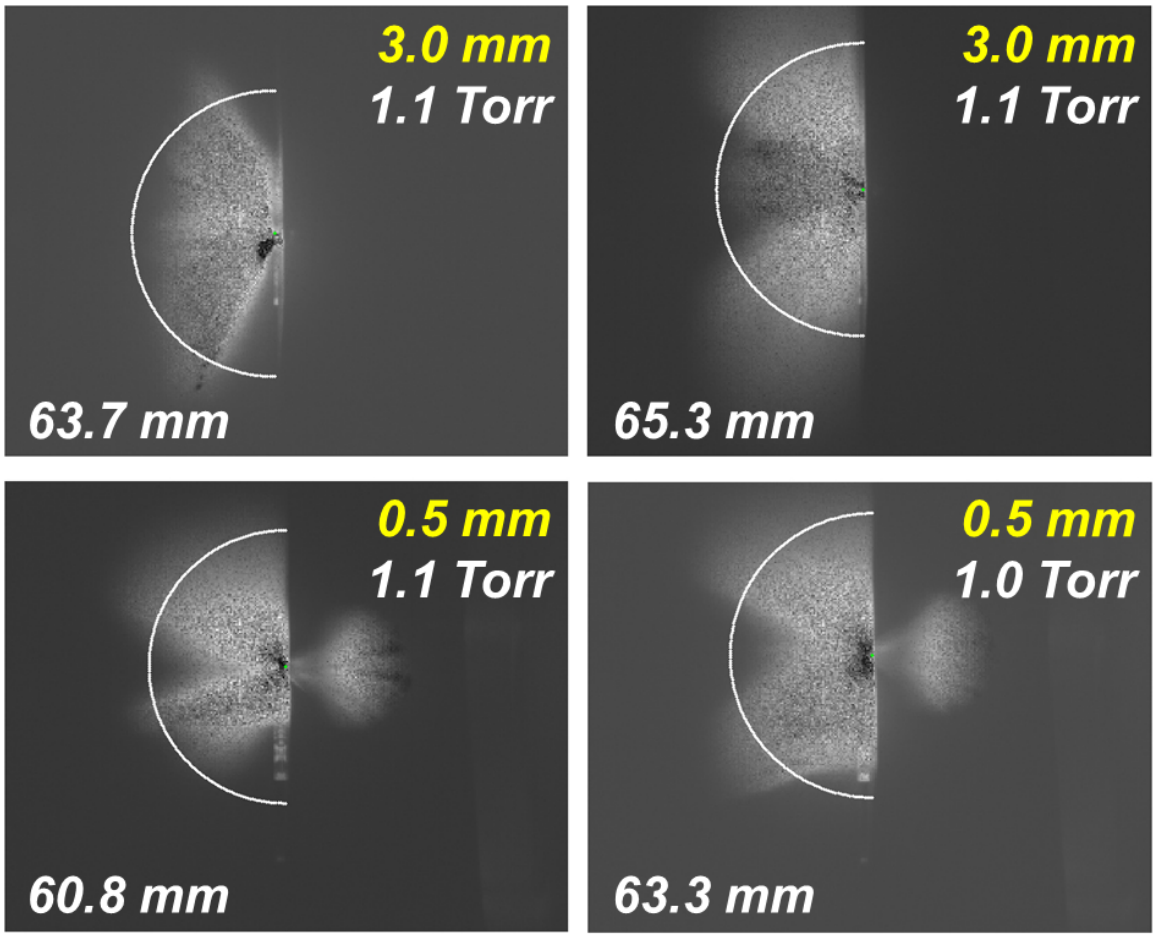

Figure 6.10: Radii of IR cloud expansion measured for the IR images obtained from the additional experiments considered with variable target plate thickness.

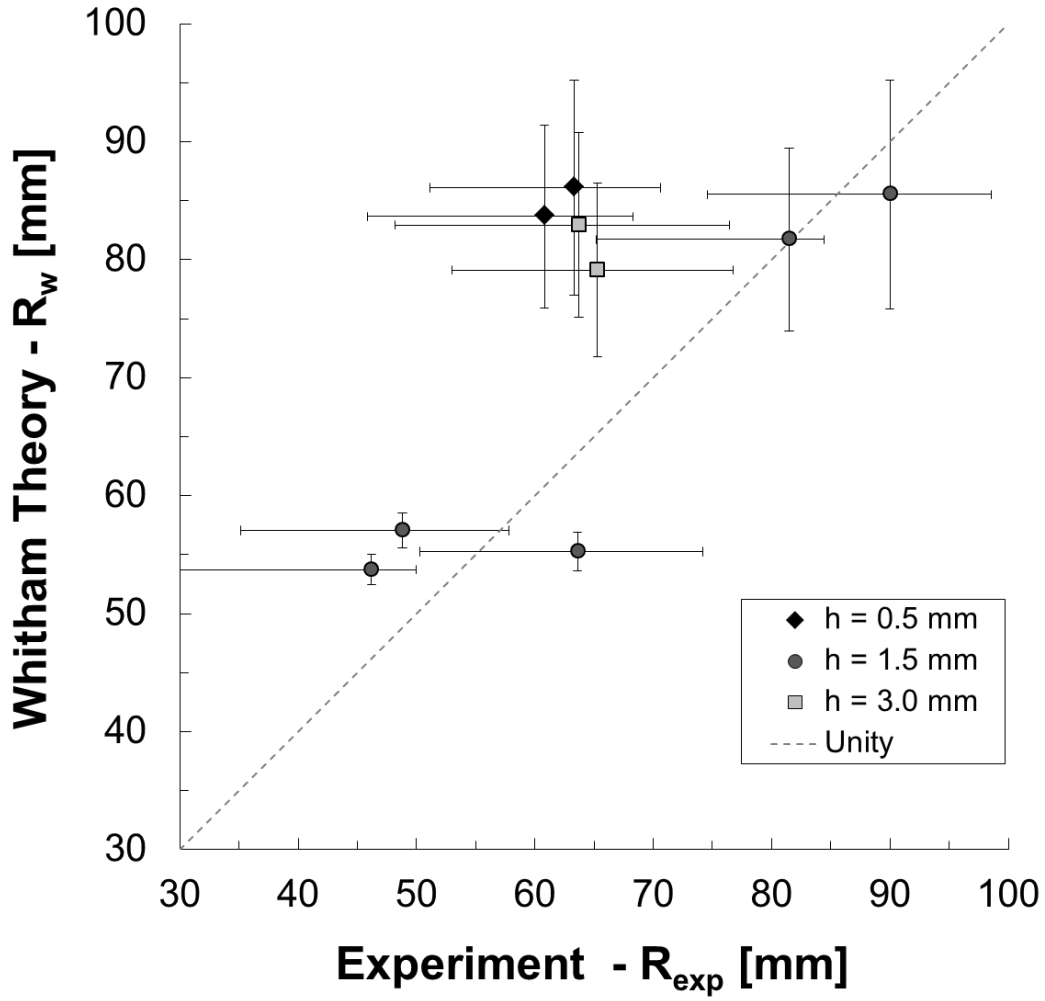

Figure 6.11: Results for the three target plate thicknesses considered comparing the measured expansion radii vs. the predicted radii. The predicted radii are computed using the previous values for K and α determined empirically for the primary $h = 1.5$ mm series of experiments.

Chapter 7

Conclusion

A comprehensive ensemble of concurrent diagnostics has been developed and implemented in the Small Particle Hypervelocity Impact Range (SPHIR) facility. The diagnostics and measurements described in this work are available for routine operation during every experiment conducted at the SPHIR facility. This suite of simultaneously operated instrumentation provides multiple complementary measurements that facilitate the characterization of many impact phenomena in a single experiment.

The Small Particle Hypervelocity Impact Range (SPHIR) facility is capable of routinely producing launch speeds of 5 to 7 km/s for launch package masses ≤ 6 mg, with maximum speeds exceeding 10 km/s. Refinement of legacy SPHIR operations procedures and the investigation of first-stage pressure have improved the velocity performance of the facility. The first state pump-tube pressure has been identified as a control on the impact velocity produced in an experiment. The average impact speed produced using 80 psi pump-tube pressure (6.4 km/s) is at least 0.57 km/s faster than the mean produced for 150 psi, with 99% confidence.

This work investigates hypervelocity impact phenomena for normal impacts of 1.8 mm nylon 6/6 cylinder projectiles and variable thickness aluminum targets. Nylon has been considered previously as a surrogate material for micrometeoroids and aluminum 6061-T6 is a common material used in spacecraft structures. The target thickness were selected with respect to the ballistic limit thickness (given mean velocity performance) to provide a range of normalized thickness ratios and produce a wide variety of impact phenomena. Accordingly, the three target thicknesses were 0.5

mm, 1.5 mm, and 3.0 mm. Additionally, the majority of previous investigations on perforation size and debris phenomena were conducted on thin plates for application to bumper shield design. Therefore, the results and models for the range of target thickness described herein enhance the understanding of the effect of target thickness on observed phenomena.

Results for the perforation area indicate the selected range of target thicknesses represent multiple regimes describing the non-monotonic scaling of target perforation with decreasing target thickness. These results are used to support the development of the OTM (optimum transportation meshfree) numerical model and a mathematical framework to quantify model uncertainty. The OTM model demonstrates good agreement with experimental results over the large (challenging) range of considered normalized target thicknesses. The scaled perforation area results are also compared to previous models and a mechanics-inspired modification of the Watts model is proposed. With this new model, the selection of a single, physically meaningful parameter is demonstrated to provide excellent agreement with experimental results. The perforation diameter is related to volume and state of debris that is thrown downrange from a hypervelocity impact. Therefore, an improved understanding of the scaling relationship to describe perforation diameter improves engineering methods for the design hypervelocity impact shield systems.

The laser side-lighting (LSL) system has been developed and implemented in the SPHIR facility for the ultra-high-speed observation of hypervelocity impact debris phenomena. This novel technique utilizes a coherent, continuous, and collimated illumination source and provides several operational advantages over other conventionally used high-speed imaging techniques. The use of a directed, continuous 600 mW visible beam represents less of a safety hazard than the historically utilized flash radiography technique. Furthermore, unlike many other impact imaging techniques, the LSL system enables continuous high-intensity illumination of the target, enabling a simpler instrument triggering system. Furthermore, the use of a coherent light source enables the measurement of additional phenomena, such as rarified atmosphere shock waves, which are immeasurable with other techniques. The use of

coherent light allows the LSL system, with small modification, to also be used for several interferometry techniques

Results from the LSL system are used to characterize the differences in the debris clouds produced in hypervelocity impacts of nylon cylinders on aluminum targets of varying thickness. Observed phenomena are consistent with observations made in previous studies for similar normalized thickness ratios. The grayscale calibration of the Cordin camera and the utilization of a collimated illumination source enables the measurement of the two-dimensional optical density of the debris cloud. This novel experimental capability is demonstrated to provide a measurement of the two-dimensional distribution of material in a debris cloud. Such a technique is particularly useful in characterizing the debris clouds produced for impacts with variable yaw angle. This technique shows potential to be useful metric in the evaluation of numerical models. A ray-tracing algorithm would be required to compute an effective optical density of debris structures produced via simulation. In principle, the LSL system could also be implemented in an orthogonal pair to provide a more complete measurement of the three-dimensional debris cloud structure.

Furthermore, the utilization of the coherent, collimated light source in the LSL system facilitates the simultaneous measurement of impact phenomena with near-IR and UV-vis spectrograph systems. Results for UV-vis emission spectra provide insight into the composition of the vapor/plasma observed in the concurrently observed IR and LSL images. Comparison of the IR and LSL images indicate two distinctly different phenomena. A high-speed, IR-emitting cloud is observed in experiments to expand at velocities much higher than the debris and ejecta phenomena observed in using the LSL system. In a double-plate target configuration, representative of geometries used in spacecraft shielding, this IR-emitting phenomena is observed to reach the rear-wall several μs before the debris cloud. Although no mechanical effects are observed on the rear-wall in response to the IR-emitting cloud, the implications of this phenomenon on hypervelocity impact shield design are currently unknown. However, the repeatable occurrence of a IR-emitting phenomenon interacting with a rear-wall, independent of the subsequent debris cloud, has been characterized for the

first time.

The expansion of this IR-emitting region is demonstrated to be dependent on the ambient atmospheric pressure in the target chamber. Dimensional analysis by Whitham for the radial expansion of a spherical blast wave is shown to describe the pressure-dependent expansion of the IR-emitting region. Refinement of the pressure-dependent blast wave observation and analysis presented herein has potential to provide insight into the amount of impactor kinetic energy dissipated through the formation of a blast wave. The considered atmospheric pressures are similar to those used in light-gas gun experiments to enable drag-induced separation of sabots from impactors. Therefore, the observed pressure-dependent expansion of IR-emitting material has implications on current procedures used in hypervelocity impact testing.

The extensive instrumentation of the facility maximizes the data output from each experiment and provides a high return on investment given the fixed costs of each shot. Because of this, experimental campaigns of several shots yield very comprehensive data sets on a host of phenomena. Such datasets are useful for the validation of models, particularly those with multi-scale features. This current work has studied the phenomena associated with the impact of nylon cylinders on aluminum targets. However, the diagnostic capabilities and techniques described can be used with a wide variety of impactors, target materials, and target configurations to investigate any number of engineering and scientific problems.

Appendix A

SPHIR Facility Operating Procedure

Contributing authors: Jon Mihaly, Jon Tandy, and Marc Adams

A.1 Cartridges

1. Get gunpowder tube, cartridges and primers from safe.
2. Be sure to keep gunpowder on covered area.
3. Take out compression tool from drawer below.
4. Insert rod *flat part up*.
5. Put primer in tool *rough side up*.
6. Put cartridge on top in groove and squeeze all the way to push in primer (*shiny part showing*).
7. Cut one small tissue into 8 squares for wadding (to pack down powder).
8. Weigh the wadding square on the balance.
9. Weigh 0.9 g (between 0.899–0.909 g) of powder from aluminum boat into red cap on other balance.

10. Write both weights (wadding and powdwer) on the side of the cartridge.
11. Use green funnel to pour powder into the cartridge.
12. Use straw to push wadding into cartridge — push and fold technique (avoid clumping).
13. Clean up and put unused powder back in tube.
14. Put gunpowder tube, cartridges and primers into safe.
15. Be sure the safe is *closed and locked*.

A.2 Impactors

- Nylon spheres are in the cardboard box — *do not lose the blue label* with sizes.
- Steel spheres (440C) are in the top right drawer of the yellow drawer box.
- Produce nylon cylinder impactor: use a razor blade to cut a new cylinder off the nylon block.
- The *length* of the cylinder needs to be the *same as the diameter* (within 1 mil or 1/1000 inch).

Method 1: The Jig

1. Use the larger jig (distance from edge to bottom of hole piece is greater).
2. Place the cylinder in the jig with the *cut edge face up*.
3. Push in gently.
4. Skim across top with razor blade at different angles until flat (do not push blade in too far or push across too flat).

5. Measure the cylinder length with calipers. If satisfactory (length = diameter) use this cylinder, if too long try to cut again, if too short discard into "under-sized" vial.

Method 2: The Mill

1. Measure the initial length using calipers (*be careful not to compress cylinder*)
2. Calculate how much to remove using mill.
3. Remove collar from mill (1.8 mm).
4. Insert cylinder into collar with *cut end up*.
5. Replace collar in mill.
6. Adjust wheel handles to arrange the mill above and on the edge of the cylinder.
7. Using the scope to view the cylinder, switch on the mill and slowly lower until first contact with the cylinder.
8. Use small dial on top handle to set to zero and set maximum lowering point to desired cut length.
9. Set to a slow mill speed (*fast speeds can cause smearing*).
10. Use the side handle to slowly feed the mill across the cylinder.
11. Make cuts of at least 3 mil (*smaller cuts cause burrs*).
12. Measure again using calipers (*be careful not to compress cylinder*).
13. If too long continue milling process.
14. When correct size acheived, weigh the impactor.
15. Write down the weight and size.
16. Put cartridge and impactor in a labeled glass vial.

A.3 Pistons

1. Write down the batch number.
2. Remove any burrs with hands.
3. Check the cup is fairly uniform and there is no debris in the cap.
4. Measure the piston length, muzzle-end diameter, and breech-end diamter using calipers until resistance (not until caliper clicks).
5. Rotate while measuring to find the range of sizes for both diameters.
6. Piston muzzle-end diameter ≈ 0.222 (must be > 0.220), breech-end diameter ≈ 0.227.
7. Measure the mass of the piston using balance (mass should be 185–195 mg).
8. Put piston in the same labeled glass vial as cartridge and impactor.

A.4 Launch-Tubes

1. Check tube to make sure it is relatively straight.
2. Fix tube in guide clamp.
3. Lubricate both the guide and chamfer tool.
4. To make chamfer gently rotate chamfer tool through the guide until the tool moves freely. (Free movement means the chamfer is cut.) Make sure *not to twist sideways* and to take out periodically to remove debris.
5. Remove tube from clamp and repeat steps 2–5 on other end.
6. To flatten breech-end of tube use the same tool with increased (but not too much) downward pressure (*making sure not to twist sideways*), remembering to lubricate and periodically remove debris. *This is critical for the eventual seal with the Mylar burst disc during operation.*

7. Continue until a clean, shiny surface is visibile.

8. Examine tube ends under the microscope if necessary to ensure a smooth interior of the bore in the region that was cut. *Small burrs or gouges left behind can survive the subsequent cleaning process and destroy or re-direct the impactor during the experiment.*

9. Clean the launch-tube with acetone.

10. Blow through tube with compressed air.

11. Tie a new piece of Kevlar thread ≈ 2 times the tube length to handle (Kevlar from McMaster, standard size 346 AKA trade size 5).

12. Tie about 5 tight figure-eight knots in the middle of the thread.

13. Run through the launch-tube with the Kevlar thread while rotating for ≈ 30 s.

14. Repeat steps 10 and 11.

15. Use aluminum wire to thread string though the tube. (String is packing twine from ACE hardware.)

16. Clean with string using two sections — the first section wet with acetone and the second section dry — for ≈ 30 s each.

17. Repeat steps 9 and 10.

18. Visually inspect bore of tube (look through) from both ends.

19. Make sure a 68.5 mil pin gauge can pass through the tube. If the 68.5 mil pin gauge does not fit through the launch-tube, *do not use the launch-tube.*

20. Measure how hard it is to push 69.5 mil pin gauge through.

21. Check the maximum pin gauge size that will go in the end (do not push hard).

22. Write down information from steps 19 and 20 on datasheet.

A.5 AR Section

1. Check smaller hole with 65 mil pin gauge — *this is the maximum size that should go through, do not use AR section otherwise.*
2. Inspect the copper gasket to make sure it is not "chopped up" (the interior diameter of the gasket should be clean with no burrs and no coverage of the interior bore of the AR section).
3. Clean with acetone and brushes — use brushes in order large to small.
4. Rinse with acetone again.
5. Blow out with air and dry outside with tissue.
6. Check the AR section is clear of any debris.
7. Redraw arrow going downrange (big to small) if necessary.

A.6 Target Preparation

1. Select target and put on centered crosshair.
2. Record all target geometry info on datasheet.
3. Align target in clamp with center of side port (if recording front and back).
4. Check laser side lighting and Cordin alignment (see separate notes).
5. Take pre-shot images with Photron and Cordin cameras using screw.
6. Align photodiode for triggering (will be finalized after practice triggering).

A.7 Loading Impactor

1. Put impactor in collet of loader with a little exposed.

2. Put breech-end (shiny end) of launch-tube face down.

3. Wind down handle to put just the top of the impactor in launch-tube.

4. Rotate bottom wheel of loader anticlockwise to push impactor in until flush with end.

5. Rotate wheel another *one half turn* to add headspace.

6. Remove launch-tube making sure the impactor does not fall out (a snug fit is critical to reach correct velocity).

A.8 Loading Launch-Tube

1. Put O-ring around muzzle-end of launch-tube (opposite end of impactor).

2. Check impactor location (breech-end or uprange).

3. Put launch-tube on in the grove of the bottom half of the clam-shell and slightly in hole (of first downrange diagnostics box).

4. Use the 25 mil feeler gauge give correct headspace between uprange surface of launch-tube and clam-shell.

5. Recheck spacing after placing on top section (top piece of clam-shell).

6. Set the manual wrench to 40 pounds of torque using the lock/unlock mechanism.

7. Bolt on top of platform using this wrench going downrange until you hear a click (*repeat to make certain*).

8. *Reset wrench to 25 pounds torque.*

A.9 AR Section Setup

1. Use the 11/16 inch puncher to create Mylar burst disc.

2. Make sure the disc stays clean.
3. *Visually confirm pump-tube is clear.*
4. Check impactor is still in position.
5. Inspect copper section of AR section: *make sure no burrs or obstruction of AR borehole.*
6. Put Mylar disc on the smaller diameter end of the AR section.
7. Insert AR section correctly (big to big, small to small) by holding small hole of AR section to 2nd stage of gun (small to small).
8. Bring pump-tube up to meet the AR section (big to big).
9. Align pump-tube pillow blocks so it is straight.
10. Finger-tighten pump-tube bolts.
11. Insert cheese wheel bolts with the double washer bolt in the top right hole.
12. Tighten gradually with wrench corner to corner (*not in circular progression yet*) with small 1/8 turns of the wrench until all bolts require click of wrench (signifying 25 pounds torque).
13. Give every bolt a final torque check using a circular progression.
14. Tighten bolts on top of pump section, uprange to downrange.

A.10 Trigger-Pull System

1. Put trigger pull on stage and attach clamps.
2. Make the "front surface" of stage block flush with the notch on the plunger. (This sets the correct stand-off distance.)

A.11 Test Triggering

1. Check view and intensities of Cordin camera exposures, balance as needed.
2. Check UV-vis trigger is set to rising edge.
3. Check UV-vis camera intensifier is ON.
4. Check trigger boxes and oscilloscope settings.
5. Arm all cameras to test trigger → flash photodiode.
6. Repeat steps as necessary.

A.12 Capture Pack

1. Assemble capture pack using foam and Mylar sheets (foam on top).
2. Place pack in tank and set 5 inches back from target.

A.13 Pre-Vacuum "Walk Around"

1. Check there is nothing left in the tank that should not be there.
2. Align photodiode trigger → check it is not blocking the laser.
3. Double-check everything in tank (target position, photodiode position/direction and nothing left inside).
4. Pull up tank side, *making sure it is straight and does not swing out.*
5. Clamp both sides.
6. Check laser alignment.
7. Close extraction vent valve (top lever).
8. Close vacuum valve and backfill valve on side on tank.

9. Close all dials on valve box: *do not over tighten.*
10. Close pump-tube valve: parallel to tube is closed.
11. Double check AR arrow points *downrange.*
12. Insert piston — *cup in back and flat in front.*
13. Bash in with press and mallet up to the red line.
14. Note down piston fit on datasheet (e.g., light tap).

A.14 Evacuating Target Chamber and Pump-Tube

1. Vacate area around tank.
2. Double-check that no person is standing near the largest glass window on the target chamber (closest to lab door).
3. While someone is next to the emergency pump stop button, open vacuum lever (pump-down valve).
4. Put tape around muzzle-end of pump-tube (where it enters diagnostics box: you will hear the hissing stop when tape sufficiently seals opening).
5. Put on cylinder shield.
6. Open vacuum valve (tank pressure < 2 Torr to proceed).
7. Put V3 to OPEN and wait until pressure settles.
8. Put V1 to V and wait till pressure settles.
9. Open pump-tube valve (tank pressure < 1 Torr to proceed).
10. Put V3 back to closed ("vacuum").
11. Evaluate leak rate of piston (< 1 mmHg increase per second).

12. Once pressure settles or > 3 mmHg put V3 back to OPEN to re-evacuate the pump-tube. Proceed when pump-tube pressure is stable.

13. *Repeat steps 10–12 two or three times, you should notice an improvement in both the leak-rate and final stable pressure in pump-tube.*

14. Ideally want final stable (evacuated) pressure in pump-tube to be as close to 0.1 mmHg, and at least < 1 mmHg.

15. Record final (evacuated) pressure of pump-tube on datasheet.

16. Close vacuum source in reverse order: pump-tube valve, V1, V3, vacuum valve.

A.15 Inserting Powder Cartridge

1. Check safety is off (forward).

2. Check cartridge wadding and primer.

3. Carefully insert cartridge: *stay clear of trigger!* (use one hand for final push).

4. Carefully make sure safety is off (*forward*).

A.16 Compressing Pump-Tube

1. Check all valves are closed.

2. Open H_2 (or He) cylinder looking at regulator valve to ensure pressure and no leaking.

3. Open regulator to 150 psi.

4. Open V4 (anti-clockwise).

5. Quickly vent using V5 $\rightarrow$ open and close — *do not over tighten.*

6. V1 to P and wait till pressure settles.

7. Check pressure level.
8. Open pump-tube valve to fill with H_2
9. Once stable close in reverse order (*do not over tighten*): close pump-tube valve, close V1, close V4, check V5 is closed, close H_2 cylinder then close regulator.
10. Note H_2 pressure on datasheet.
11. Double-check all closed.
12. Turn trigger-pull system key.
13. If using "atmosphere" open backfill valve slowly until correct pressure is reached.
14. Record final target chamber pressure on datasheet.

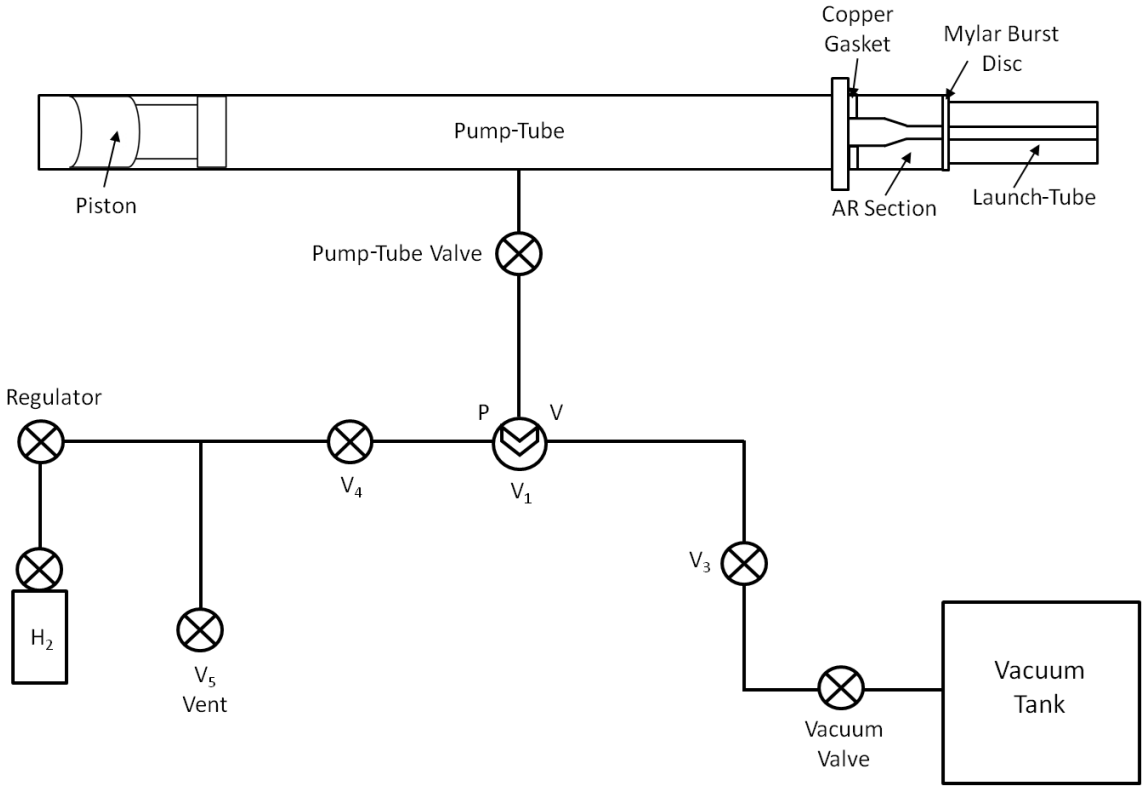

Figure A.1: Diagram of First-Stage Valve System. Figure in collaboration with and courtesy of Jon Tandy.

A.17 Firing Sequence

1. Arm UV-vis camera → press “Acquire” and check for “waiting for trigger”.
2. Check oscilloscope is set to record (“single” - reads waiting for trigger in bottom right).
3. Arm Cordin cameras → shutter open (check visually), external trigger checkedand press “arm” (button changes to disarm).
4. Check both trigger boxes are armed (flashing beacon).
5. Arm Photron camera → 150,000 fps, endless record (green).
6. Open laser shutter and ramp up to 600 mW (preset 1) and wait for current to settle.
7. Get ready to hit “acquire” button to arm IR camera during countdown.
8. Turn on second Photron monitor.
9. Put second trigger key in firing box and turn to activate launch controls.
10. Check if system has triggered and reset everything if necessary (repeat steps 1–7).
11. Countdown: “3, 2, 1, ACQUIRE (push IR acquire button), FIRE” → push fire button.

A.18 Post Experiment Procedure

1. Close laser shutter and return to low power (0.01 W).
2. Put laser back in standby mode.
3. Take out both trigger keys and put in desk drawer.
4. Save all data from cameras and oscilloscope.

5. Wait $\approx$ 15 minutes.
6. Turn off vacuum using lower vacuum lever (pump-down valve).
7. Open V5: vents H_2.
8. Open V4: vents H_2.
9. Set V1 to P: vents H_2.
10. Close valves in reverse order.
11. Backfill tank using backfill valve (fully open).
12. When tank pressure has settled open extraction vent valve (top lever).
13. Open side door of tank slightly (*make sure it does not swing out*) to allow airflow into tank.
14. Close backfill valve.
15. Set V1 to V.
16. Open V3.
17. Open vacuum valve (next to backfill).
18. Close V1, then V3, then vacuum valve.
19. Unclamp and remove trigger
20. Carefully take out cartridge and inspect for water (making note and ammount of water observed).
21. Remove cylinder shield.
22. Release bolts on pump-tube section and cheese wheel.
23. Remove AR section.

24. Release bolts on launch-tube section and remove top section.
25. Carefully remove launch-tube → put O-ring back.
26. With pin gauges, measure launch-tube and AR section diameters and record on datasheet.
27. Tighten bolts on pump-tube section.
28. Clean pump-tube (see next section).

A.19 Cleaning the Pump-tube

1. Tighten bolts on top.
2. Cover surfaces with tissues: front and end.
3. Use long brush and bore shine to clean through — rotate while pushing through.
4. Be careful not to knock gun safety pin out when pushing though.
5. Wipe brush clean and repeat 3–4 times.
6. Always make sure the brush end or sting end comes out after cleaning.
7. Take small circle swabs (≈ 6) and put on top of sting (one at a time).
8. Soak swab with acetone and pass through the pump-tube.
9. Repeat until the swab comes out almost white.
10. Loosen bolts holding pump-tube in place.

Appendix B

SPHIR Facility Performance and Velocimetry for 440C Steel Spheres

B.1 Velocimetry

Accurate, consistent, and reliable measurement of impact velocity is critical in the operation of a light-gas gun facility: data is difficult to use without confidence in the velocity measurement. The SPHIR facility has the unique problem of a very small, hard to see impactor. When the impactor is launched to speeds below 5 km/s into chamber pressures close to 1 Torr, velocimetry utilizing self-illumination is not possible. The primary technique used to measure impactor speed for 440C steel sphere projectiles ("cannonballs"), the Mylar Flash Method, is presented here. An alternative method to estimate projectile velocity, independent of the Photron high-speed camera, is also discussed.

A Photron SA-1 FASTCAM high-speed camera is used to capture images of the impact event. Typically, this camera is operated in the range of $72,000$ to $200,000$ frames per second. The camera is mounted above the target chamber looking down through a porthole such that the projectile passes through its field of view en-route to the target. A mirror located below the shot-line, is positioned in the field of view to allow imaging of the impact event on the target. The camera is triggered by the target impact flash, which is detected with a photo diode.

B.1.1 The Mylar Flash Method

Impactor velocities between 2 and 3 km/s, the lower end of the facility's velocity range, are achieved using a 22.7 mg, 1.8 mm diameter 440C stainless steel sphere. At this relatively low velocity, self-illuminated imaging of the projectile with the high-speed camera is impossible. Consequently, to measure the velocity of these slow spheres, a 12.7 µm thick Mylar sheet is placed in the camera field of view with its plane perpendicular to the velocity vector of the impactor. As the impactor passes through the Mylar, it produces a bright flash adequate for the camera to image. The thin Mylar sheet produces little or no damage to the steel ball at these perforation speeds.

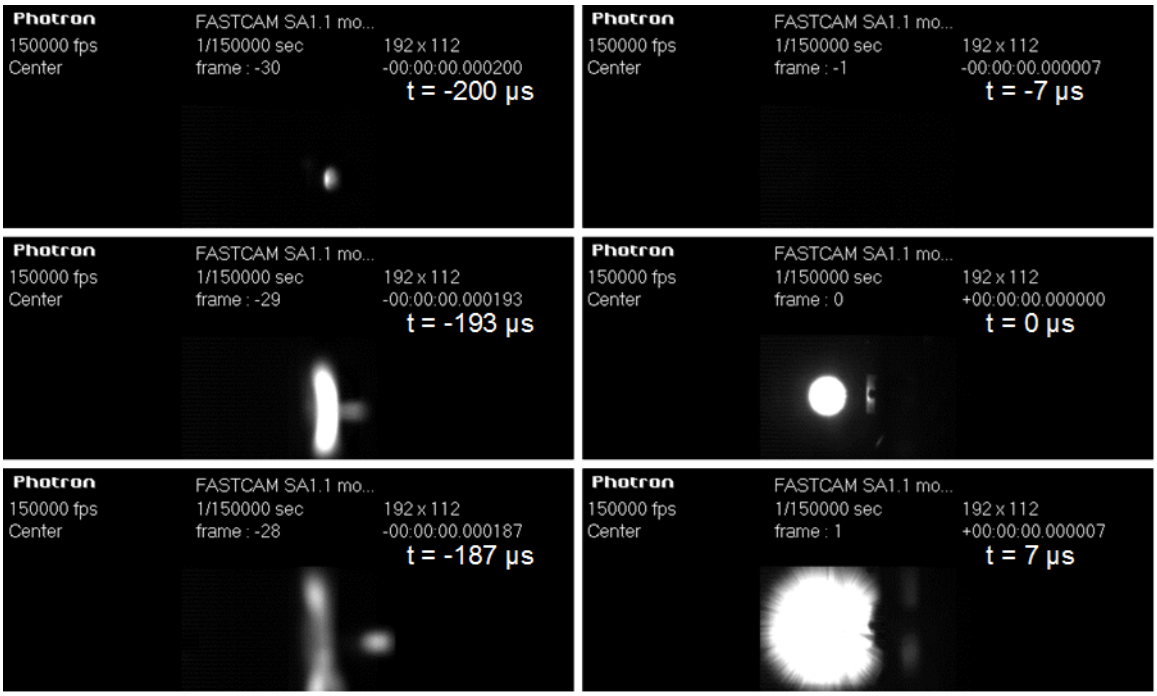

Figure B.1: Sequence of images from Photron high-speed camera used to measure the velocity of a 1.8 mm diameter 440C stainless steel sphere. The images above produced a velocity measurement of 3.0 km/s. The camera recorded this sequence at 150, 000 fps.

The Mylar sheet is located a fixed distance from the target and the impactor velocity is determined from this distance and the time-of-flight between the Mylar and target impact flashes. The uncertainty of the position of the Target and the Mylar

is small, less than 3 mm; hence, the major uncertainty in the velocity measurement is determined primarily by the framing rate of the high-speed camera.

Figure B.1 provides a frame by frame illustration of the Mylar and impact flashes used to measure the velocity of a 22.7 mg, 1.8 mm diameter 440C stainless steel sphere: the steel sphere creates a flash as it passes through the Mylar, then exits the camera's field of view, and finally impacts the target (triggering the camera). Note that the images in Figure B.1 were recorded with a frame rate of 150,000 fps. Given the geometry of the target chamber and limitations of the high-speed camera, this represents the largest frame rate that permits complete visualization of the target plate. The camera is operated at framing rates as high as 200,000 fps to measure velocity, however at these rates the ability to visualize the entire target is lost.

B.1.2 Alternative Method: Muzzle/Impact Flash

An alternate determination of the impactor velocity may be obtained through measurement of the distance and time-of-flight between the launch tube muzzle flash and the target impact flash. To perform this measurement, photo diodes were configured to record on 1 GSs^{-1}, 100 MHz bandwidth oscilloscope and positioned to look at the launch tube muzzle and at the impact site on the target. Figure B.2 presents a comparison of the results for this method compared to velocities measured by the Mylar-flash method.

The results show that the nylon 6/6 impactor velocities measured using the muzzle/target flash method are consistently lower than measurements provided by the high-speed camera. For the particular launch package used in this example, an observable muzzle flash occurs before the launch package reaches the muzzle yielding lower measured velocities for the muzzle/target flash method. Therefore, the muzzle/target flash method of velocity measurement does not provide an accurate description of the impact velocity. The level of this inaccuracy may be different for other launch package configurations or firing parameters. However, this disparity is inconsequential as this velocity technique is not considered in this work.

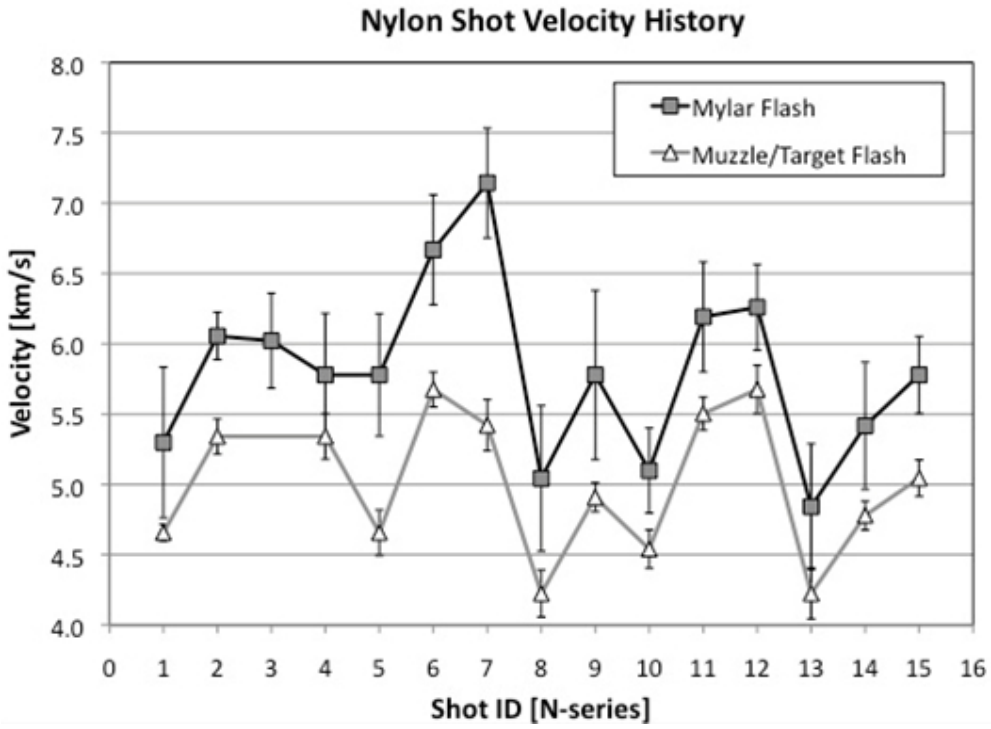

Figure B.2: Impact velocity history for a series of shots using the nylon 6/6 cylinder impactor. Comparison between velocities measured with the muzzle/impact flash method and Mylar flash method shown.

B.2 Steel Cannonball Velocity Performance

For the 440C stainless steel sphere impactor, Figure B.3 presents the history of velocities obtained during a series of 56 shots. For the data shown, the uncertainty of the velocity measurement is approximately plus and minus 2% of the measured value. The inherent variability in the impact velocity produced by the SPHIR facility is also highlighted in Figure B.3.

Considering the velocity history presented, Figure B.4 presents the cumulative probability distribution of the impact speeds obtained in this test series. If the two, low, outlier points are excluded, the distribution appears to be uniformly distributed between 2 and 3 km/s, which implies an equal probability of obtaining any velocity in this range. However, including all points, a Gaussian distribution is a better fit with a mean of 2.49 km/s and a standard deviation of 0.25 km/s.

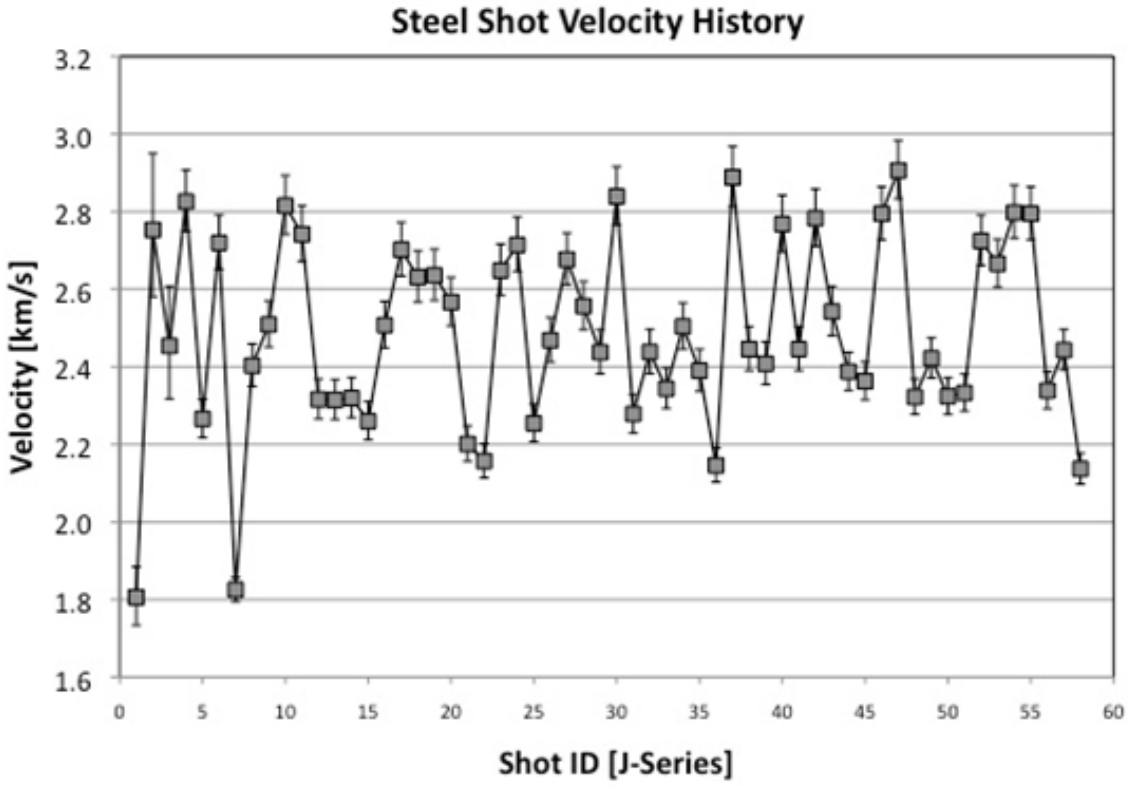

Figure B.3: Impact velocity history for a round of experiments using a 1.8 mm diameter, 22.7 mg, 440C stainless steel sphere launched using helium as the driver gas. Velocity measured with the Mylar flash method: The first three data points were measured at $72,000$ fps, all remaining points were measured at $200,000$ fps.

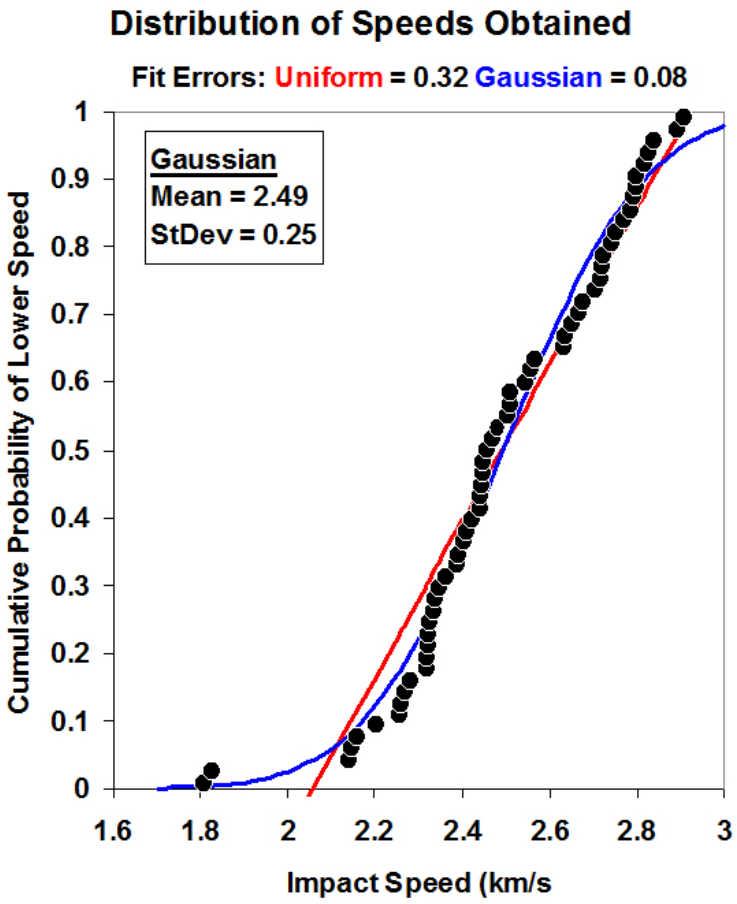

Figure B.4: The cumulative probability distribution of the impact speeds presented in Figure B.3, obtained for the 1.8 mm diameter 22.7mg 440C stainless steel sphere impactor.

Appendix C

Derivation of Blast Wave Constant K

Dimensional analysis described by Whitham [73] can be used to describe the pressure-dependent expansion of a blast wave produced in an explosion. The explosion is idealized as a sudden, symmetrical release of energy E concentrated at a point. It is also assumed that Energy is the only dimensional parameter introduced by the explosion. Lastly, the disturbance is assumed sufficiently strong such that the initial pressure and sounds speed of the ambient air are negligible compared to the pressures and velocities in disturbed flow. In this case, the strong shock relations apply. With these assumptions, the only dimensional parameter relating to the ambient gas is density ρ [73]. Accordingly, the only parameter involving length and time is $\frac{E}{\rho}$. Therefore, the dimensional analysis solution to describe the radius of the blast wave as a function of time is given by Eq. C.1.

$$R = K(\gamma)\left(\frac{E}{\rho_0}\right)^{1/5} t^{2/5} \tag{C.1}$$

Whitham describes constant K in Eq. 6.2 as a dimensionless number that is fixed from the definition of E as the total energy in the flow [73]. Reference is made by Whitham to work by G. I. Taylor [70], who provides an analytical solution for constant K. Taylor describes K as being a function of only the ratio of specific heats γ, as shown in Eq. C.1. This is an idealized assumption for a spherical blast wave.

As described by Whitham, K is fixed from the definition of the total energy in the

flow. Taylor defines the energy in the flow by Eq. C.2 and uses similarity assumptions and dimensional analysis to determine the effective K. Parameter A is defined as a constant that relates the radius of the blast wave R to the blast wave expansion speed dR/dt, as shown in Eq. C.3. The total energy in the flow is regarded as having two parts and determined by describing the kinetic energy and heat energy. Parameter B accounts for the contribution of the kinetic and heat energies, as presented by Taylor in Eq. C.4, through the integration of non-dimensional functions over the domain of the blast wave [70].

$$E = B\rho_0 A^2 \tag{C.2}$$

$$A = R^{3/2}\frac{\partial R}{\partial t} \tag{C.3}$$

$$B = 2\pi \int_0^1 \psi\phi^2\eta^2 \, d\eta + \frac{4\pi}{\gamma(\gamma-1)} \int_0^1 f\eta^2 \, d\eta \tag{C.4}$$

Given that R is the blast wave radius, r is the radial coordinate within the flow (behind the blast wave), therefore the non-dimensional spatial coordinate η is given by Eq. C.5. The non-dimensional solutions used to describe the energy by Taylor in Eq. C.4 are derived from his similarity assumptions for an expanding blast wave with constant total energy. ψ (Eq. C.6) describes the normalized flow density, ϕ (Eq. C.7) describes the normalized flow radial velocity, and f (Eq. C.8) describes the normalized pressure, where the local radial velocity is u and the speed of sound in air is a.

$$\eta = \frac{r}{R} \tag{C.5}$$

$$\psi = \frac{\rho}{\rho_0} \tag{C.6}$$

$$\phi = u\frac{\partial R^{-1}}{\partial t} \tag{C.7}$$

$$\phi = \frac{p}{p_0}a^2\frac{\partial R^{-2}}{\partial t} \tag{C.8}$$

The Rankine-Hugoniot relations describe conditions at the shockwave ($\eta = 1$). However, in order for the Rankine-Hugoniot conditions to be consistent with the similarity assumptions, it is assumed that the pressure behind the shockwave is large compared to the ambient pressure [70]. The following boundary conditions for ψ, f, and ϕ at the shockwave ($\eta = 1$) are then given by Eq. C.9, C.10, and C.11, respectively.

$$\psi = \frac{\gamma + 1}{\gamma - 1} \tag{C.9}$$

$$f = \frac{2\gamma}{\gamma + 1} \tag{C.10}$$

$$\phi = \frac{2}{\gamma + 1} \tag{C.11}$$

The functions $\psi(\eta)$, $f(\eta)$, and $\psi(\eta)$ are numerically computed and presented by Taylor for values of $\gamma = 1.4$ and $\gamma = 5/3$ [70]. These tabulated results by Taylor [70] for Eq. C.6 through C.8 are presented in Figure C.1 and for $\gamma = 1.4$ and Figure C.2 for $\gamma = 5/3$.

Numerical integration of these functions is used to determine the total kinetic and heat energy in the disturbed flow, as described in parameter B (Eq. C.4). The kinetic energy contribution is dependent upon the integration of the normalized density and flow velocity (Eq. C.12). The heat energy contribution is dependent upon the integration of the normalized pressure (Eq. C.13). For $\gamma = 1.4$, the solution to these integrals are given by Taylor. For $\gamma = 5/3$, tabulated results are numerically integrated to obtain the corresponding solution. These solutions for these integrals,

as well as the corresponding value of B are presented as a function of γ in Table C.1.

$$2\pi \int_0^1 \psi \phi^2 \eta^2 \, d\eta \tag{C.12}$$

$$\frac{4\pi}{\gamma(\gamma-1)} \int_0^1 f \eta^2 \, d\eta \tag{C.13}$$

With solutions describing the energy in the flow, K can then be determined from the definition of energy (Eq. C.2) by first eliminating parameter A through substitution of Eq. C.3 The result (Eq. C.14) can then be differentiated for R to obtain Eq. C.15.

$$R^{3/2} \frac{\partial R}{\partial t} = B^{-1/2} \frac{E}{\rho_0}^{1/2} \tag{C.14}$$

$$\tfrac{2}{5} R^{5/2} = \int B^{-1/2} \frac{E}{\rho_0}^{1/2} \, dt \tag{C.15}$$

Lastly, with the assumptions that B is a function of γ only and the total energy remains constant with time, Eq. C.15 can be integrated with respect to time to obtain the familiar dimensional analysis form of R equation Eq. C.16. It is then evident that dimensionless constant K is given by equation Eq. C.17. As presented in Table C.1, under idealized conditions, for $\gamma = 1.4$ and $\gamma = 5/3$, K is approximated as 1.03 and 1.13, respectively.

$$R = \frac{1.443}{B(\gamma)^{1/5}} \left(\frac{E}{\rho_0} \right)^{1/5} t^{2/5} \tag{C.16}$$

$$K(\gamma) = \frac{1.443}{B(\gamma)^{1/5}} \tag{C.17}$$

	$\int_0^1 \psi \phi^2 \eta^2 \, d\eta$	$\int_0^1 f \eta^2 \, d\eta$	$B(\gamma)$	$K(\gamma)$
$\gamma = 1.4$	0.185	0.187	5.358	1.03
$\gamma = 5/3$	0.146	3.307	3.307	1.13

Table C.1: Numerical integral results and solutions for blast wave constant K

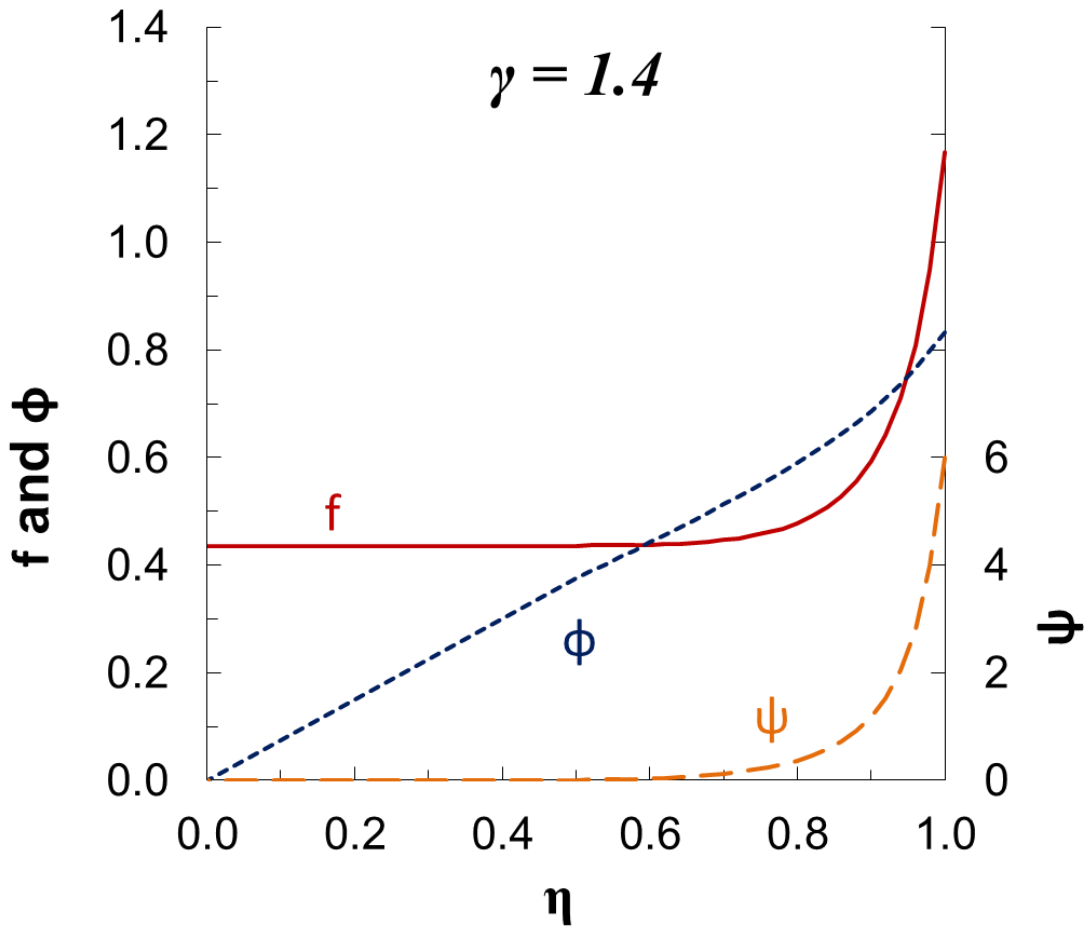

Figure C.1: Solutions provided by Taylor [70] for $\gamma = 1.4$ for the non-dimensional functions f, ϕ, and ψ as a function of non-dimensional flow coordinate η.

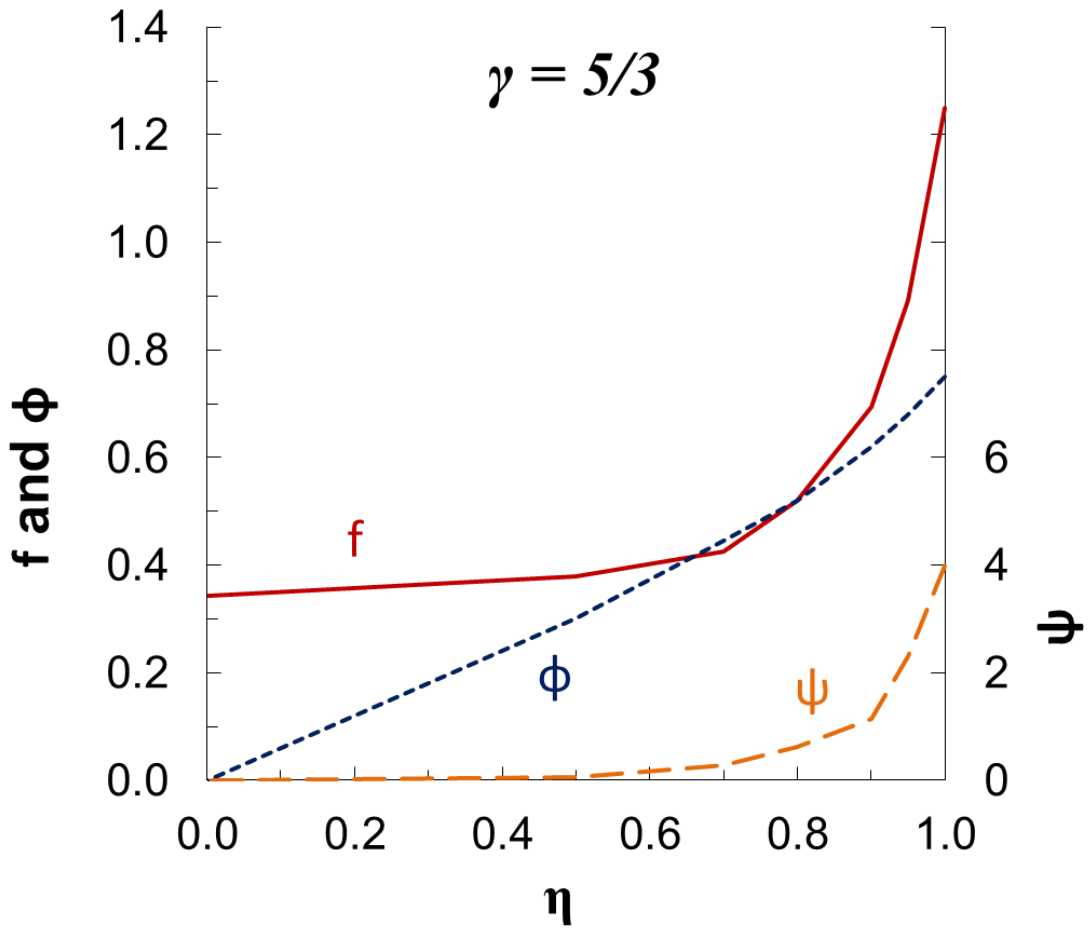

Figure C.2: Solutions provided by Taylor [70] for $\gamma = 5/3$ for the non-dimensional functions f, ϕ, and ψ as a function of non-dimensional flow coordinate η.

References

[1] M. Adams, M. Aivazis, H. N. Lan, B. Li, P. H. T. Kamga, M. McKerns, J. M. Mihaly, M. Ortiz, H. Owhadi, A. J. Rosakis, T. Sullivan, and J. Tandy. Optimal uncertainty quantification of hypervelocity impact. *Journal of the Mechanics and Physics of Solids*, pre-print submitted, 2013.

[2] M. Adams, A. Lashgari, B. Li, M. McKerns, J. Mihaly, M. Ortiz, H. Owhadi, A. Rosakis, M. Stalzer, and T. Sullivan. Rigorous model-based uncertainty quantification with application to terminal ballistics part ii. systems with uncontrollable inputs and large scatter. *Journal of the Mechanics and Physics of Solids*, 60(5), 2012.

[3] M. A. Adams. NASA JPL, personal communication.

[4] J. O. Arnold, H. E. Goldstein, and D. J. Rigali. "Follow the TPS" Appendix IV, F2 report of the Columbia Accident Investigation Board. Technical report, NASA, 2003.

[5] E. Christiansen. Handbook for designing MMOD protection. Technical Memorandum TM-2009-214785, NASA, 2009.

[6] E. L. Christiansen. Performance equations for advanced orbital debris shields. In *AIAA Space Programs and Technologies Conference*, number 92-1462, 1992.

[7] B. N. Corporation. *BNC 575*. 2955 Kerner Blvd San Rafael, CA 94901.

[8] B. G. Cour-Palais. Hypervelocity impact in metals, glass, and composites. *International Journal of Impact Engineering*, 5:221–237, 1987.

[9] L. David. Mars vs. comet in 2014: Preparing for red planet sky show. *SPACE.com*, 2013.

[10] A. Francesconi, D. Pavarin, C. Giacomuzzo, and F. Angrilli. Impact experiments on low-temperature bumpers. *International Journal of Impact Engineering*, 33(1–12):264–272, 2006.

[11] W. H. Friend, C. L. Murphy, and P. S. Gough. Review of meteoroid-bumper interaction studies at Mcgill University. Technical Report NASA CR-54858, NASA, 1969.

[12] D. J. Grosch and J. P. Riegel. Development and optimization of a micro two-stage light-gas gun. *International Journal of Impact Engineering*, 14(1–4):315–324, 1993.

[13] K. B. Hayashida and J. H. Robinson. Single wall penetration equations. Technical Report TM-103565, NASA, 1991.

[14] E. Hecht. *Optics*. Addison-Wesley, fourth edition, 2001.

[15] B. Hermalyn, P. H. Schultz, and J. T. Heineck. Early stage ejecta velocity distribution. In *40th Lunar and Planetary Science Conference*, number 2492, 2009.

[16] W. Herrmann and J. S. Wilbeck. Review of hypervelocity impact theories. *International Journal of Impact Engineering*, 5:307–322, 1987.

[17] S. A. Hill. Determination of an empirical model for the prediction of penetration hole diameter in thin plates from hypervelocity impact. *International Journal of Impact Engineering*, 30(3), 2004.

[18] H. Hornung. California Institute of Technology, personal communication, 2012.

[19] F. Horz, M. Cintala, R. P. Bernhard, and T. H. See. Dimensionally scaled penetration experiments to extract projectile sizes from space exposed surfaces. *International Journal of Impact Engineering*, 14, 1993.

[20] F. Horz, M. Cintala, R. P. Bernhard, and T. H. See. Dimensionally scaled penetration experiments: Aluminum targets and glass projectiles 50 micron to 3.2 mm in diameter. *International Journal of Impact Engineering*, 15(3), 1994.

[21] K. P. Huber and G. Herzberg. *Molecular Spectra and Molecular Structure, IV. Constants of Diatomic Molecules*. Van Nostrand Reinhold Company, 1979.

[22] D. Humes. Large craters on the meteoroid and debris environment. Technical Report NASA CP-3134, LDEF 69 Months in Space, First Post Retrieval Symposium, 1988.

[23] J. L. Hyde and E. L. Christiansen. Space shuttle meteoroid and orbital debris threat assessment handbook: Using the bumper-ii code for shuttle analysis. Technical Report JSC-29581, NASA, 2001.

[24] W. M. Isbell. Historical overview of hypervelocity impact diagnostic technology. *International Journal of Impact Engineering*, 5(1–4):389–410, 1987.

[25] W. M. Isbell. *Shock Waves Measuring the Dynamic Response of Materials*. Imperial College Press, 2005.

[26] P. C. Kassel and J. D. DiBattista. An ultra-high-speed photographic system for investigating hypervelocity impact phenomena. Technical Report TN D-6128, NASA, 1971.

[27] C. H. Konrad and R. E. Hollenbach. Techniques for determining velocity and position of small hypervelocity spheres. Technical Report Internal Report SAND75-0624, Sandia Laboratories, 1976.

[28] L. E. Lamberson. *Dynamic Optical Investigations of Hypervelocity Impact Damage*. PhD dissertation, California Institute of Technology, Graduate Aerospace Laboratories, 2010.

[29] L. E. Lamberson, V. Eliasson, and A. J. Rosakis. In situ optical investigation

of hypervelocity impact induced dynamic fracture. *Experimental Mechanics*, Special Edition Dynamic Behavior of Materials:1–10, 2011.

[30] N. Lee, S. Close, D. Lauben, I. Linscott, A. Goel, T. Johnson, J. Yee, A. Fletcher, R. Srama, S. Bugiel, A. Mocker, P. Colestock, and S. Green. Measurements of freely-expanding plasma from hypervelocity impacts. *International Journal of Impact Engineering*, 44:40 49, 2012.

[31] B. Li. California Institute of Technology, personal communication, April 2013.

[32] B. Li, F. Habbal, and M. Ortiz. Optimal transportation meshfree approximation schemes for fluid and plastic flows. *International Journal of Numerical Methods Engineering*, 83(12), 2010.

[33] J. S. Lim. *Two-Dimensional Signal and Image Processing*. Prentice Hall, Englewood Cliffs, New Jersey, 1990.

[34] J. Liou, M. J. Matney, P. D. Anz-Meador, D. Kessler, M. Jansen, and J. R. Theall. The new NASA Orbital Debris Engineering Model ORDEM2000. Technical Report TP-2002-210780, NASA, 2002.

[35] C. Lipson and N. J. Sheth. *Statistical Design and Analysis of Engineering Experiments*. McGraw-Hill, 1973.

[36] C. J. Maiden and A. R. MacMillan. Thin plate impacts. Technical Report CR-295, NASA, 1965.

[37] C. J. Maiden and A. R. McMillan. An investigation of the protection afforded to spacecraft by a thin shield. *AIAA Journal*, 2(11):1992–1998, 1964.

[38] S. P. Marsh. *LASL Shock Hugoniot Data*. University of California Press, 1980.

[39] H. McNamara, J. Jones, B. Kadfhan, R. Suggs, W. Cooke, and S. Smith. Meteoroid engineering model (mem): A meteoroid model for the inner solar system. *Earth, Moon, and Planets*, 95:123–139, 2004.

[40] M. Mello. California Institute of Technology, personal communications, 2009 to 2012.

[41] M. A. Meyers. *Dynamic Behavior of Materials*. John Wiley and Sons, Inc., 1994.

[42] J. M. Mihaly, L. E. Lamberson, M. A. Adams, and A. J. Rosakis. A low cost, small bore light-gas gun facility. In *Proceedings of the 11th Hypervelocity Impact Symposium*, pages 675–686, Freiburg, Germany, 2010.

[43] J. M. Mihaly, A. J. Rosakis, M. Adams, and J. Tandy. Imaging ejecta and debris cloud behavior using laser side-lighting. In *Proceedings of the 12th Hypervelocity Impact Symposium*, Baltimore, MD, USA, 2012. Procedia Engineering.

[44] J. M. Mihaly, J. D. Tandy, M. A. Adams, and A. J. Rosakis. In situ diagnostics for a small-bore hypervelocity impact facility. *International Journal of Impact Engineering*, in press, 2013.

[45] D. C. Montgomery and G. C. Runger. *Applied Statistics and Probability for Engineers*. John Wiley and Sons, Inc., 5th edition, 2011.

[46] R. H. Morrison. A preliminary investigation of projectile shape eeffects in hypervelocity impact of a double-sheet structure. Technical Report TN D-6944, NASA, 1972.

[47] R. W. B. Pearse and A. G. Gaydon. *The Identification of Molecular Spectra*. Chapman and Hall, London New York, fourth edition, 1976.

[48] T. Phillips. Collision Course? A Comet Heads for Mars, science.nasa.gov, March 27, 2013.

[49] A. J. Piekutowski. Debris clouds generated by hypervelocity impact of cylindrical projectiles with thin aluminum plates. *International Journal of Impact Engineering*, 5(1–4):509–518, 1987.

[50] A. J. Piekutowski. A simple dynamic model for the formation of debris clouds. *International Journal of Impact Engineering*, 10:453–471, 1990.

[51] A. J. Piekutowski. Characteristics of debris clouds produced by hypervelocity impact of aluminum spheres with thin aluminum plates. *International Journal of Impact Engineering*, 14(1–4):573–586, 1993.

[52] A. J. Piekutowski. Formation and description of debris clouds produced by hypervelocity impact. Contractor Report 4707, NASA, 1996.

[53] A. J. Piekutowski. Debris clouds produced by the hypervelocity impact of non-spherical projectiles. *International Journal of Impact Engineering*, 26(1–10):613–624, 2001.

[54] A. J. Piekutowski and K. L. Poorman. Effects of scale on the performance of whipple shields for impact velocities ranging from 7 to 10 km/s. In *Proceedings of the 12th Hypervelocity Impact Symposium*, Baltimore, MD, USA, 2012. Procedia Engineering.

[55] D. Pullin. California Institute of Technology, personal communication, April 2013.

[56] R. Putzar, F. Schaefer, and M. Lambert. Vulnerability of spacecraft harnesses to hypervelocity impacts. *International Journal of Impact Engineering*, 35(12):1728–1734, 2008.

[57] A. J. Rosakis. *Two Optical Techniques Sensitive to Gradients of Optical Path Difference: The Method of Caustics and the Coherent Gradient Sensor (CGS)*, volume III of *Experimental Techniques in Fracture (J. Epstein, Ed.)*, chapter 5, pages 125–170. 1992.

[58] W. P. Schonberg. MMOD risk assessment: Some recent developments and some suggestions for the future. Invited Lecture at NASA JPL, December 2012.

[59] P. H. Schultz, M. A. Adams, and S. Sugita. Impact flash spectroscopy. In *Lunar and Planetary Science Conference XXVII*, number 1149, 1996.

[60] G. S. Settles. *Schlieren and shadowgraph techniques: Visualizing phenomena in transparent media*. Springer-Verlag, Berlin, 2001.

[61] W. J. Smith. *Modern Optical Engineering*. McGraw-Hill, fourth edition, 2007.

[62] S. Sugita and P. H. Schultz. Interactions between impact-induced vapor clouds and the ambient atmosphere: 1. spectroscopic observations using diatomic molecular emission. *Journal od Geophysical Research*, 108(E6), 2003.

[63] S. Sugita and P. H. Schultz. Interactions between impact-induced vapor clouds and the ambient atmosphere: 2. theoretical modeling. *Journal od Geophysical Research*, 108(E6), 2003.

[64] S. Sugita and P. Schultz. Spectroscopic observation of atmospheric interaction of impact vapor clouds. In *Lunar and Planetary Science Conference XXIX*, number 1751, 1998.

[65] S. Sugita and P. Schultz. Spectroscopic observation of chemical interaction between impact-induced vapor clouds and the ambient atmosphere. In *Lunar and Planetary Science Conference XXXI*, number 2029, 2000.

[66] S. Sugita, P. Schultz, and M. Adams. In situ temperature measurements of impact-induced vapor clouds with a spectroscopic method. In *Lunar and Planetary Science Conference XXVIII*, number 1306, 1997.

[67] H. F. Swift. *Impact Dynamics*, chapter Hypervelocity Impact Mechanics. John Wiley and Sons, Inc., 1982.

[68] J. Tandy. California Institute of Technology, personal communication, April 2013.

[69] J. D. Tandy. California Institute of Technology, personal communication, January 2013.

[70] G. I. Taylor. The formation of a blast wave by a very intense explosion. i. theoretical discussion. *Proceedings of the Royal Society of London. Series A, Mathematical and Physical Sciences*, 201(1065):159–174, 1950.

[71] Thorlabs. http://www.thorlabs.us, Rectangular Step Variable Metallic Neutral Density Filters.

[72] A. Watts, D. Atkinson, and S. Rieco. Dimensional scaling for impact cratering and perforation. Independent Research and Development Project Number 069301 POD-IRAD-93-001, POD Associates, 1993.

[73] G. B. Whitham. *Linear and Nonlinear Waves*. John Wiley and Sons Inc., 1974.

[74] J. Williamsen and E. Howard. Video imaging of debris clouds following penetration of lightweight spacecraft materials. *International Journal of Impact Engineering*, 26(1–10):865–877, 2001.

[75] J. E. Williamsen, W. P. Schonberg, and H. J. Evans. Spacecraft module hole size and crack length prediction following a penetrating debris particle impact. In *Proceedings of the 12th Hypervelocity Impact Symposium*, Baltimore, MD, USA, 2012. Procedia Engineering.

[76] J. Williamsen and S. Evans. Predicting orbital debris shape and orientation effects on spacecraft shield ballistic limits based on characteristic length. *International Journal of Impact Engineering*, 33(1-12):862–871, 2006.

[77] S. Yadav, E. A. Repetto, G. Ravichandran, and M. Ortiz. A computational study of the influence of thermal softening on ballistic penetration in metals. *International Journal of Impact Engineering*, 25(8), 2001.

[78] Q. Zhang, Y. Chen, F. Huang, and R. Long. Experimental study on expansion characteristics of debris clouds produced by oblique hypervelocity impact of ly12 aluminum projectiles with thin ly12 aluminum plates. *International Journal of Impact Engineering*, 35(12):1884–1891, 2008.